Solid-State NMR of Metallic and Paramagnetic Systems

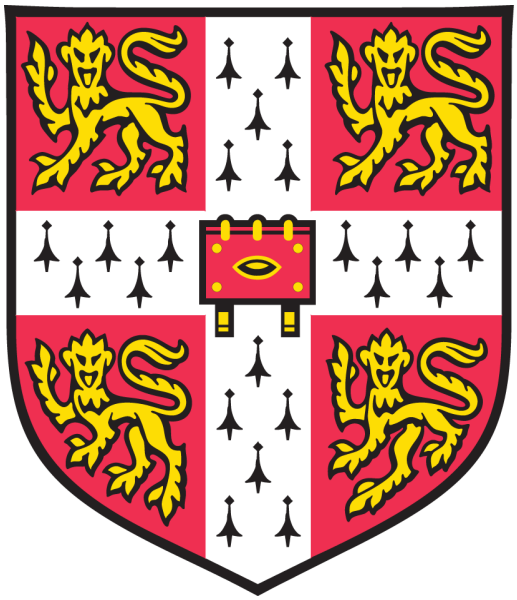

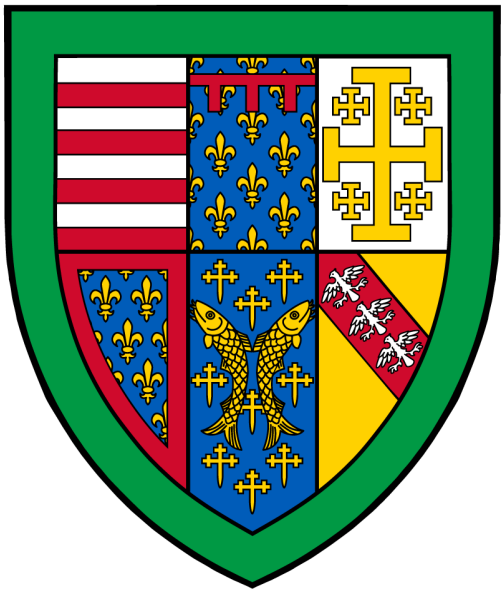

Michael Allan Hope

Queens' College

Department of Chemistry

University of Cambridge

This dissertation is submitted for the degree of

Doctor of Philosophy

May 2019

Declaration

I hereby declare that except where specific reference is made to the work of others, the contents of this dissertation are original and have not been submitted in whole or in part for consideration for any other degree or qualification in this, or any other University. This dissertation is the result of my own work and includes nothing that is the outcome of work done in collaboration, except where specifically indicated in the text. This dissertation contains less than 60,000 words excluding the table of contents, figure captions, bibliography, acknowledgments and appendices.

Michael Allan Hope

May 2019

Abstract

Solid-State NMR of Metallic and Paramagnetic Systems

Michael Allan Hope

Solid-state nuclear magnetic resonance (ssNMR) is a powerful element-specific technique to study local atomic environments in many different classes of materials; however, ssNMR-based methodologies have primarily focussed on diamagnetic systems without any unpaired electrons. In paramagnetic or metallic materials localised or delocalised unpaired electrons, respectively, couple with the nuclear magnetic moments and introduce significantly greater spectral broadening, often combined with very fast nuclear relaxation, so that these systems are challenging to study. However, these same hyperfine interactions can also provide important details of the electronic and magnetic structure for a sample.

In this work ssNMR methodologies are developed to study different paramagnetic and metallic systems, and thereby demonstrate the information that can be obtained. These strategies include investigating the temperature dependence of the NMR spectra, to distinguish paramagnetic and metallic shifts, and exploiting differences in relaxation rates to afford spectral selectivity and extract further information. Specifically, the following studies have been performed: 1) The ^{17}O NMR of Sm_2O_3, Eu_2O_3 and Sm/Eu-substituted CeO_2, for which the lanthanide ions induce paramagnetic shifts with unusual temperature dependences due to the presence of low-lying excited electronic states. The spectra of the monoclinic polymorphs of the sesquioxides are assigned and the paramagnetic shifts of the cubic polymorphs are investigated over a wide temperature range. Different local environments in the substituted CeO_2 are identified due to nearest-neighbour lanthanide ions and oxygen vacancies, and the activation energy for oxygen motion is determined from variable temperature T_1 measurements. 2) The surface-selective direct ^{17}O dynamic nuclear polarisation (DNP) NMR of CeO_2 nanoparticles. In this case exogenous paramagnetic biradicals are deliberately introduced and exploited to selectively hyperpolarise the surface of CeO_2, so that the first three (sub-)surface ^{17}O environments can be identified with high specificity. Polarisation build-up curves show that this selectivity is due to faster polarisation of the surface relative to the bulk. 3) The structure and mechanism of electrochemically metallised VO_2. By comparison with catalytically hydrogenated VO_2, electrochemical metallisation is shown to be associated with hydrogen intercalation, and the presence of metallic and paramagnetic phases is explored with ^{1}H, ^{2}H, ^{17}O and ^{51}V NMR. By selectively deuterating the ionic liquid electrolyte, hydrogenation is then shown to arise from electrolyte breakdown, and the degree of hydrogenation and resultant phases are investigated as a function of the particle size and the temperature of electrochemical metallisation.

Acknowledgements

Foremost, I would like to thank Professor Clare Grey for her inspiration and guidance. It can take me months to understand or appreciate why something Clare has said is true, or worth pursuing, but invariably I should have listened in the first place. I have thoroughly enjoyed our scientific discussions, difficult though they can be, and the greatest test of any idea is to "get it past Clare". I have always felt challenged to improve all aspects of my science whilst supported to do so; this is a remarkable combination.

I am grateful to all the members of the Grey group, both past and present, who have taught me new techniques, given me new ideas, and with whom I've had a lot of fun on the way. The benefits of working in such an outstanding, collaborative and caring group cannot be overstated. There are far too many people to mention them all individually, but I would specifically like to thank Dr Alex Forse for first teaching me how to perform ssNMR, Dr Kent Griffith for his day-to-day support, direction and insight, especially for the VO_2 project, and Dr David Halat for his infectious enthusiasm for NMR, encyclopaedic knowledge of the literature, and great sense of humour. Phil Reeves also deserves a mention for his role as graphic design consultant, and as a good friend.

I would like to thank everyone who has proofread this thesis, often at short notice: Drs Matt Dunstan, Kent Griffith, David Halat, Jae Lee, Katharina Märker and Chris O'Keefe; and, above all, my father who proofread it cover to cover in a week. I am grateful to the Oppenheimer foundation for funding as well as to all collaborators, listed on the following page, for their contributions.

Some of the work presented here was performed by others, specifically: the lanthanide oxide DFT calculations were performed by Jae Lee; Matthias Groh helped with flame-sealing; the analysis of errors in T_1 data was performed by David Halat; the ESR spectrum of Gd-CeO_2 was measured by Euan Bassey; and the VO_2 films were produced by Bin Cui. I am also grateful to Prof. Stuart Parkin for introducing us to the enigma of VO_2 electrolyte gating, and to Dr. Siân Dutton for many discussions of the more physics-related phenomena.

I would like to thank my family for laying the foundations which have allowed me to get this far – raising me was undoubtedly more effort than a simple PhD – as well as Georgia and Lissa for making a home to come back to. Finally, I must thank Georgia for her continual support and for keeping me (more or less) balanced throughout my studies.

List of Publications

Publications included in this thesis:

Hope, M. A.; Halat, D. M.; Lee, J; Grey, C. P. A ^{17}O Paramagnetic NMR Study of Sm_2O_3, Eu_2O_3, and Sm/Eu-substituted CeO_2. *Solid State NMR*; *in revision.*

Hope, M. A.; Halat, D. M.; Magusin, P. C. M. M.; Paul, S.; Peng, L.; Grey, C. P. Surface-Selective Direct ^{17}O DNP NMR of CeO_2 Nanoparticles. *Chem. Commun.* **2017**, *53* (13), 2142–2145.

Hope, M. A.; Griffith, K. J.; Cui, B.; Gao, F.; Dutton, S. E.; Parkin, S. S. P.; Grey, C. P. The Role of Ionic Liquid Breakdown in the Electrochemical Metallization of VO_2 : An NMR Study of Gating Mechanisms and VO_2 Reduction. *J. Am. Chem. Soc.* **2018**, *140* (48), 16685–16696.

Publications not included in this thesis:

Hope, M. A.; Forse, A. C.; Griffith, K. J.; Lukatskaya, M. R.; Ghidiu, M.; Gogotsi, Y.; Grey, C. P. NMR Reveals the Surface Functionalisation of Ti_3C_2 MXene. *Phys. Chem. Chem. Phys.* **2016**, *18* (7), 5099–5102.

Chen, J; Wu, X-P; **Hope, M.A.**; Qian, K; Halat, D. M; Liu, T; Li, Y; Shen, L; Ke, X; Wen, Y; Du, J-H; Magusin, P. C. M. M.; Ding, W; Gong, X-Q; Grey, C. P.; Peng, L. Polar Surface Structure of Oxide Nanocrystals Revealed with Solid-State NMR Spectroscopy. *Submitted.*

List of Abbreviations

CP – cross polarisation

CSA – chemical shift anisotropy

DFT – density functional theory

DNP – dynamic nuclear polarisation

ESR – electron spin resonance

FC – field cooled

FWHM – full-width at half-maximum

ICSD – inorganic crystal structure database

MAS – magic angle spinning

MATPASS – magic angle turning phase adjusted spinning sidebands

MIT – metal–insulation transition

NMR – nuclear magnetic resonance

rf – radiofrequency

SEM – scanning electron microscopy

ssNMR – solid-state nuclear magnetic resonance

STEM – scanning transmission electron microscopy

TEM – transmission electron microscopy

TGA – thermogravimetric analysis

VOCS – variable offset cumulative spectroscopy

VT – variable temperature

XRD – X-ray diffraction

ZFC – zero-field cooled

ZFS – zero-field splitting

Table of Contents

Chapter 1: Introduction

"Pushing the boundaries of NMR, through rotor crashes"

Anon., Grey Group whiteboard

One of the primary objectives of materials chemistry is to develop new functional materials with improved properties for a given application. In order to design such materials, one must understand the factors which dictate the relevant properties at the atomic scale; developing such structure–property relationships is at the heart of material chemistry. Historically, research has focussed on the long-range structure accessible from diffraction-based techniques. This is an extremely powerful approach, which can unambiguously solve the structure of a bulk, perfectly ordered, material. However, many functionally relevant materials do not satisfy these criteria: they are disordered, nanoparticulate, or derive their activity from their surfaces. For these materials, it is the *local* structure which determines the potential performance, and this can be altogether more challenging to investigate. Solid-state nuclear magnetic resonance (ssNMR) spectroscopy is one technique which has proved to be exceedingly versatile for the study of local structure in materials.

NMR spectroscopy is the study of nuclear spin energy levels in the presence of a large applied magnetic field. The splitting of these energy levels depends primarily on the nucleus in question, and as such NMR is an element-specific technique, but the splitting also depends on the environment of the nucleus, which modifies the local magnetic field. Minor differences in the nuclear environment can result in a significant shift in the resonant frequency (relative to the linewidth, which is often very narrow due to long nuclear spin lifetimes), so that NMR spectroscopy is a very sensitive probe of local structure. More complicated manipulations of the nuclear spin systems, which exploit the spin–spin interactions, can reveal atomic connectivity and proximity, while relaxation phenomena can provide further insight, including information on motional dynamics.

For these reasons, liquid/solution state NMR has been an integral, and routine, component of the toolbox of analytical chemistry for over 50 years.[1] In liquids, molecules tumble rapidly averaging out anisotropic interactions, which yields narrow NMR resonances and hence greater signal-to-noise and resolution. In solids, on the other hand, these anisotropic interactions are generally still present which can result in substantial spectral broadening, increasing the difficulty of extracting useful information in ssNMR experiments. Despite this, effective

methodologies and hardware have been developed to permit the study of solid materials with NMR, including magic angle spinning (MAS), higher magnetic fields, and advanced pulse sequences; today, most ssNMR experiments are as routine as solution NMR, albeit more specialised.[2–4]

Developments in ssNMR spectroscopy have, however, primarily focussed on diamagnetic systems without any unpaired electrons. In paramagnetic and metallic materials there are localised and delocalised unpaired electrons, respectively, which can couple with the nuclear spins.[5] The magnetic moment associated with unpaired electrons is ~3 orders of magnitude greater than that of nuclear spins, and consequently this coupling can introduce substantial spectral broadening, often combined with very fast nuclear relaxation, so that these systems remain challenging to study. Nevertheless, these same interactions can provide important information about a sample, including the electronic structure and oxidation state of paramagnetic ions, and the spatial relation between different nuclei and the paramagnetic centre, either via the orientationally dependent dipolar coupling, or the pathway of intervening orbitals mediating a Fermi contact shift.

1.1 Thesis Overview

In this thesis, methodologies are presented for the investigation of paramagnetic and metallic systems with ssNMR. This takes the form of three different investigations for which pertinent questions could be addressed using ssNMR; by exploring these systems and addressing the scientific questions, methods have been developed which are applicable to other challenging systems. Specifically, the following studies will be described:

- Chapter 3: The ^{17}O NMR of the paramagnetic lanthanide oxides Sm_2O_3 and Eu_2O_3, as well as Sm- and Eu- substituted CeO_2. This introduces the challenges of ^{17}O NMR, while also being a challenging paramagnetic system; nevertheless, the information which can be extracted from such paramagnetic systems will be demonstrated.
- Chapter 4: The ^{17}O dynamic nuclear polarisation (DNP) NMR of CeO_2. In this study, paramagnetism is exploited to enhance the NMR signal, rather than reducing the signal-to-noise ratio, as is more common in conventional ssNMR experiments.
- Chapter 5: The structure and mechanism of electrolyte gated VO_2. This is a more general, multinuclear NMR study, which demonstrates the presence of both

paramagnetic and metallic phases after electrochemically induced hydrogenation of VO_2. The origin of the hydrogen is then proved by isotopic substitution.

Before presenting this work, the background and theory underlying the ssNMR experiments will be described in Chapter 2, including the key interactions influencing the NMR systems (§2.1), the causes of nuclear relaxation and the information contained therein (§2.2), and the theory of DNP (§2.3). Then afterwards, in Chapter 6, some general conclusions are drawn from the work and the outlook considered.

For the remainder of this chapter, the systems above will be introduced, along with the common themes connecting them.

1.2 ^{17}O NMR

A significant proportion of scientifically and industrially relevant materials are oxides or contain oxygen; oxygen NMR could therefore provide a wealth of information on these materials. Unfortunately, the only stable NMR active nucleus of oxygen is ^{17}O, which has a natural abundance of just 0.037%, and is quadrupolar ($I = 5/2$); the former drastically reduces the acquirable signal, so that isotopic enrichment, or some other signal enhancement method, is almost always required, while the latter can result in spectral broadening, further reducing the signal as well as affecting the achievable resolution. Despite this, ^{17}O NMR spectroscopy has been successfully applied to many diamagnetic systems.[6,7]

Prior paramagnetic ssNMR studies have typically focussed on nuclei further removed from the paramagnetic centre, e.g. ^{7}Li in Li-ion battery cathode materials such as transition metal oxides, where the spin-transfer pathways from unpaired electrons to the NMR-active nucleus involve intervening O sites.[8,9] The aforementioned challenges associated with ^{17}O NMR are compounded in paramagnetic systems because there is often direct bonding between the paramagnetic ion and oxygen sites. Nonetheless, the sensitivity of paramagnetic ^{17}O NMR spectra to distances from, and the electronic and magnetic properties of, the paramagnetic centre has enabled insights in recent years into materials as diverse as metal-organic frameworks,[10] battery materials,[11] mixed ionic-electronic conductors,[12,13] and phases of geological and radiochemical relevance.[14,15]

Notwithstanding this previous work, the behaviour of paramagnetic ^{17}O NMR shifts even in relatively simple systems, such as polymorphs of the lanthanide oxides and other lanthanide-substituted phases, still remain unexplored. In Chapter 3, the ^{17}O spectra of the monoclinic

polymorphs of Sm_2O_3 and Eu_2O_3 are reported for the first time; the spectra are then assigned, primarily on the basis of careful quantification and differences in the quadrupolar coupling constants, which can be correlated with the multiplicity and distortion of the crystallographic oxygen sites.

The NMR experiments on CeO_2 and *Ln*-substituted CeO_2 in Chapters 4 and 3, respectively, utilise ^{17}O, since cerium has no stable NMR active nuclides. In addition to its technological relevance (see below), CeO_2 is a useful material on which to develop ^{17}O NMR methodologies, as it has a cubic structure exhibiting an extremely narrow ^{17}O resonance;[16] therefore, the broadening induced by modifications of the structure, i.e. at a surface or due to the presence of a paramagnetic substituent, is less likely to result in overlapping or unobservable signals, than for materials with broader and/or multiple signals in the pristine sample. However, the same tactics developed here should still be applicable to less ideal samples.

Finally, ^{17}O NMR is employed in Chapter 5 to study the electronic structure of the phases present in reduced VO_2. Although ^{51}V can be used to identify metallic phases, for paramagnetic phases the unpaired electrons are present on the vanadium atom, so that the ^{51}V nucleus relaxes too quickly to be observed; ^{17}O NMR can, however, be used instead. Furthermore, even for metallic phases, the significantly narrower ^{17}O linewidth allows minor differences in the electronic density of states to be observed, which are not apparent in the ^{51}V NMR spectrum.

1.3 Dynamic Nuclear Polarisation (DNP)

Dynamic nuclear polarisation (DNP) exploits the ~10^3 times greater gyromagnetic ratio of paramagnetic electrons to hyperpolarise nuclear spins and hence increase the signal in NMR experiments. DNP was first proposed by Overhauser in 1953,[17] and then demonstrated experimentally in the same year by Carver and Slichter, using the paramagnetism of the conduction electrons in lithium metal.[18] The mechanisms of DNP will be discussed in detail in §2.3, but the driving force in all cases is saturation of the ESR transition, which requires high power irradiation at the ESR frequency. In the experiments of Carver and Slichter, a magnetic field of 3 mT was used, so that the ESR frequency occurred at 84 MHz and high power radiofrequency hardware could be used to saturate the transition. To achieve high resolution in NMR experiments, on the other hand, magnetic fields of ~10 T are used, for which the ESR frequency occurs at ~300 GHz, in the microwave range. Until the mid-1990s, high-power microwave sources at these frequencies were not available, and DNP was not widely adopted; with the advent of gyrotron microwave sources, however, DNP became feasible at high field,[19]

and following extensive method development by the group of Griffin, and others, commercial DNP NMR systems are now available: as a result, DNP is currently a very active area of research.

In a typical DNP experiment, the paramagnetic source is an organic radical dissolved in a glass-forming solvent, which is added to the sample. For solid samples, the radicals are external to the particles, and since DNP hyperpolarisation is a short-range effect, the surfaces can be selectively hyperpolarised relative to the bulk; this is sometimes referred to as surface enhanced nuclear spectroscopy (DNP SENS).[20–22] Although, surface-selective DNP had been demonstrated for various systems, Chapter 4 reports the first example of surface-selective direct ^{17}O DNP NMR (that is to say not via cross polarisation from hyperpolarised ^{1}H nuclei). Some initial results on endogenous ^{17}O DNP, where the radical source is doped into the bulk of the sample, are also presented for 1 at% Gd-doped CeO_2; this is the method of choice to enhance the NMR signal from the bulk of particles, rather than the surface, for systems with slow spin-diffusion (such as ^{17}O, due to its low natural abundance and quadrupolar nature).

1.4 Utilising NMR Relaxation

Relaxation in NMR is the process by which transverse magnetisation is lost, and the equilibrium longitudinal magnetisation is restored. The types and mechanisms of relaxation will be discussed in §2.2 and relaxation phenomena have been exploited throughout this work to achieve greater selectivity and extract additional information.

To selectively observe environments with fast relaxation, a relaxation filter can be used: two spectra are recorded which allow the spins to relax for different lengths of time, and then an appropriate difference taken. This technique is used in Chapter 5 to detect the fast-relaxing metallic ^{1}H environments in the electrolyte gated thin film of VO_2, in the presence of a slow-relaxing diamagnetic background, despite the fact that the former signal is orders of magnitude less intense. In Chapter 3, a relaxation filter is used to selectively observe the ^{17}O environments in Eu-substituted CeO_2 which have Eu nearest neighbours, and hence relax more quickly due to the paramagnetic relaxation enhancement.

The relaxation rate can also provide important mechanistic information. In Chapter 3, the oxide-ion motion of *Ln*-substituted CeO_2 is investigated via the ^{17}O relaxation constant, while in Chapter 4 the surface selectivity of ^{17}O DNP is shown to arise from the faster build-up of

hyperpolarisation for the surface sites relative to the bulk; this build-up is closely related to relaxation, but in the presence of DNP.

1.5 Variable Temperature (VT) NMR

Many of the interactions responsible for the NMR frequency or relaxation properties are temperature dependent; VT NMR can therefore yield information which is not available at a single temperature. For example, paramagnetic shifts are typically highly temperature dependent, while Knight shifts in metals are not; this difference is used to distinguish metallic and paramagnetic phases of hydrogenated VO_2 in Chapter 5. The temperature dependence of paramagnetic shifts is also exploited in Chapter 3 to separate the ^{17}O resonances from different crystallographic sites in monoclinic Sm_2O_3, and to confirm which ^{17}O signals in *Ln*-substituted CeO_2 arise from *Ln* nearest neighbours. The temperature dependence of paramagnetic shifts is not always straightforward, however, for example in the presence of low-lying excited electronic states; this is explored by measuring the ^{17}O shifts of cubic Sm_2O_3 and Eu_2O_3 over a wide temperature range.

Motion is also strongly affected by temperature, typically following an Arrhenius dependence. VT ^{17}O NMR is therefore used in Chapter 3 to extract the activation energy for oxide-ion motion in *Ln*-substituted CeO_2. VT ^{17}O NMR is also used in Chapter 4 to show that the broad linewidth of the (sub-)surface oxygen signals arises from a distribution of environments, which at room temperature interchange rapidly to yield sharp motionally averaged resonances.

1.6 Paramagnetism of Lanthanides

Lanthanides can have very large electron magnetic moments due to partial filling of the seven *f*-orbitals; moreover, the *f*-orbitals are contracted and hence do not interact strongly with bonded atoms, so that there is minimal crystal field splitting and therefore little driving force to undergo electron pairing and reduce the magnetic moment. These factors result in large paramagnetic NMR shifts, which can complicate spectra and render them challenging to record, but have also been exploited to provide useful structural information in systems such as lanthanide pyrochlores[23,24] and doped calcium scandate[25], which have applications as catalysts and phosphors. Furthermore, due to the chemical similarity of lanthanides, the lanthanide ion can often be exchanged without significantly changing the structure and bonding of the system, which allows the paramagnetic shifts to be investigated as a function of the electron moment.

The magnetism of lanthanide ions can be complex, but a great deal of theoretical and experimental work has gone into understanding this magnetism as well as the electron spin resonance (ESR – the electron analogue of NMR), NMR, and optical spectra.[5,26,27] This has primarily been driven by their applications, such as lasers, high-flux magnets and phosphors, but as a result, there is a strong theoretical basis on which to predict the temperature dependence of the lanthanide-induced paramagnetic shifts in NMR; an example of such analysis is presented in Chapter 3, for the non-trivial cases of Sm^{3+} and Eu^{3+}.

1.7 CeO_2

Among the lanthanide oxides, ceria (CeO_2) is arguably the most technologically important: it finds use as a catalyst in CO oxidation and NO reduction,[28,29] as an oxygen storage material for chemical looping and in automotive catalytic converters,[30,31] and is among the best known isotropic oxide-ion conductors in the intermediate temperature range (400 – 800 °C).[32–34] This last property is significantly enhanced by means of aliovalent doping, commonly using trivalent lanthanide ions,[34–36] leading to an increase in oxygen vacancy concentration due to charge compensation and a concomitant rise in oxide-ion conductivity. The exemplar phase of this class of conductors is Gd-doped ceria,[37] which remains a common electrolyte (and anode component) used in solid oxide fuel cells.[38,39] In Chapter 3, the local structure of Sm- and Eu-substituted CeO_2 are investigated with ssNMR and the oxide-ion conductivity is explored.

For the applications of CeO_2 as a heterogeneous catalysis, the catalytic activity and mechanism are determined by the surface structure. The techniques traditionally used to investigate surfaces often require ultra-high vacuum conditions (e.g. X-ray photoelectron spectroscopy, Auger electron spectroscopy and secondary-ion mass spectrometry) or investigate only a very small proportion of the sample (e.g. scanning tunnelling microscopy and atomic force microscopy).[40] In Chapter 4, surface-selective NMR is employed to investigate CeO_2 nanoparticles, providing local structural information which is representative of the entire sample, under ambient pressure conditions.

1.8 Metallic and Paramagnetic Phases Derived from VO_2

Chapter 5 is concerned with VO_2, which is famous for its metal–insulator transition (MIT): below 67 ^oC VO_2 is an insulator, while above it is a metal;[41] this modification of the electronic structure is associated with a change in the ^{51}V NMR shift of nearly 6000 ppm,[42] and a similar effect in the ^{17}O NMR is reported here. The electronic structure of VO_2 can also be altered by

reduction, both chemically and electrochemically, which introduces more electrons into the band structure. Specifically, hydrogenation is shown to produce first a metallic phase and then a localised paramagnetic phase; ^{1}H NMR is an excellent probe of the electronic structure for the hydrogenated phases, exhibiting a Knight shift and Fermi contact paramagnetic shift, respectively, whereby these two cases can be distinguished.

There has been significant interest in electronically inducing the MIT for proposed applications as Mott transistors and memory devices,[43,44] most recently using the technique of electrolyte gating, which is essentially an electrochemical reduction.[45,46] Since NMR is element specific, it is relatively easy to prove with ^{1}H NMR that this reduction is associated with hydrogen intercalation, for bulk samples of VO_2; the concomitant changes in electronic structure are corroborated with ^{17}O and ^{51}V NMR. Furthermore, it is shown that the hydrogen arises from breakdown of the ionic liquid electrolyte, by measuring the ^{2}H NMR spectrum following selective deuteration.

Previous work on electrolyte gating has focussed on thin films, for which excellent control of the structure and geometry can be achieved. However, the very small amount of sample in thin film systems is a challenge for NMR spectroscopy, given the inherently low sensitivity afforded by the small energy scales involved. Nevertheless, hydrogen in a metallic environment in an electrolyte gated thin film of VO_2 is identified by ^{1}H NMR, corroborating the applicability of the results obtained for bulk VO_2, although a very long experimental time was required.

Chapter 2: Solid-State NMR Spectroscopy

2.1 Key Interactions in NMR Spectra

There are a number of different contributions to the resonant frequency observed in ssNMR spectra that are important to consider for the systems presented in this thesis.

2.1.1 Chemical Shielding

Chemical shielding is the familiar effect which is most commonly responsible for dispersion in NMR spectra, whereby the response of electrons to the applied magnetic field modifies the field experienced at the nucleus. The chemical shielding is described by a second rank tensor, **σ**, which relates the applied magnetic field to the local field at the nucleus, both of which are vector quantities. The effect of chemical shielding on the system is then given by the chemical shielding Hamiltonian,

$$\widehat{H}_{cs} = \gamma \hat{\mathbf{I}} \cdot \boldsymbol{\sigma} \cdot \mathbf{B_0}, \tag{2.1}$$

where γ is the gyromagnetic ratio of the nucleus, $\hat{\mathbf{I}}$ is the nuclear spin operator and $\mathbf{B_0}$ is the applied field.[2]

There are two contributions to the chemical shielding tensor, the diamagnetic term and the paramagnetic term: $\boldsymbol{\sigma} = \boldsymbol{\sigma^d} + \boldsymbol{\sigma^p}$. The diamagnetic term, so called because it opposes the applied field, arises from the induced circulation of electrons which produces a secondary opposite field; this reduces the observed shift. The paramagnetic term, which augments the applied field, arises from the mixing in of excited states by the applied field, the orbital angular momenta of which couple with the nucleus; this increases the observed shift. The components of these tensors are given by:

$$\sigma^d_{\gamma\gamma} = \frac{\mu_0}{4\pi}\frac{e^2}{2m_e}\left\langle \Psi_0 \left| \sum_\lambda \frac{\alpha_\lambda^2 + \beta_\lambda^2}{r_\lambda^3} \right| \Psi_0 \right\rangle \tag{2.2}$$

$$\sigma^p_{\alpha\beta} = -\frac{\mu_0}{4\pi}\frac{e^2}{2m_e}\sum_{i\in occ}\sum_{j\in unocc}\frac{\langle\psi_i|\hat{l}_\alpha|\psi_j\rangle\left\langle\psi_j\left|\frac{\hat{l}_\beta}{r^3}\right|\psi_i\right\rangle}{E_j - E_i} \tag{2.3}$$

where α, β and γ are the Cartesian axes, μ_0 is the permeability of a vacuum, e is the electronic charge, m_e is the mass of the electron, Ψ_0 is the all-electron ground-state wavefunction, λ is a sum over electrons, $\hat{l}_\alpha$ are the components of the orbital angular momentum operator, ψ_i and ψ_j are occupied and unoccupied one electron wavefunctions respectively and E_i and E_j their energies. The diamagnetic term is dominated by core electrons, while the paramagnetic term depends on the existence of high-lying occupied states and low-lying unoccupied states which are related by a rotation. When present, this latter term tends to dominate.

Chemical shielding results in a change in the frequency of the NMR signal, which is typically measured relative to a reference compound to give the chemical shift:

$$\delta = \frac{\nu - \nu_{ref}}{\nu_{ref}}. \tag{2.4}$$

As the chemical shielding is orientationally dependent, so too are the NMR frequency and hence the chemical shift. The chemical shift can therefore also be described by a tensor, $\boldsymbol{\delta}$, which has the same principal axes as the shielding tensor and components given by

$$\delta_{\alpha\beta} = \frac{\sigma_{\alpha\beta}^{ref} - \sigma_{\alpha\beta}}{1 - \sigma_{\alpha\beta}} \approx \sigma_{\alpha\beta}^{ref} - \sigma_{\alpha\beta}. \tag{2.5}$$

The chemical shift tensor can be described by three parameters, which in the Haeberlen convention are:[47] the isotropic shift (δ_{iso}), the anisotropy (Δ), and the asymmetry (η), which are defined in terms of the principal components as:

$$\delta_{iso} = \frac{1}{3}\left(\delta_{xx} + \delta_{yy} + \delta_{zz}\right) \tag{2.6}$$

$$\Delta = \delta_{zz} - \delta_{iso} \tag{2.7}$$

$$\eta_\sigma = \frac{\delta_{yy} - \delta_{xx}}{\Delta}, \tag{2.8}$$

given that $|\delta_{zz} - \delta_{iso}| \geq |\delta_{xx} - \delta_{iso}| \geq |\delta_{yy} - \delta_{iso}|$. The observed chemical shift is then

$$\delta(\theta, \phi) = \delta_{iso} + \frac{1}{2}\Delta(3\cos^2\theta - 1 + \eta_\sigma \sin^2\theta \cos 2\phi) \tag{2.9}$$

where θ and ϕ are the polar angles relating the principal axes of the chemical shift tensor to the direction of the applied field. The angular dependence is known as chemical shift anisotropy (CSA). In a polycrystalline sample, crystallites are present in all orientations so the observed

signal is found by integrating over the angular dependence, resulting in a broad distribution of shifts with a width and lineshape given by the anisotropy and asymmetry. This is known as a powder pattern (Figure 2.1, top).

In a magic angle spinning (MAS) experiment, the sample is spun at the magic angle (54.7°) which is the body diagonal of a cube. This averages terms with second-rank orientational dependence such as the CSA; spinning infinitely quickly would, therefore, give a single peak at the isotropic shift. Spinning at a finite speed splits the powder pattern into spinning sidebands separated by the spinning frequency, which trace out the static pattern and can be used to calculate the chemical shielding parameters (Figure 2.1, bottom). MAS increases signal to noise by concentrating the signal in the spinning sidebands and increases resolution so that different chemical environments can be distinguished.

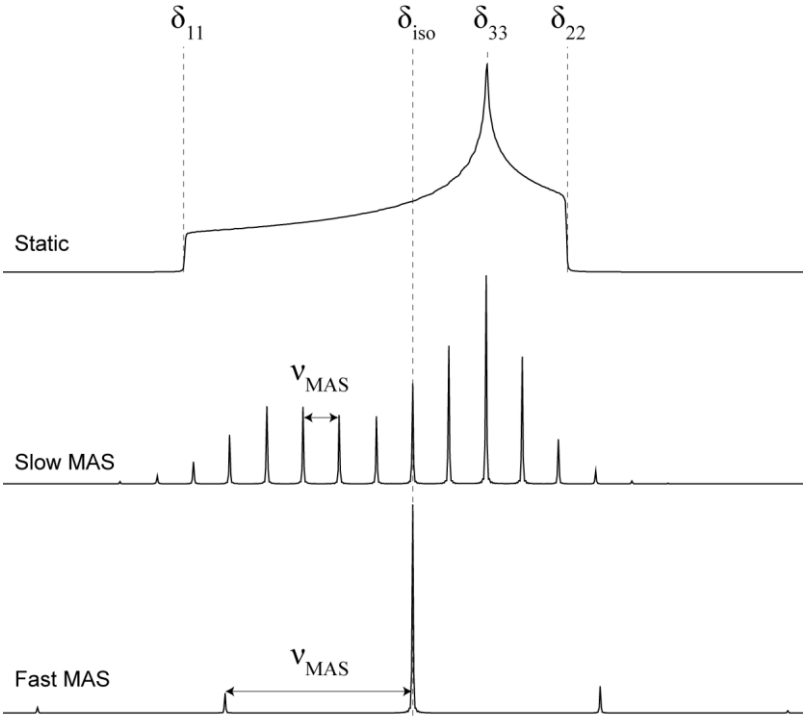

Figure 2.1: Simulated spectra showing the effect of chemical shift anisotropy under static conditions and with different MAS frequencies, ν_{MAS}, for a positive Δ and η = 0.35.

2.1.2 Quadrupolar Coupling

For a nucleus with spin *I*, there are 2*I* + 1 nuclear spin levels with the projection onto the *z* axis, *m*, taking values in integer steps from −*I* to *I*. The signal recorded in NMR spectroscopy can be thought of as arising from transitions between nuclear spin levels, so that for nuclei with I > ½, there are multiple possible allowed transitions with Δ*m* = ±1. Nuclei with I > ½ also possess an electric quadrupolar moment which interacts with any electric field gradient (EFG)

present at the nucleus; this interaction affects the nuclear spin energy levels and hence the spectrum recorded by NMR spectroscopy. The strength of the coupling depends on the size of the nuclear quadrupole moment, *eQ*, where *e* is the elementary charge, and the electric field gradient described by the second rank tensor, **V**, according to the quadrupolar Hamiltonian:

$$\widehat{H}_Q = \frac{eQ}{2I(2I-1)\hbar}\,\hat{\mathbf{I}}\cdot\mathbf{V}\cdot\hat{\mathbf{I}}. \tag{2.10}$$

Similarly to the chemical shift tensor, the electric field gradient tensor can be described by the anisotropy, *eq*, and the asymmetry, η_Q, defined in the principal axis frame of the tensor as:

$$eq = V_{11} \tag{2.11}$$

$$\eta_Q = \frac{V_{22} - V_{33}}{V_{11}} \tag{2.12}$$

for $|V_{11}| \geq |V_{22}| \geq |V_{33}|$. The EFG satisfies Laplace's equation so the isotropic component of the electric field gradient tensor must be zero.[48,*] Typically the magnitude of the quadrupolar coupling is reported as the quadrupolar coupling constant, C_Q, which combines the magnitudes of the nuclear quadrupole moment and the electric field gradient anisotropy. In units of frequency,

$$C_Q = \frac{e^2qQ}{h}. \tag{2.13}$$

If the applied magnetic field is sufficiently large compared to the quadrupolar coupling, then the latter can be considered as a perturbation of the Zeeman splitting, caused by the interaction of the magnetic field with the nuclear magnetic moment. For a transition between nuclear spin states $m-1$ and m, the first order perturbation to the frequency is:[2,49]

$$\nu^{(1)}_{m-1,m} = \frac{3C_Q}{4I(2I-1)}\left(m-\frac{1}{2}\right)\left[3\cos^2\theta - 1 + \eta_Q\sin^2\theta\cos 2\phi\right] \tag{2.14}$$

where θ and ϕ are the polar angles relating the principal axes of the EFG tensor to the direction of the applied field. For quadrupolar nuclei with half integer spin, including ^{51}V with I = 7/2 and ^{17}O with I = 5/2, this shows that the central transition (m = ½) is unaffected to first order by the quadrupolar coupling, whereas the satellite transitions ($m \neq$ ½) have a second-rank

[*] In fact, this is only true if there is no charge density at the nucleus, according to Poisson's equation. However, the only orbitals which have a non-zero density at the nucleus are s orbitals and these are spherically symmetrical so cannot give rise to an electric field gradient.

orientational dependence equivalent to that of the chemical shift anisotropy. The orientational dependence arises because the applied field is the axis of quantisation for the nuclear magnetic dipole, which fixes the orientation of the nuclear quadrupole relative to the field, whereas the EFG is fixed relative to the orientation of the crystallite. The static NMR spectrum for a half-integer spin quadrupolar nucleus is therefore, to first order and ignoring the effects of CSA, a superposition of a sharp peak for the central transition and the powder patterns for the satellite transitions (Figure 2.2). Under MAS, the powder patterns of the satellite transitions will be split into spinning sidebands, analogously to the case of CSA, due to averaging of the second-rank angular dependence.

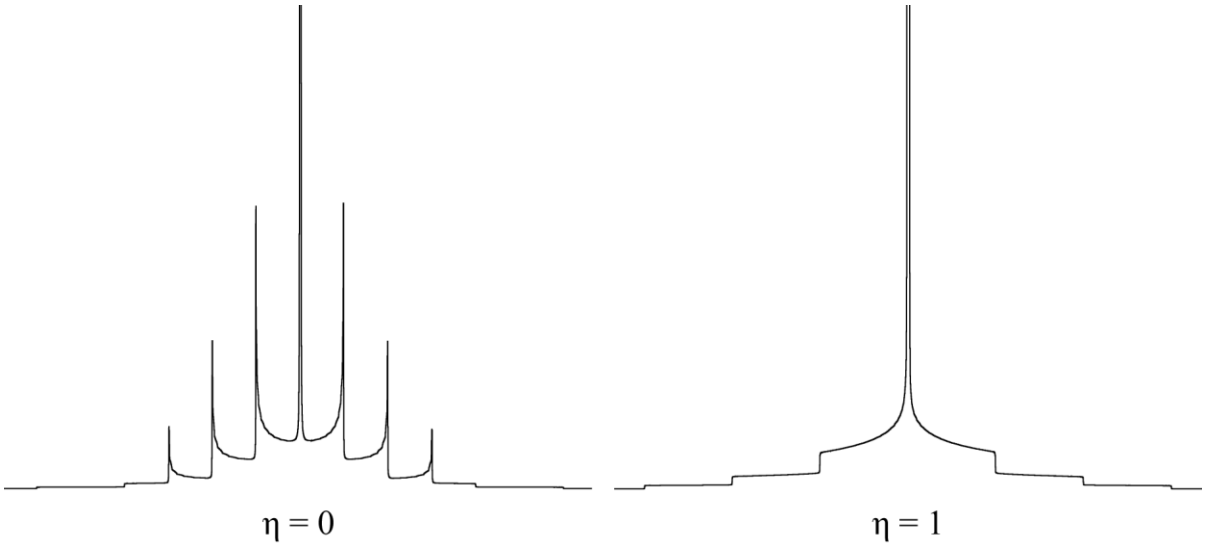

Figure 2.2: Simulated static quadrupolar NMR spectra for a spin 7/2 nucleus, showing the sharp central transition and the broad powder patterns of the satellite transitions for asymmetries of η = 0 and η = 1.

The central transition is, however, affected to second order by the quadrupolar coupling, according to:

$$\nu^{(2)}_{-\frac{1}{2},\frac{1}{2}} = \left(\frac{C_Q}{4I(2I-1)}\right)^2 \frac{2}{\nu_0} \left\{ \begin{array}{c} \left[I(I+1) - \frac{3}{4}\right] V^Q_{00}(\eta_Q) \\ +8\left[I(I+1) - \frac{3}{4}\right] V^Q_{20}(\theta, \phi; \eta_Q) \\ +18\left[I(I+1) - \frac{3}{4}\right] V^Q_{40}(\theta, \phi; \eta_Q) \end{array} \right\} \quad (2.15)$$

where $V^Q_{k0}(\theta, \phi; \eta_Q)$ contains the k^{th} rank orientational dependence for the given asymmetry and ν_0 is the Larmor frequency. From this it can be seen that

- The second order correction is proportional to $(C_Q)^2/\nu_0$, so will be significant for large values of C_Q but is minimised by greater static field strengths.

- There is a 0^{th} rank, isotropic term which contributes to the isotropic shift. Therefore, the measured chemical shift of quadrupolar nuclei contains a contribution from the second order quadrupolar coupling.
- There is a 4^{th} rank term which is not fully averaged by MAS so, if $\left(C_Q\right)^2/\nu_0$ is sufficiently large, the central transition (and the sidebands of the satellite transitions, which also have a second order correction) will exhibit characteristic second-order broadened lineshapes, the shape of which depends on the quadrupolar coupling constant and asymmetry.

For nuclei with integer spin, such as ^{2}H with $I = 1$, there is no central transition which can result in very broad spectra due to the 1^{st} order quadrupolar broadening.

It should be noted that if quadrupolar and CSA effects are both present, there is no requirement that the principal axes of the CSA and EFG tensors be aligned and, therefore, their relative orientations should be specified, as it affects the appearance of the NMR spectrum. This is achieved by the Euler angles: α, β and γ which, in the ZXZ convention, relate the principal axes of the tensors in the following way: a rotation about the *z* axis by α, followed by a rotation about the *x* axis by β, and a rotation again about the *z* axis by γ.

Another consequence of quadrupolar coupling can be a change in the nutation frequency, depending on the relative strengths of the quadrupolar coupling and the radiofrequency (rf) field.[50] If the rf field is much greater than the quadrupolar coupling then the central transition and the satellite transitions are all excited equally; this is known as non-selective excitation and the magnetisation nutates at the same rate as would be expected for a spin-half nucleus. However, if the rf field is much weaker than the quadrupolar coupling (and on resonance with the central transition), then only the central transition is excited and not the satellite transitions; this is known as selective excitation, and results in faster nutation by a factor of $I + \frac{1}{2}$ (shown for $I = \frac{5}{2}$ in Figure 2.3, i.e. 3 times faster nutation). In this case optimal excitation is achieved for a shorter nominal pulse length of $\frac{\pi}{2I+1}$, rather than for a $\frac{\pi}{2}$ pulse. Experimentally, a fixed rf power is often used, but environments with different quadrupolar coupling constants may be present, resulting in different nutation behaviours (which may also be intermediate between the selective and non-selective limits). There are two important consequences of this change in nutation: firstly, if a signal has a greater relative intensity using a quadrupolar $\frac{\pi}{2I+1}$ pulse than for a $\frac{\pi}{2}$ pulse, then it must have a larger quadrupolar coupling constant; secondly, in order to

achieve a quantitative comparison of signal intensities between sites with different quadrupolar coupling constants within a sample, a short pulse length must be used (i.e. within the approximately linear region in Figure 2.3; however, pulses this short will significantly decrease the observed signal, so using the quadrupolar pulse length of $\frac{\pi}{2I+1}$ is often a reasonable trade-off between quantitativeness and signal-to-noise).

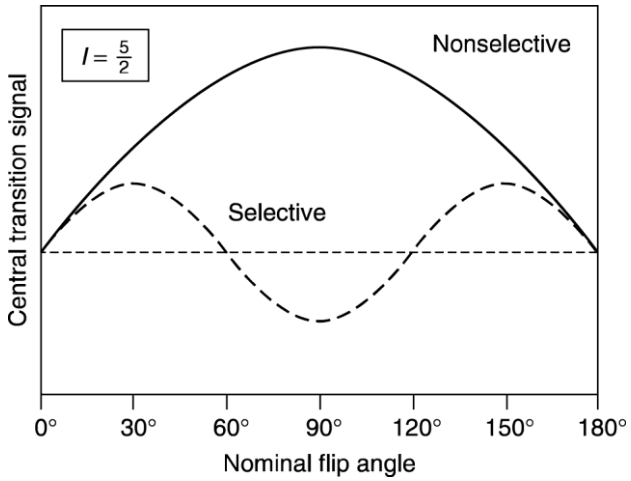

Figure 2.3: Selective and non-selective nutation profiles for $I = \frac{5}{2}$. Reproduced from Vega.[50]

2.1.3 Paramagnetic Shifts

Paramagnetic shifts are caused by the hyperfine coupling of nuclei to localised unpaired electron spins (although this can induce both positive and negative shifts).[5,9] Hyperfine coupling is described by the Hamiltonian

$$\hat{H}_{IS} = \hat{\mathbf{I}} \cdot \mathbf{A} \cdot \hat{\mathbf{S}} \tag{2.16}$$

where $\hat{\mathbf{I}}$ and $\hat{\mathbf{S}}$ are the nuclear and electron spin operators and $\mathbf{A}$ is the hyperfine coupling tensor. Hyperfine coupling can be mediated by two mechanisms: Fermi-contact or dipolar coupling, i.e $\mathbf{A} = \mathbf{A^{FC}} + \mathbf{A^{dip}}$.

Fermi-Contact

Fermi-contact is caused by the transfer of unpaired spin density to the nucleus of interest; as *s* orbitals are the only orbitals with a coefficient at the nucleus, the Fermi-contact shift therefore depends on the unpaired spin density in the s orbital(s) of a given nucleus. This is similar to J coupling between nuclear spins, but there are two important differences: firstly, the gyromagnetic ratio of the electron is ~3 orders of magnitude greater than nuclear gyromagnetic ratios and secondly the relaxation of electron spins is typically much faster than the NMR

spectral timescale (10^{-12} – 10^{-9} s c.f. ~10^{-6} s). The latter causes the nuclear spin to couple with the time average of the electron spin, $\langle S_z \rangle$, rather than the $2S$ + 1 individual spin states, m_s, resulting in an isotropic shift in the NMR frequency rather than the splitting observed for J coupling; the former means that $\langle S_z \rangle$ can be appreciable, which can give rise to large NMR shifts.

Fermi-contact is purely isotropic, so $\mathbf{A^{FC}} = A_{iso}\mathbf{1}$, where $\mathbf{1}$ is the identity matrix, and

$$A_{iso} = \frac{\mu_0 \mu_B g_e \hbar \gamma}{3S} \rho^{\alpha-\beta}(\boldsymbol{R_N}); \tag{2.17}$$

here μ_0 is the permeability of free space, μ_B is the Bohr magneton, g_e is the electron g-factor, γ is the nuclear gyromagnetic ratio and S is the electron spin. This results in a chemical shift

$$\delta_{FC} = \frac{A_{\text{iso}} \langle S_z \rangle}{\hbar \omega_0} = \frac{A_{\text{iso}} \langle S_z \rangle}{\gamma B_0}, \tag{2.18}$$

where ω_0 is the nuclear Larmor frequency and B_0 is the applied magnetic field. The magnitude of the Fermi-contact shift therefore depends on the degree of unpaired spin density at the nucleus of interest, $\rho^{\alpha-\beta}(\boldsymbol{R_N})$, and hence on the intervening orbitals between the nucleus and the paramagnetic centre, known as the bond pathway;[51,52] the most common bond pathways have been catalogued, but can often be deduced by the relative symmetry of the orbital containing the paramagnetic electron and the intervening orbitals:

1. If the orbitals have a degree of spatial overlap and the same symmetry they will mix to form an extended orbital over which an unpaired spin can delocalise. This is known as the delocalisation mechanism and results in a positive spin pathway (Figure 2.4a)
2. If a filled orbital (which may comprise orbitals from multiple atoms) and the paramagnetic orbital have different symmetries then they cannot mix, but in regions where they have spatial overlap the filled orbital will be spin-polarised parallel to the paramagnetic spin due to Hund's third rule; this leaves a net antiparallel spin density in the rest of the orbital. Therefore, for a nucleus located in the latter region of the orbital, the pathway is negative. This is known as the polarisation mechanism (Figure 2.4b).

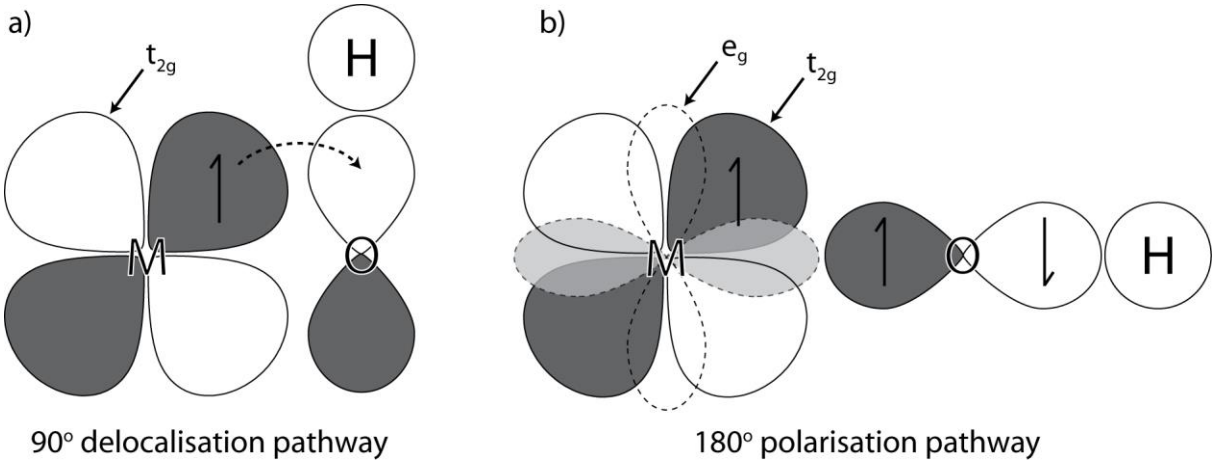

Figure 2.4: Schematic illustrations of a) a delocalisation pathway and b) a polarisation pathway. In (a) the M t_{2g} and OH σ orbitals mix; the unpaired electron occupies the antibonding combination and therefore partially delocalises onto the H, yielding a positive ^{1}H shift. In (b) the M e_g and OH σ orbitals mix so that the filled bonding combination has some spatial overlap with the paramagnetic M t_{2g} orbital; the left of the orbital is therefore polarised parallel, leaving a net antiparallel spin density on the right, and hence a negative ^{1}H shift.

Dipolar Hyperfine Coupling

The dipolar hyperfine coupling is analogous to heteronuclear dipolar coupling, with the exception that again the nucleus couples to the average spin $\langle S_z \rangle$, rather than to each spin state. The tensor elements are given in the point dipole approximation by

$$A_{ij}^{dip} = b_{SI}\left(3r_i r_j - \delta_{ij}\right); b_{SI} = \frac{\mu_0 \mu_B g_e \hbar \gamma}{4\pi |\boldsymbol{r}|^3} \tag{2.19}$$

where δ_{ij} is the Kronecker delta function and $\boldsymbol{r}$ is the nucleus–electron vector. The dipolar hyperfine coupling tensor, like any dipolar interaction, is traceless so for magnetically isotropic systems does not result in an isotropic chemical shift. Instead it causes an anisotropic broadening which is akin to a CSA (see 2.1.1), but often significantly larger in magnitude.

Pseudo-contact

If the magnetic susceptibility is anisotropic, there is a cross term between the dipolar hyperfine coupling and the anisotropic susceptibility which *can* cause an isotropic shift, known as a pseudo-contact shift.[5] Anisotropy can be introduced by the crystal field splitting for sites of non-cubic symmetry and is often found to be large for electrons which possess orbital angular momentum as well as spin, especially in the presence of appreciable spin–orbit coupling. The pseudo-contact shift is therefore sensitive to the symmetry and magnitude of the crystal-field splitting, relative to the thermal energy, as well as to the spin–orbit coupling constant and the total angular momentum of the system. Furthermore, because the pseudo-contact shift is

mediated by dipolar coupling, there is a well-defined relationship between the shift and both the magnitude and orientation of the vector separating the paramagnetic centre and the nucleus of interest; this can be used for structure determination, although most typically in solution-state NMR.[53] For small crystal field splitting less than the thermal energy kT, which is applicable to lanthanide ions, the pseudo-contact shift can be calculated by the method of Bleaney:[5,54]

$$\delta_{PCS} = -\frac{\mu_0 \mu_B^2 g_J^2 J(J+1)(2J-1)(2J+3)}{120\pi r^3 (kT)^2} \langle J||\alpha||J\rangle \times [(3\cos^2\theta - 1)A_2^0\langle r^2\rangle + \sin^2\theta \cos 2\phi \, A_2^2\langle r^2\rangle], \quad (2.20)$$

where θ and ϕ are the angles relating the internuclear vector and the principal axes of the crystal field splitting tensor, $A_2^0\langle r^2\rangle$ and $A_2^2\langle r^2\rangle$ give the axial and rhombic components of the crystal field splitting, respectively, in units of energy, and

$$\langle J||\alpha||J\rangle \equiv \frac{\langle JM_J|\sum(z^2 - r^2)|JM_J\rangle}{\langle JM_J|3\hat{J}_z^2 - \hat{\boldsymbol{J}}^2\,|JM_J\rangle\langle r^2\rangle} \quad (2.21)$$

is the rank-2 spherical tensor operator reduced matrix element which depends on S, L and J, but is independent of M_J. These have been tabulated for the ground levels of the lanthanides.[26,55]

When present, the Fermi-contact shift tends to dominate, but when the Fermi-contact shift is small or absent, the pseudo-contact shift can be the dominant mechanism, especially for heavier elements with correspondingly larger spin–orbit coupling.

Temperature Dependence

For an energetically isolated electronic state (i.e. one for which there are no other states within the thermal energy), the time-averaged electron spin obeys a Curie–Weiss temperature dependence

$$\langle S_z\rangle = -\frac{g_e \mu_B B_0}{3k_B(T - \Theta)} S(S+1), \quad (2.22)$$

where Θ is the Weiss constant, which accounts for the effect of ferromagnetic or antiferromagnetic interactions between the electrons. The paramagnetic shift is then given by

$$\delta_{FC} = -\frac{A_{iso} g_e \mu_B S(S+1)}{3\gamma k_B (T - \Theta)}. \quad (2.23)$$

A plot of $1/\delta$ against T should, therefore, yield a straight line, assuming that the paramagnetic shift is much greater than any diamagnetic shift, and this can be used to identify paramagnetic shifts. However, for a pure paramagnet with $\Theta = 0$, a plot of δ against $1/T$ would be more appropriate as this is unaffected by the presence of a diamagnetic shift contribution.

The presence of low-lying electronic states complicates the picture significantly, resulting in deviation from Curie(–Weiss) temperature dependence; this will be explored in more detail in Chapter 3.

2.1.4 Knight Shifts

In metallic samples, the Knight shift is the change in resonance frequency caused by the hyperfine interaction between the nucleus and delocalised conduction electrons, rather than the localised electrons which cause paramagnetic shifts. This is described in terms of the Knight shift tensor, $\boldsymbol{\mathcal{K}}$, according to the Knight shift Hamiltonian:

$$\hat{H}_K = \gamma \hat{\mathbf{I}} \cdot \boldsymbol{\mathcal{K}} \cdot \mathbf{B_0} \quad (2.24)$$

where γ is the nuclear gyromagnetic ratio and $\mathbf{B_0}$ the applied field. The isotropic component of $\boldsymbol{\mathcal{K}}$, which results in the shift of the isotropic frequency, is denoted $\mathcal{K}$. There are four main interactions which can contribute to the Knight shift:[56,57]

1. Direct Contact Interaction/*s*-Band Pauli Paramagnetism

In an applied magnetic field, there is a shift of the up and down spin bands of a metal, but there must still be a common Fermi level. This results in a difference in population between the bands and thus a net spin polarisation which augments the applied field, which is known as Pauli paramagnetism (Figure 2.5). If there is any contribution from an s-band at the Fermi level then this band will be spin polarised which causes a Fermi-contact shift, analogous to the paramagnetic Fermi-contact shift. The polarisation of the *s*-orbital augments that of the applied field, so the hyperfine interaction results in a positive Knight shift, given by

$$\mathcal{K}_s = \frac{8\pi}{3} \chi_s \langle \psi_s(0) \rangle_{E_F} \quad (2.25)$$

where χ_s is the Pauli paramagnetic susceptibility of the *s* band and $\langle \psi_s(0) \rangle_{E_F}$ is the s-band electron density in the vicinity of the nucleus at the Fermi level. The direct contact Knight shift

is typically temperature independent because the Pauli paramagnetic susceptibilities of *s* bands are largely temperature independent.

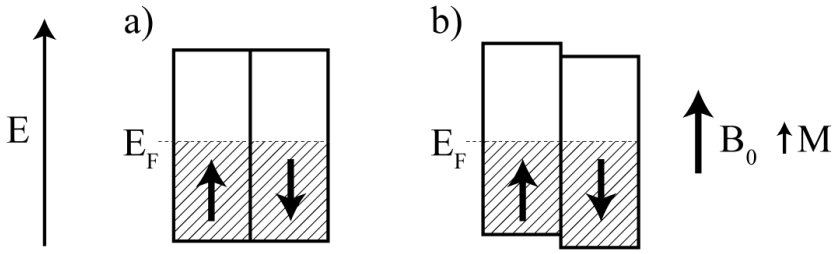

Figure 2.5: Schematic representation of Pauli paramagnetism showing the energies of the up and down spin bands in a) the absence and b) the presence of an applied field, B_0. The shifting of the bands results in an up and down spin population imbalance and thus a magnetisation of the sample, M, which augments the applied field. Note that the gyromagnetic ratio of the electron is negative, so that spins which are antiparallel to the applied field are lowered in energy.

2. Spin Dipolar/Anisotropic Knight Shift

Analogously to localised electron spins, the spin density arising from Pauli paramagnetism can also couple to the nucleus via the spin-dipolar interaction, irrespective of the nature of the orbitals comprising the conduction band. This can be calculated in the same way as for the localised paramagnetic dipolar coupling and again does not result in an isotropic shift, but rather an anisotropic broadening. Furthermore, because the Pauli paramagnetic susceptibility is small, this anisotropic broadening is generally small.

3. Indirect Contact/Core Polarisation

When the conduction band does not comprise *s* orbitals, there can be no direct contact with the nucleus; however, the Pauli paramagnetic polarisation of the conduction band can induce a polarisation in the core s orbitals in the presence of an applied magnetic field, via the exchange interaction, which is then transferred to the nucleus. The spatial extent of the up and down spin electrons of the core orbital, which has zero net spin, are changed differentially so that there is a net spin polarisation at the nucleus. Typically, the up spin-orbital expands due to the favourable exchange interaction with the spin up polarised conduction band, resulting in a net spin down polarisation at the nucleus and hence a negative Knight shift (Figure 2.6).[*]

[*] In fact, if the valence orbital is 2*p* or 3*p* then the core-polarisation Knight shift is positive.[56] This must be because the filled 2*s* and 3*s* orbitals actually have a greater spatial extent than the 2*p* and 3*p* orbitals, respectively, so that the argument above is reversed; furthermore, this effect must outweigh the negative contribution from core-polarisation of the 1*s* orbital and 1*s* and 2*s* orbitals, respectively.

This contribution to the Knight shift can be temperature dependent, especially for bands comprising *d* orbitals, due to the temperature dependence of the Pauli paramagnetic susceptibility. This arises because a) the narrowness of *d* bands means that thermal excitation is closer to saturation and b) the small spatial extent of the *d* orbitals accentuates the exchange–correlation effects which augment susceptibility.[*,58]

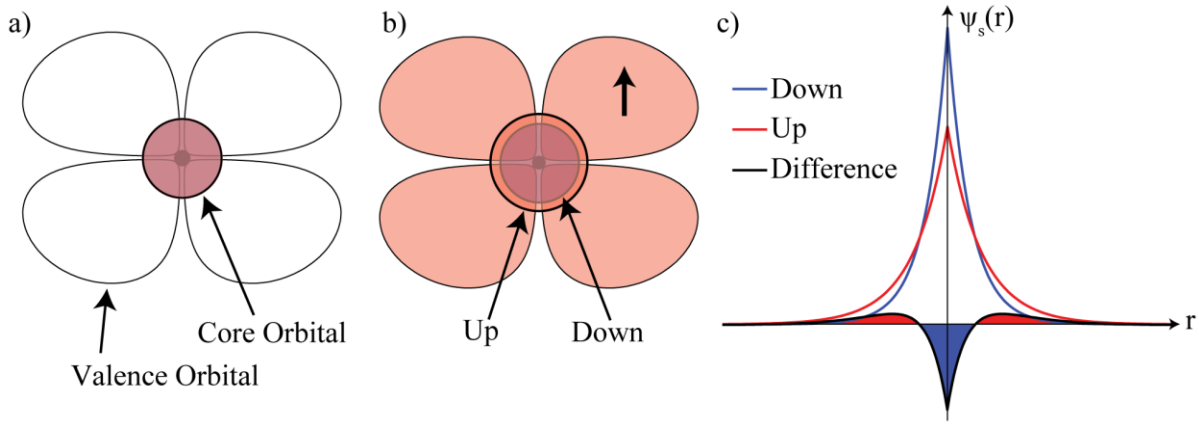

Figure 2.6: Schematic explanation of the core polarisation effect, showing the extent of the spin up and spin down components of a core *s* orbital in the absence (a) and the presence (b) of a polarised conduction orbital. The radial dependence of these components in the latter case is plotted in (c), greatly exaggerated and assuming a 1*s* orbital for simplicity, showing the resultant net down spin density at the nucleus which causes the negative core polarisation Knight shift.

4. Van Vleck Paramagnetism or Orbital Knight Shift

The orbital Knight shift is commonly considered as a separate term, but actually has the same origin as the paramagnetic contribution to the chemical shielding ($\boldsymbol{\sigma^p}$, see 2.1.1). The only modification is that the integration must also be carried out over the electron wavevectors for a delocalised system. The isotropic component is then given by:

$$\mathcal{K}_{orb} = \frac{2\mu_B}{IB_0} \sum_{\substack{i \\ E<E_F}} \sum_{\substack{j \\ E>E_F}} \frac{\langle i|\mathbf{B_0}\cdot\hat{\boldsymbol{\ell}}|j\rangle \left\langle j\left|\frac{2\hat{\boldsymbol{\ell}}\cdot\hat{\mathbf{I}}}{r^3}\right|i\right\rangle \delta(\boldsymbol{k_j}-\boldsymbol{k_i})}{E_i - E_j} \tag{2.26}$$

where *i* and *j* denote the occupied and excited states respectively, $\hat{\boldsymbol{\ell}}$ is the orbital angular momentum operator and δ is the delta function which only allows mixing in of excited states with the same wavevector. This term can be appreciable for metals with unquenched orbital angular momentum because for a partially filled band, the separation between filled and empty

[*] Like-spins experience less electrostatic repulsion due to Fermi holes, hence electron repulsion favours the paramagnetic state. In small orbitals with greater electrostatic repulsion, paramagnetism is more favoured.

states is small (e.g. V, Cr, Nb and W metals[57]). Furthermore, a Van Vleck Knight shift can also be found in semiconductors if the bandgap is sufficiently small, because states above and below the bandgap can mix, although the shift is not technically a Knight shift in this case.

2.2 Relaxation

In addition to the information encoded in the frequency of NMR signals, the relaxation properties can also provide insight into the physical properties of a system.[1]

2.2.1 T_1 Relaxation

Longitudinal, spin-lattice, or T_1 relaxation results in the return of longitudinal magnetisation, i.e. the component parallel to the applied field, to the equilibrium value following a perturbation (such as an NMR experiment). In doing so, the nucleus exchanges heat with the lattice. For a spin-half nucleus, the longitudinal relaxation is characterised by a single relaxation constant, T_1, according to

$$\frac{\mathrm{d}M}{\mathrm{d}t} = -\frac{M - M_0}{T_1}, \tag{2.27}$$

where M is the magnetisation and M_0 is the equilibrium magnetisation. If at time $t = 0$ the magnetisation is zero, e.g. in a saturation recovery experiment, the magnetisation is subsequently given by

$$M = M_0\left[1 - \exp\left(-\frac{t}{T_1}\right)\right]. \tag{2.28}$$

For a quadrupolar nucleus, i.e. $I > \frac{1}{2}$, the magnetisation depends on the relative populations of all the spin states and so cannot be described by a single parameter (in general, $2I$ parameters are required). Consequently, the longitudinal relaxation cannot rigorously be characterised by a single time constant, instead multiple time constants are required which also depend on the initial population distribution, the rates of single and multiple quantum transitions, and on the relative energies of all the spin states.[50] Furthermore, in the presence of quadrupolar coupling, these energies are also orientationally dependent (see 2.1.2). However, despite all these complications, the various relaxation constants are often sufficiently similar that calculating a single T_1 constant for a sample can still be meaningful. Nevertheless, care must be taken when interpreting the relaxometry of quadrupolar nuclei.

Longitudinal relaxation is driven by fluctuating fields at the nucleus,[1] which can have a number of origins: for diamagnetic samples, often fluctuations in the dipolar coupling dominate, caused by molecular/ionic motion, whereas for quadrupolar nuclei, there can be fluctuations in the quadrupolar coupling, caused by changes in the local electric field gradient due to motion, either of the nucleus in question or other nearby ions. In paramagnetic and metallic samples, however, there are further sources of relaxation to consider.

Paramagnetic Relaxation

In paramagnetic samples, relaxation can be caused by fluctuations in the hyperfine coupling; this can also be due to motion, but is more commonly caused by fluctuations in the electron spin.[5] As previously mentioned, electronic relaxation typically occurs faster than nuclear relaxation (10^{-12} – 10^{-9} s), but still results in appreciable spectral density at the Larmor frequency. This can cause significantly faster relaxation than for diamagnetic samples, which is termed paramagnetic relaxation enhancement (PRE) and can be used to identify paramagnetic phases. In fact, if the electron correlation time is too long (approaching the NMR timescale ~10^{-7} s), the PRE is so effective that no NMR signal can be observed; this is known as paramagnetic quenching.

Relaxation due to the Fermi-contact and dipolar hyperfine interactions are referred to as the Bloembergen and Solomon mechanisms, respectively, and the total contribution to the nuclear T_1 is given by the Solomon–Bloembergen–Morgan equation:

$$\frac{1}{T_1} = \frac{2}{3}S(S+1)\left(\frac{A_{iso}}{\hbar}\right)^2 \frac{T_{2e}}{1+(\omega_{0S}-\omega_{0I})^2T_{2e}^2} + \frac{2}{15}S(S+1)\left(\frac{b_{SI}}{\hbar}\right)^2\left[\frac{3T_{1e}}{1+\omega_{0I}^2T_{1e}^2} + \frac{6T_{2e}}{1+(\omega_{0S}+\omega_{0I})^2T_{2e}^2} + \frac{T_{2e}}{1+(\omega_{0S}-\omega_{0I})^2T_{2e}^2}\right], \quad (2.29)$$

where T_{1e} and T_{2e} are the longitudinal and transverse electronic relaxation constants, respectively, and the dipolar coupling constant b_{SI} is defined in equation (2.19).[5] As can perhaps be seen, analysis of paramagnetic relaxation is often prohibitively complicated, however these analytical expressions have previously been used as structure constraints for the solving of protein structures.[59]

Metallic Relaxation

In metals, relaxation can be caused by fluctuations in the conduction electron spins, which can also result in significantly faster relaxation than in diamagnetic samples. In simple metals with non-interacting electrons, this relaxation is given by the Korringa relation:[5,57,60]

$$T_1\mathcal{K}^2 = \frac{\hbar}{4\pi kT}\left(\frac{\gamma_e}{\gamma_n}\right)^2, \tag{2.30}$$

where $\mathcal{K}$ is the Knight shift (see 2.1.4) and γ_e and γ_n are the electron and nuclear gyromagnetic ratios, respectively. This relation can be understood by considering that only electrons near the Fermi level can undergo fluctuations, because there must be an empty state with the opposite spin for the electron to move into, which is sufficiently close in energy. Therefore, the relaxation rate is proportional to the number of filled states within a small energy δ below the Fermi level, and to the number of available states within δ above the Fermi level, i.e.

$$\frac{1}{T_1} \propto \psi(E_F - \delta < E < E_F)\psi(E_F < E < E_F + \delta), \tag{2.31}$$

where $\psi(E)$ is the density of states at an energy E. If the density of states is sufficiently flat in the vicinity of the Fermi level then both of these terms are approximately equal to the density of states at the Fermi level, $\psi(E_F)$, which also determines the magnitude of the Knight shift (equation (2.25)). Therefore,

$$\frac{1}{T_1} \propto \psi(E_F)^2 \propto \mathcal{K}^2. \tag{2.32}$$

The temperature factor arises from Fermi-Dirac statistics which cause a finite smearing of which states are filled in the vicinity of the Fermi level. The higher the temperature, the greater the smearing and therefore the more electrons with accessible states to allow spin fluctuations, and the faster the relaxation rate. The Korringa relation can be used to identify metallic systems, but only in the simplest cases.

Motional Relaxation

When the dominant cause of relaxation is motion, the temperature dependence of the relaxation can yield useful information on the magnitude, rate, and activation energy of the motion; however, this requires a model for how the motion induces relaxation. For both dipolar relaxation and quadrupolar relaxation, the T_1 is given by the spectral densities, $J(\omega)$, at the Larmor frequency and at twice the Larmor frequency:

$$\frac{1}{T_1} = A[J(\omega_0) + J(2\omega_0)], \tag{2.33}$$

where the prefactor A depends on the magnitude of the interaction driving the relaxation and on the nature of the motion causing fluctuations in it. In idealised cases, A can be calculated analytically: for homonuclear dipolar relaxation between two nuclei separated by a distance r, with gyromagnetic ratios γ, assuming isotropic rotation and no vibrational motion,

$$A = \frac{3\mu_0^2\hbar^2\gamma^4}{160\pi^2 r^6}, \tag{2.34}$$

where μ_0 is the permeability of free space;[1] while for isotropic motion of a quadrupolar nucleus

$$A = \frac{4(2I+3)}{5I^2(2I-1)}\left(1 + \frac{1}{3}\eta_Q^2\right)\frac{3}{160}\left(C_Q\right)^2, \tag{2.35}$$

for quadrupolar coupling constant C_Q and asymmetry η_Q (see §2.1.2).[61] However, for even slightly more complicated scenarios, these expressions become exceedingly complex; analysis of the relaxation rates is nevertheless possible, because where necessary the prefactor can be treated as a variable parameter, or calculated from the relaxation rate at the T_1 minimum, if this is experimentally accessible.

To proceed, a form must be assumed for the spectral density, the most common of which is given by Bloembergen-Purcell-Pound (BPP) theory, whereby the motion is described by a mono-exponentially decaying autocorrelation function

$$G(t) = \exp\left(-\frac{t}{\tau_c}\right), \tag{2.36}$$

with a correlation time τ_c. Fourier transformation of the autocorrelation function then gives a Lorentzian spectral density function

$$J(\omega) = \frac{\tau_c}{1 + \omega^2\tau_c^2}. \tag{2.37}$$

Substituting this into (2.33), the following limiting behaviours result:

Fast motion regime, high T: $\tau_c\omega_0 \ll 1, \quad \frac{1}{T_1} = 5A \cdot \tau_c$ (2.38)

Slow motion regime, low T: $\tau_c\omega_0 \gg 1, \quad \frac{1}{T_1} = \frac{2A}{\omega_0^2} \cdot \frac{1}{\tau_c}.$ (2.39)

Therefore, between these two limits there must be a minimum in T_1, which by differentiation occurs when

$$\tau_c = \frac{0.616}{\omega_0}. \tag{2.40}$$

If the motion follows an Arrhenius dependence

$$\tau_c = \tau_0 \exp\left(\frac{E_a}{RT}\right), \tag{2.41}$$

then so too will the spin–lattice relaxation in the limiting regimes:

$$T_1 \propto \exp\left(\pm\frac{E_a}{RT}\right), \tag{2.42}$$

where the sign depends on the regime. An Arrhenius plot of $\ln T_1$ versus $1/T$ should therefore yield a characteristic V-shaped curve (Figure 2.7) and the activation energy for the motion can be extracted from the gradient(s). This analysis is performed to investigate oxide-ion motion in Chapter 3.

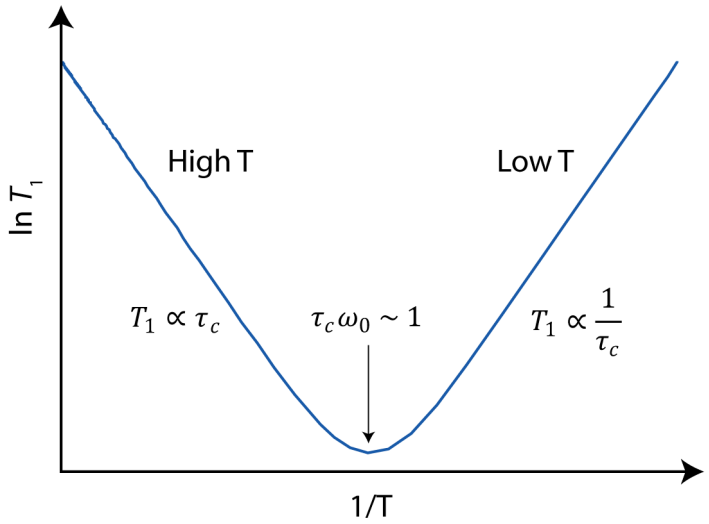

Figure 2.7: Schematic Arrhenius plot of motionally-induced T_1 relaxation.

2.2.2 $T_{1\rho}$ Relaxation

The $T_{1\rho}$ constant characterises the decay of magnetisation in the rotating frame.[62] To measure $T_{1\rho}$, transverse magnetisation is excited and continuous wave radiofrequency power is then applied on resonance; in the rotating frame, this corresponds to a static magnetic field in the transverse plane, about which the magnetisation is spin-locked. The decay of this magnetisation then depends on the spectral density at the frequency determined by the radiofrequency power,

ω_1, rather than that at the Larmor frequency, ω_0. As radiofrequency powers are typically around 10 – 100 kHz, this allows motion to be probed at complementary timescales to T_1 measurements;[63] however, spin-locking can be challenging in some systems, especially for quadrupolar nuclei, and this method was not used in the work presented here.

2.2.3 T_2 Relaxation

Transverse, spin–spin, or T_2 relaxation measures the decay of magnetisation in the transverse plane following excitation. T_2 relaxation is a random process which, like T_1 relaxation, is driven by fluctuating fields at the nucleus; however, because spin–spin flip-flop transitions can occur without any net change in energy, T_2 relaxation is also driven by spectral density at zero frequency. For this reason, T_2 relaxation in solids is often much faster than T_1 relaxation, whereas for liquids in the fast-motion regime the two rates are typically equal.[*,64]

In the limit of a single, well-defined, nuclear environment, the only cause of decay in the time-domain free-induction decay (FID) measured in an NMR experiment is T_2 relaxation; following Fourier transformation, this is therefore the only cause of spectral broadening in the frequency-domain, and the T_2 constant can be extracted directly from the linewidth at full-width-half-maximum (FWHM):[1]

$$T_2 = \frac{1}{\pi \cdot \mathrm{FWHM}}. \tag{2.43}$$

In this case, the signal is said to be homogeneously broadened. However, for ssNMR of materials, signals are almost always heterogeneously broadened, i.e. the linewidth is caused by a distribution of local environments due to, even small, variations in the interactions described in §2.1; inhomogeneous broadening can also be induced by field inhomogeneities in the sample.[3] The T_2 constant given by equation (2.43) when the linewidth is inhomogeneously broadened is referred to as T_2^*. The true T_2 constant can therefore no longer be determined from the linewidth, but is instead measured using an echo experiment, which takes the form p_1 – τ – p_2 – τ – *acquire*. The first pulse excites transverse magnetisation and the second pulse should refocus any dephasing so that the signal decay measured for progressively longer echo delays is only due to T_2 relaxation, i.e.

[*] The only requirement for the two constants is that $T_2 < 2T_1$, because as the longitudinal component increases, the transverse component must decay so that the total magnitude of the magnetisation does not increase.

$$M(\tau) = M_0 \exp\left(-\frac{2\tau}{T_2}\right). \quad (2.44)$$

By performing multiple experiments with different echo delays, τ, the T_2 can be extracted.

The choice of echo pulse sequence depends on the nature of the dephasing to be refocussed. The most common is the Hahn echo, π/2 – τ – π – τ – *acquire*, which refocuses dephasing due to terms which are linear in the nuclear spin, including differences in chemical shift (which may arise from CSA or B_0 field inhomogeneities), heteronuclear dipolar coupling, and second-order quadrupolar coupling. To refocus terms which are bilinear in the nuclear spin, a solid echo must be used (π/2 – τ – π/2 – τ – *acquire*, where the two pulses differ in phase by 90°); such interactions include first order quadrupolar coupling (i.e. for integer-spin nuclei which do not have a central transition) and homonuclear dipolar coupling (if this is not removed by fast MAS).[2] Dephasing may still occur during the echo, however, if the pulse length is not perfectly set, due to B_1 field inhomogeneities, or if both linear and bilinear terms are present (dephasing due to linear terms will still occur during a solid echo, for example, even if the dominant dephasing due to a bilinear term has been refocused). These dephasings are *not* T_2 relaxation because they are not random processes and could, in principle, be refocused in an ideal system with an appropriate pulse sequence. An effective decay constant is measured in this case, sometimes denoted T_2', which includes both the "true" T_2 relaxation and any additional dephasing.

Motional Relaxation

Motion can cause T_2 relaxation by inducing fluctuating fields at the nucleus, and this can be analysed in an equivalent way to T_1 relaxation (see 2.2.1), further including the effect of spectral density at zero frequency. It can be shown that the effect of this additional contribution is that T_2 takes a constant value in the slow-motion regime, unlike T_1 and $T_{1\rho}$ which increase again after passing through a minimum (as in Figure 2.7). However, minima in the effective T_2 measured in an echo experiment as a function of temperature have been reported, for example in the study of lithium diffusion;[65] clearly in this case a different mechanism must be in effect.

The origin of this effective T_2 decay is as follows: a spin which is in one environment during the first half of the echo develops a certain relative phase, which would normally be removed over the course of the second half of the echo; however, if the spin changes environment at any point during the echo, the phases developed in each half of the echo will not perfectly cancel, resulting in a dephasing relative to other spins and a reduction in the observed signal. For

slower motion, the probability of changing environment during the echo is reduced, reducing the dephasing, and for fast motion any given spin experiences many different environments during each half-echo, which is equivalent to experiencing the same average environment, so that the echo is again effective at refocussing the phase. The T_2 minimum is a similar phenomenon to the line broadening observed during the intermediate regime for chemical exchange,[64] and the minimum is observed when the rate of motion is on the order of the separation of the resonant frequencies of the environments which are sampled by the motion,[65] as this dictates the relative dephasing caused by sampling different environments.

Relaxation due to Diffusion

In a similar way to motionally driven dephasing during an echo, diffusion within a magnetic field gradient also causes dephasing because in this case, the magnetic field experienced by a spin changes during the echo, which changes the precession frequency, so that the phases evolved over the two halves of the echo again do not cancel. The magnetic field gradient may be internal, e.g. due to magnetic susceptibility effects,[66] or an applied external gradient if the aim is to investigate the diffusional processes.[67] However, this diffusional relaxation can mask the T_2 relaxation; to overcome this, a Carr–Purcell–Meiboom–Gill (CPMG) pulse sequence can be used, where during the T_2 relaxation time, rather than a single echo, a train of echoes is used: $\pi/2 - (\tau - \pi - \tau)_N$ – *acquire*. Instead of varying the echo delay, τ, this is fixed and the number of echoes, N, is varied; the numerator of (2.44) then becomes $2N\tau$, and again the T_2 can be extracted. The advantage of the CPMG pulse sequence is that by making the echo spacing arbitrarily short (although it must be rotor synchronised in an MAS experiment), no diffusion occurs during an individual echo so the refocussing of each echo is still effective, leaving only the true T_2 relaxation over the total echo train. However, care must be taken choosing the echo delay, τ, because if it is too short then in some cases, due to the finite length of the pulses, the train of π pulses can spin lock the magnetisation, so that decay occurs via $T_{1\rho}$ relaxation rather than T_2.[68] Another application of the CPMG pulse sequence, if the signal is measured between each echo, is to greatly enhance the acquired signal in systems where the T_2 is significantly longer than the T_2^*, especially in the case of a long T_1 constant; this is because many echoes can be recorded for a single excitation.[69]

2.3 Dynamic Nuclear Polarisation (DNP)

As discussed in Chapter 1, DNP is the harnessing of the greater polarisation of paramagnetic electrons to hyperpolarise nuclear spins and thereby increase the NMR signal.[70]

In an applied magnetic field, B_0, the spin states for a paramagnetic electron are split according to the Zeeman interaction; for the case of S = $\frac{1}{2}$, the two spin states $m_S = \pm\frac{1}{2}$ have energy $\pm\hbar\gamma_e B_0$, where $\gamma_e = -g_e\mu_B/\hbar$ is the electron gyromagnetic ratio. At equilibrium, the population of the spin states takes a Boltzmann distribution, resulting in a population difference and hence a spin polarisation; it is this polarisation which forms the basis of electron paramagnetic resonance (ESR) spectroscopy, analogous to the nuclear spin polarisation investigated with NMR spectroscopy. However, because as previously mentioned the electron gyromagnetic ratio is ~3 orders of magnitude greater than nuclear gyromagnetic ratios, ESR is performed at microwave frequencies (tens to hundreds of GHz) rather than the radiofrequency (tens to hundreds of MHz) used for NMR and, furthermore, the electron spin polarisation is correspondingly larger.

There are various mechanisms of DNP, the most relevant of which will be discussed below, but in all cases the driving force is the (at least partial) saturation of the ESR frequency by the application of high power microwave radiation—that is to say the populations of the electron spin states are equalised, reducing the spin polarisation. If the electron–nuclear hyperfine interactions are tailored appropriately, this can be done in such a way that some of this polarisation is concurrently, or subsequently, transferred to the nuclear spin bath.

Thermodynamically, DNP can be considered as a heat pump (Figure 2.8): hyperpolarisation of the nuclear spin bath is equivalent to reducing the effective temperature for the Boltzmann population of the levels, i.e. the aim of DNP is to cool the nuclear spins. This is achieved by pumping heat from the nuclear spin bath to the electron spin bath, which is driven by the application of microwave power. The reason this works is, because the energy splitting of the electron spin levels is greater than for the nuclear spin levels, the electron spin bath has a significantly larger heat capacity, and thus can accept the heat pumped from the nuclear spin bath. This is (somewhat) equivalent to the significant cooling which can be achieved in a fridge or freezer by pumping heat into the much larger surroundings, at the expense of the electricity required to drive the heat pump.

DNP is typically performed with a fixed frequency microwave source so that, in order to match this frequency to that required by the electron–nuclear system, the magnetic field must be varied. The optimal frequency will always be close to the ESR frequency, which itself is generally close to that of a free electron, so the field should not need to be swept by a large amount. Nevertheless, the enhancement in nuclear spin polarisation achieved by DNP can vary

significantly over such a narrow range of magnetic field, and this field profile is characteristic of the DNP mechanism. The three most common mechanisms of DNP are the Overhauser effect, the solid effect and the cross effect; these will now be considered in turn.

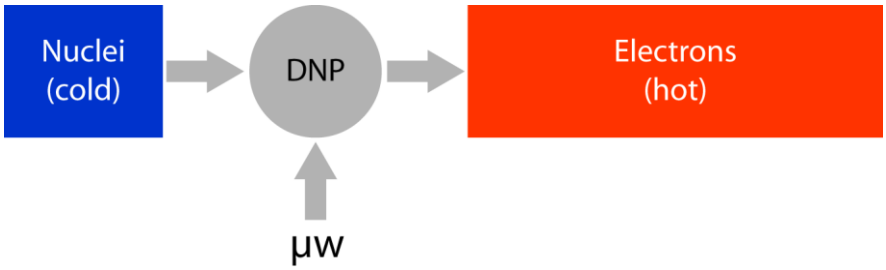

Figure 2.8: Schematic representation of DNP as a heat pump. The application of microwave power (μw) pumps heat from the nuclear spin bath to the electron spin bath, which has a larger heat capacity.

2.3.1 The Overhauser Effect

The Overhauser effect was the original mechanism of DNP proposed by Overhauser in 1953 and then experimentally observed by Carver and Slichter in lithium metal.[17,18] The mechanism is simply a cross-relaxation of the electron spin via a nuclear spin, in an equivalent fashion to the nuclear cross-relaxation that is exploited in nuclear Overhauser effect (NOE)-based experiments in NMR. This mechanism is illustrated in Figure 2.9, where the electron and nuclear spin states are denoted $|m_S m_I\rangle$, using α and β to denote $+\frac{1}{2}$ and $-\frac{1}{2}$, respectively. The pure ESR transitions at ω_{0S} are driven by the applied microwave irradiation (wavy lines), and then cross relaxation occurs via the zero quantum (ZQ) and double quantum (DQ) transitions (straight lines); these transitions are described in Table 2.1. Nuclear hyperpolarisation is generated if the rates of ZQ and DQ relaxation differ.

Table 2.1: Definition and frequencies of the zero and double quantum transitions in the e–n system.

Zero Quantum (ZQ)	$\|\alpha\beta\rangle \leftrightarrow \|\beta\alpha\rangle$	$\omega_{0S} + \omega_{0I}$
Double Quantum (DQ)	$\|\alpha\alpha\rangle \leftrightarrow \|\beta\beta\rangle$	$\omega_{0S} - \omega_{0I}$

In order for this cross-relaxation to occur, there must be a fluctuating hyperfine interaction with spectral density at the ZQ or DQ frequencies. For metals such as lithium, these fluctuations are caused by motion of the itinerant conduction electrons, and in liquids they can be caused by molecular diffusion; however, the Overhauser effect has also been observed in insulating solids, and the origin of the necessary spectral density in this case is still under investigation.[70,71]

The field profile for the Overhauser effect is shown in Figure 2.10; the only condition is that the microwave frequency matches the ESR frequency, so a single broad enhancement profile is observed at ω_{0S}. The sign of the enhancement depends on the sign of the nuclear gyromagnetic ratio and whether ZQ or DQ relaxation dominates: a positive enhancement is generated for a positive gyromagnetic ratio if ZQ > DQ (i.e. $\beta \rightarrow \alpha > \alpha \rightarrow \beta$).

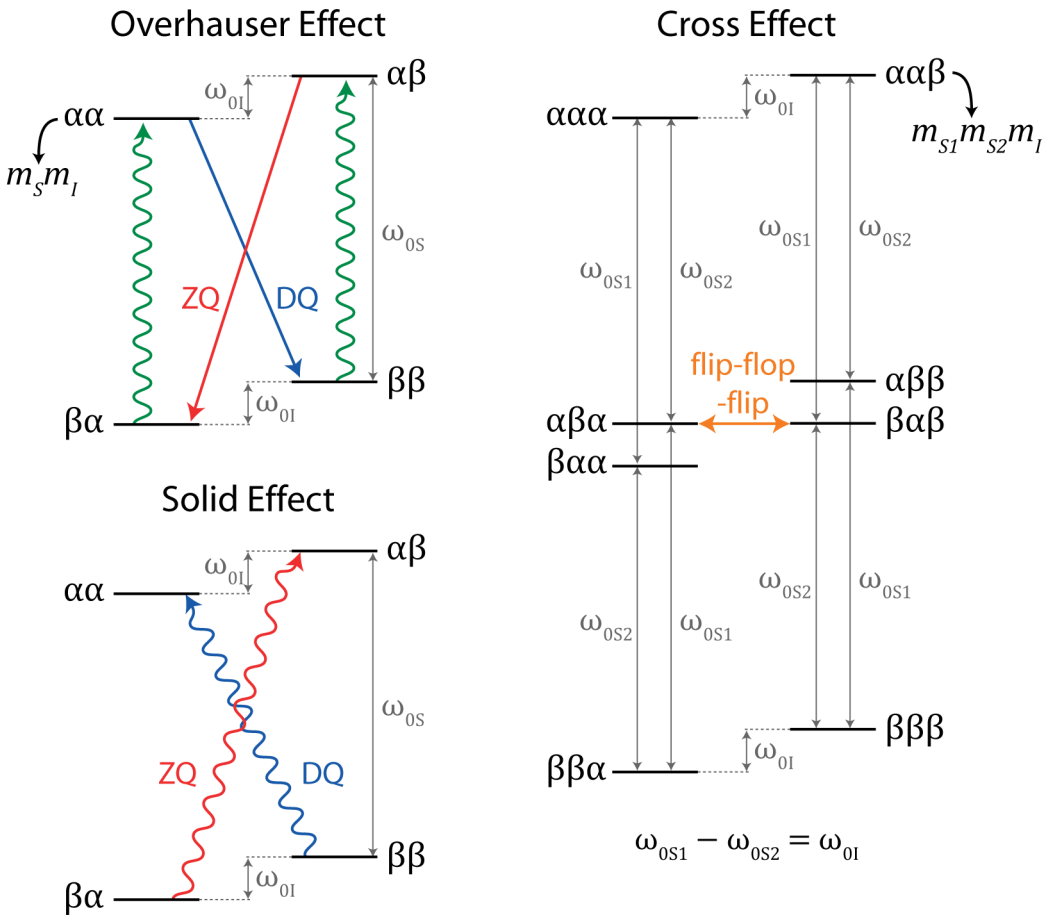

Figure 2.9: Schematic energy level diagrams for different DNP mechanisms with a positive nuclear gyromagnetic ratio. Wavy lines indicate transitions driven by applied radiation, while straight arrows indicate spontaneous transitions. Based on the diagrams of Thankamony et al.[70]

2.3.2 The Solid Effect

The solid effect occurs when the ZQ and DQ transitions (Table 2.1) are driven by the microwave radiation (Figure 2.9); these transitions are nominally forbidden, but are weakly allowed due to mixing of the spin states by the hyperfine coupling. The field profile (Figure 2.10) therefore shows two distinct features at the ZQ and DQ frequencies, which are separated by twice the nuclear Larmor frequency. For a positive gyromagnetic ratio, the DQ transition corresponds to a positive nuclear enhancement ($\beta \rightarrow \alpha$), while the ZQ transition corresponds to a negative nuclear enhancement ($\alpha \rightarrow \beta$). A well resolved solid effect is only observed if the

heterogeneous ESR linewidth is less than ω_{0I}; if this is not the case, then an enhancement can still be observed due to a differential solid effect, whereby for a given microwave frequency/magnetic field strength the rate of one transition is greater than that of the other, but the magnitude of the enhancement is significantly reduced.

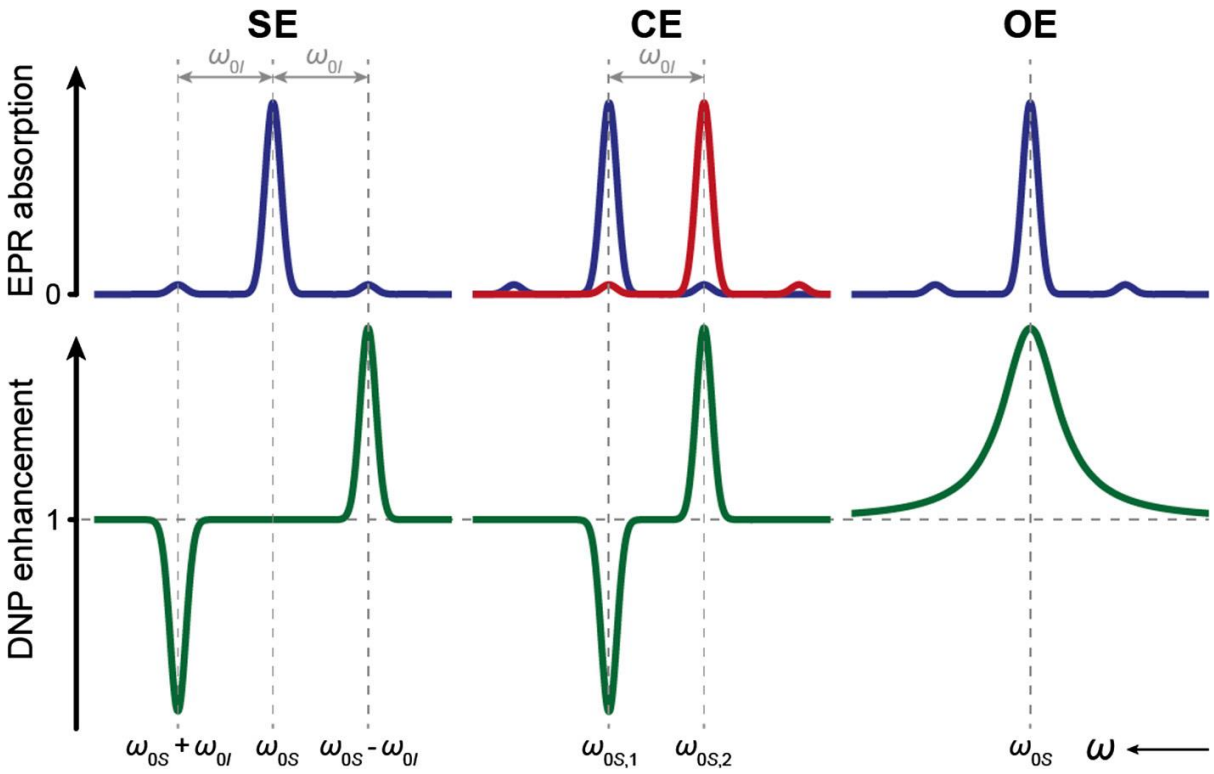

Figure 2.10: Field profiles for the solid effect (SE), cross effect (CE) and Overhauser effect (OE). Reproduced from Thankamony et al.[70]

2.3.3 The Cross Effect

The cross effect is a three-spin process, involving two electrons and a nuclear spin ($|m_{S1}m_{S2}m_I\rangle$). Specifically, the spin system undergoes three-spin flip-flop-flip transitions, e.g. $|\alpha\beta\alpha\rangle \leftrightarrow |\beta\alpha\beta\rangle$, which are only possible if the ESR frequencies of the two electrons differ by the nuclear Larmor frequency: $|\omega_{0S1} - \omega_{0S2}| = \omega_{0I}$. For a non-equilibrium population of one of the electron spins (or any population difference between the two spins), the rates of flip-flop-flip transitions in each direction are not equal, resulting in hyperpolarisation of the nuclear spin. Therefore, in the field profile for the cross effect (Figure 2.10), enhancements are observed when the microwave frequency matches the ESR frequencies of either *S*1 or *S*2, and the peak frequencies are separated by the nuclear Larmor frequency ω_{0I}, because the cross effect requires that the electron ESR frequencies differ by ω_{0I}.

In practise it is challenging to find a system for which the necessary frequency matching is realised between two narrow-line radicals, although a proof of principle has been demonstrated.[72] Instead, radicals are used with inhomogeneously broadened ESR spectra due to g-tensor anisotropy which are wider than the Larmor frequency; the ESR frequency then depends on the orientation of the radical and at least some radicals will be oriented such that their electron frequencies are separated by ω_{0I}, and can therefore induce hyperpolarisation via the cross effect. Biradicals, where there are two radical centres on the same molecule, are particularly successful for the cross effect because the strong intramolecular dipolar coupling fulfils the second requirement for flip-flop-flip transitions that the electron spins be coupled.

Thus far, the cross effect has implicitly been considered under static conditions, however it is much more common to perform experiments under MAS; this complicates the analysis, but in fact results in a greater enhancement over the sample than would be predicted if only appropriately oriented biradicals could contribute to DNP. Because the electron spin energies depend on the orientation of the molecule (and hence the g-tensor) with respect to the field, the energies of each of the e–e–n states described in Figure 2.9 will evolve over the course of a rotor period and in some cases will cross (Figure 2.11, left). However, at these crossings, small off-diagonal elements caused by the e–e and hyperfine couplings cause mixing of the states so that one state evolves into the other and the level crossing is avoided (Figure 2.11, right); this allows adiabatic transfer of populations at certain points during the rotor period. The probability of adiabatic transfer depends on the magnitude of the off-diagonal elements and the "speed" at which the states cross, i.e. the spinning rate: the greater the off-diagonal coupling, and the slower the spinning rate, the more likely the level crossing will be avoided.

The effect of MAS is to temporally separate the microwave and cross effect matching conditions: at some point in the rotor period, the ESR frequency will match the microwave frequency, which allows a non-equilibrium spin population to be induced, then at another point the cross effect condition will be achieved ($|\omega_{0S1} - \omega_{0S2}| = \omega_{0I}$), permitting flip-flop-flip transitions and thereby nuclear hyperpolarisation. Consequently, a significantly greater proportion of the biradicals can contribute to DNP than in the static case (the magnitude of the MAS induced variation in the e–e coupling still depends on the orientation of the e–e vector with respect to the angle of rotation, so not all molecules will experience avoided level crossings).

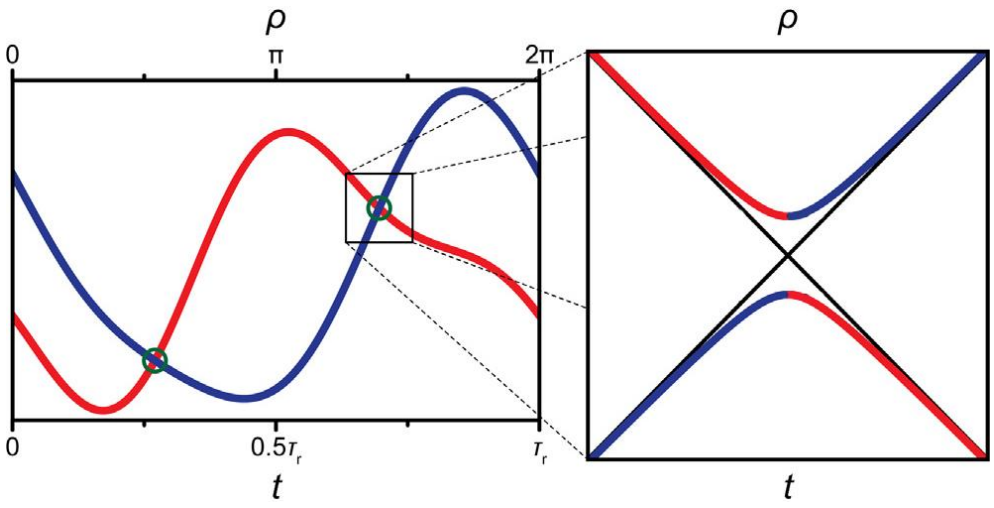

Figure 2.11: Schematic representation of the evolution of two e–e–n states (blue and red) as a function of rotor angle, ρ, or time in units of rotor period, τ_r, showing an avoided level crossing. Reproduced from Thankamony et al.[70]

One might worry that because the ESR frequency of both electron spins will pass through the microwave frequency over the course of a rotor period, both will be equally saturated and thus there would be no population difference to induce nuclear hyperpolarisation; however, due to the strong e–e coupling, adiabatic e–e flip-flops are very likely ($1 - P \sim 10^{-6}$), whereby polarisation is passed from one electron to the other, therefore effectively "the same" electron is polarised each time the microwave frequency is encountered. The probability of flip-flop-flip transitions is much less, $P \sim 10^{-3}$, because the combined e–e–n coupling is significantly weaker but, as long as the nuclear T_1 relaxation is sufficiently long (which is typically the case), there will be many level-crossing events per relaxation constant, and therefore appreciable nuclear hyperpolarisation can still develop.

2.3.4 Typical DNP Experiments

DNP experiments are almost always performed at low temperatures. This is to slow the electron spin relaxation and therefore allow a greater saturation to be achieved given the currently achievable microwave powers. Sample cooling is more difficult under MAS because the bearing and drive gas flows used for spinning must be cooled, in addition to the application of further cooled gas (variable temperature or VT gas); however, commercial systems are available which utilise liquid nitrogen cooling and operate at ~100 K. Further enhancements can be achieved with liquid helium cooling, especially at higher magnetic fields,[73] but this can be technologically challenging and/or prohibitively expensive depending on the efficiency of helium recirculation, and is by no means a standard setup.

The unpaired electron source in DNP experiments can be endogenous, if the material intrinsically contains paramagnetic centres or if they can be doped into the structure,[74] but exogenous DNP, where an external radical source is added, is a more generally applicable technique and as such is far more common. A significant effort has been made to optimise the radical/solvent system (often referred to as "DNP juice"), and the most successful standard combinations which have emerged are AMUPol in water/glycerol[75] and TEKPol in tetrachloroethane (TCE)[76] (Figure 2.12). These are both organic nitroxide based biradicals and operate via the cross effect; these aqueous and organic radical systems are complementary, and the choice depends on the stability and insolubility of the sample in each. The specific solvents are used because they form glasses at the low operating temperatures rather than crystallising, which would exclude the radicals from the solvent, instead of uniformly dispersing them as required. In the most common sample preparation, the radical solution is added to the solid sample until it has fully wet the surface and filled any macro- and meso-pores, but just before there is any free solution and the sample forms a slurry (in practise, at this point slightly more solid sample can be added to return to a solid); this is known as incipient wetness impregnation[21] and has two advantages: most importantly, any excess solution reduces the filling factor of sample in the rotor and hence the signal, but secondly, solids are significantly easier to pack than slurries, which results in reduced transfer losses.

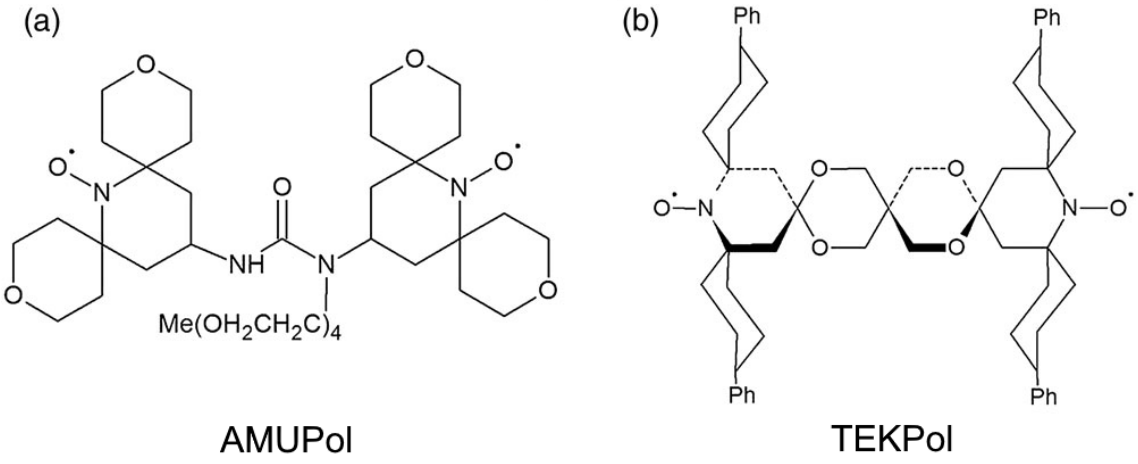

Figure 2.12: Structure of the biradicals AMUPol and TEKPol. Reproduced from Zhao et al.[77]

2.3.5 Direct and Indirect DNP

DNP can be applied in two ways (Figure 2.13): In both cases the first step is a build-up time, equivalent to the recycle delay in conventional ssNMR experiments, during which the nuclei hyperpolarise. Then in *direct* DNP, the nucleus of interest is directly observed, whereas in *indirect* DNP, ^{1}H nuclei are first polarised and cross polarisation (CP) is subsequently used to

transfer the ^{1}H polarisation to the nucleus of interest. The latter approach typically leads to larger enhancement factors because ^{1}H spin diffusion is very effective at spreading the nuclear hyperpolarisation away from the radicals, resulting in a greater and more uniform hyperpolarisation of the ^{1}H spin bath throughout the sample. Furthermore, the build-up times for protons are often shorter than for other nuclei due to the high gyromagnetic ratio, allowing more scans per unit time. However, the obvious disadvantage of indirect DNP is that to study the bulk of a sample it must contain a continuous network of ^{1}H nuclei, which often is not the case. Further difficulties can arise for quadrupolar nuclei due to the difficulty of spin-locking, which reduces the CP efficiency.

In these schematic pulse sequences, the microwave irradiation is shown to be continuous wave, which is most commonly the case. However, with specialised hardware, pulsed DNP experiments are also possible which can increase signal enhancements and allow for novel experiments.[78]

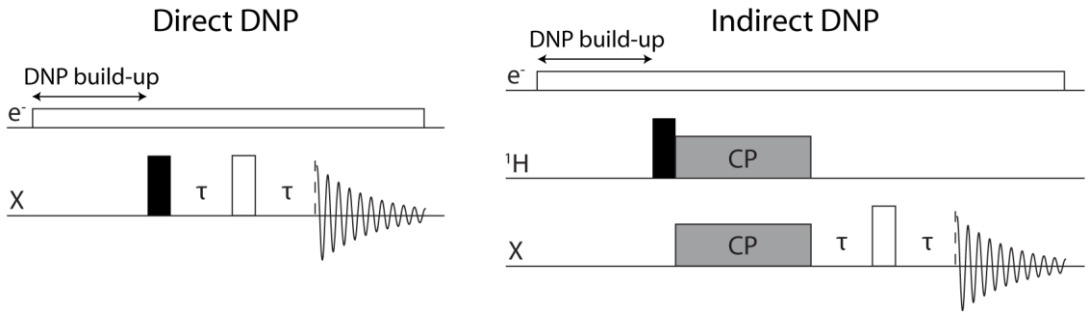

Figure 2.13: Pulse sequences for direct and indirect DNP, shown with echo detection and continuous microwave irradiation.

Chapter 3: A ^{17}O Paramagnetic NMR Study of Sm_2O_3, Eu_2O_3, and Sm/Eu-Substituted CeO_2

3.1 Abstract

Paramagnetic solid-state NMR of lanthanide (*Ln*) containing materials can be challenging due to the high electron spin states possible for the *Ln f* electrons, which result in large paramagnetic shifts, and these difficulties are compounded for ^{17}O due to the low natural abundance and quadrupolar character; in this chapter, strategies are developed to overcome these issues and determine local structural information in lanthanide oxides. First, the ^{17}O NMR spectra of monoclinic Sm_2O_3 and Eu_2O_3 are assigned for the first time, primarily based on the relative intensities and the magnitudes of the quadrupolar coupling constants. Then the temperature dependences of the Sm^{3+} and Eu^{3+} magnetic susceptibilities are investigated by measuring the ^{17}O shift of the cubic sesquioxides over a wide temperature range. This reveals non-Curie temperature dependence due to the presence of low-lying electronic states, which is reproduced by calculating the electron spin as a function of temperature, yielding Fermi contact shifts which agree well with the experimental values. The additional contribution of a pseudo-contact shift for Sm_2O_3 is also considered.

Using the understanding of the magnetic behaviour gained from the sesquioxides, the local oxygen environments in 15 at% Sm- and Eu-substituted CeO_2 are explored, with the ^{17}O NMR spectrum exhibiting signals due to environments with zero, one and two nearest neighbour *Ln* ions, as well as further splitting due to oxygen vacancies. Finally, the activation energy for oxygen vacancy motion is determined in these systems to be 0.35 ± 0.02 eV, from the Arrhenius temperature dependence of the ^{17}O T_1 relaxation constants, which is found to be independent of the *Ln* ion within error. The relation of this activation energy to literature values for oxygen diffusion in *Ln*-substituted CeO_2 is discussed to infer mechanistic information that can be applied to further develop these materials as solid-state oxide-ion conductors.

3.2 Introduction

The most stable oxidation state for most lanthanides is 3+, corresponding to the sesquioxides Ln_2O_3. The sesquioxides can adopt three different structures: hexagonal (A), monoclinic (B) and cubic (C); with decreasing ionic radius, moving across the lanthanide series, the most stable phase at intermediate temperatures changes from A to B and then to C, although it is sometimes possible to stabilise different polymorphs depending on the thermal history.[79] A survey of the ^{17}O NMR shifts of the lanthanide oxides has previously been made by Yang, Shore and Oldfield,[80] however, their work did not include an example of a sesquioxide with the B-type monoclinic structure (Figure 3.1a). Of the lanthanides which can adopt the B-type structure, Sm_2O_3 and Eu_2O_3 are the easiest to prepare as the B phases are stable to the lowest temperatures out of the lanthanide sesquioxides (except for Pm_2O_3, but Pm is radioactive); these two materials were thus chosen for investigation of their ^{17}O paramagnetic NMR shifts.

The magnetic behaviours of Sm^{3+} and Eu^{3+} are also of interest because both ions have low lying electronic levels (the first of which are ~1000 cm^{-1} and ~250 cm^{-1} above the ground state for Sm^{3+} and Eu^{3+}, respectively) which have larger magnetic moments than the ground states.[81] This affects the magnetic susceptibility in two ways: firstly, the excited state can be thermally occupied, which increases the effective magnetic moment; secondly, the second-order mixing of these states results in an appreciable temperature-independent Van Vleck susceptibility, particularly for Eu^{3+}. Given that the ground-state of Eu^{3+} is non-magnetic to first order ($J = 0$), the effect of the excited state is especially important. The magnetic susceptibility of Sm^{3+} in fact exhibits a broad minimum at around 400 K, due to the competition of the Curie temperature dependence for each level and the Boltzmann population of the excited electronic level with a larger moment. To study the temperature dependence of the Sm^{3+} and Eu^{3+} magnetic susceptibilities, the ^{17}O paramagnetic shift of cubic Sm_2O_3 and Eu_2O_3 were measured over a wide temperature range. The cubic polymorphs were chosen for this investigation as there is only a single crystallographic oxygen site in this structure,[82] simplifying the spectra.

As was first reported by Lewis et al. for the ^{17}O NMR signal of aqueous solutions of trivalent lanthanide ions,[83] the paramagnetic shift for atoms directly bonded to lanthanides is positive for Ce^{3+}–Sm^{3+} and then negative for Eu^{3+}–Yb^{3+}. The paramagnetic shift in these cases arises from a polarisation mechanism:[83,84] the bonding interaction is primarily between a lone pair on the oxygen and the empty 6s orbital on the lanthanide, which causes a small degree of delocalisation of the oxygen electrons onto the lanthanide; then, due to the exchange

interaction, the electron density at the lanthanide is polarised parallel to the time-averaged lanthanide electron spin ($\langle S_z \rangle$), leaving a net anti-parallel spin density at the oxygen nucleus, which causes a Fermi-contact shift. The sign and magnitude of this Fermi-contact shift is then determined by the lanthanide electron spin, the variation of which across the lanthanides explains the observed trend in chemical shifts.

The simplest case to consider is Gd^{3+}, which has a spin-only ground term (^8S): the magnetic moment aligns parallel to the field, which results in an antiparallel spin moment at the oxygen nucleus due to the polarisation mechanism, and hence the negative observed paramagnetic shift. In the second half of the lanthanide series, Tb^{3+}–Tm^{3+}, the orbital magnetic moment augments the spin magnetic moment (for greater than half-filled shells, spin–orbit coupling favours parallel spin and orbital angular momenta in the ground-state), so aligning the magnetic moment parallel to the field still requires a parallel spin moment, resulting in a negative paramagnetic oxygen shift. For Eu^{3+} (with a ^7F ground term), the spin magnetic moment outweighs the orbital magnetic moment, so once again the spin magnetic moment aligns parallel to the field, which yields a negative paramagnetic shift for the oxygen. However, for Ce^{3+}–Sm^{3+}, the orbital magnetic moment is greater than the spin magnetic moment; the orbital magnetic moment therefore aligns parallel to the field and, since for less than half filled shells spin–orbit coupling favours an antiparallel arrangement of the spin and orbital angular momenta in the ground-state, this results in an antiparallel spin moment at the lanthanide and therefore a positive paramagnetic shift for oxygen due to the polarisation mechanism. The lanthanide electron spins $\langle S_z \rangle$ have been calculated by Golding and Halton,[84] and Yang et al. showed that there was an excellent correlation between $\langle S_z \rangle$ and the ^{17}O chemical shift in lanthanide oxides.[80]

As discussed in §1.7, lanthanide-substituted CeO_2 based materials are important oxide-ion conductors, with applications in solid oxide fuel cells;[33] however, to optimise the performance of these materials, a greater understanding is required of the oxygen conductivity mechanism. While the mechanism and activation energy barriers in *Ln*-substituted CeO_2 phases have typically been probed through impedance spectroscopy, DC conductivity, and oxygen permeability methods,[85–90] variable-temperature solid-state NMR studies have also provided complementary and atomic-level insights. Fuda et al. first showed that ^{17}O spin-lattice relaxation (T_1) measurements (up to 1000 °C) of CeO_2 and Y-substituted CeO_2 sensitively probed oxide-ion motion with a component at the Larmor frequency; Adler et al. later reinterpreted the multiple T_1 minima as evidence of two distinct time scales for motion

corresponding to nearby oxygen vacancy hops and exchange of the observed oxygen itself with vacancies.[91] Studies by Kim and Stebbins on the Sc-substituted and Y-substituted CeO_2 systems also showed how the ^{17}O (and $^{45}Sc/^{89}Y$) chemical shifts reflect the local distribution of aliovalent dopants, with evidence of cation–vacancy pairing.[92,93]

Recent efforts by Heinzmann et al. have shown that ^{17}O NMR (and T_1) measurements can be applied to Gd-substituted CeO_2 to quantify doping behaviour and to extract activation energy values that can be ascribed to oxide-ion motion.[94] However, ^{17}O NMR and/or relaxometry-based techniques have not been used to study conduction in other *Ln*-substituted CeO_2 materials, likely due to the aforementioned difficulties in interpreting NMR spectra of paramagnetic phases. The lessons learned regarding the magnetic behaviour of Sm^{3+} and $Eu^{3+,}$ as seen in the paramagnetic ^{17}O NMR of the monoclinic Ln_2O_3 polymorphs, are therefore used to guide the analysis of variable-temperature ^{17}O spectra of Sm- and Eu-substituted CeO_2.

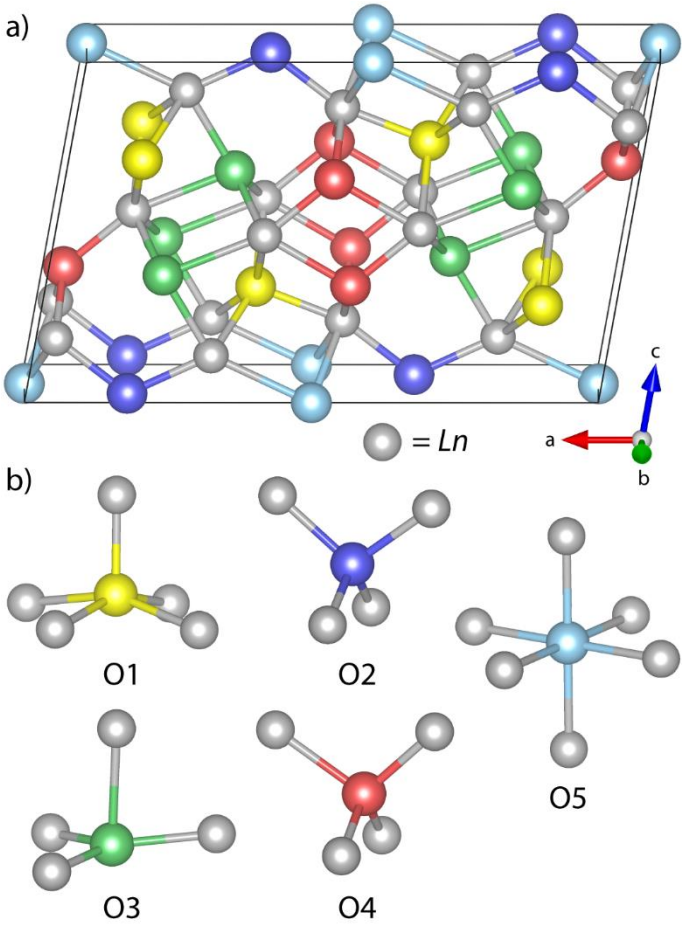

Figure 3.1: a) Crystal structure, and b) local environments of the crystallographically distinct oxygen sites, of the monoclinic (B) Ln_2O_3 phase. Lanthanide ions are shown in silver and the oxygen ions are coloured according to the different O1 – O5 sites. The structure was generated from ICSD entry 34291 (B-Sm_2O_3),[95] using the VESTA software package[96].

3.3 Experimental Methods

3.3.1 Synthesis

The quartz tubes were flame-sealed by Dr Matthias Groh, University of Cambridge.

Cubic Sm_2O_3 was prepared by decomposing $Sm(OH)_3$ (Alfa Aesar, 99%) at 750 ^oC under air for 12 hours.[*,97] 15 at% Sm- and Eu-substituted CeO_2 were synthesised by grinding stoichiometric quantities of Sm_2O_3 (Aldrich, 99.9%) or Eu_2O_3 (Acros Organics, 99.99%) and CeO_2 (Aldrich, 99.9%), pelletising at 750 MPa under partial vacuum, and firing at 1500 ^oC for 48 hours.

^{17}O enriched samples of Sm- and Eu-substituted CeO_2 and cubic Eu_2O_3 were obtained by loading the samples into an alumina tube, which was placed inside a quartz tube filled with $^{17}O_2$ gas (70%, NUKEM Isotopes), sealed with a stopcock, and then annealed at 1000 ^oC in a tube furnace for 15 hours. Cubic Sm_2O_3 was ^{17}O enriched by the same procedure at 750 ^oC for one week. Monoclinic Sm_2O_3 and Eu_2O_3 were enriched in an alumina tube inside a flame-sealed quartz tube under a $^{17}O_2$ atmosphere, annealed at 1200 ^oC in a box furnace for 48 hours. Prior to ^{17}O-enrichment, all Eu_2O_3 samples were dried *in vacuo* at 100 ^oC and transferred to an argon glovebox for subsequent preparation due to the highly hygroscopic nature of the material.

3.3.2 Characterisation

Powder X-ray diffraction (XRD) patterns were recorded in reflection mode with sample rotation on a PANalytical Empyrean diffractometer emitting Cu Kα (1.540598 Å + 1.544426 Å) radiation. Eu_2O_3 samples were packed into a Kapton sample holder to avoid hydration. Phase identification was achieved by profile matching using the X'Pert HighScore Plus 2.2 software (PANalytical) and by comparison with the following Inorganic Crystal Structure Database (ICSD) entries: CeO_2 (72155),[98] cubic Sm_2O_3 (40475),[82] monoclinic Sm_2O_3 (34291),[95] cubic Eu_2O_3 (40472)[82] and monoclinic Eu_2O_3 (8056)[99]. Rietveld refinement was performed with the TOPAS academic software package.[100]

[*] The commercial Sm_2O_3 sample contained both the cubic and monoclinic phases, and it was not possible to obtain a pure cubic sample from this mixture.

3.3.3 NMR

Least-squares refinement of the saturation recovery data was performed by Dr David Halat, University of Cambridge.

Table 3.1: Summary of experimental NMR parameters.

Sample	Field /T	Rotor Size /mm	MAS /kHz	Recycle delay /s	RF power /kHz	Acquisition Time	Notes
Sm_2O_3 monoclinic	9.40	1.9	30	0.05	104	10 min – 1.5h	$\pi/2$, $\pi/6$ & VT
Eu_2O_3 monoclinic	4.70	1.3	60	0.1	222	5d	
	9.40			0.2 or 1	119	2d – 4d	$\pi/2$ vs. $\pi/6$ and quantification
	9.40	1.9	40 or 35	0.1, 1 or 2	104	1d – 3.5d	VT, T_1 & T_2 comparison
Sm_2O_3 cubic	9.40	1.9	40	0.05	119	2 min	Room temperature
		4	10		109	1.5 min	Low VT
		7	4		48	7 min	High VT (laser)
Eu_2O_3 cubic	7.05	1.3	40	0.15	167	12.5 min	Room temperature, Avance III
	9.40	4	10		109	1 min	Low VT
		7	3 or 4		48	10 min – 1h	High VT (laser)
Sm-CeO_2	7.05	1.9	40	1	132	30 min	Avance
	4.70	4	14	–	85	1h – 8h	VT T_1
Eu-CeO_2	7.05	1.3	60	1 or 0.1	167	9h	Avance III
			40	–		1h – 4.5h	Avance III, higher VT & T_1
		4	14	–	69	1.25h	Avance III, lower VT T_1

NMR spectra were recorded on a 4.70 T or 7.05 T Bruker Avance III spectrometer or a 7.05 T or 9.40 T Bruker Avance spectrometer, using 1.3, 1.9, 4, or 7 mm probes. Most variable-temperature spectra were acquired by applying heated or cooled nitrogen gas, with cooling achieved either with liquid nitrogen or with a Bruker cooling unit (BCU), except for the high-temperature spectra of cubic Sm_2O_3 and Eu_2O_3 which were acquired by heating the sample with an infrared laser using a 7 mm Bruker laser probe. The sample temperature was determined using an *ex-situ* calibration with the temperature-dependent ^{207}Pb NMR shift of $Pb(NO_3)_2$,[101] except for the laser heated samples where the temperature was determined *in-situ* by grinding the sample with KBr and measuring the temperature-dependent ^{79}Br NMR shift.[102] Spectra

were recorded using a Hahn echo with pulse lengths corresponding to optimal excitation in the liquid and quadrupolar limits ($\pi/2$-τ-π-τ-acquire, or $\pi/6$-τ-$\pi/3$-τ-acquire for I = 5/2, respectively). The isotropic resonance for the cubic Eu_2O_3 spectra was determined at low temperatures by using a MATPASS sideband separation pulse sequence,[103] and at high temperature by comparison of spectra recorded at 3 and 4 kHz MAS. Longitudinal relaxation constants T_1 were determined by total least-squares refinement of the saturation recovery data to a stretched exponential function using IGOR Pro. Spectra were referenced to liquid H_2O at 0 ppm except for spectra recorded with a 1.9 mm probe which were referenced to CeO_2 at 877 ppm.[104] NMR spectra were deconvoluted using the dmfit software.[105] Full experimental details for each sample are summarised in Table 3.1.

3.4 Results and Discussion

3.4.1 Monoclinic Sm_2O_3 and Eu_2O_3

Monoclinic Sm_2O_3 and Eu_2O_3 were ^{17}O-enriched as detailed in §3.3.1; the procedure required the use of a flame-sealed quartz tube in a box furnace in order to achieve an enrichment temperature of 1200 °C, which was necessary to ensure formation of the monoclinic phase.[97] Phase purity was determined by Rietveld refinement of the diffraction pattern (see Appendix A).

Five crystallographically distinct oxygen sites are present in the monoclinic B-type sesquioxide structure (Figure 3.1b); however in the room-temperature ^{17}O NMR spectrum of monoclinic Sm_2O_3 (~40 °C sample temperature, Figure 3.2, top), only four signals can be distinguished. By cooling the sample to −44 °C, the magnetic susceptibility increases, resulting in larger paramagnetic shifts so that all five resonances can be individually resolved (Figure 3.2, middle). The observed shift increases with decreasing temperature, indicating that the Curie paramagnetic shift is positive, which is consistent with the paramagnetic shift mechanism as described in §3.2.

In order to determine the multiplicities of each signal, a quantitative spectrum was recorded with a shorter, quadrupolar $\pi/6$ pulse (Figure 3.2, bottom), ensuring that quadrupolar nutation effects did not alter the relative signal intensities; the integrated intensities are given in Table 3.2. The signal at 19 ppm has approximately half the intensity of the other signals, so can be assigned to the O5 (2*e*) site, which has half the crystallographic multiplicity of the other oxygen sites. The low frequency of this resonance is also consistent with the higher, six-fold

(~octahedral) coordination of the O5 site; the paramagnetic contribution to the shift is small for Sm^{3+}, so the chemical shift is dominated by the diamagnetic contribution, and greater coordination typically leads to a lower frequency chemical shift for ^{17}O.[16] Furthermore, by comparing the spectra acquired with different pulse lengths, it can be seen that the sites at 108 ppm and 255 ppm have greater relative intensities in the $\pi/6$ spectrum and thus larger quadrupolar coupling constants, C_Q. In the monoclinic structure (Figure 3.1), two oxygen sites possess more distorted coordination environments, O1 (4*i*) which is five-fold coordinated square pyramidal, and O3 (4*i*) which is four-fold coordinated trigonal pyramidal; these are therefore assigned to the two resonances with larger C_Qs,[106] with the five-fold coordinate O1 having the smaller chemical shift, again due to a lower frequency diamagnetic contribution, arising from the higher coordination. The remaining two sites, O2 and O4 (4*i*), have very similar four-fold (~tetrahedral) coordination environments; the shifts of the signals at 162 ppm and 194 ppm are likewise insufficiently different to permit a definitive assignment.

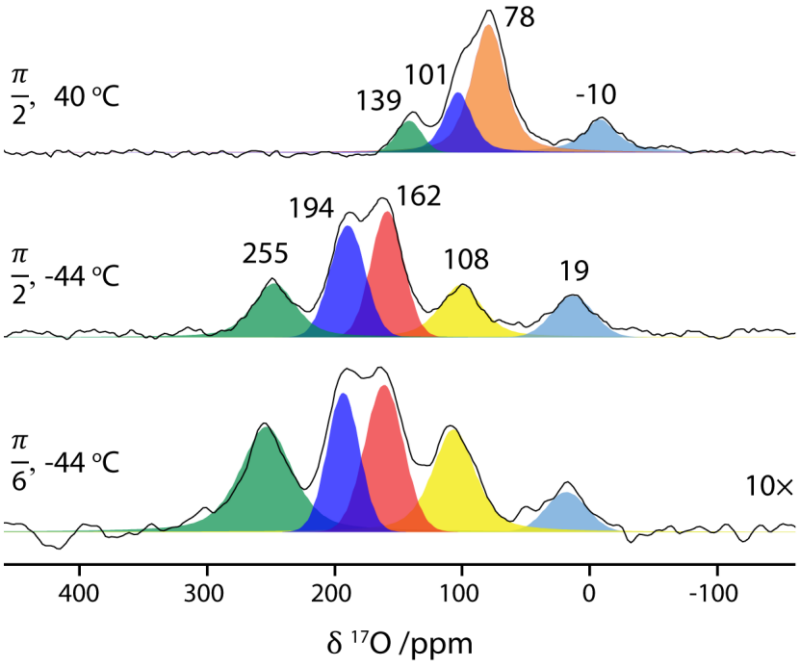

Figure 3.2: ^{17}O NMR spectra of monoclinic Sm_2O_3 recorded at 9.40 T and 30 kHz MAS with a recycle delay of 0.05 s, with and without sample cooling, and using Hahn echo pulse sequences with either $\pi/2$ or quadrupolar $\pi/6$ pulses ($\pi/2$-τ-π-τ-acquire or $\pi/6$-τ-$\pi/3$-τ-acquire). The signal observed at 78 ppm in the 40 °C spectrum (orange) is attributed to the overlap of the peaks at 162 and 108 ppm observed at −44 °C (red and yellow, respectively).

Table 3.2 Summary of the ^{17}O chemical shifts, integrated intensities and assignments for the oxygen sites in monoclinic Sm_2O_3 at −44 ºC. The calculated quadrupolar coupling constants C_Q are shown for the Hyb35 functional, see Appendix B. *Calculations were performed by Jae Lee, University of Cambridge.*

Experimental Shift /ppm	**Relative Integration /%**	**Assignment**	**Coordination**	**Calculated C_Q /MHz**
19	9	O5 (2*e*)	~Oct. (6)	0.15
108	24	O1 (4*i*)	Square pyr. (5)	1.34
162	20	O2, O4 (4*i*)	~Tet. (4)	0.67
194	20			0.26
255	27	O3 (4*i*)	Trig. pyr. (4)	1.09

Since the ^{17}O NMR shifts in monoclinic Sm_2O_3 are dominated by the diamagnetic shift, the spectrum is expected to be similar to that of diamagnetic isostructural monoclinic Y_2O_3.[107] Therefore, to gain insight into the diamagnetic contributions to the observed shifts, the isotropic ^{17}O chemical shifts for Y_2O_3 were calculated using density functional theory (DFT) (see Appendix B). The calculated chemical shifts for monoclinic Y_2O_3 are in good agreement with the previous experimental results,[107] if the experimental assignments of the similar O2 and O4 sites are reversed; furthermore, the calculation confirms the trend of decreasing chemical shift with increasing coordination, which was used to assign the spectrum of Sm_2O_3. However, within the three four-fold coordinated sites, the orderings of the shifts differ between Y_2O_3 and Sm_2O_3: for Y_2O_3 the O3 site resonates at a lower frequency (346 ppm) than O2 and O4 (377 ppm and 383 ppm), whereas for Sm_2O_3 the O3 site resonates at a higher frequency (255 ppm) than O2 and O4 (162 ppm and 194 ppm). This may be due to the paramagnetic shift contributions in Sm_2O_3, or simply slightly different diamagnetic shift contributions between Sm_2O_3 and Y_2O_3.

The biggest difference between the ^{17}O spectra of Sm_2O_3 and Y_2O_3 is that for the latter all of the signals are observed at significantly higher frequencies (242 – 383 ppm) than for Sm_2O_3 (19 – 255 ppm). Given that for Sm_2O_3 the paramagnetic contribution to the chemical shift is positive, the lower frequency shifts observed for Sm_2O_3 imply a significantly less positive diamagnetic shift contribution, which is attributed to the weak covalency of the Sm–O bonding due to the contracted Sm valence orbitals, since covalent bonding acts to deshield the oxygen and hence increases the chemical shift.[108] The temperature-independent Van Vleck paramagnetism of the ground state, due to mixing in of the low-lying first excited electronic state, has a negative contribution to the shift, so will also contribute to the lower frequency shifts observed for Sm_2O_3.[109,110]

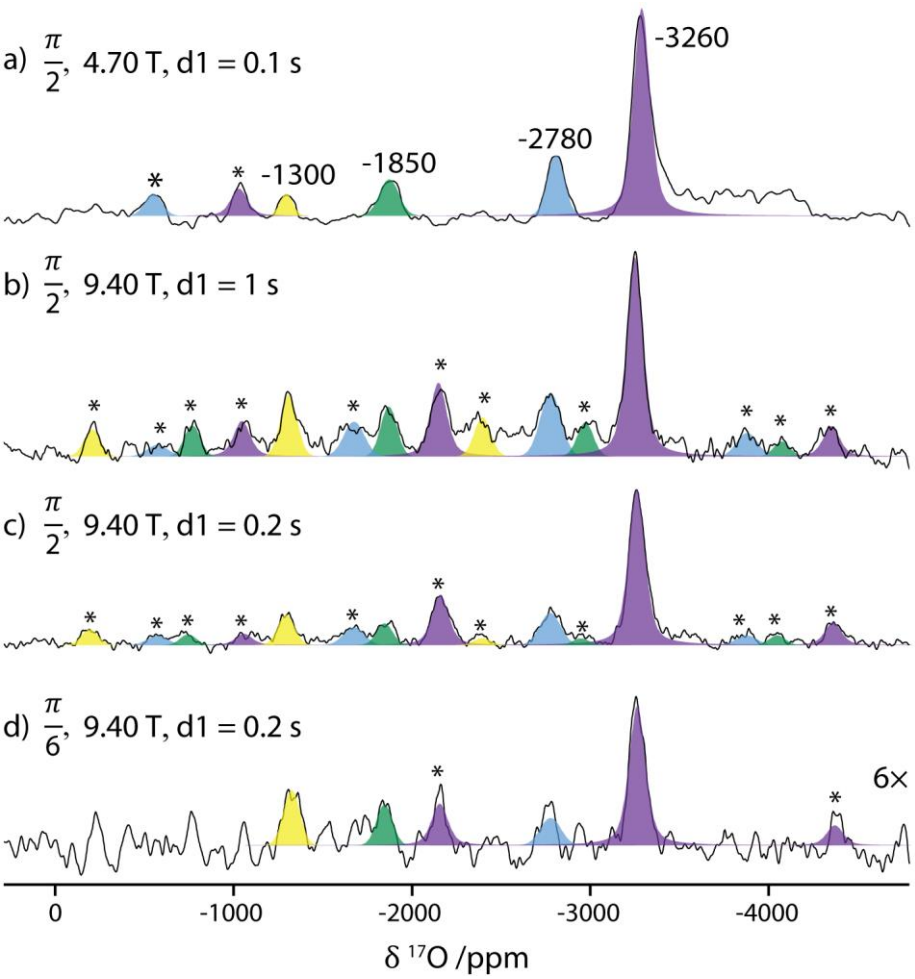

Figure 3.3: ^{17}O NMR spectra of monoclinic Eu_2O_3 recorded at 60 kHz MAS and either 4.70 T or 9.40 T, using a Hahn echo with either $\pi/2$ or $\pi/6$ pulses and the indicated recycle delays, d1. Spinning sidebands are marked with an asterisk. Although there is greater sideband separation at 4.70 T, the signal-to-noise is greater at 9.40 T.

The ^{17}O NMR spectrum of monoclinic Eu_2O_3 recorded at 4.70 T and 60 kHz MAS is shown in Figure 3.3a, with the signals summarised in Table 3.3; the low field and fast MAS are necessary to sufficiently separate the spinning sidebands due to the wide dispersion of paramagnetic chemical shifts. Four isotropic resonances can be observed, but the signal at −3260 ppm has a significantly higher intensity than the others; this is not due to differential T_2 relaxation, because the signal intensities are unchanged when the echo length is doubled (Figure 3.4a), nor to differential T_1 relaxation, because although a 0.1 s recycle delay does not yield a quantitative spectrum, the signal still has a significantly greater relative intensity with a quantitative 1 s recycle delay (Figure 3.3b and Figure 3.4b). Therefore, the −3260 ppm resonance is attributed to a superposition of signals from two crystallographic sites: since the two most similar sites are the O2 and O4 tetrahedrally-coordinated oxygens, this signal is most likely due to these environments. Although the O2 and O4 sites could be distinguished in Sm_2O_3, the linewidth for Eu_2O_3 (110 ppm) is significantly larger than that for Sm_2O_3 (30 ppm), so it is unsurprising

that the signals cannot be resolved for the former. An additional spectrum was recorded at −20 °C (Figure 3.4c), but the two resonances could still not be resolved. The change in paramagnetic shifts at this lower temperature also causes the −2780 and −3260 ppm signals to be spaced by the MAS frequency, so that the isotropic resonances and spinning sidebands of these signals coincide.

Table 3.3: Summary of the ^{17}O chemical shifts, integrated intensities and tentative assignments for the oxygen sites in monoclinic Eu_2O_3 at 45 °C. The calculated hyperfine coupling constants A_{iso} are shown for the Hyb35 functional, see Appendix B. *Calculations were performed by Jae Lee, University of Cambridge.*

Shift /ppm	**Relative Integration /%**	**Assignment**	**Coordination**	**Calculated A_{iso} /MHz**
−3260	38	O2, O4 (4*i*)	~Tet. (4)	−4.02, −3.18
−2780	14	O5 (2*e*)	~Oct. (6)	−2.04
−1850	24	O3 (4*i*)	Trig. pyr. (4)	−2.64
−1300	24	O1 (4*i*)	Square pyr. (5)	−2.04

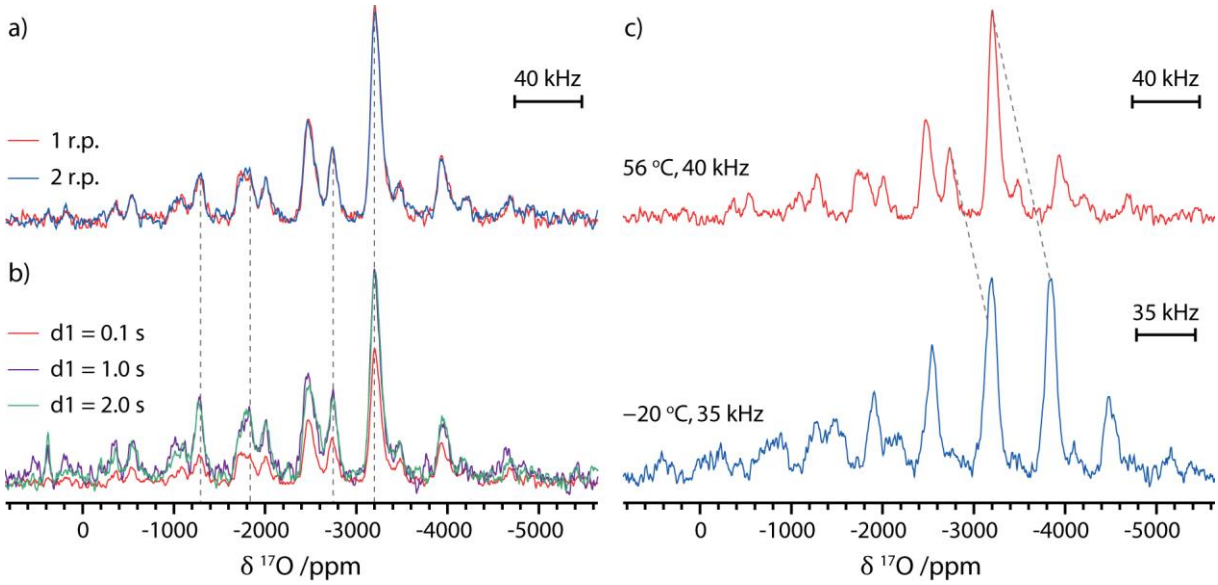

Figure 3.4: ^{17}O NMR spectra of monoclinic Eu_2O_3 recorded with different a) number of rotor periods (r.p.) in each half echo, b) recycle delays and c) sample temperatures. Spectra were recorded using a Hahn echo pulse sequence at 9.40 T and 40 kHz MAS, except the low temperature spectrum which was recorded at 35 kHz. Recycle delays of 0.1 s were used except for b). Isotropic resonances are marked with dashed lines, although there is significant overlap of the isotropic resonances with the spinning sidebands.

Of the remaining resonances, those at −1850 and −1300 ppm show an increased relative intensity in the $\pi/6$ spectrum so are assigned to the more distorted O1 and O3 sites (comparison of Figure 3.3 c and d, see Table 3.4). The diamagnetic shift contribution by which the two sites were distinguished for Sm_2O_3 makes a far smaller relative contribution to the shift in the more paramagnetic Eu_2O_3, so cannot be used to further distinguish the sites; however, on the basis of the larger calculated hyperfine coupling constant A_{iso} (Table 3.3), the O3 site is tentatively

assigned to the more paramagnetically shifted −1850 ppm signal and O1 therefore to the −1300 ppm signal. By a process of elimination, the signal at −2780 ppm is attributed to the O5 site. To support this assignment, the integrated intensities for each resonance in the spectrum recorded with a quantitative recycle delay of 1 s and a π/2 pulse (Figure 3.3b) were weighted by the relative intensities between the spectra recorded with π/2 and π/6 pulses (but non-quantitative recycle delays). This accounts for the non-quantitative excitation afforded by π/2 pulses to afford a quantitative comparison between the resonances (Table 3.4). Based on the assignment and crystallographic multiplicities, the relative integrated intensities should occur in the ratio 44:11:22:22, which agrees reasonably well with the experimental values (38:14:24:24), corroborating the assignment.

Table 3.4: Determination of the relative integrations of the signals in the ^{17}O NMR spectrum of monoclinic Eu_2O_3. The integrated intensity with an approximately quantitative recycle delay (d1) of 1 s is weighted by the ratio of the amplitudes of each signal recorded with π/2 and π/6 pulses, but with recycle delays of 0.2 s.

Shift /ppm	**Relative integration π/2, d1 = 1 s**	**Amplitude π/2, d1 = 0.2s /Arb. Units**	**Amplitude π/6, d1 = 0.2s /Arb. Units**	**Ratio of π/6:π/2 Amplitudes**	**Corrected relative integration**
−3260	50%	97.5	14.3	0.15	38%
−2780	20%	20.1	2.8	0.14	14%
−1850	15%	13.6	4.2	0.31	24%
−1300	15%	19.1	5.6	0.30	24%

Although it is not currently possible to directly calculate the chemical shifts for paramagnetic systems, the isotropic hyperfine coupling constant A_{iso} and quadrupolar coupling constant C_Q were calculated using the DFT-based code CRYSTAL (see Appendix B). The use of a lower quality oxygen basis set not specifically designed for hyperfine-type calculations, which is necessary here to be compatible with the available lanthanide basis sets, is likely to hinder the quantitative prediction of these parameters; nevertheless, some qualitative agreements between the experiment and theoretical assignments could be obtained.

As previously noted, the principal contribution to the observed ^{17}O shifts in Sm_2O_3 arises from the chemical shift component, which provides the basis for the assignment. Due to the small paramagnetic contribution, the calculated hyperfine coupling constants A_{iso} cannot be directly correlated to the observed shifts. However, the calculated quadrupolar constants C_Q (Table 3.2) confirm that the O1 and O3 sites are more distorted, as previously asserted, supporting the assignment of the 108 ppm and 255 ppm signals on the basis of the increased intensity in the π/6 spectrum. For Eu_2O_3, on the other hand, the paramagnetic shift dominates, so it is informative to compare the shift to the calculated A_{iso} values (Table 3.3); despite the imperfect

quantitative agreement, qualitative information can still be extracted. The two sites with the largest calculated A_{iso} are O2 and O4, corroborating the assignment of these sites to the most paramagnetically shifted signal at −3260 ppm (although one would expect the signals to have approximately the same A_{iso} given they are observed at the same frequency). The A_{iso} for the other three sites are smaller, and although a less negative experimental shift might therefore be expected for O5, some of this discrepancy may be accounted for by the lower frequency diamagnetic contribution due to the six-fold coordination (as seen for Y_2O_3 and Sm_2O_3). The calculated A_{iso} for O3 is slightly larger than that for O1, on which basis the −1300 and –1850 ppm signals are tentatively assigned.

3.4.2 Cubic Sm_2O_3 and Eu_2O_3 – Variable Temperature NMR

The room temperature ^{17}O NMR spectra of cubic Sm_2O_3 and Eu_2O_3 are shown in Figure 3.5, with shifts of 2 ppm and −3075 ppm, respectively. These are in agreement with the previous results of Yang, Shore and Oldfield (10 ppm and −3290 ppm),[80] considering that the additional frictional heating of the faster MAS rate used here will reduce the paramagnetic shift, yielding less positive and less negative shifts for Sm_2O_3 and Eu_2O_3, respectively. The oxygen site in the cubic Ln_2O_3 polymorph is four-fold coordinated, with a geometry intermediate between those of the trigonal pyramidal O3 site and the approximately tetrahedral O2 and O4 sites in the monoclinic structure; this is consistent with the similarity between the cubic Eu_2O_3 ^{17}O shift (−3075 ppm) and the shift of the O2 and O4 sites in monoclinic Eu_2O_3 (−3260 ppm). The ^{17}O shift of cubic Sm_2O_3 (2 ppm), on the other hand, is at a lower frequency than the four-fold coordinated sites in monoclinic Sm_2O_3 (101 ppm and 139 ppm at room temperature); this is most likely to be due to a less positive diamagnetic shift in the cubic phase caused by reduced covalency in the less dense structure (the cell volume per formula unit is 81.6 $Å^3$ for the cubic structure, c.f. 74.8 $Å^3$ for the monoclinic structure).

The temperature dependence of the Sm^{3+} and Eu^{3+} magnetism can be explored by measuring the ^{17}O paramagnetic shift over a wide temperature range. Figure 3.6a shows the ^{17}O shift of cubic Sm_2O_3 as a function of temperature: at lower temperatures the paramagnetic shift increases due to the increased expectation value of the electron spin, as was observed for monoclinic Sm_2O_3 (Figure 3.2); however, at higher temperatures, there is little temperature dependence of the shift. This behaviour can be most easily seen when plotted as a function of reciprocal temperature (Figure 3.6b), where a clear deviation from the linear Curie temperature dependence is seen below around $1000/T = 3\ K^{-1}$ (T = 333 K). This is ascribed to thermal

occupation at the elevated temperatures of an excited state with a higher moment than the ground state.

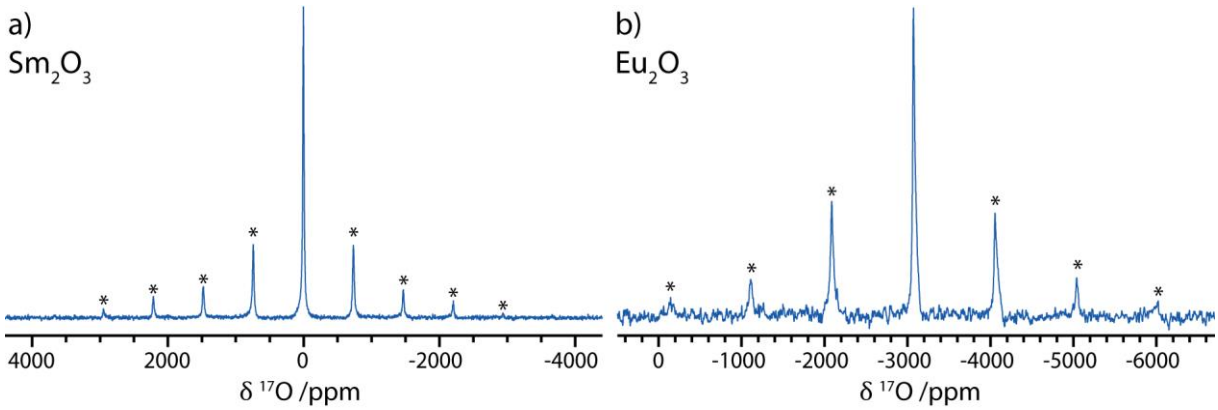

Figure 3.5: ^{17}O NMR spectrum of cubic a) Sm_2O_3 and b) Eu_2O_3, recorded with 40 kHz MAS and a Hahn echo pulse sequence at a) 9.40 T and b) 7.05 T, with recycle delays of a) 0.05 s and b) 0.15 s. Spinning sidebands are marked with asterisks.

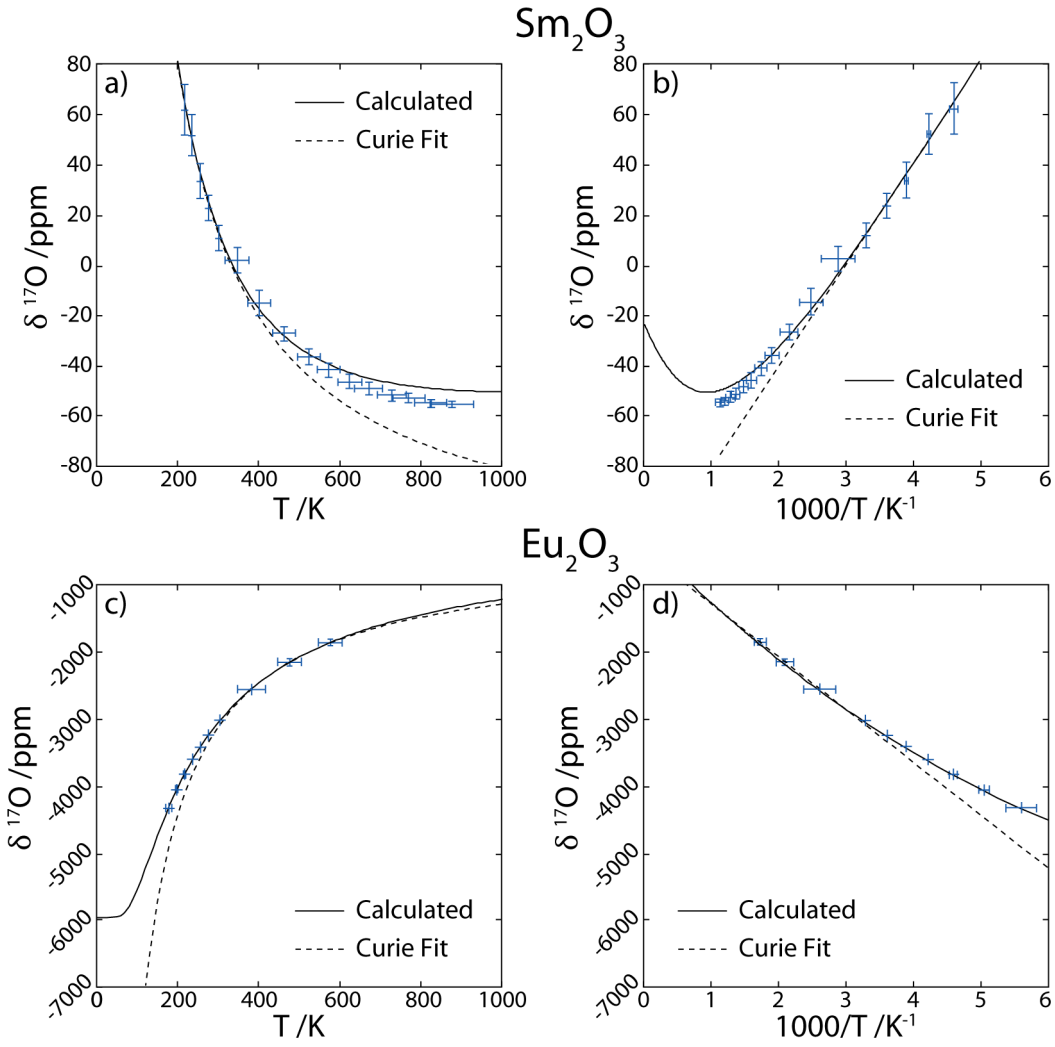

Figure 3.6: ^{17}O chemical shifts of cubic Sm_2O_3 (a, b) and Eu_2O_3 (c, d) as a function of temperature at 9.40 T, recorded with a Hahn echo pulse sequence and recycle delays of 0.05 s and 0.15 s, respectively. The high- and low-temperature spectra were recorded at 4 and 10 kHz MAS, respectively. Shown too are empirical fits assuming

a Curie temperature dependence (dashed lines), and the shifts predicted from the calculated electron spin (solid lines).

The ^{17}O shift of Eu_2O_3 exhibits a greater temperature dependence than that of Sm_2O_3 (Figure 3.6 c and d), as expected given the larger paramagnetic shift. The magnetic behaviour of Eu^{3+} is determined by the thermal population of multiple excited levels with different magnetic moments and the Curie temperature dependence of each, combined with a very large Van Vleck paramagnetism of the ground state, which itself has no Curie paramagnetism because $J = 0$. As a result, any agreement between a Curie fit and the experimental data is essentially fortuitous, rather than reflecting any functional dependence. In the case of Sm^{3+}, on the other hand, the ground-state has a non-zero moment and there is no appreciable thermal occupation of other levels below ~300 K, so paramagnetic shifts do follow the Curie law below room temperature, as has been shown previously.[110,111]

To quantitatively analyse the temperature dependence of the ^{17}O NMR spectra, the paramagnetic shifts for cubic Sm_2O_3 and Eu_2O_3 were predicted by calculating the electron spin per unit field using the method of Golding and Halton.[84] First the contribution for each J level was calculated using

$$\frac{\langle S_z \rangle_J}{B_0} = -\mu_B \left[\frac{g_J(g_J - 1)J(J+1)}{3kT} + \frac{2(g_J - 1)(g_J - 2)}{3\lambda} \right], \tag{3.1}$$

where B_0 is the magnetic field, μ_B is the Bohr magneton, k is the Boltzmann constant and $\lambda = \zeta/2S$ is the spin–orbit coupling constant, for which the values presented in Golding and Halton were used. These two terms represent the Curie and Van Vleck contributions, respectively (a derivation is given in Appendix C). The Landé g-factor is given by

$$g_J = \frac{3}{2} + \frac{S(S+1) - L(L+1)}{2J(J+1)}, \tag{3.2}$$

except when $J = 0$, as is this the case for the $^7F_0$ ground-state of Eu^{3+}, for which it can be written as $g_J = L + 2$ (see Appendix C).

The overall spin for the system was then found by a Boltzmann weighting of the levels:

$$\frac{\langle S_z \rangle}{B_0} = \frac{\sum \frac{\langle S_z \rangle_J}{B_0} (2J+1) \exp\left(-\frac{E_J}{kT}\right)}{\sum (2J+1) \exp\left(-\frac{E_J}{kT}\right)}, \tag{3.3}$$

where $E_J = \lambda J(J+1)/2$.

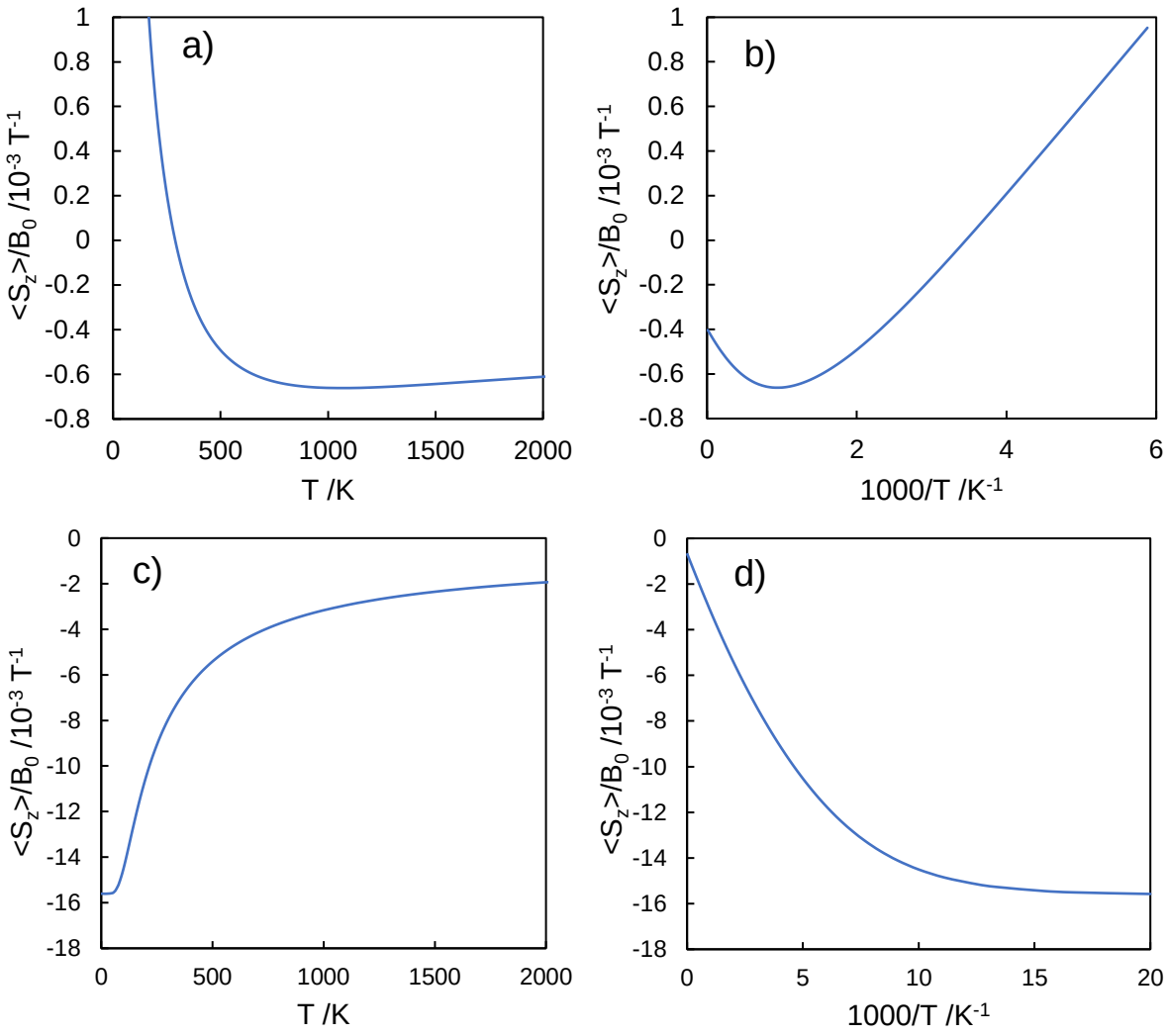

Figure 3.7: Calculated average electron spin, $\langle S_z \rangle$, as a function of temperature and reciprocal temperature for Sm^{3+} (a & b) and Eu^{3+} (c & d).

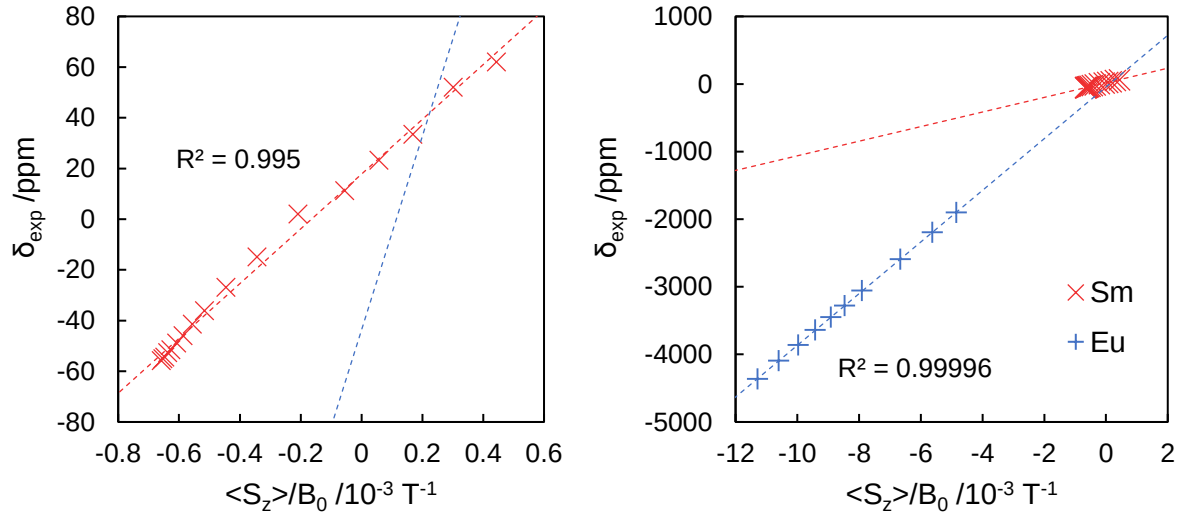

Figure 3.8: Plots of the experimental ^{17}O NMR shifts of cubic Sm_2O_3 and Eu_2O_3 against the calculated electron spin, as an implicit function of temperature.

The temperature dependences of the calculated spin for Sm^{3+} and Eu^{3+} are shown in Figure 3.7, which broadly reproduce the features observed in the variable temperature ^{17}O NMR experiments performed on cubic Sm_2O_3 and Eu_2O_3 (Figure 3.6). In particular, for Sm^{3+}, a minimum in the spin is predicted at ~1000 K, which is significantly higher than the minimum in the susceptibility (~400 K). This occurs because the Curie and Van Vleck paramagnetic terms can have different coefficients as well as different signs in the expressions for the magnetic susceptibility and the electron spin, respectively; paramagnetic shifts are only proportional to the magnetic susceptibility in the case that only Curie(–Weiss) paramagnetism is present. For Eu^{3+}, on the other hand, the spin approaches a constant value below ~70 K due to the temperature-independent Van Vleck paramagnetism of the ground state, as expected.

The linear relationship between the experimental shifts and the calculated spins can be seen in Figure 3.8, and the agreement for Eu_2O_3, in particular, is excellent. From the linear regression, the hyperfine coupling constant (A_{iso}) and diamagnetic shift (δ_0) were extracted according to

$$\delta_{exp} = \frac{A_{iso}}{\gamma} \times \frac{\langle S_z \rangle}{B_0} + \delta_0, \tag{3.4}$$

where γ is the nuclear gyromagnetic ratio (see §2.1.3); these parameters are shown in Table 3.5. The hyperfine coupling constants are negative due to the polarisation mechanism mediated by the lanthanide 6*s* orbital (see §3.2), and the value determined for Eu_2O_3 (−2.206 MHz) is in reasonable agreement with that determined by Yang, Shore and Oldfield (−2.7 MHz).[80] The latter was deduced from the relationship between the room temperature ^{17}O shift of different lanthanide sesquioxides and the calculated electron spin, with the assumption that the same hyperfine coupling constant applied across the lanthanide series; A_{iso} will in fact vary across the lanthanide series, and the value obtained by Yang et al. will be skewed towards the values for lanthanides with greater spins, which may partially explain the discrepancy in the values.

Table 3.5: Hyperfine coupling constants (A_{iso}) and diamagnetic shifts (δ_0) determined assuming a linear regression between the calculated electron spins and the experimental ^{17}O NMR shifts for cubic Sm_2O_3 and Eu_2O_3, as an implicit function of temperature.

	A_{iso} /MHz	δ_0 /ppm
Sm_2O_3	−0.604 ± 0.03	17 ± 2
Eu_2O_3	−2.206 ± 0.005	−44 ± 7

Extrapolating the linear relationship determined for Eu_2O_3 to small electron spins yields shifts which are approximately coincident with the experimental shifts for Sm_2O_3 (Figure 3.8), however the linear relationship determined for Sm_2O_3 has a very different gradient to that of

Eu_2O_3 (reflected in the different hyperfine coupling constants in Table 3.5). Given that these materials share the same structure, and that the "average" hyperfine coupling constant across the lanthanide series was determined by Yang, Shore and Oldfield to be −2.7 MHz, it is unlikely that the hyperfine coupling constant for Sm_2O_3 could be as small as −0.604 MHz. Nevertheless, by using the values in Table 3.5, the calculated shifts match well with the experimental results (Figure 3.6, solid lines), although the agreement is better for Eu_2O_3. For Sm_2O_3, on the other hand, there is a deviation of the experimental shifts from the calculated values at high temperatures.

These discrepancies for Sm_2O_3 may be due to a temperature dependence of the diamagnetic shift being erroneously accounted for in the temperature dependence of the paramagnetic shift, because the paramagnetic shift in Sm_2O_3 is less significant than the diamagnetic shift (as seen for monoclinic Sm_2O_3, §3.4.1). Another consideration is the pseudo-contact shift, which has a strong temperature dependence (§2.1.3); although normally far less significant than Fermi-contact shifts when the latter is present, a pseudo-contact shift could make a greater contribution in this case because it depends on the anisotropy of the total magnetic moment, rather than just the magnitude of the spin, which is small for Sm^{3+}, and because the direct *Ln*–O bonding results in a small r^3 factor.

To determine whether a pseudo-contact shift could cause the observed discrepancies between the experimental shifts and calculated spin for Sm_2O_3, an estimate for the pseudo-contact shift can be made using the expression given in equation (2.20):

$$\delta_{PCS} = -\frac{\mu_0 \mu_B^2 g_J^2 J(J+1)(2J-1)(2J+3)}{120\pi r^3 (kT)^2} \langle J||\alpha||J\rangle \times [(3\cos^2\theta - 1)A_2^0\langle r^2\rangle + \sin^2\theta \cos 2\phi\, A_2^2\langle r^2\rangle]. \quad (3.5)$$

This formula only applies in the limit that the magnetic moment can be considered as a point dipole, which is undoubtedly invalid given the short *Ln*–O distance, however it is sufficient for a first approximation.

For the ground state of Sm^{3+}, the constant values are given by

$$\frac{\mu_0 \mu_B^2 g_J^2 J(J+1)(2J-1)(2J+3)}{120\pi k^2} \langle J||\alpha||J\rangle = 1.42 \times 10^{-9}\ \mathrm{m^3\ K^2\ J^{-1}},$$

and the total pseudo-contact shift can be written as a sum of the contributions from different Sm nearest neighbours:

$$\delta_{PCS} = -1.42 \times 10^{-9} \frac{W(T)}{T^2} \sum \frac{1}{r^3} [(3\cos^2\theta - 1)A_2^0\langle r^2\rangle + \sin^2\theta \cos 2\phi\, A_2^2\langle r^2\rangle]. \quad (3.6)$$

$W(T)$ is an additional temperature dependent factor determined by Bleaney due to the low-lying excited electronic states of Sm^{3+}, given by[54]

$$W(T) = 1 + a\frac{kT}{\Delta E} + b\left(\frac{kT}{\Delta E}\right)^2 + \frac{c(kT)^2}{\Delta E \Delta E'}, \quad (3.7)$$

where ΔE is the energy separation of the ground state and the first excited state, and $\Delta E'$ is the energy separation of the first and second excited states. For Sm^{3+}, $a = -11.25$, $b = -3$ and $c = 4.5$, resulting in a negative $W(T)$ above 122 K and hence a change in the sign of the pseudo-contact shift. Equation (3.6) is only valid up to around room temperature, above which the thermal population of excited states must also be considered, and the corresponding correction factors for equation (3.7) must be derived.

In cubic Sm_2O_3 ($Ia\bar{3}$) there are two different samarium sites at Wyckoff positions 8b and 24d: the former has three-fold symmetry, while the latter has two-fold symmetry. Each oxygen, in the general position 48e, has one 8b and three 24d Sm nearest neighbours.[82] The Sm–O distances and the crystal field splitting parameters, determined from optical measurements of single crystals of *Ln* doped isomorphic cubic Y_2O_3, are shown in Table 3.6.

Table 3.6: Sm–O distances[82] and crystal field splitting parameters for the two Sm sites in cubic Sm_2O_3. The crystal field splitting of the 8b site is for Eu/Y_2O_3,[111] and that of the 24d site is for Sm/Y_2O_3.[112] The rhombic splitting of the axial 8b site is necessarily zero.

	r /Å	$A_2^0\langle r^2\rangle$ /cm^{-1}	$A_2^2\langle r^2\rangle$ /cm^{-1}
8b	2.311	586	–
24d	2.293, 2.445, 2.363	−105	−892

The crystal field tensor orientation for the 8b site is unambiguously determined by the three-fold symmetry axis, which is aligned at 8° to the Sm–O bond, yielding a pseudo-contact shift at 300 K of +42 ppm from equation (3.6). The contributions from the 24d sites are more difficult to calculate, because the only requirement of the crystal field splitting tensor is that one principal axis is parallel to the two-fold symmetry axis, and as a result it is not possible to determine the angular factors in equation (3.6). The maximum possible contribution from each of the three 24d Sm^{3+} nearest neighbours is ca. ±40 ppm, although the magnitudes are more likely to be significantly lower, especially as the axial and rhombic contributions can oppose.

Without knowing the orientation of the 24d site crystal field splitting tensor, it is thus not possible to determine even the sign of the pseudo-contact shift, but nevertheless it can be seen that a pseudo-contact with a comparable magnitude to the experimentally observed chemical shifts (Figure 3.6) is feasible. Furthermore, as the pseudo-contact shift is expected to decrease at higher temperatures due to the $1/T^2$ dependence (presuming that the additional temperature dependence due to thermal population of excited states does not outweigh this factor), a positive pseudo-contact shift contribution—which is arguably more likely given that the only known contribution, from the 8b site, is large and positive—would explain the more negative experimental shifts observed at high temperatures relative to the calculated values: a positive contribution which decreases in magnitude at higher temperatures results in a more negative observed shift.

3.4.3 Sm- and Eu- Substituted CeO_2

Sm- and Eu- substituted CeO_2 were synthesised as detailed in §3.3.1. Bulk incorporation of the lanthanide ions was demonstrated by XRD (see Appendix A), which exclusively showed reflections from the cubic fluorite CeO_2 structure, but with expanded unit cell parameters of 5.433 Å and 5.426 Å respectively, as compared to 5.412 Å for pure CeO_2;[98] this is consistent with the ionic radii of the lanthanide ions: $Sm^{3+} > Eu^{3+} > Ce^{4+}$.[113]

The deconvoluted ^{17}O NMR spectrum of 15 at% Sm-substituted CeO_2 (Figure 3.9a, top) broadly shows three distinct regions of intensity: ~850 ppm, ~700 ppm and ~550 ppm. A similar spectrum was previously observed for diamagnetic 15 at% Y-substituted CeO_2,[92] for which the three regions were ascribed to oxygen environments with zero, one, and two Y nearest neighbours, respectively. Analogously, the signals observed in the three regions here are ascribed to oxygen environments with zero, one, and two Sm nearest neighbours. This assignment is consistent with the lower intensity of the ~550 ppm region, due to the decreased likelihood of having two Sm nearest neighbours (note that the intensity of the ~850 ppm region is not quantitative given the short recycle delay of 1 s).

In addition to the shift caused by Sm nearest neighbours, further splitting of the resonances is observed which, as was also reported for Y-substituted CeO_2, is ascribed to nearest neighbour oxygen vacancies; for every two trivalent ions substituted for Ce^{4+}, an oxygen vacancy (v_O) is formed. Specifically, the 833 and 694 ppm signals are ascribed to environments with one nearest neighbour oxygen vacancy, and zero or one nearest neighbour Sm atom(s), respectively. The 565 ppm signal (ascribed to two Sm nearest neighbours) is, however, too

broad to distinguish the environments with and without neighbouring oxygen vacancies. Finally, two components can be distinguished for the highest frequency signal with no Sm or oxygen vacancy nearest neighbours: a sharper component centred at 877 ppm and a broad component at 879 ppm. The former is assigned to environments with the pure CeO_2 structure and no substitution in the long-range vicinity, consistent with the very sharp peak of pure CeO_2 at 877 ppm,[104] while the latter is ascribed to environments with next-nearest neighbour Sm substitution and/or oxygen vacancies resulting in a heterogeneously broadened signal.

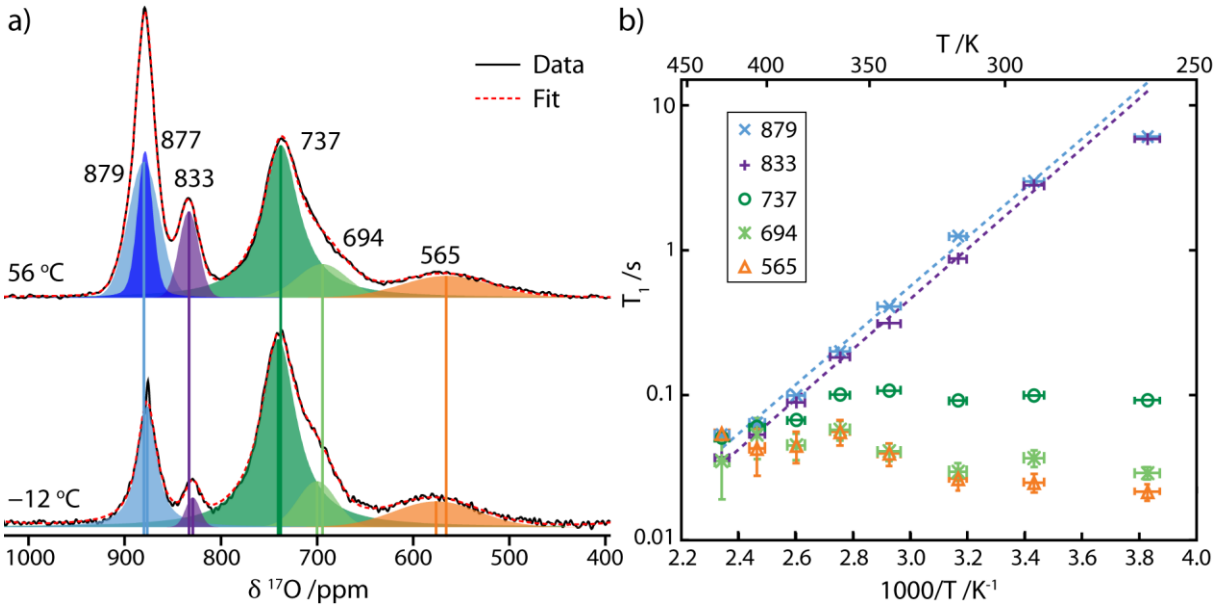

Figure 3.9: a) Deconvoluted ^{17}O NMR spectra of 15 at% Sm-substituted CeO_2 at two different temperatures, recorded with a Hahn echo pulse sequence and a 1 s recycle delay. The high temperature spectrum was recorded at 7.05 T and 40 kHz MAS, while the low temperature spectrum was recorded at 4.70 T and 14 kHz. b) Arrhenius plot of the T_1 constant for each environment as a function of temperature, measured with a saturation recovery experiment at 4.70 T and 14 kHz MAS.

These assignments could be corroborated by recording a second spectrum at lower temperature (Figure 3.9a, bottom, and Table 3.7). The paramagnetic shift due to Sm is small and positive (as observed for Sm_2O_3), the magnitude of which increases at lower temperatures; consequently, the observed chemical shift also increases (becomes more positive) at lower temperature for the signals with Sm nearest neighbours, with the greatest increase seen for the environment with two Sm nearest neighbours. Although the paramagnetic shift is positive, the net effect of Sm nearest neighbours is to reduce the ^{17}O shift, because the diamagnetic shift contribution dominates. Furthermore, the change in diamagnetic shift is greater (more negative) for Sm substitution (~150 ppm/Sm) than for Y substitution (~50 ppm/Y), which is consistent with the less positive chemical shifts observed for Sm_2O_3 than for Y_2O_3 (see above).

Table 3.7: Summary of ^{17}O environments in Sm-substituted CeO_2, with the number of Sm and oxygen vacancy (v_O) nearest neighbours, and the chemical shifts observed at 56 °C and −12 °C.

Assignment	Shift @ 56 °C /ppm	Shift @ −12 °C /ppm	Difference /ppm
0×Sm, 0×v_O	877	876	−1
	879		−3
0×Sm, 1×v_O	833	829	−4
1×Sm, 0×v_O	737	740	+3
1×Sm, 1×v_O	694	700	+5
2×Sm	565	576	+11

In order to investigate oxygen diffusion in Sm-substituted CeO_2, the spin-lattice relaxation (T_1) constants for each site were measured as a function of temperature (Figure 3.9b); the T_1 of the sharp component at 877 ppm was too long to practically measure in a reasonable time frame. The environments with Sm nearest neighbours have markedly short T_1 constants (on the order of 1 – 10 ms) due to paramagnetic relaxation enhancement,[5] for which there is no appreciable temperature dependence over this range. The T_1 constants for the 879 ppm and 833 ppm signals, on the other hand, exhibit a clear Arrhenius temperature dependence with a positive gradient, which is evidence of motion faster than the Larmor frequency (27 MHz at 4.70 T), see §2.2.1.[1,91] At the lowest temperature, the T_1 constants deviate from Arrhenius behaviour, which is ascribed to the contribution of a different relaxation mechanism that begins to outweigh the relaxation due to motion. The gradients are equivalent within error for both resonances and correspond to an activation energy of (0.35 ± 0.01) eV. The lack of Arrhenius dependence for the T_1 constants of the environments with Sm nearest neighbours is attributable to the rapid paramagnetic relaxation, which dominates over the relaxation induced by oxygen motion.

The ^{17}O NMR spectrum of Eu-substituted CeO_2 (Figure 3.10a) is similar to that of Sm-substituted CeO_2, but spans a much wider range, because the paramagnetic shift due to Eu^{3+} is both larger than that for Sm^{3+}, and negative so that it reinforces the change in diamagnetic shift. The signal for environments with no Eu nearest neighbours, centred at 867 ppm, is broader than that for Sm-substituted CeO_2 due to interactions with next-nearest-neighbour Eu ions; however, a shoulder can be distinguished, centred at 839 ppm, which is ascribed to environments with a nearest-neighbour oxygen vacancy. A second signal can also be observed at 267 ppm, which is ascribed to environments with a nearest-neighbour Eu atom. In order to identify further signals which arise from environments with Eu nearest neighbours, a T_1-filtered spectrum was acquired (Figure 3.10b), by taking the difference between spectra recorded with recycle delays of 1 s and 0.1 s, scaled so as to remove the slower-relaxing signal at ~850 ppm;

this highlights additional intensity between 0 and −1000 ppm. As the chemical shift contribution from lanthanide neighbours is approximately additive,[23] the signal at −498 ppm is ascribed to environments with two Eu nearest neighbours.

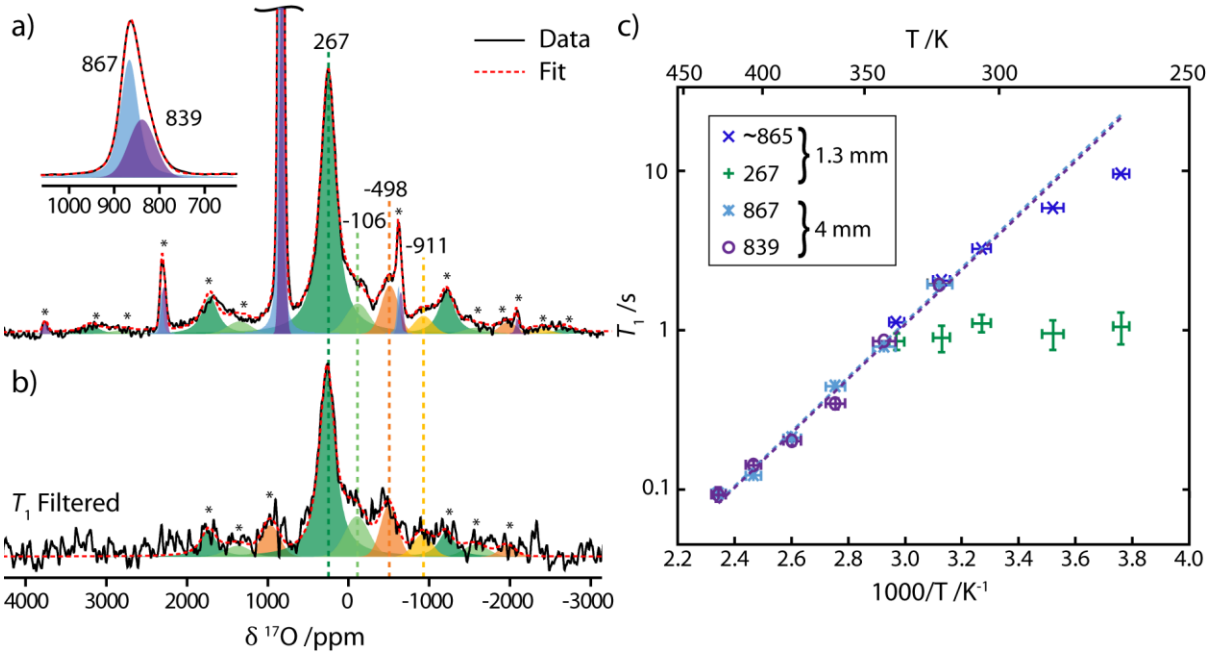

Figure 3.10: a) Deconvoluted ^{17}O NMR spectrum of 15 at% Eu-substituted CeO_2, recorded at 7.05 T and 60 kHz MAS, with a Hahn echo pulse sequence and a recycle delay of 1 s, as well as an expansion of the ~865 ppm signal. b) T_1-filtered ^{17}O spectrum, obtained by taking the difference between two spectra recorded with recycle delays of 1 s and 0.1 s, scaled so as to remove the ~865 ppm signal with a longer T_1 constant. Sidebands are marked with an asterisk. c) Arrhenius plot of the T_1 constants as a function of temperature at 7.05 T. The lower temperature experiments were performed with a 1.3 mm probe at 40 kHz MAS; the two components of the ~865 ppm signal were not sufficiently distinct to be differentiated. The higher temperature experiments were performed with a 4 mm probe at 14 kHz MAS, for which both components of the ~865 ppm signal could be distinguished, but the 267 ppm resonance could not be resolved.

There are two further resonances which can be distinguished, at −106 ppm and −911 ppm. These are similar to the shoulders observed for Sm- and Y-substituted CeO_2, which were assigned to nearest-neighbour oxygen vacancies; however for Eu-CeO_2 the additional signals are shifted to lower frequency by ~400 ppm relative to the main resonance, compared to 44 ppm and 20 ppm for Sm- and Y-CeO_2 respectively. These signals in Eu-CeO_2 are therefore instead assigned to environments with one and two nearest-neighbour Eu ions respectively, where (one of) the adjacent Eu atom(s) has an oxygen vacancy in *its* nearest-neighbour coordination shell: this undercoordination of the Eu atom will result in stronger bonding to the oxygen of interest, and hence a larger transferred spin density and a greater paramagnetic shift. This is consistent with the greater relative intensity of the −911 ppm signal to the −498 ppm signal, compared with that of the −106 ppm signal to the 267 ppm signal, because the former

signals arise from environments with two Eu nearest-neighbours, and so are more likely to have an oxygen vacancy in the coordination shell of one of the ions.

To confirm the assignment, a second spectrum was recorded at a lower temperature (Figure 3.11 and Table 3.8). The shift for environments with nearest-neighbour Eu atoms decreases at lower temperature, due to an increase in the magnetic susceptibility and hence in the magnitude of the paramagnetic shift. Furthermore, the amount by which the paramagnetic shift increases scales with the magnitude of the paramagnetic shift, i.e. the more shifted signals decrease in frequency even further. This corroborates the increased hyperfine coupling due to a second Eu nearest-neighbour or due to the presence of an oxygen vacancy in the coordination shell of a nearest-neighbour Eu atom.

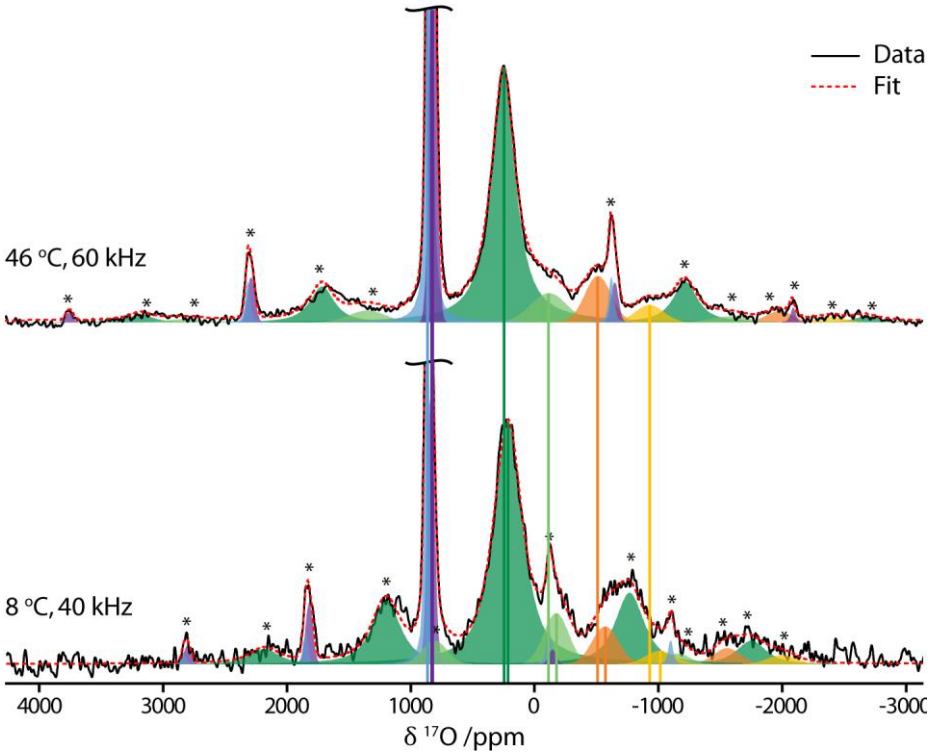

Figure 3.11: ^{17}O NMR spectra of 15 at% Eu-substituted CeO_2 at two different temperatures, recorded at 7.05 T with a 1 s recycle delay using a Hahn echo pulse sequence. The higher temperature spectrum was recorded at 60 kHz MAS and the lower temperature spectrum at 40 kHz MAS with the application of BCU-cooled nitrogen gas. The evolution of the chemical shifts is highlighted, although there is a significant error in determining the position of the lowest frequency isotropic resonance (yellow) due to overlapping sidebands.

Table 3.8: Summary of the ^{17}O environments in Eu-substituted CeO_2, and the chemical shifts observed at 46 °C and 8 °C..

Assignment	Shift @ 46 °C /ppm	Shift @ 8 °C /ppm	Difference /ppm
0×Eu, 0×v_O	867	867	0
0×Eu, 1×v_O	839	836	−3
1×Eu	267	215	−52
1×Eu + v_O	−106	−175	−69
2×Eu	−498	−571	−73
2×Eu + v_O	−911	−1014	−103

To investigate oxygen diffusion in Eu-substituted CeO_2, the T_1 constants were similarly measured as a function of temperature (Figure 3.10c). The lower temperature experiments were performed at 40 kHz MAS, which allowed the 267 ppm resonance to be distinguished, however the T_1 constants for the lower frequency signals could not be measured accurately due to insufficient signal-to-noise levels. The higher temperature experiments were performed at 14 kHz MAS, which was insufficient to resolve the 267 ppm signal. A similar result is observed as for the Sm-substituted CeO_2: the lower frequency signal at 267 ppm, ascribed to environments with a Eu nearest neighbour, possesses a short T_1 constant (~1 s) induced by paramagnetic relaxation, which shows no significant temperature dependence over the observable range. The higher-frequency ~865 ppm signal, on the other hand, again displays a marked Arrhenius-like temperature dependence of its T_1 constant, which corresponds to an activation energy of (0.34 ± 0.02) eV for both components.

Oxygen diffusion in CeO_2 is known to arise from the motion of oxygen vacancies,[33,34] which in this case are introduced by substitution with trivalent ions. The motion of these vacancies causes fluctuations in the electric field gradient at an oxygen nucleus and hence in the quadrupolar coupling, thereby inducing longitudinal relaxation.[91,114] The activation energies for oxygen vacancy motion in Sm- and Eu-substituted CeO_2 determined here are the same within error; this supports the prevalent assumption that the activation energy for vacancy hops is largely independent of the substituent.[33]

The activation energy for oxygen diffusion in 15 at% Sm-substituted CeO_2 has previously been reported as 1.00 eV from the DC conductivity[87] and 0.84 eV from impedance spectroscopy[88]. An activation energy for oxygen diffusion in 15 at% Eu-substituted CeO_2 has not been reported previously, but impedance spectroscopy experiments have yielded activation energies for 10

at% and 20 at% Eu-substituted CeO_2 of 0.64 eV and 0.89 eV, respectively.[89,90] Direct measurements of the diffusion profiles of ^{18}O in 10 at% Gd-substituted CeO_2, by depth profiling with secondary-ion mass spectrometry (SIMS), reveal a similar activation energy of 0.10 eV.[115]

These values are all significantly higher than the activation energies observed here (0.35 eV). The discrepancy between the activation energies determined by NMR and by other techniques for oxygen diffusion has been discussed by Kim et al.,[116] and was ascribed to two main factors. Firstly, bulk diffusion techniques measure the motion of vacancies that contributes to the macroscopic transport, whereas NMR is sensitive to any vacancy motion; in particular if a vacancy hops back after a forward hop it will contribute to nuclear relaxation but not to bulk diffusion. Secondly, vacancies can be trapped by defects: at low temperatures the positively charged oxygen vacancies associate with the negatively charged trivalent ion substitutional defects.[33] The activation energy for bulk diffusion includes the energy required to dissociate these vacancy–defect pairs, whereas nuclear relaxation can be caused by vacancy hops where the vacancy remains associated. An association energy of ~0.5 eV can be predicted for trivalent substituents on the basis of a point-defect model,[117] which brings the activation energy observed here more in line with the values for bulk oxygen transport.

The point-defect model is insufficient, however, to explain the variations in the total activation energy for oxygen motion with different trivalent substituents, as in this case the charge on the defects is the same; instead one must also consider the degree of lattice strain, which also acts to trap oxygen vacancies, so that the lowest association energy is observed when the ionic radius of the substituent matches that of Ce^{4+}.[33] The ionic radius of Eu^{3+} (1.09 Å) is closer to that of Ce^{4+} (1.01 Å) than to that of Sm^{3+} (1.10 Å),[113] which explains the lower activation energies for overall vacancy diffusion reported in the literature for Eu-CeO_2, as the association energy will be lower than for Sm-CeO_2; however, as the results presented here show, the activation energies for vacancy *motion* are the same, in agreement with the current understanding of ionic transport in CeO_2.

3.5 Conclusions

The ^{17}O NMR spectra for monoclinic Sm_2O_3 and Eu_2O_3 have been reported for the first time and the resonances assigned, primarily on the basis of the integrated intensities and the magnitude of the quadrupolar coupling constants. Further assignment for Sm_2O_3 is based on

the diamagnetic chemical shifts as estimated from the O coordination, which dominate for Sm_2O_3 due to the modest spin of Sm^{3+} and hence small paramagnetic shifts. DFT calculations of the quadrupolar and hyperfine coupling constants provide qualitative insights and help to corroborate the assignments, as well as permit a tentative assignment of two otherwise unassignable resonances in Eu_2O_3.

The effect of low-lying excited electronic states on the magnetic susceptibilities of Sm^{3+} and Eu^{3+} have been investigated by recording the ^{17}O spectra of the cubic sesquioxides over a wide temperature range. In particular, above room temperature the shift of Sm_2O_3 deviates from Curie temperature dependence due to the thermal population of an excited state with a greater magnetic moment, while the shift of Eu_2O_3 at lower temperatures is dominated by the temperature-independent Van Vleck paramagnetism of the ground-state. The electron spin ($\langle S_z \rangle$) was calculated as a function of temperature, yielding predicted shifts which reproduce the aforementioned behaviour and agree well with experiment. The predicted hyperfine coupling constant for Sm_2O_3, however, is not in agreement with those for the other lanthanide sesquioxides, which may be due to a temperature dependence of the diamagnetic shift or the presence of a pseudo-contact shift, either of which are being erroneously attributed to the Fermi contact shift.

The ^{17}O NMR spectra have also been recorded for 15 at% Sm- and Eu- substituted CeO_2 which reveal signals due to environments with zero, one and two *Ln* nearest neighbours, as well as further splitting due to the presence of oxygen vacancies. The T_1 constants have been measured as a function of temperature and while the environments with *Ln* nearest neighbours show largely temperature-independent short T_1 constants due to the paramagnetic relaxation enhancement, the T_1 constants for environments without *Ln* nearest neighbours exhibit a clear Arrhenius temperature dependence, corresponding to an activation energy of 0.35 eV, which is the same within error for both Sm- and Eu- substituted CeO_2 and for environments both with and without nearest neighbour oxygen vacancies. This Arrhenius behaviour is ascribed to motion of oxygen vacancies and the activation energy is compared to literature values for oxygen transport: NMR is sensitive to local motion, so does not include the vacancy–defect association energy which also contributes to the activation energy for bulk oxygen motion, explaining the larger activation energies reported in these materials using other techniques. This mechanistic information will hopefully aid in developing future improvements to the performance of these materials as solid-state oxide-ion conductors.

Chapter 4: A ^{17}O DNP NMR Study of CeO_2

4.1 Abstract

In this work surface selective direct ^{17}O dynamic nuclear polarisation (DNP) NMR was demonstrated for the first time, using CeO_2 nanoparticles mixed with the biradical TEKPol, for which the first three oxygen layers of CeO_2 can be distinguished with high selectivity. Polarisation build-up curves show that the polarisation of the (sub-)surface sites builds up faster than the bulk, accounting for the remarkable surface selectivity. These direct DNP experiments are compared with indirect ($^{1}H \rightarrow ^{17}O$) DNP experiments, but while the latter can identify minority –OH terminations and adsorbed H_2O, only the former can observe the pristine (sub-)surface oxygen environments. The linewidths of the (sub-)surface signals are significantly greater at the low temperatures required for DNP than at room temperature; this is shown to be due to freezing out of the surface dynamics resulting in a distribution of shifts, which are motionally averaged at room temperature. The identification and characterisation of surface species with NMR is important to understand and optimise materials for applications in various areas, and the methodology presented here could enable this analysis for many significant oxide materials; however, the broader linewidths observed at low temperature may hamper the application to systems which already have broader bulk signals. Finally, using 1 at% Gd-doped CeO_2, endogenous DNP has been performed with Gd^{3+} as the polarisation source, yielding moderate enhancements of the bulk ^{17}O signal; further optimisation is required, however.

4.2 Introduction

Nanoparticulate transition metal oxides are of technological importance in various areas of chemistry and materials science, such as catalysis, energy storage and electronics.[118–121] However, optimisation of materials for these applications necessitates thorough knowledge of structure–function relationships, which in turn requires an accurate description of the local surface structure. In catalytic processes, oxygen at or near the surface of, for example, CeO_2 nanoparticles is believed to constitute (part of) the catalytically active sites,[122] yet the identity and role of specific surface oxide environments in this and other nanoparticle systems remains uncertain.

As discussed in Chapter 1, NMR spectroscopy can reveal a wealth of chemical and structural information on the atomic scale, and previous work has shown that ^{17}O ssNMR spectroscopy is a powerful tool to investigate the structure and activity of zeolites,[123] metal oxide nanoparticles,[124,125] and other functionally relevant oxides.[12] However, the inherent difficulty of attaining sufficient signal to noise in NMR spectroscopy is exacerbated for experiments on ^{17}O, the only NMR-active nucleus of oxygen, as its low natural abundance (0.037%) leads to lower intensity, and its quadrupolar character (I = 5/2) can result in additional spectral broadening.

The challenges of acquiring ssNMR spectra are further confounded when studying surface environments, as they typically constitute a small fraction of the sample. Nonetheless, in recent work by Wang et al., ^{17}O ssNMR spectra of nanoparticulate CeO_2 have been recorded and assigned to specific surface environments *via* a combination of surface-selective enrichment (with $H_2{}^{17}O$) and density functional theory (DFT) calculations.[125] However, in this case the surface-selective enrichment is only possible due to the high reactivity of ceria.

A more general approach to overcome the sensitivity problems inherent to ssNMR is the use of dynamic nuclear polarisation (DNP),[126] which has seen a significant resurgence in recent years (see §1.3). In a typical exogenous DNP experiment, the sample is impregnated with radicals in a frozen glassy solvent, and the spin polarisation of the unpaired electrons on the radicals is transferred to the NMR-active nuclei *via* application of high-frequency microwave radiation. As the equilibrium polarisation of the electron is much greater than that of nuclei, NMR signal enhancements exceeding a factor of 600 have been achieved.[73]

DNP can be applied in two ways: in *direct* DNP, the nucleus of interest is directly polarised by the radicals, whereas in *indirect* DNP, ^{1}H nuclei are first polarised and cross polarisation (CP) is then used to transfer the ^{1}H polarisation to the nucleus of interest (see §2.3.5). The latter approach typically leads to larger enhancement factors and permits shorter recycle delays, but requires ^{1}H nuclei embedded in the sample. In particular, indirect DNP has been used to record the ^{13}C NMR spectra of surface organic species covalently incorporated into silica frameworks,[20] the ^{17}O NMR spectra of surface hydroxyl groups in mesoporous silica nanoparticle samples[127] and the ^{27}Al NMR spectra of surface sites in γ-alumina nanoparticles.[128] Direct DNP has been used to record the ^{27}Al NMR spectra of surface sites in mesoporous alumina–silica[129] and the ^{17}O NMR spectra of MgO.[130] However, direct DNP had not previously been used to perform surface-sensitive ^{17}O ssNMR spectroscopy. In this work,

CeO_2 nanoparticles have been investigated to establish the feasibility of surface-selective direct DNP ^{17}O NMR. Subsequently this method has been applied by other researches to investigate the surface oxygen environments in γ-alumina,[131] and the linking oxygen species for single-site Zr or Y catalysts immobilised on mesoporous silica.[132]

4.3 Experimental Methods

4.3.1 Synthesis

Commercial CeO_2 nanoparticles (Sigma Aldrich) were enriched with 70% $^{17}O_2$ gas (Cambridge Isotope Laboratories) at 350 ^oC for 24 hours and subsequently handled under an inert atmosphere (Ar or N_2 gloveboxes). To perform exogenous DNP experiments, the nanoparticles were wetted with the TEKPol biradical[76] in 1,1,2,2-tetrachloroethane (TCE); this combination has been chosen rather than the alternative AMUPol/H_2O mixture,[75] as the presence of un-enriched water can lead to removal of ^{17}O from the first layer.[125,133]

1 at% Gd-doped CeO_2 was prepared by grinding stoichiometric quantities of Gd_2O_3 (Alfa Aesar) and micron-sized CeO_2 (Aldrich) pelletising at 750 MPa under partial vacuum and firing at 1500 ^oC for 48 hours. ^{17}O enrichment was subsequently performed at 1000 ^oC for 15 hours.

4.3.2 Characterisation

Continuous-wave X-band ESR measurements were performed on a Bruker E500 X-band spectrometer with an ER 4122SHQE cavity, tuned to 9.373 GHz. The external magnetic field was modulated at 100 kHz with a modulation amplitude of 0.4 mT. The microwave power was set to 0.6325 mW, which was sufficient to avoid saturation of the resonance. The adsorption spectra was calculated from a cumulative sum of the experimental derivative spectra.

Transmission electron microscopy (TEM) images were attained using a JEOL JEM-3010 electron microscope fitted with a LaB_6 filament operating at an accelerating voltage of 250 kV. TEM images were recorded using a Gatan Multiscan 794 1k × 1k CCD camera. Image analysis was performed using the free ImageJ software.

4.3.3 DNP and NMR

All DNP NMR experiments were performed at the UK DNP MAS NMR Facility at the University of Nottingham on a 14.09 T AVANCE III HD spectrometer, corresponding to a ^1H Larmor frequency of 600 MHz, with a 395 GHz gyrotron microwave source and using a 3.2

mm double resonance wide-bore probe. Microwave source powers, measured in the waveguide, were used of 7 W for the exogenous direct DNP experiments, 12 W for the indirect ^{1}H-^{17}O DNP experiments, and 16 W for the endogenous direct DNP experiments, because these were found to give the optimal balance between saturating the radical electron spin resonance (ESR) transitions and minimising sample heating. Direct DNP experiments used a pre-saturated Hahn echo pulse sequence, with a single rotor period echo delay, while indirect DNP experiments comprised a $^{1}H \rightarrow ^{17}O$ cross polarisation block followed by a ^{17}O Hahn echo. Experiments were performed under low-temperature MAS (~95 K, 12.5 kHz) with radio-frequency strengths of 56 kHz for the ^{17}O direct DNP experiments and 96 kHz for the ^{1}H $\pi/2$ in the indirect DNP experiments. Cross polarisation in the indirect DNP experiments was established with a lower power for ^{17}O of 1 kHz and a ^{1}H power of 73 kHz; a Hahn echo was appended to the sequence to suppress background distortions, and the ^{17}O NMR spectrum was recorded with ^{1}H decoupling using a swept-frequency two-pulse phase modulation (SW-TPPM) sequence.[134,135] DNP spectra were referenced to room temperature bulk CeO_2 at 877 ppm.

A conventional ^{17}O ssNMR spectrum of CeO_2 nanoparticles was recorded on a 11.7 T AVANCE III spectrometer, corresponding to a ^{1}H Larmor frequency of 500 MHz, using a 2.5 mm double resonance probe and a radio-frequency strength of 91 kHz. Variable temperature conventional ^{17}O NMR spectra were recorded on a 9.4 T AVANCE spectrometer, corresponding to a ^{1}H Larmor frequency of 400 MHz, using a 4 mm double resonance probe and a radio-frequency strength of 50 kHz. The sample temperature was determined by an ex-situ calibration using the temperature dependent ^{207}Pb shift of $Pb(NO_3)_2$.[101] Conventional ssNMR ^{17}O spectra were referenced to H_2O at 0 ppm.

Spectra were deconvoluted using the dmfit software.[105]

4.4 Results and Discussion

The CeO_2 nanoparticles were first investigated using TEM (Figure 4.1a); this showed a predominantly octahedral morphology with an average particle size of 11 ± 5 nm. Identification of the (111) fringes with a spacing of 3.12 Å revealed that the particles were dominated by (111) facets, the structure of which is shown in Figure 4.1b. TEM analysis of the enriched samples revealed minor coarsening with a subsequent average particle size of 15 ± 3 nm.

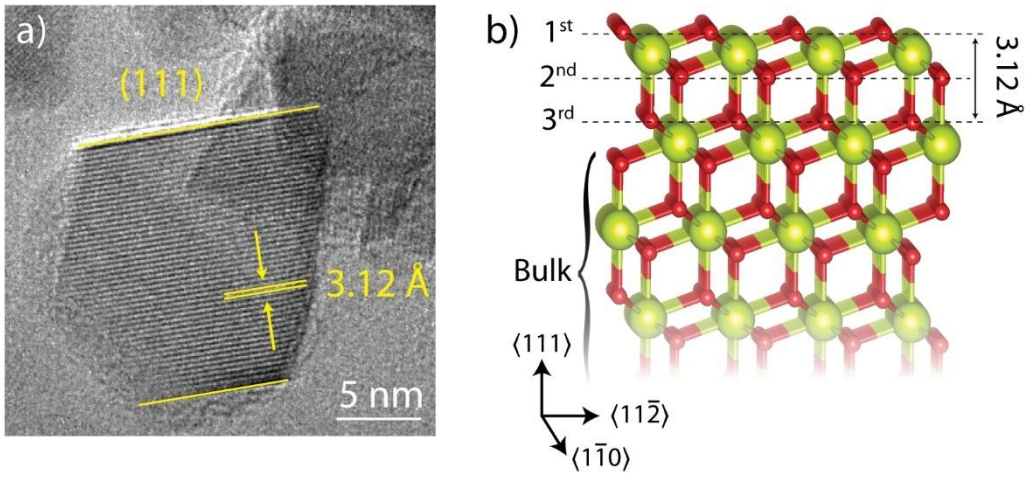

Figure 4.1: a) HRTEM image of a CeO_2 nanoparticle showing (111) fringes, (111) surfaces and an octahedral morphology (in projection), and b) the structure of a (111) O-terminated CeO_2 surface showing the first three oxygen layers and the (111) spacing. Cerium atoms are depicted as larger and yellow while oxygen atoms are smaller and red. *The TEM image was recorded by Dr David Jefferson, University of Cambridge.*

4.4.1 Direct DNP

Direct ^{17}O DNP NMR experiments were then performed on the enriched CeO_2 particles, mixed with TEKPol biradicals in TCE. Figure 4.2 shows the ^{17}O ssNMR spectra recorded with and without microwave irradiation ("ON" and "OFF", respectively), with 8 scans and a recycle delay of 60 s. Without microwave irradiation, only the sharp signal due to the single bulk oxygen environment could be observed, whereas under microwave irradiation three new features were distinguished; these are ascribed to (sub-)surface sites selectively enhanced by TEKPol radicals in the vicinity of the surface. By comparison with the DFT calculations of Wang et al.,[125] these features at 1055, 893, and 843 ppm are identified as oxygen sites within the first, second and third (sub-)surface layers, respectively (labelled in Figure 4.1b). There is some discrepancy between the chemical shifts observed in this work and those reported by Wang et al., which is ascribed to minor differences between the CeO_2 samples. The (sub-)surface sites also have a larger anisotropy than the bulk as evidenced by the greater intensity of their spinning sideband manifolds, consistent with the reduction of symmetry at the surface.

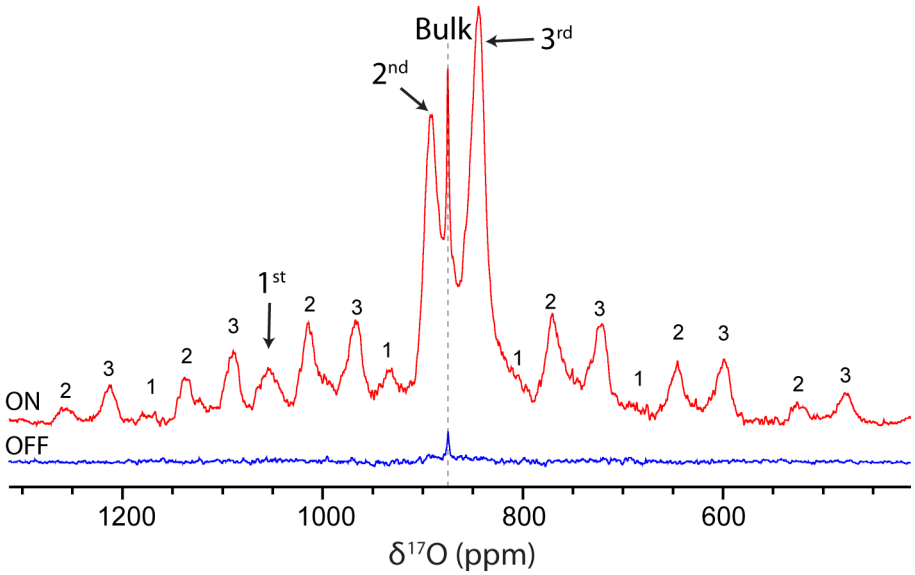

Figure 4.2: ^{17}O NMR (14.1 T) spectra of ^{17}O enriched CeO_2 nanoparticles mixed with the TEKPol radical in TCE, with and without microwave irradiation, using a pre-saturated Hahn echo experiment. The spectra were recorded at 95 K. The OFF spectrum was recorded at 12.5 kHz MAS, whereas the ON spectrum was recorded at 10 kHz in order to separate the spinning sidebands from the signal arising from the first layer. Spinning sidebands are labelled according to the layer of the signal from which they arise.

4.4.2 DNP Build-up Curves

The observed surface selectivity in direct DNP occurs because the radicals are external to the particle and the rate of polarisation transfer from the radical to a nucleus falls off rapidly (as $1/r^6$).[136] Nuclei at the surface can therefore be hyper-polarised by the radicals, but for sites within the deep sub-surface layers, the excess nuclear spin polarisation must travel via spin diffusion, which is thought to be slow for ^{17}O (in part due to the low natural abundance and gyromagnetic ratio),[137] leading to a longer build-up time.

To test this hypothesis, the DNP build-up time constant (T_{DNP}) was determined for each feature using a saturation recovery experiment. The nuclear magnetisation was first nullified with a saturation pulse train and then allowed to build up *via* DNP for a variable time before measuring the resulting magnetisation by recording the ^{17}O NMR spectrum. The build-up time was found by fitting the signal intensity to a stretched exponential function of the form

$$I = I_0\left(1 - \exp\left[-\left(\frac{t}{T_{DNP}}\right)^{\beta}\right]\right), \tag{4.1}$$

with I_0 the maximum signal intensity and $0 < \beta < 1$ the stretching exponent. A stretched exponential function describes a build-up process consisting of a distribution of time constants characterised by T_{DNP}; a smaller β parameter indicates a broader distribution.[138] The build-up curves are shown in Figure 4.3, with fitted time constants T_{DNP} in Table 4.1. The bulk site

exhibits a slow build-up (continuing beyond the maximum recorded time of 1600 s), as spin polarisation must diffuse a significant distance. In contrast, T_{DNP} of the (sub-)surface sites is much shorter, accounting for the observed surface selectivity.

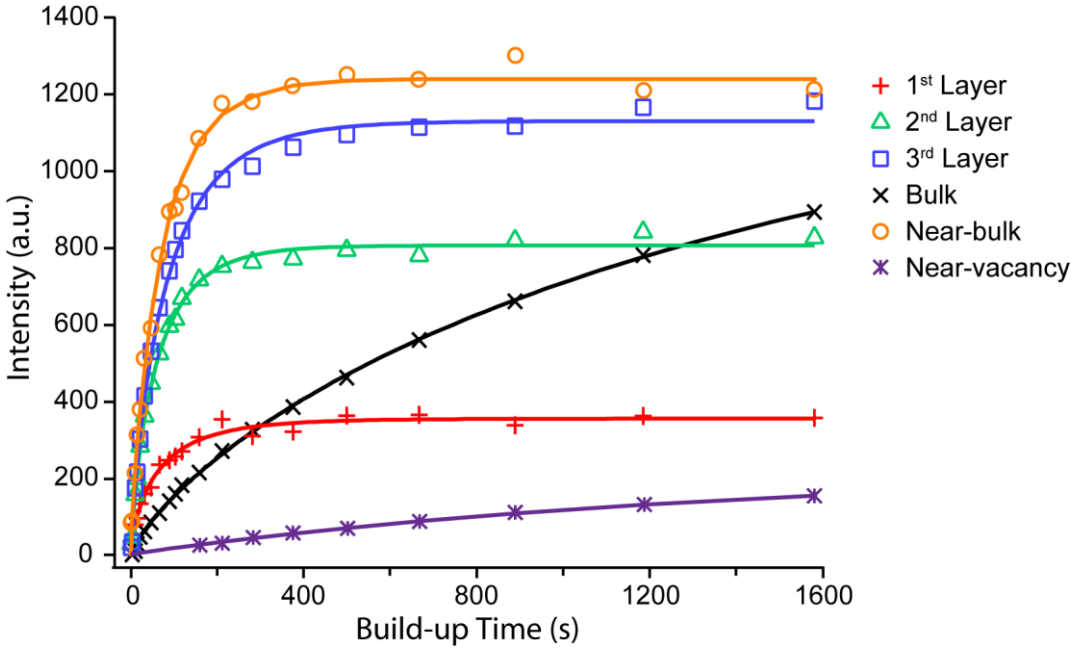

Figure 4.3: The ^{17}O saturation recovery build-up curves for the different environments in CeO_2 nanoparticles and the fitted stretched exponential functions. The integrated intensity is determined by deconvoluting the isotropic peaks.

Table 4.1: Stretched exponential parameters used to fit all the deconvoluted signals in the ^{17}O saturation recovery experiments performed on CeO_2 nanoparticles. Errors reflect one standard deviation in fitted parameters as determined through total least squares fitting. The signals with long build-up constants cannot be accurately fitted with the available data, so the parameters are approximate and the actual T_{DNP} values may be significantly larger. *The errors in the fitted parameters were determined by Dr David Halat, University of Cambridge.*

	Shift / ppm	**T_{DNP} / s**	**I_0 / arb. units**	**β**
Bulk	875	~2100	1630	0.75
1st layer	1055	67 ± 6	355 ± 7	0.72 ± 0.05
2nd layer	893	62 ± 2	806 ± 7	0.82 ± 0.03
3rd layer	843	85 ± 3	1130 ± 12	0.82 ± 0.03
Near-bulk	872	66 ± 4	1205 ± 15	0.87 ± 0.04
Near-vacancy	858	~1400	225	1

In addition to the obvious bulk and (sub-)surface signals, a further broad peak at 872 ppm was required to deconvolute the spectra (Figure 4.4). As this shift is close to that of bulk CeO_2 (875 ppm at 95 K), this signal is ascribed to "near-bulk" environments, which are close to the surface so have a broader distribution of shifts than the well-defined bulk signal. This is corroborated

by the short T_{DNP} for the near-bulk signal, which is similar to those of the distinct (sub-)surface signals, indicating that the environments must be sufficiently close to the surface to be effectively enhanced by DNP.

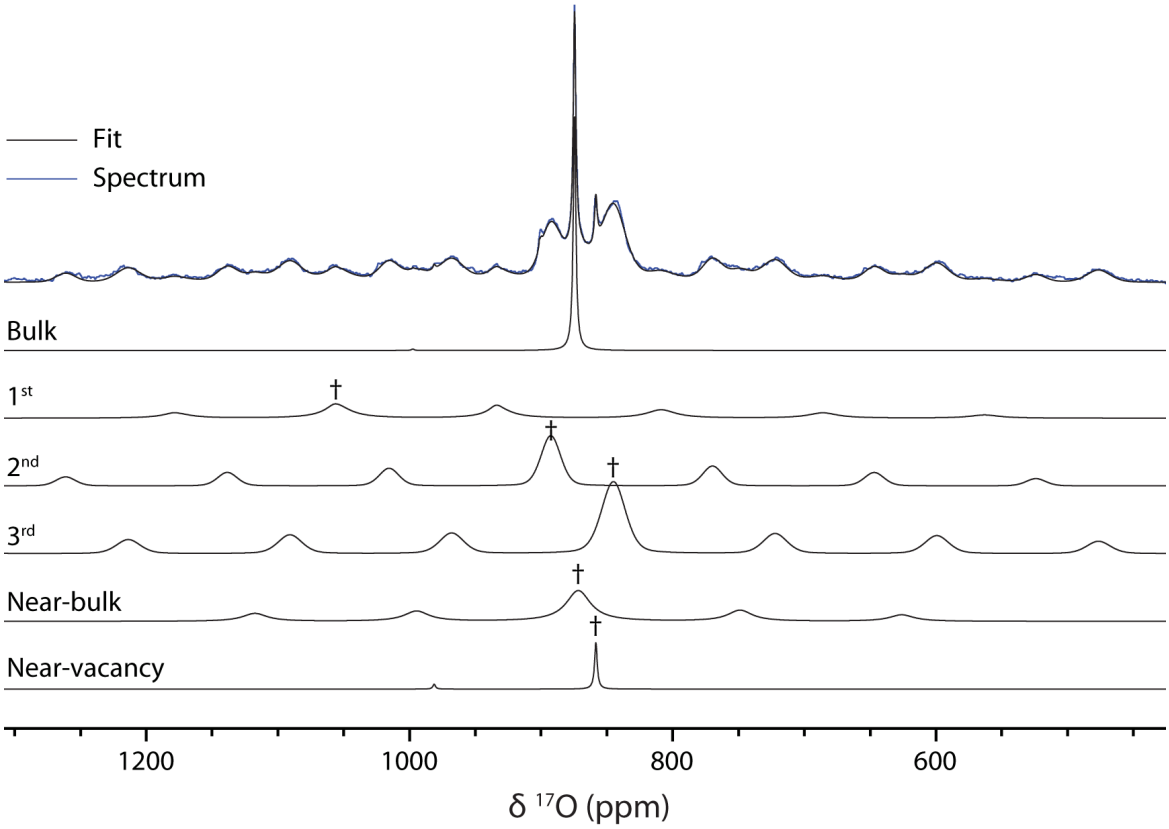

Figure 4.4: Direct ^{17}O DNP NMR spectrum (14.1 T) of ^{17}O enriched CeO_2 nanoparticles recorded at 10 kHz MAS with a pre-saturated Hahn echo pulse sequence and a recycle delay of 1581 s, showing the deconvoluted signals, for which the isotropic resonances are indicated by a dagger.

At very long build-up times, a sharp signal can be observed at 858 ppm (Figure 4.4). The direct DNP build-up time constants for this signal cannot be determined accurately as the saturation recovery experiment did not extend to long enough build-up times, however it is clear from the build-up curve (Figure 4.3) that the time constant is long. The sharp nature of the peak and the long T_{DNP} suggests that this signal arises from environments in the bulk of the nanoparticles, which are well-defined and only hyperpolarise slowly. Wang et al. observed a similar signal at 845 ppm in the room temperature spectrum of reduced samples of CeO_2;[125] reduction introduces both paramagnetic Ce^{3+} ions and oxygen vacancies, so this signal was ascribed to oxygen ions with either an oxygen vacancy in the first anion coordination shell or a Ce^{3+} ion in the second cation coordination shell (Ce^{3+} ions in the first cation coordination shell would induce significantly greater paramagnetic shifts and faster relaxation). Ceria nanoparticles are often oxygen deficient (with vacancy concentrations as high as 9% having been reported for 3

nm nanoparticles[139]), so the 858 ppm peak observed here is ascribed to oxygen sites within the bulk of the nanoparticles with nearest neighbour oxygen vacancies; the difference in chemical shift is ascribed to the difference in temperature between the DNP spectrum (95 K) and the room temperature spectrum of Wang et al. Oxygen vacancies are a more likely explanation than Ce^{3+} ions in this case because 1) the signal is sharp, whereas vicinity to Ce^{3+} would be likely to cause paramagnetic broadening, 2) the magnitude of a paramagnetic shift increases with decreasing temperature, so a less positive shift, further from the bulk signal, would be expected at the low temperatures used for DNP experiments, rather than the more positive observed shift, and 3) a similar signal is observed for Sm-substituted CeO_2, where oxygen vacancies are introduced without the addition of Ce^{3+} ions (see §3.4.3). Oxygen environments near to Ce^{3+} ions must also be present if the sample is oxygen deficient, but they are not observed in these spectra, which is most likely to be due to the additional broadening and the faster paramagnetic relaxation associated with the Ce^{3+} ions.

The maximum signal intensity of the (sub-)surface sites is given by a combination of the enrichment level, the DNP enhancement and the degree of quenching (loss of signal due to broadening and extremely fast nuclear relaxation very near the radicals).[140] The conventional ssNMR spectrum recorded without radicals shows that the enrichment of the first three (sub-)surface layers is approximately equal (Figure 4.5 and Table 4.2); the differences observed in the maximum signal intensity therefore show that the first layer is quenched more than the second layer, which in turn is quenched more than the third layer, due to closer proximity to the radicals, and that the greater degree of quenching closer to the surface outweighs any increase in DNP enhancement.

Table 4.2: Fitted intensity ratios relative to the first layer for the ^{17}O (sub-)surface signals in CeO_2 nanoparticles recorded with conventional NMR and DNP, as determined by spectra which are quantitative with respect to the (sub-)surface sites with recycle delays of 5 s and 375 s respectively. N.B. the ratios are not comparable between the experiments but are normalised with respect to the first layer.

	1st Layer		**2nd Layer**		**3rd Layer**
Conventional ssNMR	1	:	1.08	:	1.12
DNP	1	:	2.41	:	3.31

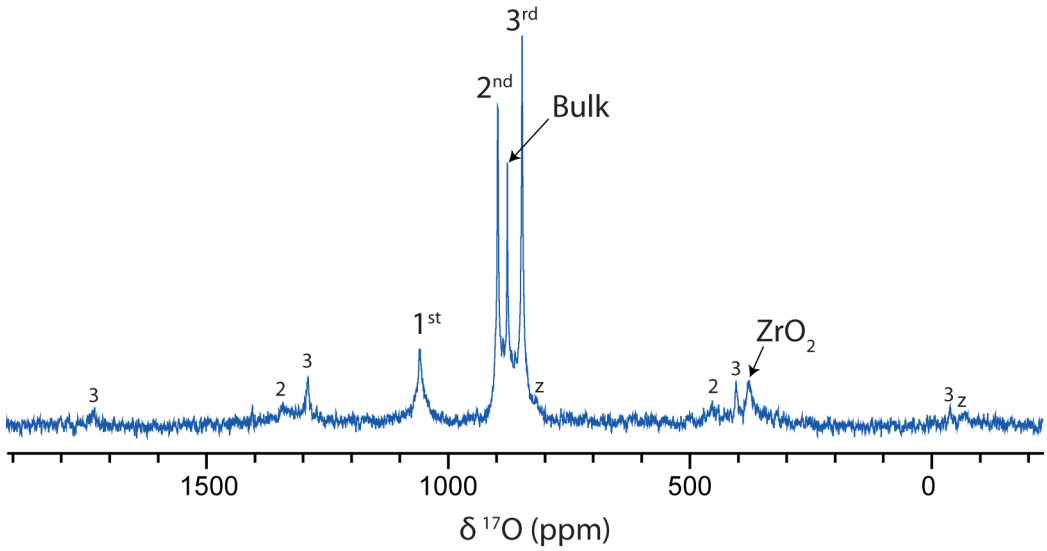

Figure 4.5: Conventional ^{17}O NMR spectrum (11.7 T) of ^{17}O enriched CeO_2 nanoparticles recorded overnight at room temperature with a recycle delay of 5 s under 30 kHz MAS with 13904 scans. The signal due to the ZrO_2 rotor can also be observed at 377 ppm. The sidebands are labelled with the numeral of the layer from which they arise, or with 'z' for the ZrO_2 signal. Frictional heating under MAS results in a sample temperature of approximately 315 K.

4.4.3 Effect of Enrichment Level and Air Exposure

A second experiment was performed on a sample of the same nanoparticles but enriched with a higher pressure of $^{17}O_2$ and stored under ambient conditions (Figure 4.6a, Table 4.3). For this sample, the second and third layer sites are again selectively enhanced by DNP, but the signal arising from the first layer is not observed due to exchange with $^{16}O_2$ in the air. The bulk signal is more intense than previously, indicating an increased incorporation of ^{17}O due to the higher $^{17}O_2$ pressure during enrichment; the build-up time constant for the bulk signal is also smaller than the previous sample (Figure 4.6b, T_{DNP} = 586 s c.f. ~2100 s), which is ascribed to faster spin diffusion into the bulk due to the greater enrichment, because spin diffusion is strongly dependent on the concentration of the spin-active nucleus. Again, the deeper third layer has a longer build-up time than the second layer, but both time constants are slightly longer than those for the aforementioned sample. This may also be due to the greater enrichment, because there are more nuclei for each radical to hyperpolarise; the polarisation of the electron is split between more nuclei and each therefore takes longer to hyperpolarise.

The higher enrichment level also allows the (sub-)surface sites to be observed without DNP in a long (12 h) experiment, and hence DNP enhancements ($\varepsilon_{ON/OFF}$) for the second and third layers can be measured as 56 and 29, respectively. The greater enhancement of the second layer is presumably due to less efficient hyperpolarisation of the more distant third layer (the quenching due to radicals is present with or without microwave irradiation, so does not affect

the enhancement factor). The bulk site exhibits only a very minor enhancement as it is dominated by atoms far from the surface which are not hyperpolarised. We note, however, that as a recycle delay of 60 s is insufficient to obtain the maximum signal either with or without microwave irradiation, the observed enhancement factors for all sites will be dependent on the recycle delay. As has been previously addressed by Lee et al., $\varepsilon_{ON/OFF}$ should be seen as a guide to the DNP enhancement rather than a fundamental parameter.[140] These results show that the DNP NMR spectra of CeO_2 nanoparticles are sensitive to details of sample preparation which affect the enrichment level; this can in turn give insight into the mechanisms of DNP by modulating the rates of hyperpolarisation and spin diffusion.

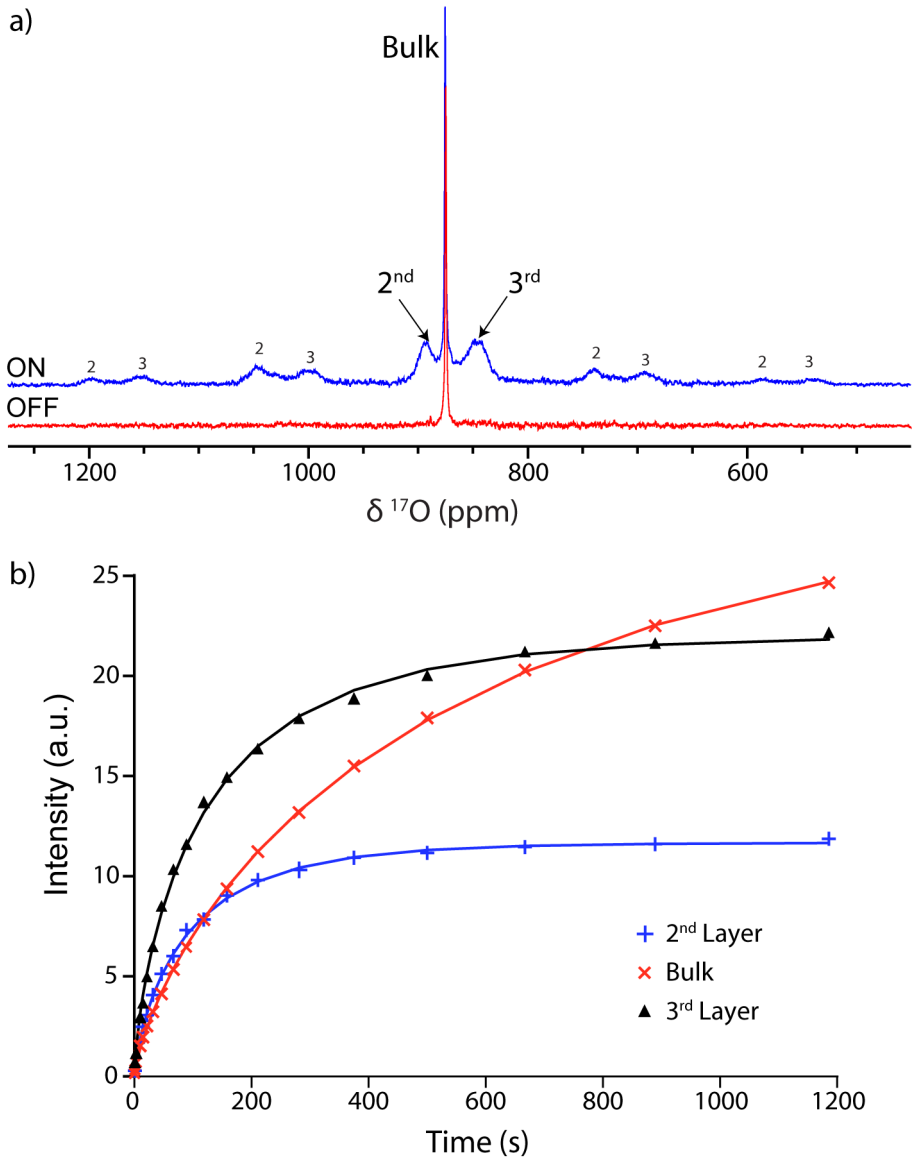

Figure 4.6: a) ^{17}O NMR (14.1 T) spectra of air-exposed ^{17}O enriched CeO_2 nanoparticles mixed with the TEKPol radical in 1,1,2,2-tetrachloroethane (TCE), with and without microwave irradiation, performed at 12.5 kHz MAS using a presaturated Hahn echo experiment and a recycle delay of 60 s. b) ^{17}O DNP build-up curves.

Table 4.3: Chemical shifts, DNP enhancements and fitted DNP build-up time constants for the three environments observed in ^{17}O enriched CeO_2 nanoparticles prepared under ambient conditions.

Assignment	Shift /ppm	$\varepsilon_{ON/OFF}$	T_{DNP} /s
2nd Layer	893	56	97.9
Bulk	875	1.3	586
3rd Layer	846	29	134

4.4.4 Indirect DNP

To compare with the direct DNP experiments, indirect DNP ($^{1}H \rightarrow ^{17}O$) NMR spectra were also recorded on the first nanoparticulate CeO_2 sample (Figure 4.7). These reveal ^{17}O signals centred at 225 ppm and −20 ppm, which are ascribed to Ce-OH terminations and H_2O molecules adsorbed to the surface, respectively, again in agreement with Wang et al.[125] These assignments are supported by the short CP contact time of 200 μs required to attain the maximum CP intensity, which is indicative of direct O–H bonding; the signal is attenuated with longer contact times. These signals could not be observed with direct DNP, even when the carrier frequency was varied, but require the greater enhancement factors achievable with indirect DNP. The indirect DNP experiments do not, however, exhibit evidence for the (sub-)surface sites identified *via* direct DNP NMR, even under conditions of longer contact times and variable rf carrier frequencies (efficient CP is only observed to signals close to the carrier frequency). The lack of (sub-)surface oxygen features is attributed to the $1/r^6$ dependence of CP on distance and the difficulty of spin-locking the quadrupolar ^{17}O nucleus, so that only oxygen atoms directly bonded to hydrogen can be readily seen.[141] Furthermore, there are few hydroxyl terminations and adsorbed water molecules on surfaces of CeO_2 samples oxidised at >300 ^{o}C,[142] and the hydrophobic TCE solvent does not adsorb strongly, so insufficient protons exist in the vicinity of the surface to permit efficient CP. Therefore, direct DNP is needed in this case to observe surface and sub-surface oxygen sites in nanoparticulate CeO_2.

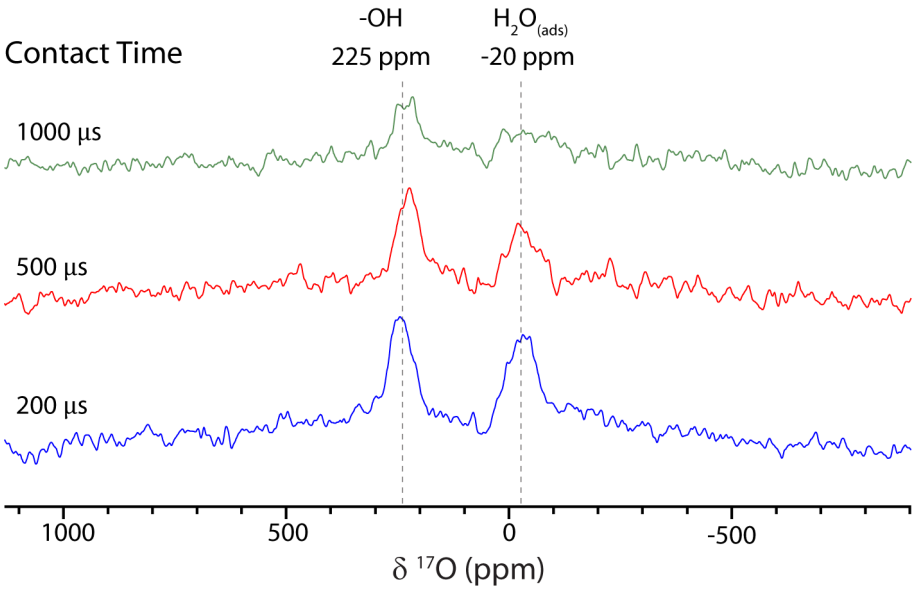

Figure 4.7: The indirect DNP ^{17}O NMR (14.1 T) spectra of ^{17}O enriched CeO_2 nanoparticles impregnated with TEKPol in TCE, recorded at 12.5 kHz MAS with a recycle delay of 4.3 s, 320 scans and variable contact times for the $^{1}H \rightarrow ^{17}O$ cross polarisation. The ^{17}O magnetisation was pre-saturated to avoid the direct DNP signal.

4.4.5 Field Sweep

The DNP enhancement in this case is due to the cross effect which depends on the matching of the microwave frequency, the electron spin resonance (ESR) spectrum of the radical and the NMR frequency of the nucleus in question.[126] In practice the microwave frequency is fixed and as the latter two are dependent on the magnetic field of the NMR spectrometer, the magnetic field can be varied to some degree to optimise the DNP enhancement which yields a characteristic field profile of the enhancement (see §2.3).

A field sweep experiment was performed for the CeO_2 sample prepared under ambient conditions (Figure 4.8) and shows the positive lobe of the TEKPol field profile. All other experiments were performed at $\nu_0(^{17}O)$ = 81.44 MHz and it can be seen that the observed enhancements were near optimal. The surface selectivity of direct DNP can also be seen in the field profiles in that the profile from the bulk signal is flatter than for the sub-surface signals; this is because there is less enhancement of the bulk signal under DNP conditions as the nuclei are far from the radicals, but there are more bulk sites so without DNP, i.e. when the field is incorrectly set, there is more bulk signal.

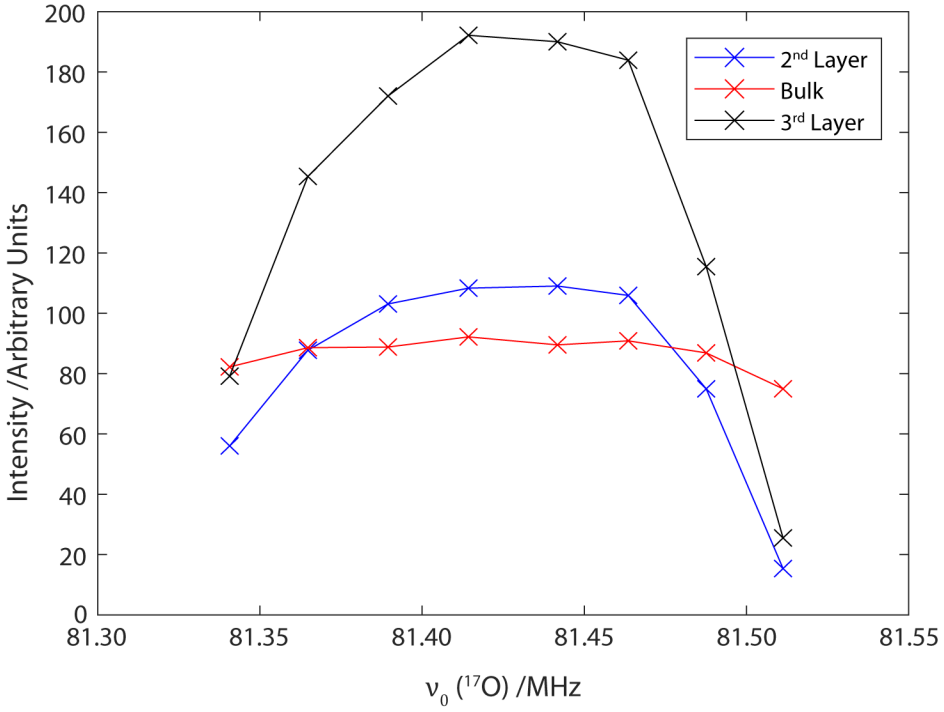

Figure 4.8: A field sweep experiment showing the fitted intensities of the three environments in the ^{17}O enriched CeO_2 nanoparticle/TEKPol/TCE sample packed under ambient conditions as a function of the ^{17}O Larmor frequency.

4.4.6 Conventional Variable Temperature NMR

The (sub-)surface signals observed in the ^{17}O direct DNP spectrum (Figure 4.2) have significantly greater linewidths than the bulk signal, which is evidence of a distribution of environments for the sites in each of the (sub-)surface layers; i.e. the surface does not have a precisely fixed spatial configuration, but rather can exhibit a range of slightly different arrangements, in a relatively flat energy landscape. However, in the room temperature conventional ^{17}O NMR spectrum (Figure 4.5), significantly narrower peaks are observed for the (sub-)surface layers: this is due to motional narrowing of the signals because the thermal energy causes the oxygen atoms to sample the different surface configurations faster than the NMR timescale.[1] This observation is in agreement with previous TEM studies,[143] in which the dynamic motion of the surface atoms in CeO_2 can clearly be observed in real time, although for {100} surfaces rather than the {111} surfaces studied here.

The motional averaging can be frozen out by modest cooling (Figure 4.9), and by 240 K the linewidths are similar to those of the DNP experiments recorded at 95 K (Figure 4.2). The fact that broad signals are observed for the (sub-)surface environments in the conventional low temperature NMR experiments rules out the biradicals as the cause of broadening in the DNP

experiments, and the motional narrowing at higher temperatures proves that the linewidth is due to a distribution of environments.

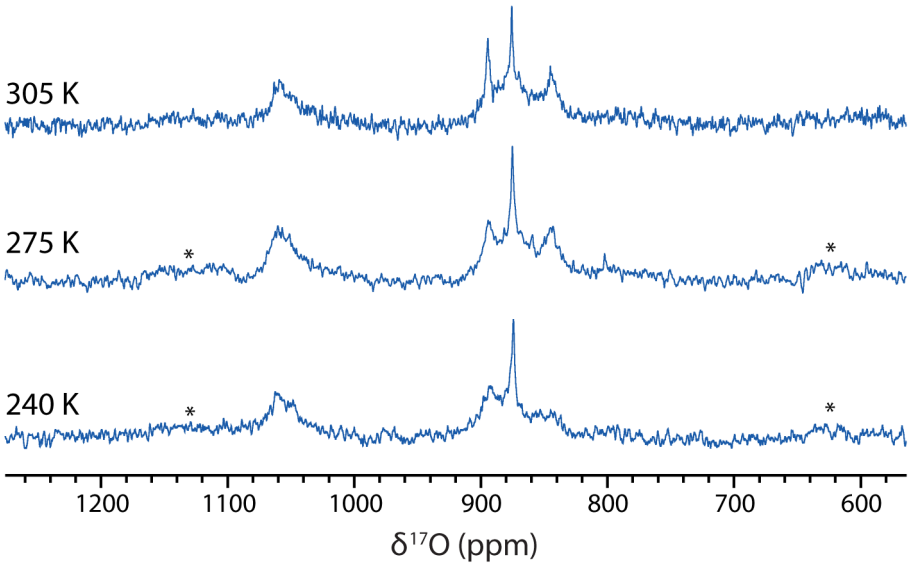

Figure 4.9: Conventional variable temperature ^{17}O NMR spectra (9.4 T) of ^{17}O enriched CeO_2 nanoparticles, recorded at 14 kHz MAS, using a Hahn echo pulse sequence, with a recycle delay of 0.1 s and between 128,000 and 350,000 scans. Temperature calibration was performed ex-situ using the ^{207}Pb shift of $Pb(NO_3)_2$.

4.4.7 Endogenous DNP of Gd-CeO_2

Unlike exogenous DNP where a radical source must be added to the sample, endogenous DNP makes use of paramagnetic centres contained in the sample. For the study of metal oxides, high spin metal centres, such as Mn^{2+} or Gd^{3+}, can be doped into the material, and endogenous DNP of $^{6/7}Li$ and natural abundance ^{17}O has previously been demonstrated by this method for the battery material $Li_4Ti_5O_{12}$.[74,144] The primary advantage of endogenous DNP is that the paramagnetic centres are dispersed within the sample, so that bulk solids can be studied, as opposed to exogenous DNP where the radicals are excluded from the solid. Surface selective DNP, on the other hand, obviously cannot be performed in this way, unless the doping process itself is surface selective (e.g. for coatings or surface-immobilised catalysts). Here, the feasibility of performing endogenous ^{17}O DNP NMR on CeO_2 doped with 1 at% Gd^{3+} is explored.

In Figure 4.10a the endogenous direct ^{17}O MAS DNP NMR spectra of ^{17}O enriched, 1 at% Gd-doped CeO_2 are shown with and without microwave irradiation. A modest, negative, DNP enhancement is achieved with enhancement factors determined from the amplitude of the centreband, and from the total integrated spectral area, of $\varepsilon_{amp} = -5.2$ and $\varepsilon_{area} = -4.0$, respectively. Figure 4.10b shows a comparison of the two spectra, scaled so that the broad

components of the centreband are coincident: the sidebands have a lower enhancement compared to the centreband, which explains why ε_{area} is less than ε_{amp}. This difference could arise because the environments which contribute more to the sideband intensity are those which are closer to a Gd dopant, and therefore experience greater dipolar hyperfine coupling (see §2.1.3); these environments will also have a shorter nuclear T_1 relaxation constant, reducing the equilibrium hyperpolarisation which can build up, and hence reducing the enhancement.

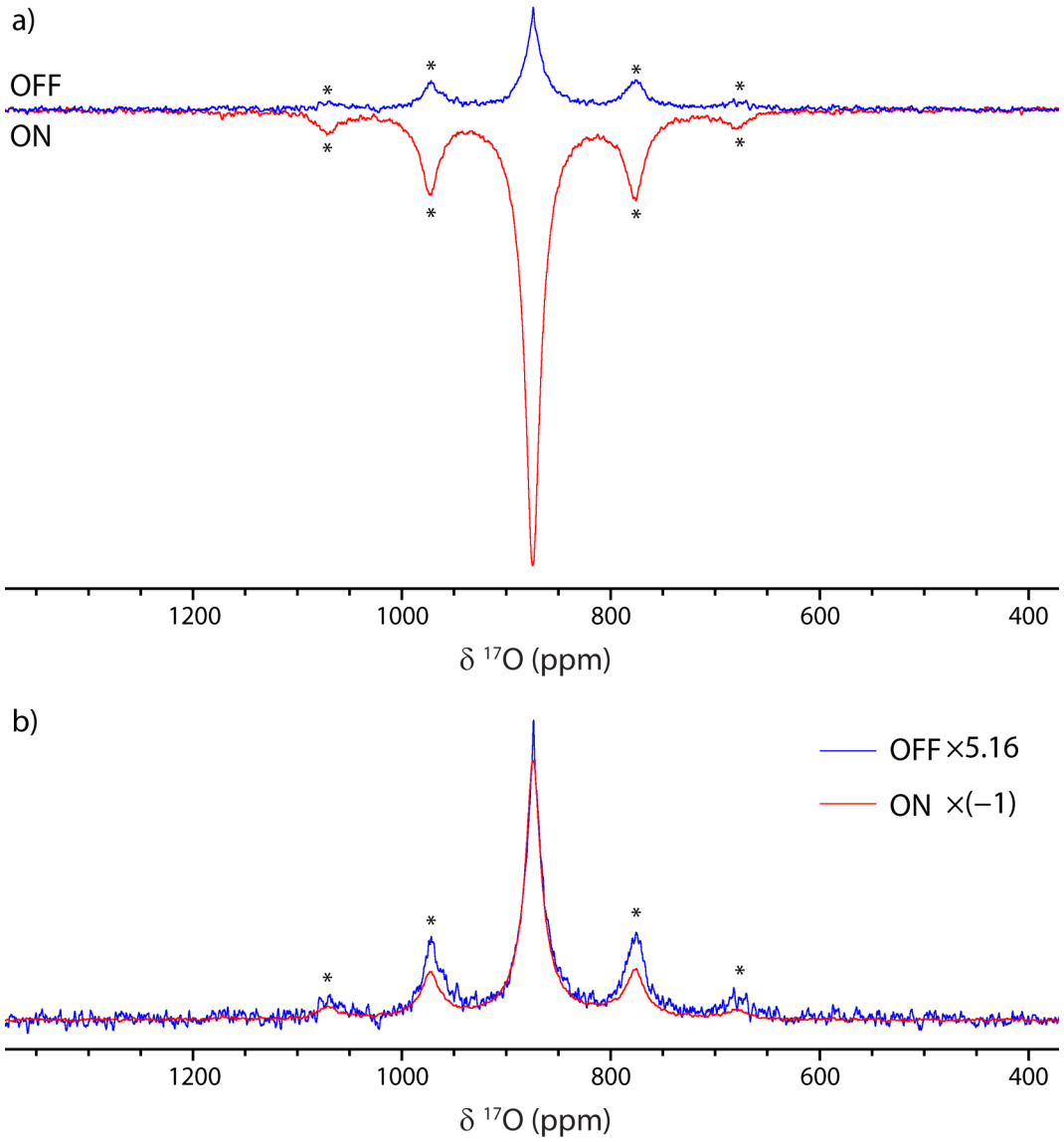

Figure 4.10: ^{17}O direct DNP NMR spectra of 1 at% Gd-CeO_2 with and without microwave irradiation, recorded at 14.1 T and 8 kHz MAS, with a 5 s recycle delay and 16 W microwave source power, using a pre-saturated Hahn echo pulse sequence. Spinning sidebands are marked with asterisks. The spectra have been rescaled in (b) to allow comparison of the centreband and sideband intensities.

To aid interpretation of the observed DNP phenomena, the continuous-wave X-band ESR spectrum of the sample was recorded (Figure 4.11b). Gd^{3+} has spin S = 7/2 and although the environment in CeO_2 is cubic, so that there is no second-rank splitting (known as zero-field

splitting, ZFS), the system is subject to fourth-rank and sixth-rank couplings;[145] however, significantly sharper features would still be expected. There are two isotopes of Gd to which hyperfine coupling can occur, ^{155}Gd and ^{157}Gd, both with $I = 3/2$; however, they have very low gyromagnetic ratios with hyperfine coupling constants ~0.5 mT,[146] and do not affect the spectrum significantly in this case. One contribution to the substantial broadening is the large degree of dipolar coupling between the spins at this comparatively high concentration. Another consideration is the presence of oxygen vacancies, introduced by the aliovalent doping: a vacancy present in the vicinity of the Gd^{3+} dopant breaks the local cubic symmetry and therefore introduces a significant ZFS. Furthermore, the probability of this occurring is greater than would be predicted by a random distribution of vacancies, since association of the oppositely charged substitutional defects and oxygen vacancies is energetically favoured.[92,147] Nevertheless, the spectrum does exhibit a peak in intensity, which would correspond to a g-factor of 1.97 (c.f. the true value of 1.99 previously determined[145] by fitting the ESR spectrum of 0.01% Gd-CeO_2).

The breadth of the ESR spectrum suggests that a differential solid effect mechanism could be operating in the DNP experiments (see §2.3.2). The observed negative enhancement can then be explained by the form of the ESR spectrum: based on the calculated g-factor, the maximum ESR intensity will occur at a higher magnetic field than that used in the DNP experiments, and the gradient of the ESR spectrum with respect to the field is positive. By considering Figure 4.12, it can be seen that there are more spins which resonate at a lower frequency $\omega_{0S} = \omega_{\mu w} - \omega_{0I}$, than spins which resonate at the higher frequency $\omega_{0S} = \omega_{\mu w} + \omega_{0I}$; the former induce negative hyperpolarisation, while the latter induce positive hyperpolarisation, so the net hyperpolarisation is thus negative. A differential solid effect would also explain the low enhancement, because the positive and negative enhancements largely cancel each other out. A cross effect mechanism could also be operating at this concentration level, because there is sufficient dipolar coupling between electron spins to allow cross effect transitions (see §2.3.3), which complicates the interpretation.[74,148,149]

A field sweep was performed from 14.08 – 14.16 T (Figure 4.11a), but there was little change in enhancement over the accessible range of magnetic fields; this is also explained by the broad lineshape of the ESR spectrum, because the intensity (or, more importantly for the differential solid effect, the gradient) changes very little over the narrow range of magnetic field strength. To improve the DNP enhancement, a lower concentration of Gd^{3+} could be used which would both reduce the dipolar coupling and decrease the probability of oxygen vacancies being

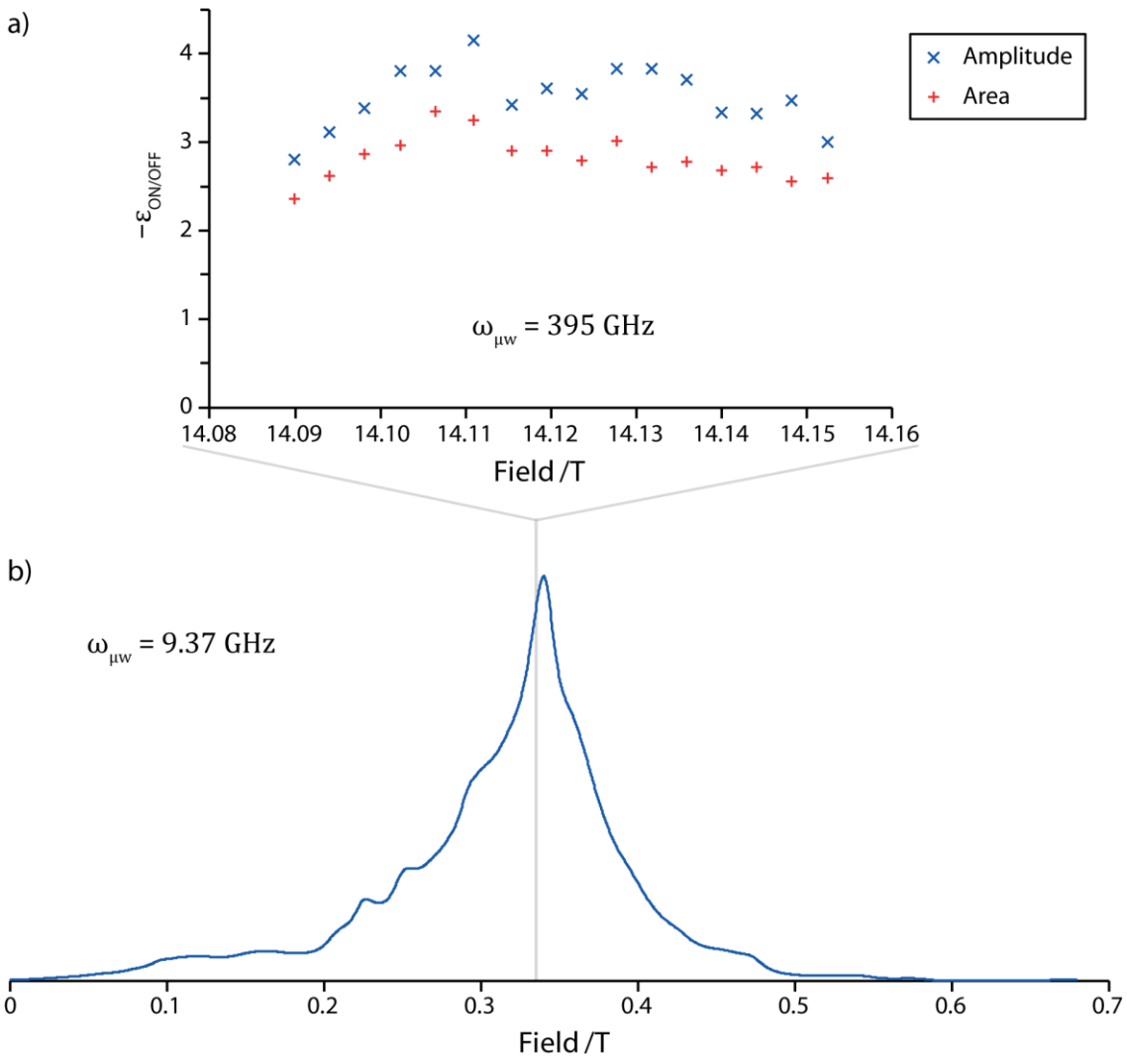

Figure 4.11: a) Field profile of DNP enhancement factors, by amplitude and by area, with a microwave power of 12 W, and b) the X band (9.37 GHz) ESR spectrum for 1 at% Gd-CeO_2. The absorption ESR spectrum was calculated from a numerical integration of the experimental derivative spectrum. The grey line indicates the region of the ESR spectrum explored in the DNP field sweep, accounting for the different microwave frequencies. *The ESR spectrum was recorded by Euan Bassey, University of Cambridge*.

present near the dopants (although association would still be energetically favoured). This would reduce the broadening of the ESR spectrum and hence lessen the cancellation of positive and negative enhancements. However, decreasing the dopant concentration will also increase the average distance from any given oxygen to a paramagnetic centre, and as spin diffusion is slow for ^{17}O, this could reduce the enhancement; the optimum dopant level is therefore a compromise between these factors. Another option is to use an alternative metal dopant that exhibits sharper ESR lines. Mn^{2+} is a possible choice, although the ESR signal is split by hyperfine coupling to the ^{55}Mn nucleus with $I = 5/2$, so that only a sixth of the spins can be on resonance with the microwave irradiation at any given moment. Furthermore, it can be difficult to ensure the correct oxidation state for Mn in the sample, given that high temperature solid-

state syntheses will cause oxidation, whereas lanthanide ions remain stable in the 3+ oxidation state up to very high temperatures. Nevertheless, by using a coprecipitation synthesis, Mn^{2+} can be incorporated in CeO_2,[150] which could afford a greater enhancement from endogenous DNP.

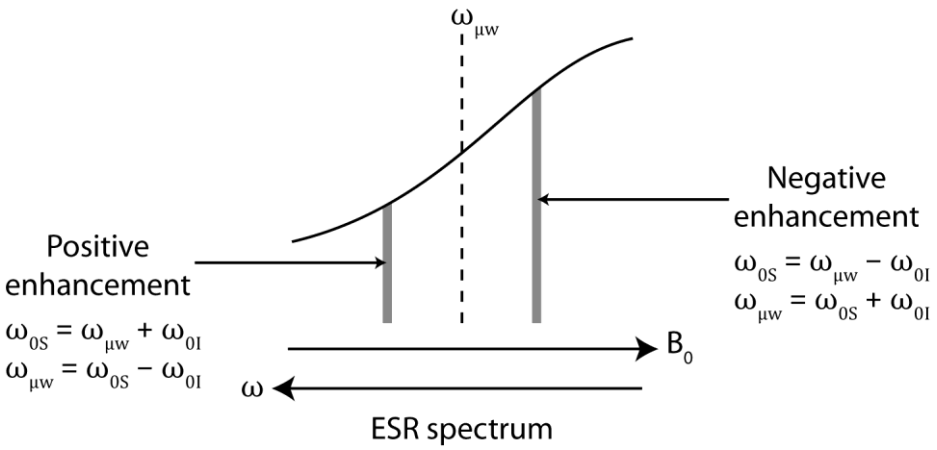

Figure 4.12: Schematic representation of the net negative differential solid effect in the case that the ESR spectrum has a positive gradient with respect to the magnetic field at the applied microwave frequency.

4.5 Conclusions

In this work, surface-selective direct ^{17}O DNP NMR spectroscopy has been demonstrated for the first time, using a system of CeO_2 nanoparticles, for which the first three layers can be distinguished with high selectivity. This selectivity is ascribed to the slow spin diffusion of ^{17}O polarisation into the bulk, so that only the (sub-)surface sites are efficiently hyperpolarised by radicals in the vicinity of the surface. This is corroborated by the build-up curves for the different signals and by comparison between samples with different degrees of enrichment.

The saturation recovery spectra recorded with different build-up times also reveal near-bulk and near-vacancy signals; the former is ascribed to oxygen ions deeper than the three distinguishable (sub-)surface layers, but still sufficiently close to the surface to be effectively hyperpolarised and to have a broader distribution of environments than the bulk site, while the latter has a narrow linewidth and long build-up time constant, suggesting a bulk environment with a different chemical shift due to a nearest neighbour oxygen vacancy.

It is shown that although indirect DNP can be used to identify –OH terminations and adsorbed water on the CeO_2 surface, it is not possible to observe the aforementioned (sub-)surface sites *via* this approach due to the scarcity of protons near the surface and the difficulty of long-distance $^{1}H \rightarrow ^{17}O$ cross polarisation; (sub-)surface sites can only be detected with direct DNP.

The DNP experiments are compared with conventional ssNMR experiments, with the latter exhibiting significantly narrower signals at room temperature; by performing low temperature experiments, this is shown to be due to motional narrowing, highlighting the dynamic nature of the surface. In contrast, the broad resonances at lower temperatures, including the DNP spectra, indicate that the surface structure has been frozen into a distribution of different configurations.

These experiments demonstrate the utility of direct ^{17}O DNP in identifying signals which arise from the surfaces of oxide materials, especially those in which protons are not available to allow indirect DNP experiments. Once these signals have been determined, they can be used to gain insight into the surface structure, most likely in combination with theoretical calculations, or to observe changes in the surface after further reaction or aging. However, application of this methodology to new systems may prove challenging if the signal from the bulk environment is broader, due to disorder in structure or substitution for example, or if there are multiple bulk sites. The bulk resonance in CeO_2 is exceptionally sharp, yet it is only just possible to resolve three (sub-)surface signals at this field and spinning speed; for broader bulk resonances, it may be impossible to resolve any surface signals. This is particularly problematic for DNP experiments due to the low temperatures required, which has the dual effects of freezing out any motional narrowing, which may improve the spectral resolution at room temperature, and reducing the maximum spinning speed for a given rotor size. While the latter may be addressed by using a faster spinning probe or in some cases by using a lower magnetic field (which increases the effective sideband separation in ppm), it may still be beneficial in such systems to forgo DNP and use an alternative method of surface enhancement, such as selective enrichment.

Finally, to enhance the bulk of CeO_2 particles, it is shown that endogenous DNP can be used. Here, a minor enhancement has been demonstrated for 1 at% Gd-doped CeO_2 which, by reference to the ESR spectrum, is most likely to be due to a differential solid effect mechanism. However, to apply this method to potential applications in systems with low sample masses and/or for which isotopic enrichment is not possible, further optimisation of the enhancement is required, by varying both the concentration and the identity of the paramagnetic dopant.

Chapter 5: An NMR Study of the Hydrogenation and Electrochemical Metallisation of VO_2 by Electrolyte Gating

5.1 Abstract

Metallization of initially insulating VO_2 *via* ionic liquid electrolytes, otherwise known as electrolyte gating, has recently been a topic of much interest for possible applications such as Mott transistors and memory devices. Metallization has been shown to take place electrochemically and, there has previously been evidence for the removal of small amounts of oxygen during ionic liquid gating. Hydrogen intercalation has also been proposed, but the source of the hydrogen has remained unclear. In this work, solid-state MAS NMR spectroscopy (^1H, ^2H, ^{17}O and ^{51}V) is used to investigate the thermal metal–insulator transition in VO_2, before progressing to catalytically hydrogenated VO_2 and electrochemically metallized VO_2. Electrochemical metallisation of bulk VO_2 particles is shown to be associated with intercalation of hydrogen, the degree of which can be measured with quantitative ^1H NMR spectroscopy. Possible sources of the hydrogen are explored, and by using a selectively deuterated ionic liquid, it is revealed that hydrogenation is due to deprotonation of the ionic liquid; specifically, for the commonly used dialkyl-imidazolium based ionic liquids, it is the "carbene" proton which is responsible. Increasing the temperature of the electrochemistry is shown to increase the degree of hydrogenation, forming first a less hydrogenated metallic orthorhombic phase then a more hydrogenated insulating Curie–Weiss paramagnetic orthorhombic phase, both of which were also observed for catalytically hydrogenated VO_2. The NMR results are supported by magnetic susceptibility measurements, which corroborate the degree of Pauli and Curie–Weiss paramagnetism. Finally, NMR spectroscopy is used to identify the presence of hydrogen in an electrolyte gated thin film of VO_2, suggesting that electrolyte breakdown, proton intercalation and reactions with decomposition products within the electrolyte should not be ignored when interpreting the electronic and structural changes observed in electrochemical gating experiments.

5.2 Introduction

In 1959 it was discovered that upon heating to above 67 °C, vanadium dioxide (VO_2) transitions from an insulating to a metallic state with an increase in electronic conductivity of several orders of magnitude;[41] since then, VO_2 has been the subject of extensive study to understand the subtle interplay between electronic correlations and a Peierls distortion that underlie this metal–insulator transition (MIT).[151–153] More recently there has been interest in electronically inducing this transition (otherwise known as gating) for possible applications such as Mott transistors[43] and memory devices;[44] this research has focused on thin films of VO_2. It was reported by Nakano et al.[154] that non-thermal metallisation of VO_2 films, induced by application of a gate voltage to an electrolyte at the surface of the film (Figure 5.1a, left), was a purely capacitive effect, whereby the ionic liquid forms a double layer at the solid–liquid interface and hence induces a large electric field in the sample. Jeong et al.[45] later showed that the metallisation was in fact due to the electrochemical reduction of the vanadium and consequent introduction of electrons into the band structure. This reduction must be charge balanced, and Jeong et al. proposed the simultaneous creation of oxygen vacancies on the basis of ^{18}O secondary ion mass spectrometry (SIMS) data, which showed an excess of ^{18}O at the surface of devices that had been repeatedly gated and reverse gated in an $^{18}O_2$ atmosphere; this is the generally accepted mechanism in the literature.[155–160] The same group later showed that oxygen plays a role in ionic liquid gating of several other oxides including WO_3, again by ^{18}O SIMS.[161] Most recently they directly observed oxygen vacancies, using in-situ transmission electron microscopy, in $SrCoO_{2.5}$ produced by electrolyte gating of $SrCoO_3$.[162] On the other hand, Shibuya and Sawa[163] observed hydrogen intercalation by ^1H SIMS after electrolyte gating of VO_2, which could also charge balance the reduction; however, the source of hydrogen remained unclear.

Hydrogen can be intercalated into VO_2 in the channels parallel to the rutile *c* axis (Figure 5.1b, bottom); this is a possible mechanism of the metallisation of VO_2 *via* electrolyte gating because metallisation has also been observed after explicit hydrogenation of VO_2 by various techniques: (i) electrolytically by splitting of H_2O in a water-infiltrated nanoporous glass solid electrolyte[164] or a humid-air nanogap,[165] (ii) galvanically by electrical contact with a sacrificial anode in acidic solution,[166] and (iii) catalytically *via* hydrogen spillover.[167,168] While these studies were all based on nanosized VO_2, either thin films or nanowires, hydrogenation of bulk VO_2 has also been investigated electrochemically[169] and catalytically,[170] albeit with the studies

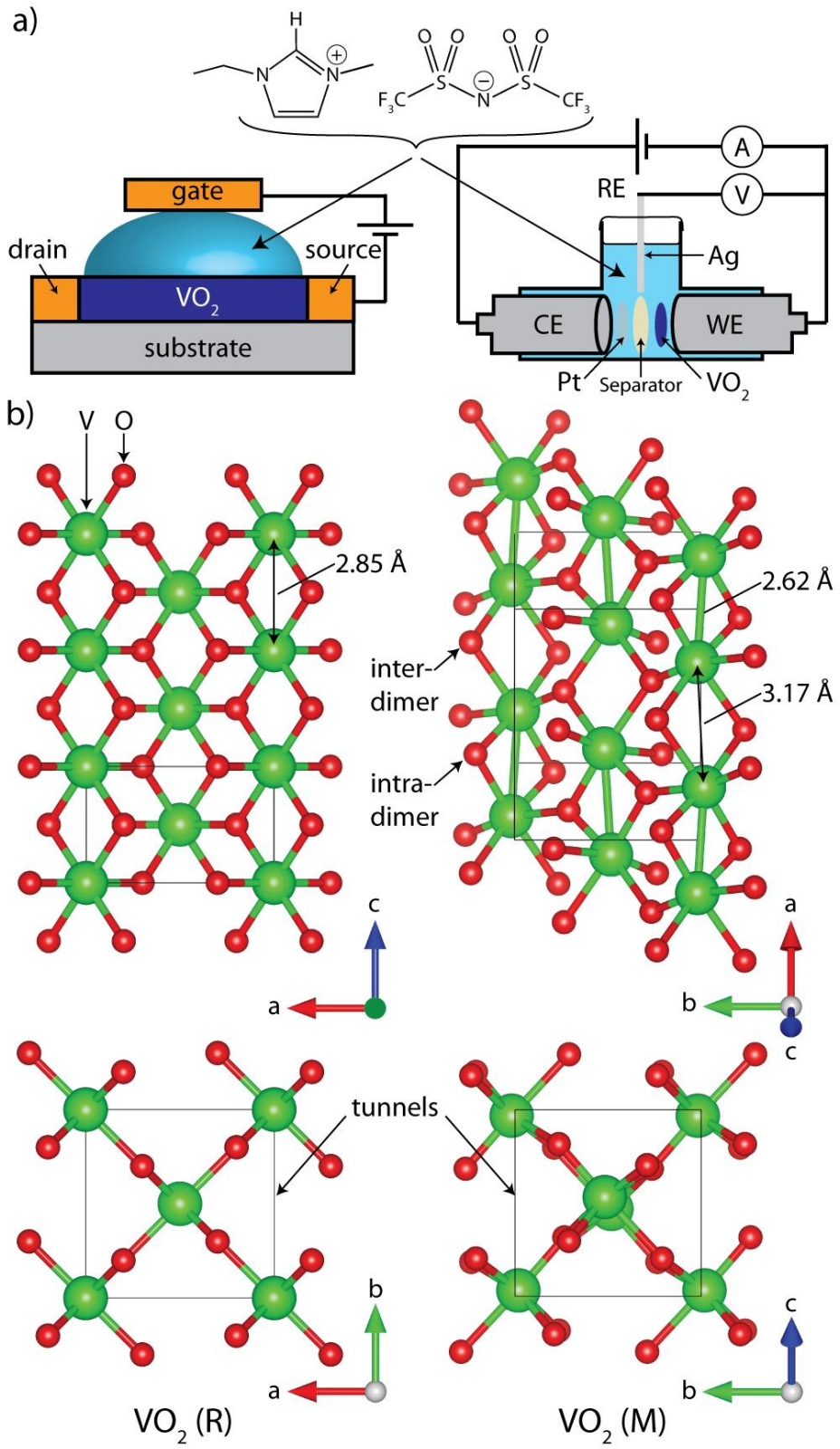

Figure 5.1: a) Left: schematic of a thin film electrolyte gating experiment, where a potential is applied across the gate electrode and the resistance between the source and drain is measured. Right: schematic of the three-electrode cell used in this work for electrochemical experiments on bulk VO_2 showing the VO_2 working electrode (WE), Pt counter electrode (CE) and Ag wire pseudo-reference electrode (RE); shown too is a commonly used ionic liquid, EMIm TFSI. b) Structures of the metallic, rutile, high temperature VO_2(R) phase, and the insulating, monoclinic, low temperature VO_2(M) phase. VO_2(R) has a single oxygen site in the asymmetric unit, while VO_2(M) has two oxygen sites, bridging vanadium atoms either within or between vanadium dimers.

focusing on the structural rather than the electronic properties. Nevertheless questions remain, including whether ionic liquid gating is associated with hydrogenation of the VO_2? If so, what is the source of hydrogen? And, most importantly, what is the cause of metallisation?

As discussed in Chapter 1, ssNMR is a useful tool to study the metallization of VO_2 as it is an element-specific probe of both the crystal and electronic local structures.[42,171] In particular, Knight shifts (§2.1.4) are a direct measure of the local density of states at the Fermi level for the nucleus in question; they can be used to identify metallic environments and are typically temperature-independent.[56] Paramagnetic shifts due to localised spins (§2.1.3), on the other hand, have a strong temperature dependence.[5] These different shift mechanisms can, therefore, be used to determine the local electronic structure.

In this work, multi-nuclear NMR spectroscopy (^{1}H, ^{2}H, ^{17}O and ^{51}V) is utilized to study the crystal and electronic structure of electrochemically metallized VO_2 samples and explore the mechanism of electrochemical metallisation, using the imidazolium-based ionic liquids that are commonly used for electrolyte gating experiments;[45,155–158] these NMR results are supported by X-ray diffraction (XRD), resistivity and magnetic susceptibility measurements. First, the NMR of pristine micron-sized VO_2 particles are investigated above and below the MIT temperature, before the magnetic and electronic properties of catalytically hydrogenated VO_2 are examined. The results are compared with electrochemically reduced bulk VO_2, and the effect of increasing the temperature at which the electrochemistry is performed is investigated. To explore the source of hydrogen in these experiments, ^{2}H NMR measurements were performed on bulk VO_2 which was electrochemically reduced with a selectively deuterated ionic liquid; this reveals that deprotonation of the ionic liquid occurs at the voltages used in these experiments, resulting in the observed hydrogenation of VO_2.

These experiments are performed on polycrystalline micron-sized particles to allow bulk characterisation techniques to more easily be applied, namely ssNMR, XRD and magnetic susceptibility measurements. For the electrochemical experiments, composite films including a binder and conductive carbon are used to afford mechanical and electrical connectivity, although the presence of carbon and the low density preclude resistivity measurements. To investigate the effect of the bulk kinetics on the VO_2 reduction, nanoparticles are also studied, again in the form of composite films: these have shorter length scales for diffusion, but at the expense of poorer XRD resolution, greater difficulty in achieving the correct oxidation state, and less uniform electrochemistry. To confirm the applicability of these results to the previous

electrolyte gating experiments on thin films, NMR spectroscopy is then used to identify intercalated hydrogen in a thin film sample of VO_2 which has been electrolyte-gated with an imidazolium-based ionic liquid, although this is approaching the sensitivity limits of NMR. Finally, the implications for electrolyte gating are discussed.

5.3 Experimental Methods

5.3.1 Synthesis

Bulk VO_2 was synthesised by comproportionating an equimolar mixture of V_2O_3 and V_2O_5 in an evacuated quartz tube at 600 ºC for 48 hours to yield ~2 μm particles. The V_2O_5 (Sigma-Aldrich, 99.99%) was first dried *in vacuo* at 640 ºC for four days and the V_2O_3 was synthesised by reducing V_2O_5 in 5% H_2/Ar (10 mL/min) at 650 ºC for 24 hours.[172] ^{17}O-enriched VO_2 was prepared in the same way, but starting from ^{17}O-enriched V_2O_5, which was prepared by oxidizing metallic vanadium powder (Sigma-Aldrich, 99.5%) in 70 at% $^{17}O_2$ gas (Cambridge Isotope Laboratories) at 620 ºC for two days.

Catalytically hydrogenated VO_2 was prepared by mixing the comproportionated VO_2 with Pd nanoparticles (Sciventions, aqueous suspension, 1.5 mg/mL) before removing the water *in vacuo* at 100 ºC to give 1 wt% Pd. The Pd/VO_2 was then hydrogenated in flowing 25% H_2/N_2 at 180 ºC for 15 hours. A second sample was also prepared by hydrogenation in flowing 5% H_2/Ar at 220 ºC for 15 hours. Hydrogenated samples were handled in an argon glovebox.

VO_2 nanoparticles were synthesised by ball milling the comproportionated VO_2 (500 mg) in a 50 mL zirconia jar with five 10 mm diameter zirconia balls, for 8 × 15 minutes using a Fritsch Pulverisette 23 shaker mill.

5.3.2 Characterisation

Powder X-ray diffraction (XRD) patterns were recorded in reflection mode with sample rotation on a PANalytical Empyrean diffractometer emitting Cu Kα (1.540598 Å + 1.544426 Å) radiation. Air-sensitive samples were packed into a Kapton sample holder. Phase identification was achieved by profile matching using PANalytical's X'Pert HighScore Plus 2.2 software and by comparison with the following ICSD entries: 1473 (V_2O_3),[173] 74705 (VO_2 M),[174] 1504 (VO_2 R)[175] and 15798 (V_2O_5).[176] Rietveld refinement was performed using the Topas Academic software package.[100] Structures were visualized with the VESTA software

package.[96] Thermogravimetric analysis (TGA) was performed under flowing N_2 using a Mettler Toledo TGA/SDTA 851 thermobalance with a 100 μL Al_2O_3 crucible.

Resistivity measurements were performed on pressed pellets (750 MPa, 30 minutes, under partial vacuum) using the four-point probe technique and a Quantum Design Physical Property Measurement System (PPMS Dynacool). Susceptibility measurements were performed using a Quantum Design Magnetic Property Measurement System (MPMS3) and an applied field of 100 Oe.

Scanning electron microscopy (SEM) and scanning transmission electron microscopy (STEM) were performed using a TESCAN MIRA3 FEG-SEM with acceleration voltages of 5 kV or 30 kV. The samples were stuck to carbon tape or dispersed on holey carbon grids and coated with ~10 nm of Cr. Average particles sizes were determined from the measured images using ImageJ software.[177]

5.3.3 NMR

For NMR experiments, samples were packed into ZrO_2 rotors. All the NMR spectra were recorded on either a 4.70 T or a 7.05 T Bruker Avance III spectrometer, except one ^{2}H NMR spectrum of D_xVO_2 which was recorded on an 11.75 T Bruker Avance III spectrometer. The relatively low magnetic fields used here are advantageous for investigating the NMR of paramagnetic and metallic materials because the paramagnetic and Knight shifts are linear in the applied field, and so constant in chemical shift (see §2.1), whereas the sideband separation afforded by magic angle spinning is constant in frequency; greater sideband separation, and hence resolution of signals, can therefore be achieved at lower magnetic fields for the same MAS frequency; furthermore, spinning of metallic samples is easier at lower magnetic fields. Most experiments used a Bruker 1.3 mm HX probe and either 40 kHz or 60 kHz MAS frequency, except (a) the ^{2}H NMR spectra at 4.70 T and 7.05 T which used a Bruker 2.5 mm HX probe and 30 kHz MAS, (b) the ^{1}H NMR spectra of the VO_2 thin film which used a Bruker 1.9 mm HX probe and 40 kHz MAS, and (c) the wide temperature range ^{1}H NMR spectra of Pd/H_xVO_2 which used a Bruker 4 mm HX probe and 14 kHz MAS. All experiments used a Hahn echo pulse sequence ($\pi/2$-τ-π-τ-*acquire*) unless otherwise stated. ^{1}H and ^{17}O sideband separation experiments were recorded by taking the isotropic slice from a MATPASS experiment,[103] and ^{1}H T_1 (spin-lattice) measurements were recorded with an inversion recovery pulse sequence. ^{51}V variable offset cumulative spectra (VOCS) were recorded by summing spectra recorded with different carrier frequencies, with retuning of the probe between

experiments being performed by an external automatic tuning/matching (eATM) robot.[178] Quantitative ^{1}H NMR spectra were recorded at 4.70 T and 60 kHz MAS, with the sample centre-packed between PTFE tape to ensure excitation of the full sample mass; the integrated intensity was then compared to a calibration with known masses of adamantane, also centre-packed. The T_2 relaxation constants were sufficiently long that no correction for transverse decay was required. For ^{1}H quantification, the catalytically hydrogenated samples were ground with a known mass of KBr to minimize skin depth penetration effects. ^{1}H NMR spectra of the VO_2 thin film were recorded using a DEPTH background suppression pulse sequence ($\pi/2$-τ-π-2τ-π-τ-*acquire*),[179] and then background-subtracted by first recording the sample then recording the background of an empty rotor with the same experiment and taking the difference. The T_1 filtered spectrum was obtained by recording two spectra with recycle delays of 0.05 s and 0.1 s, background-subtracting both, then taking the difference, scaling the spectra to minimize the diamagnetic signals which have longer T_1 relaxation constants.

Variable temperature NMR experiments were performed by application of heated or cooled nitrogen, with cooling achieved either with a Bruker cooling unit (BCU) or a liquid nitrogen heat exchanger. The sample temperature was determined from an *ex-situ* calibration using the temperature-dependent ^{207}Pb shift of $Pb(NO_3)_2$,[101] except for variable temperature ^{1}H spectra of catalytically hydrogenated VO_2, which was ground with KBr and the temperature measured *in-situ* from the ^{79}Br shift and T_1 constant.[102] ^{1}H NMR spectra were referenced relative to adamantane at 1.81 ppm, ^{2}H spectra to D_2O at 4.8 ppm, ^{17}O spectra to CeO_2 at 877 ppm and ^{51}V spectra to NH_4VO_3 at −571 ppm. Spectra were deconvoluted using the dmfit program.[105]

5.3.4 Electrochemistry

The majority of the electrochemical experiments were performed with 1-ethyl-3-methylimidazolium bis(trifluoromethylsulfonyl)imide (EMIm TFSI, Sigma Aldrich, ≥97%). The water content was determined with a Metrohm 899 Karl Fischer Coulometer to be 340 ppm as received and 34 ppm after drying *in vacuo* for two days. Additional electrochemical experiments were performed with 1-ethylimidazolium bis(trifluoromethylsulfonyl)imide (EIm TFSI, Io-li-tec, 98%), 1-ethyl-2,3-dimethylimidazolium bis(trifluoromethanesulfonyl)imide (EM_2Im TFSI, Tokyo Chemical Industry UK Ltd., 98%) and diethylmethyl(2-methoxyethyl)ammonium bis(trifluoromethylsulfonyl)imide (DEME TFSI, Io-li-tec, 99%). ½" perfluoroalkoxy (PFA) Swagelok cells were used with a Ag wire pseudo-reference electrode,

a platinum mesh counter electrode, a glass fibre separator and stainless-steel plungers (Figure 5.1a, right).

Composite free-standing films were prepared comprising 80 wt% VO_2 particles, 10 wt% PTFE binder and 10 wt% conductive carbon nanoparticles to ensure good electrical contact. VO_2 was ground with carbon super P (TIMCAL) before the addition of PTFE (60 wt% dispersion in H_2O, Sigma Aldrich). Ethanol was added followed by mixing to a dough-like consistency, rolling and drying at 60 °C to yield films of 75–150 μm thickness. The electrochemical experiments were performed using a Bio-Logic potentiostat/galvanostat running the EC-Lab software and experiments at elevated temperatures were performed in an oven. Cells were disassembled in an argon glovebox and the VO_2 films washed with dimethyl carbonate (2 x 2.5 ml, 99.5%, anhydrous, Sigma Aldrich) before drying *in vacuo* for 20 minutes. The carbon and PTFE in the composite films make only a small and temperature-independent contribution to the magnetic susceptibility.

The potential of the Ag wire pseudo-reference electrode was calibrated relative to the ferrocene–ferrocenium (Fc/Fc^+) couple by recording cyclic voltammograms of 10 mM ferrocene in EMIm TFSI at each temperature, with a scan rate of 10 mV s^{-1}. The potential of the reference electrode at 200 °C was extrapolated because ferrocene is not stable at this temperature.[180] The potential *vs.* Fc/Fc^+ is related to the potential *vs.* the standard hydrogen electrode (SHE) according to $E - E_{SHE} = E - E_{Fc/Fc^+} + 0.478\ \mathrm{V}$;[181] the temperature dependence of this conversion is expected to be minimal.[182]

5.3.5 Thin Films

Thin films were prepared by Dr Bin Cui at the Max Planck Institute of Microstructure Physics, Halle, Germany.

Single-crystalline VO_2 films of 10×10 mm^2 area and around 200 nm thickness were deposited on (001) TiO_2 substrates by pulsed laser deposition (248 nm KrF laser) with an oxygen pressure of 0.014 mbar and a growth temperature of 400 °C. The electrolyte gating for the thin film sample was performed potentiostatically according to previously reported procedures,[45] under a vacuum of ~3×10^{-6} mbar at 280 K. The VO_2 thin film and a gold counter electrode were covered by a drop of EMIm TFSI and a gate voltage of 3 V was applied between the VO_2 thin film and the gold electrode for two hours. After gating, the ionic liquid was removed by ultrasonic cleaning in acetone and ethanol.

5.3.6 DFT Calculations

The correlated nature of the electrons in VO_2 makes the use of DFT to calculate the electronic structure challenging, and a number of approaches have previously been applied to accurately study VO_2, including Hubbard U corrections,[183] hybrid functionals[184] and dynamical mean field theory.[185] However, for these methods, calculations of magnetic resonance properties using the Gauge Including Projector Augmented Waves (GIPAW) method are either too computationally expensive or not currently implemented; instead, for the purposes of spectral assignment and estimation of quadrupolar parameters, the GIPAW method was applied here using a generalised gradient approximation (GGA) approach.

DFT calculations of NMR parameters were performed using the CASTEP plane wave density functional theory (DFT) code[186–189] and the PBE exchange-correlation functional,[190] with a plane wave cut-off energy of 700 eV and a 6 × 6 × 6 Monkhorst−Pack *k*-point mesh. The relationship between the calculated chemical shielding and the experimental chemical shift was determined by calculating the isotropic value of the ^{17}O NMR shielding tensor for selected diamagnetic binary first-row transition metal oxides (Sc_2O_3, rutile TiO_2 and V_2O_5) and plotting this against the experimental isotropic chemical shift ($\delta_{iso} = -0.735\sigma_{iso} + 55.8$).[4] The atomic positions and unit cell parameters were relaxed from the experimental structures, which were taken from ICSD entries 26841,[191] 62677,[192] and 15798,[176] respectively.

The calculation of the NMR parameters in monoclinic, insulating, VO_2 was performed using the experimental XRD structure (ICSD entry 34033[193]). The structure was relaxed using a Hubbard U correction of 0.5 eV to account for the electron correlations and stabilise the insulating structure, then the NMR parameters were calculated without the Hubbard U but with fixed electronic occupancy so as to retain the insulating ground state. The second-order quadrupolar shifts expected at 7.05 T were determined using the MagresView software package.[194]

5.4 Results and Discussion

5.4.1 The Thermal Transition of Pure VO_2

The high temperature, metallic phase of VO_2 adopts the rutile structure ($P4_2/mnm$) with the V d^1 electrons delocalised into a conduction band; the transition to the low temperature, insulating, phase is associated with a Peierls distortion to the lower symmetry monoclinic structure ($P2_1/c$), with the V d^1 electrons pairing to form V–V dimers (Figure 5.1b). As has

been previously reported, this phase transition results in an extremely large change in shift of the ^{51}V NMR signal from 2065 ppm in the insulating state to −3765 ppm in the metallic state (observed here for micron-sized VO_2 particles, Figure 5.2a).[42,195] The positive shift is due to a Van Vleck or orbital Knight shift, which is characteristic of an insulating state with a small bandgap, whereas the negative shift is due to an indirect or core-polarisation Knight shift, which is characteristic of a metallic state where the band structure has no appreciable contribution from *s* orbitals at the Fermi level, as is the case in VO_2 (see §2.1.4).[56] The ^{17}O NMR spectra (Figure 5.2b) show a similar effect: above the MIT a negative shift of −505 ppm

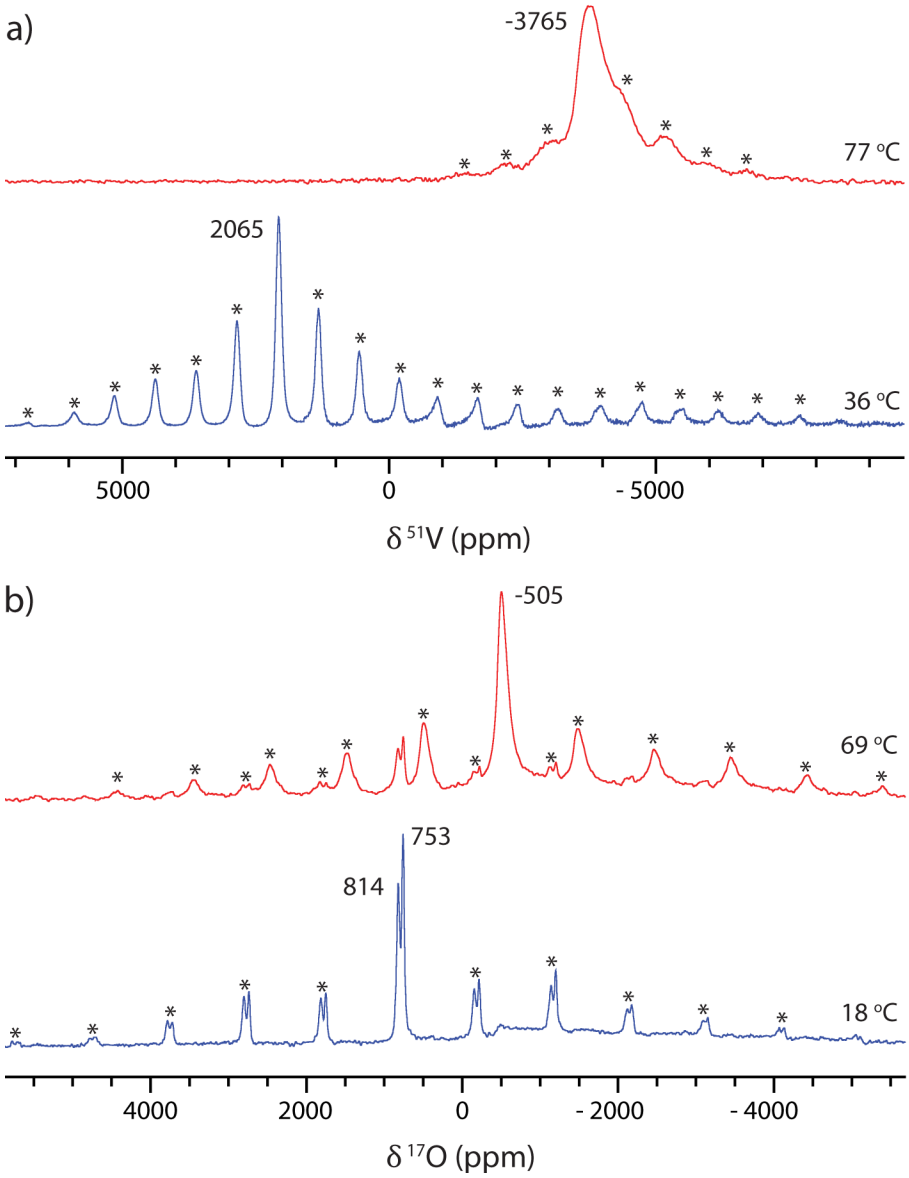

Figure 5.2: a) ^{51}V and b) ^{17}O NMR spectra of VO_2 above and below the MIT, recorded at 7.05 T with a Hahn echo pulse sequence. Spinning sidebands have been marked with an asterisk and the spectra have been scaled to give comparable intensities, rather than being quantitatively comparable. The ^{51}V NMR spectra were recorded at 60 kHz MAS, summing two spectra recorded with carrier frequencies of 2000 ppm and −4750 ppm. The ^{17}O NMR spectra were recorded at 40 kHz MAS. Some of the insulating phase remains in the high temperature ^{17}O NMR spectra, and vice versa, due to spinning induced temperature gradients within the rotor and the finite width of the MIT.

is observed due to the core-polarisation Knight shift of the metallic state, and below the MIT a positive shift is observed due to the Van Vleck Knight shift of the insulating state. The low temperature spectrum also exhibits a splitting of the ^{17}O NMR signal due to the two crystallographically distinct oxygen sites in the lower symmetry monoclinic structure (Figure 5.1b, right): the peaks at 753 ppm and 814 ppm are tentatively assigned to the inter- and intra-vanadium dimer oxygen environments, respectively, on the basis of approximate DFT NMR shielding calculations (Table 5.1); although the exact agreement with the experimental values is not excellent, the difference between the two oxygen environments is clear, enabling their assignment. The ^{17}O NMR spectrum of VO_2 has only previously been reported below the transition,[16] and the two signals were not assigned, but the shifts are in agreement with those found here. Note that the observed ^{17}O NMR shifts are not corrected for the second-order quadrupolar shift, which from the DFT calculations is expected to contribute around −10 ppm to the observed shift at this field, based on the calculated quadrupolar coupling constants of ~1.6 MHz.

Table 5.1: Calculated and experimental ^{17}O chemical shifts in monoclinic, insulating, VO_2 as well as the calculated quadrupolar coupling constants, C_Q, and resultant second-order quadrupolar shifts at 7.05 T.

	Experimental Shift /ppm	**Calculated Shift /ppm**	**Calculated C_Q /MHz**	**Second-order quadrupolar shift /ppm**
Inter-dimer	753	696	1.72	−12
Intra-dimer	814	832	1.56	−10

5.4.2 Catalytic Hydrogenation

In order to explore the crystal and electronic structures of hydrogenated VO_2 and the resultant NMR signatures, catalytically hydrogenated VO_2 was prepared following the method of Filinchuk et al.[170] *via* catalytic spillover from palladium nanoparticles. Following hydrogenation at 180 °C, a hydrogen content determined from thermogravimetric analysis (TGA) of $x = 0.365$ was obtained. Rietveld refinement using the powder X-ray diffraction (XRD) pattern showed the presence of a small amount of unreacted VO_2 and a mixture of two orthorhombic phases (*Pnnm*), one with a larger unit cell and orthorhombic distortion than the other (with ratios for the *a* and *b* cell parameters of $b/a = 1.112$ and 1.036, respectively, see Appendix D). Other than the orthorhombic distortion, the orthorhombic phases have the same structure as the high temperature VO_2 rutile phase (Figure 5.1b, left).

This result is in contrast to those of Filinchuk et al. who only found the orthorhombic phase with the smaller unit cell, which they denoted O1, after hydrogenation at 190 °C. However, Chippindale et al.[169] showed that both the size of the unit cell and the orthorhombic distortion scale with the degree of hydrogenation x, suggesting that the second phase identified in this work is a more hydrogenated analogue of the first. Modifying the notation of Filinchuk et al., the less and more hydrogenated orthorhombic phases will be referred to as O1a and O1b respectively. Using the relationship between the orthorhombic distortion and the hydrogen content reported by Chippindale et al.,[169] the hydrogen content of both phases can be predicted, which, combined with the phase fractions determined from Rietveld analysis (see Appendix D), results in a total hydrogen content of $x = 0.42(7)$ for this sample. This is in reasonable agreement with that determined by TGA.

Four-point resistivity measurements of pressed pellets of VO_2 and Pd/H_xVO_2 (Figure 5.3a) clearly show the MIT in pristine VO_2 at 340 K. This is almost completely suppressed in Pd/H_xVO_2 (the MIT of the residual unreacted VO_2 can, however, still just be seen); furthermore, the resistivity of the Pd/H_xVO_2 is ~500 times lower than that of insulating VO_2, although the temperature dependence is still not fully metallic (this is most likely due to grain boundary effects given that these samples could not be hot-pressed). Zero-field cooled susceptibility measurements (Figure 5.3b) corroborate the resistivity data: the Pd/H_xVO_2 exhibits an increased temperature-independent susceptibility due to the Pauli paramagnetism of the metallic phase, as well as suppression of the MIT, although there is also an increased Curie paramagnetic component, which is indicative of localised spins.

The ^{51}V NMR spectrum (Figure 5.3c) confirms the presence of vanadium atoms in a metallic environment in Pd/H_xVO_2, with almost complete loss of the insulating VO_2 peak at 2065 ppm and the appearance of a resonance at negative shift, as seen for pure VO_2 above the MIT; however, the signal in this case is very broad and the spinning sidebands cannot be resolved, which is most likely to be due to a greater distribution of local vanadium environments caused by inhomogeneous hydrogenation. The ^{1}H MAS NMR spectrum of Pd/H_xVO_2 contained a series of overlapping signals and thus a MATPASS sideband separation pulse sequence was used so that only the isotropic resonances are seen[103] (Figure 5.3d, bottom); the spectrum shows two signals centred around 110 ppm and 445 ppm, as well as a diamagnetic peak around 0 ppm, which is ascribed to ubiquitous diamagnetic hydrogen-containing impurities. To aid assignment of the ^{1}H NMR spectrum, a second sample of Pd/H_xVO_2 was synthesised at 220 °C and found from XRD to have a greater phase fraction of O1b (36 wt% *c.f.* 12 wt% for the

sample synthesised at 180 °C). The ^{1}H NMR spectrum of this sample had a correspondingly greater intensity for the signal at 445 ppm (Figure 5.3d, top), allowing the 115 and 445 ppm regions to be assigned to O1a and O1b respectively.

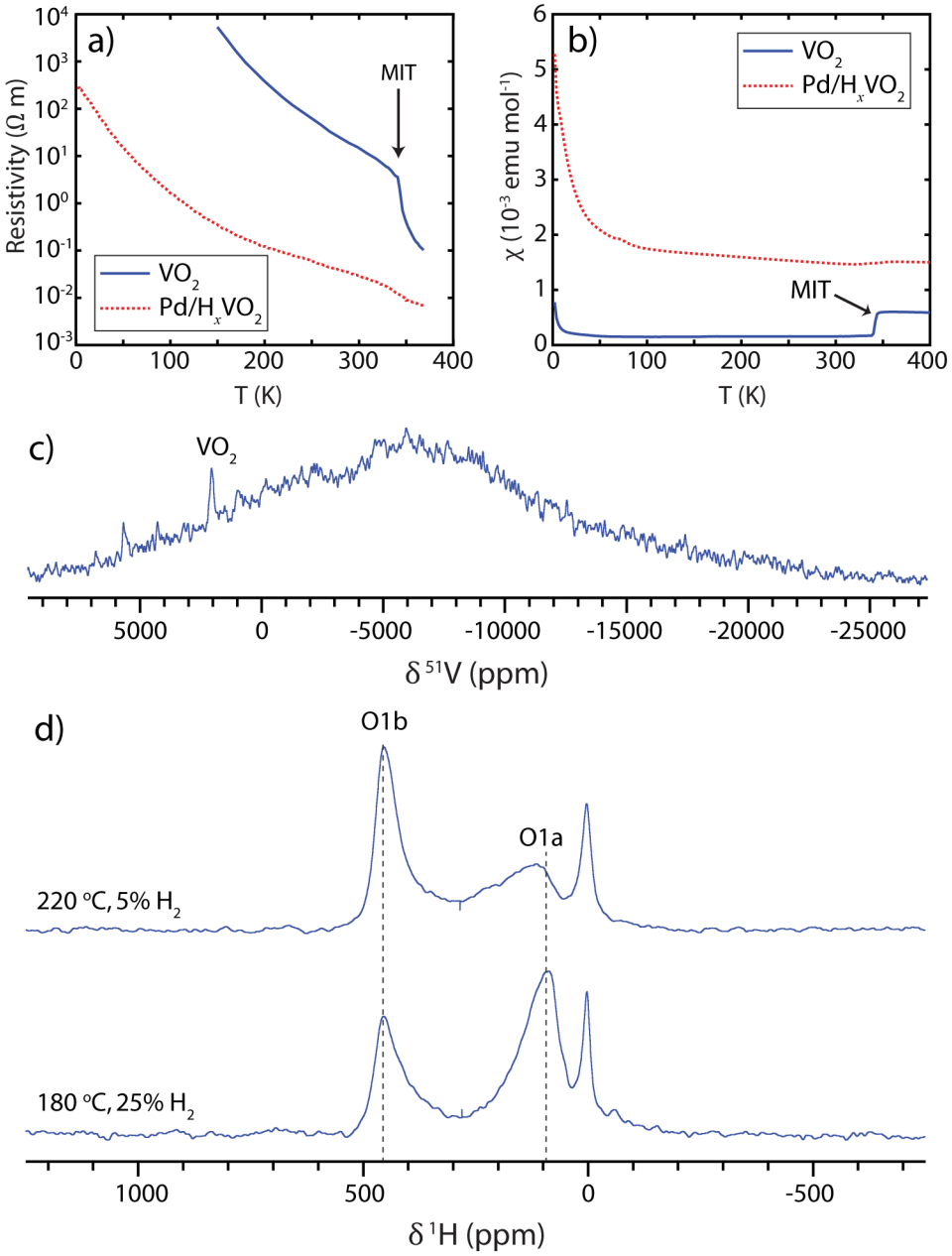

Figure 5.3: a) Resistivity and b) zero-field cooled magnetic susceptibility of VO_2 before and after catalytic hydrogenation, and c) ^{51}V and d) ^{1}H NMR spectra of the catalytically hydrogenated VO_2. The ^{51}V NMR spectrum was recorded at 4.70 T, 60 kHz MAS and a sample temperature of ~50 °C, using a Hahn echo pulse sequence and variable offset cumulative spectra (VOCS) acquisition. Spectra were acquired in steps of 5000 ppm between carrier frequencies of 5000 ppm and −20000 ppm and summed to produce the spectrum shown above. The residual signal due to insulating VO_2 at 2065 ppm is indicated. The ^{1}H NMR spectra are the isotropic slice of 2D MATPASS sideband separation spectra for the two different hydrogenation procedures, recorded at 4.70 T, 40 kHz MAS and a sample temperature of ~30 °C. All other data refer to the sample hydrogenated at 180 °C.

In order to determine the origin of the large ^{1}H NMR shifts, variable temperature ^{1}H NMR spectra were recorded: Figure 5.4a shows the ^{1}H MATPASS NMR spectra of Pd/H_xVO_2 between 18 ºC and 69 ºC. The O1a peak appears to move to higher frequency with increasing temperature, but this is actually due to the lower frequency regions relaxing more quickly at higher temperatures and hence less of this signal being observed relative to the higher frequency regions; this effect makes it challenging to determine whether the chemical shifts are temperature-dependent, but the chemical shift certainly does not decrease with increasing temperature, ruling out a paramagnetic shift. The major interaction responsible for the O1a shift is therefore likely to be a Knight shift, indicating that this phase is metallic; this is a positive, direct contact Knight shift because the only valence orbital for hydrogen is the 1*s* orbital.

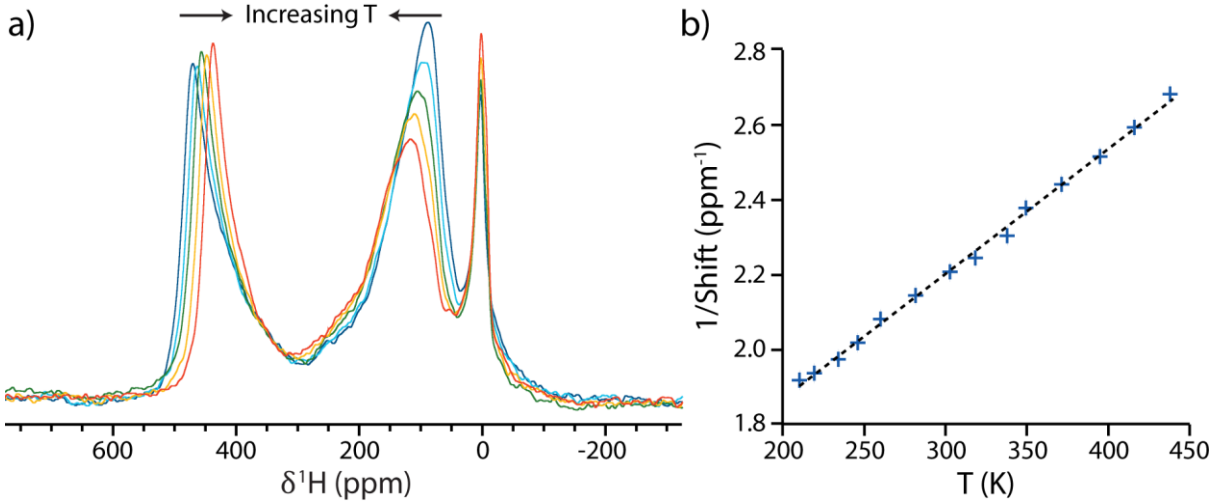

Figure 5.4: a) Variable temperature ^{1}H MATPASS NMR (7.05 T) spectra at 60 kHz MAS with sample temperatures between 18 ºC and 69 ºC. b) A plot of 1/shift against T for the ^{1}H O1b shift in Pd/H_xVO_2. The spectra were recorded using a single-pulse experiment at 14 kHz MAS and 4.70 T. In both cases the sample temperature was determined with an in-situ KBr NMR thermometer.

The O1b shift, on the other hand, does decrease with increasing temperature; to establish whether this shift followed the expected Curie–Weiss temperature dependence, a wider temperature range was explored using a 4 mm rotor with a zirconia cap. A single pulse experiment was used because the lower maximum spinning speed of 14 kHz for the larger rotor, and fast T_2 relaxation of the sample, prevented rotor synchronised experiments such as a MATPASS or a Hahn echo; the background in the single pulse experiment then obscured the O1a signal so that only the O1b signal could be distinguished. Figure 5.4b shows a plot of 1/shift versus temperature for the O1b signal, which exhibits the expected linear Curie–Weiss dependence, confirming that this is a paramagnetic shift, which is positive due to the 90º π delocalisation pathway (see §2.1.3). The paramagnetic shift is due to localised electron spins

which suggests that this phase is insulating, as also recently found for highly catalytically hydrogenated thin films of HVO_2 (x = 1);[167] the insulating state for HVO_2 is shown to arise from the large degree of hydrogenation which causes the lattice to expand, reducing the overlap between the vanadium *d* orbitals and hence decreasing the valence bandwidth so that there is Mott localisation of the electrons, as for the insulating phase of pristine VO_2.

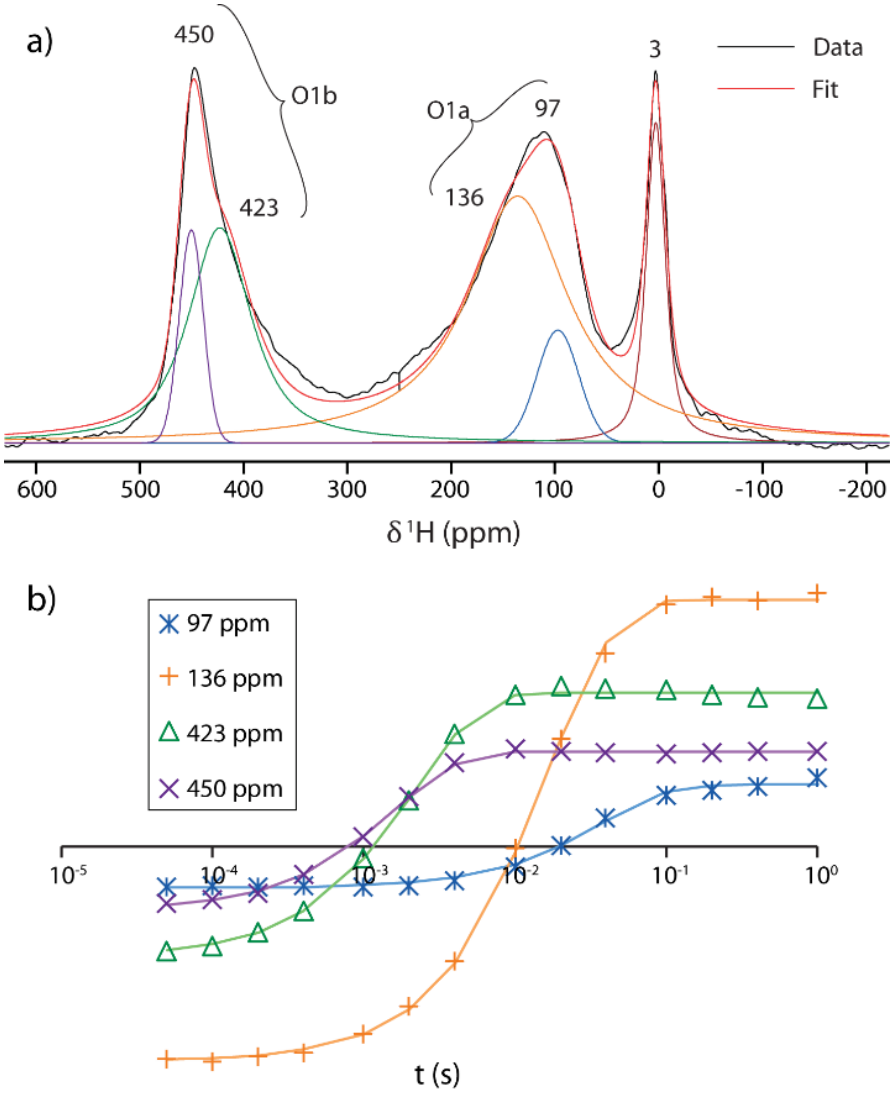

Figure 5.5: a) Gaussian-Lorentzian deconvolution of the ^{1}H MATPASS NMR spectrum of catalytically hydrogenated Pd/H_xVO_2. b) Intensity as a function of relaxation delay for different environments in the ^{1}H inversion recovery NMR spectra of catalytically hydrogenated Pd/H_xVO_2. Both experiments were recorded at 7.05 T, 60 kHz MAS and ~50 ^{o}C sample temperature.

Table 5.2: Fitted T_1 relaxation constants for different environments from the ^{1}H inversion recovery NMR spectra of catalytically hydrogenated Pd/H_xVO_2 at ~50 ^{o}C.

Shift /ppm	97	136	423	450
$\boldsymbol{T_1}$ **/s**	0.039	0.017	0.0022	0.0016

These assignments are corroborated by the ^{1}H T_1 relaxation constants, measured with an inversion recovery experiment (Figure 5.5b); although both the O1a and O1b NMR signals represent a distribution of environments, the inversion recovery data can be fit reasonably well by deconvoluting the signal from each phase as two Gaussian-Lorentzian peaks, as shown in Figure 5.5a for the MATPASS ^{1}H NMR spectrum. The fitted T_1 constants (Table 5.2) show that both phases relax much more quickly than diamagnetic protons (T_1 ~ 1 – 10 s), and the localised paramagnetic O1b signal relaxes an order of magnitude faster than the metallic O1a signal, as expected. Furthermore, within the signal of each phase, the component with a higher shift has a shorter relaxation constant; this is as expected because a higher shift corresponds to a more metallic or more paramagnetic environment respectively, for which the relaxation is consequently faster.

These NMR experiments thus confirm the Curie and Pauli components identified in the magnetic susceptibility measurements. The amount of hydrogenation could also be determined with quantitative ^{1}H NMR spectroscopy, which yielded hydrogen contents for the two phases that are in reasonable agreement with the TGA and XRD results (Table 5.3), further corroborating the assignments.

Table 5.3: Comparison of the sample hydrogen content (x in H_xVO_2), and its distribution between the two orthorhombic phases, as determined by thermogravimetric analysis (TGA), Rietveld refinement of the XRD pattern and quantitative ^{1}H NMR spectroscopy. The average hydrogen content of the sample is determined from the XRD data by taking the product of the O1a/O1b phase fraction (%) and the phase hydrogen content predicted from the orthorhombic distortion. The error in the last digit is shown in brackets. Discrepancies between the XRD and NMR quantifications are discussed in Appendix D.

	TGA	XRD	NMR
O1a		86 % × 0.33(5) = 0.28(5)	0.19(2)
O1b		12 % × 1.1(1) = 0.14(3)	0.17(2)
Total	0.365(3)	0.42(7)	0.36(3)

To summarize, catalytic hydrogenation of VO_2 yielded two orthorhombic phases: a less hydrogenated, metallic, Pauli paramagnetic phase denoted O1a; and a more hydrogenated, Curie–Weiss paramagnetic phase denoted O1b; the individual hydrogen content of each was determined by X-ray crystallography and by quantitative ^{1}H NMR spectroscopy.

5.4.3 Electrochemical Hydrogenation – Room Temperature

Having studied the thermal MIT in pure VO_2 and the effect of catalytic hydrogenation, electrochemical metallisation of VO_2 was investigated. The experiments were performed on bulk VO_2, using ~15 mg free-standing composite films made with standard

battery/supercapacitor electrode preparation techniques. Unlike previous potentiostatic electrolyte gating experiments,[45,154–160,163] here galvanostatic reduction was used, so that the energetics of different processes could be inferred from the potential, which was measured relative to a silver wire pseudo-reference electrode (Figure 5.1a, right). The use of the reference electrode avoids electrode polarisation effects and allows the potential of the insertion reaction to be measured relative to a known potential, which is particularly important in this case because the reaction that occurs at the counter electrode has not been established definitively. The ionic liquid used was 1-ethyl-3-methylimidazolium bis(trifluoromethylsulfonyl)imide (EMIm TFSI, Figure 5.1a, top)—a standard electrolyte used in electrolyte gating experiments—and the counter electrode was platinum mesh. A specific current of 6.46 mA g^{-1} was applied for 50 h, which, assuming 100% coulombic efficiency, corresponds to one electron transferred per vanadium atom.

After performing the electrochemistry, the cell was disassembled under an inert atmosphere and the VO_2 electrode was characterized *ex-situ*. The presence of protons in a metallic environment is clearly revealed via the observation of a resonance at 110 ppm in the ^{1}H NMR spectrum (Figure 5.6a); a second peak is observed at approximately 0 ppm, which is ascribed to protons in diamagnetic local environments, from imperfect washing of the electrolyte, electrolyte breakdown products and other hydrogen-containing impurities. Quantification of the ^{1}H NMR spectrum, however, yields a hydrogen content of only $x = 0.037$, despite charge corresponding to one electron per vanadium ion being transferred. Examination of the electrochemistry shows that the electrochemical potential (Figure 5.7) initially decreases before reaching a plateau at around −1.6 V *vs.* Fc/Fc^+. A second sample was prepared where the electrochemistry was stopped after transferring 0.075 electrons per vanadium, i.e. at the beginning of the plateau; this sample had an essentially identical hydrogen content of $x = 0.035$, which shows that the plateau does not correspond to the hydrogenation reaction, but rather a competing side reaction that prevents further hydrogenation. Electrochemical reduction of VO_2 in an organic electrolyte was previously found to compete with hydrogen evolution,[169] i.e. the hydrogen evolves as H_2 rather than intercalating into the VO_2 (the origin of the hydrogen will be discussed later); this is likely to be the case here, given that the voltage falls below the hydrogen evolution voltage in EMIm TFSI (−0.07 V vs. Fc/Fc^+), although hydrogen evolution can be negligible until much lower voltages depending on the catalytic properties of the electrode and the source of the hydrogen.[196] Alternative side reactions could also include cation or anion decomposition.[197]

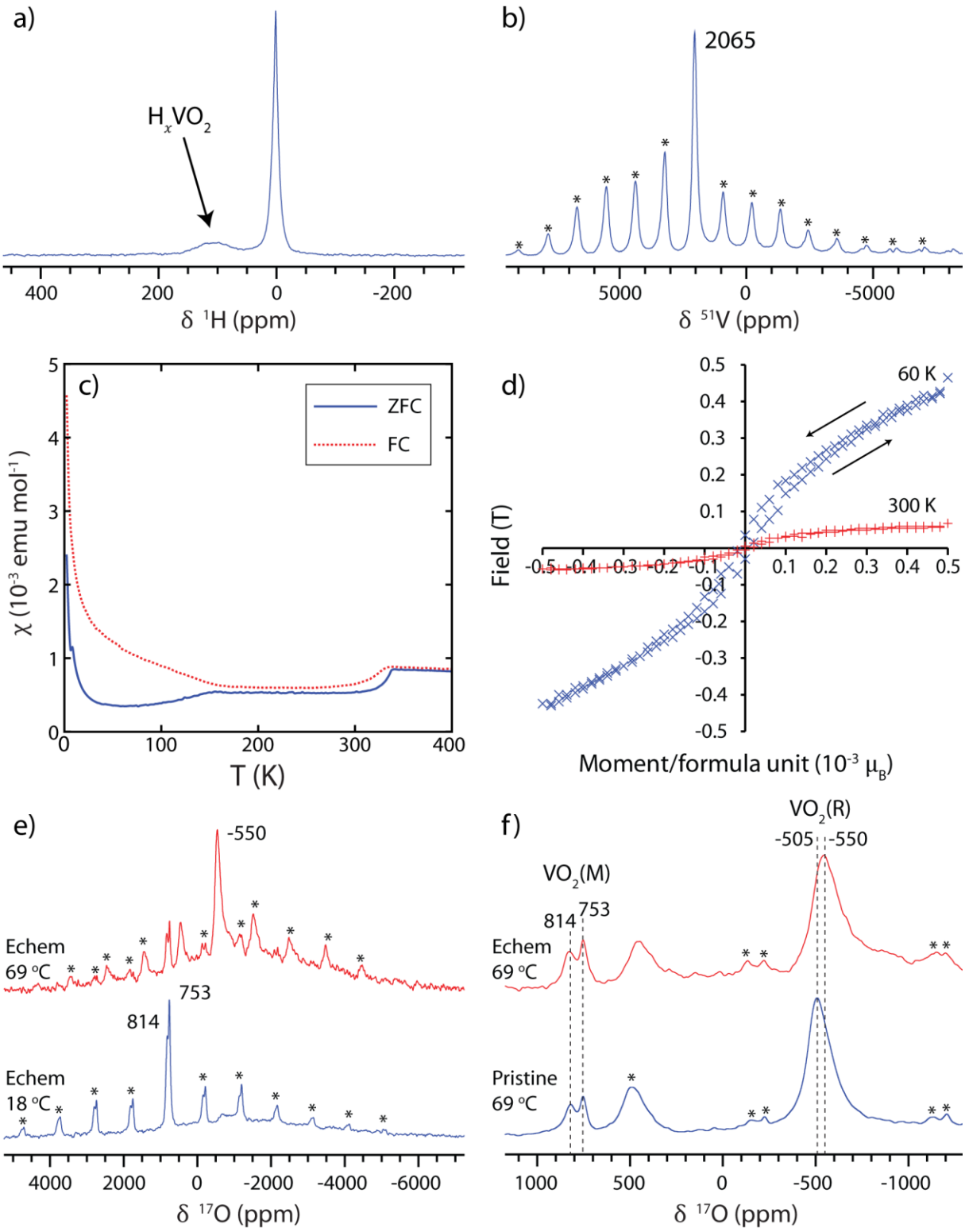

Figure 5.6: a) ^{1}H NMR spectrum, b) ^{51}V NMR spectrum, c) zero-field cooled (ZFC) and field cooled (FC) magnetic susceptibilities, d) magnetisation vs. field, and e) ^{17}O NMR spectra, for VO_2 after electrochemical reduction at room temperature. f) shows an expanded comparison of the high temperature ^{17}O NMR spectra for the pristine and reduced samples. The ^{1}H NMR spectrum is the isotropic slice of a 2D MATPASS sideband separation spectrum which was recorded at 4.70 T, 40 kHz MAS and a sample temperature of ~30 °C. The ^{51}V VOCS NMR spectrum was recorded at 4.70 T, 60 kHz MAS and a sample temperature of ~50 °C using a Hahn echo pulse sequence and variable offset cumulative spectra (VOCS) acquisition with carrier frequencies from 5000 ppm to −20000 ppm in steps of 5000 ppm (although only the region of interest is shown here). The ^{17}O NMR spectra were recorded at 7.05 T, and 40 kHz MAS. Spinning sidebands are indicated with an asterisk.

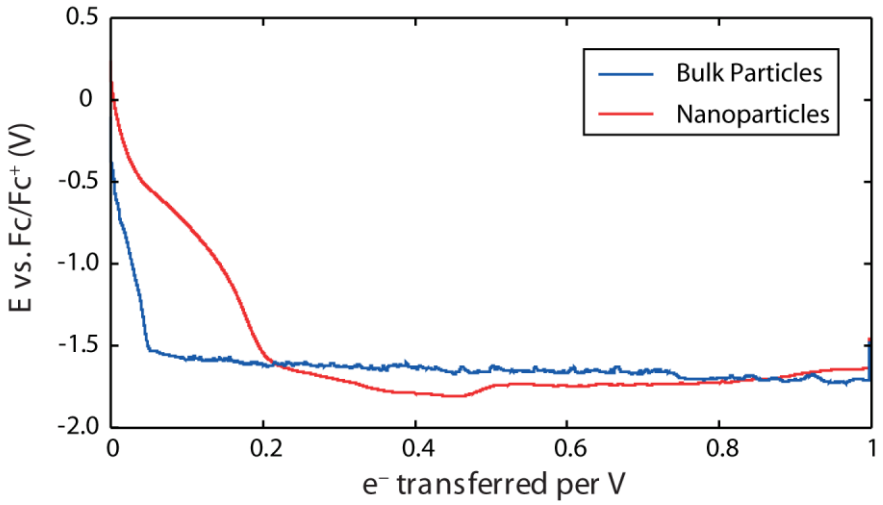

Figure 5.7: Voltage profiles for bulk (~2 μm) and nanoparticulate (~30 nm) VO_2 electrochemically reduced at room temperature with EMIm TFSI.

These results suggest localized metallisation, as may be expected for low electron doping levels,[153] but not complete metallisation; unfortunately, resistivity measurements of these films are not possible due to the conductive carbon and the low density, so the degree of metallisation must be inferred. Metallic nanodomains have previously been observed in pure VO_2 just below the MIT,[199] and could also explain the behaviour observed here for H_xVO_2 with a low level of hydrogenation: there is a Knight shift for the ^1H nuclei, indicating that the hydrogen is in a metallic environment, but the whole sample cannot have been metallized because the ^{51}V NMR spectrum is dominated by vanadium in an insulating environment. Furthermore, metallic nanodomains can also result in cluster glass behaviour, with ferromagnetic coupling within domains but weak and disordered coupling between domains, which would explain the spin glass-like effects observed in the magnetic measurements.

Since the previous electrolyte gating experiments were observed to be reversible,[45,154] a bulk VO_2 sample was electrochemically reduced galvanostatically for 24 hours before reversing the current for 24 hours (Figure 5.8); the ^1H NMR spectrum then shows no H_xVO_2 signal, indicating that the electrochemical hydrogenation is also reversible. Closer examination of the voltage profile shows that during reduction the potential of the VO_2 working electrode reaches a limiting plateau, with only the initial sloping region corresponding to hydrogenation of VO_2. When the current is switched to VO_2 oxidation, the working electrode potential increases again while the VO_2 dehydrogenates, before reaching a limiting potential corresponding to the anodic limit of the ionic liquid, at approximately the same potential observed at the Pt counter electrode during reduction. Notably, however, on oxidation the potential of the Pt counter electrode is significantly lower than that observed at the VO_2 electrode during its reduction:

this indicates that the cathodic stability of the ionic liquid is decreased at a VO_2 electrode relative to a Pt electrode, possibly explaining why electrolyte breakdown reactions are significant in this system at voltages which are within the typically reported stability window.[200]

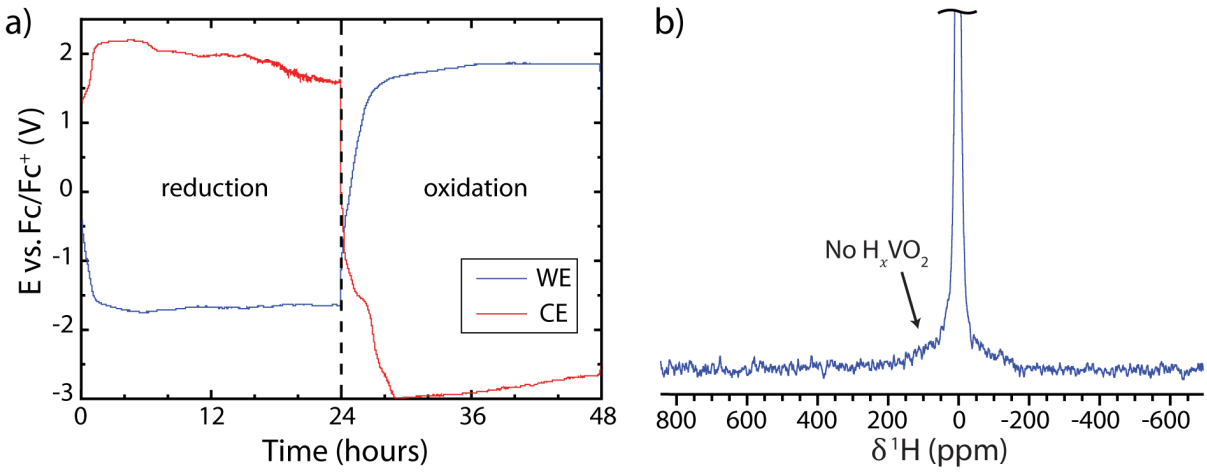

Figure 5.8: a) Voltage profiles for the VO_2 working electrode (WE) and Pt counter electrode (CE), and b) ^1H NMR spectrum of reversibly electrochemically hydrogenated VO_2. The spectrum was recorded at 40 kHz MAS and 4.70 T with a MATPASS pulse sequence.

The localized/incomplete metallisation achieved for bulk VO_2 at room temperature contrasts with the previously reported complete metallisation observed for thin film samples. One possible explanation for this difference is the strain present in epitaxial thin films grown on TiO_2 (001) substrates; the strain favours the metallic state, as evidenced by the reduction of the thermal MIT temperature to −3 °C.[157] However, for VO_2 grown on Al_2O_3 ($10\bar{1}0$) substrates there is minimal strain and the MIT is observed at 67 °C, as for bulk VO_2, yet full metallisation is still achieved in electrolyte gating experiments;[45] this suggests that strain is not necessary for metallisation. Instead, this could be a kinetic effect: due to the small sample volume in a thin film and the shorter diffusion distances, a greater degree of electrochemical reduction could be achieved before competing side reactions limit the hydrogenation. This is supported by the observation of Passarello et al.[158] that complete suppression of the MIT could not be achieved for 1 μm bars of VO_2, whereas it could be achieved for 0.5 μm bars in the same setup; the average VO_2 particle size used in this work as determined by SEM is 1.9 μm (Figure 5.9), which could explain the lack of complete metallisation observed.

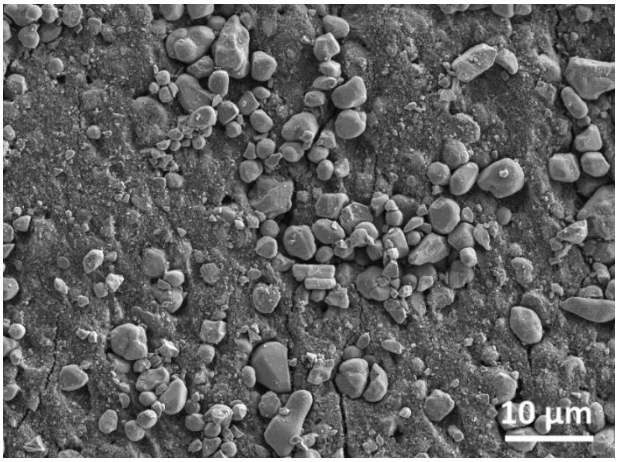

Figure 5.9: SEM micrograph of bulk VO_2 with 10 wt% PTFE and 10 wt% conductive carbon nanoparticles.

To determine whether the electrochemical hydrogenation of bulk VO_2 at room temperature was limited by the particle size, VO_2 nanoparticles were synthesised by ball milling. SEM reveals micron-sized secondary particles, comprising primary particles averaging ~30 nm in diameter, with particles as small as 10 nm being distinguishable in the STEM image (Figure 5.10). On galvanostatic electrochemical reduction, the voltage profile (Figure 5.7) exhibits a less steep gradient than that for bulk VO_2 and more charge is transferred before hitting the limiting plateau at around −1.6 V. The ^{1}H NMR spectrum (Figure 5.11a) shows greater hydrogenation, and quantification yields a hydrogen content of $x = 0.20$, *c.f.* 0.037 for bulk VO_2; the hydrogen content also matches well with the amount of charge transferred before reaching the limiting plateau. The ^{51}V NMR spectrum (Figure 5.11b) does show a broad signal at negative shift due to vanadium in a metallic environment, however some of the signal from insulating VO_2(M) remains. Some side products are also evident, with a signal from diamagnetic vanadium being observed at −570 ppm. The lack of uniform metallisation in this case is ascribed to the difficulty of electrically contacting all the nanoparticles with the conductive carbon, which is compounded by the presence of secondary agglomerates; it is likely that some particles are electrically or electrochemically isolated and hence are not reduced, giving rise to the residual VO_2(M) signal. Nevertheless, the greater hydrogenation observed for nanoparticulate VO_2 as compared to bulk VO_2 suggests that particle size is the reason that full metallisation is not observed for the latter. This is most likely to be due to sluggish kinetics of hydrogen diffusion and/or nucleation and growth of the new phases, relative to competing electrochemical side reactions such as hydrogen evolution.

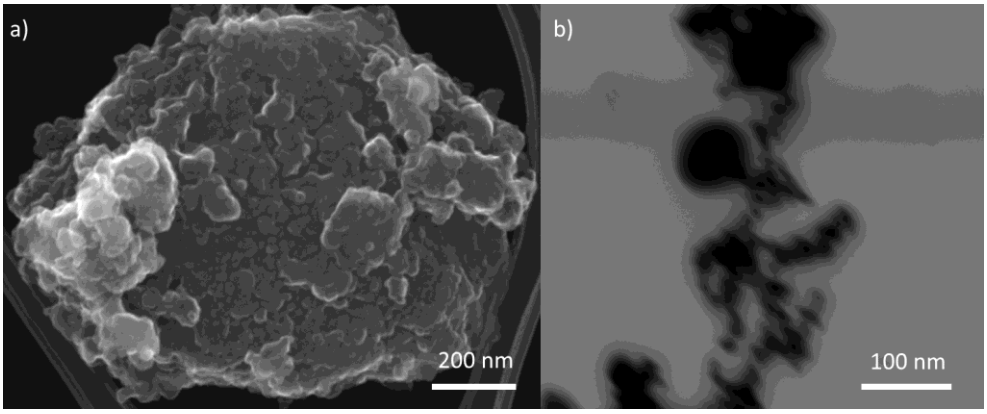

Figure 5.10: a) SEM image of ball-milled VO_2 nanoparticles, showing a larger secondary particle comprising smaller primary particles, and b) STEM image showing some unagglomerated primary particles.

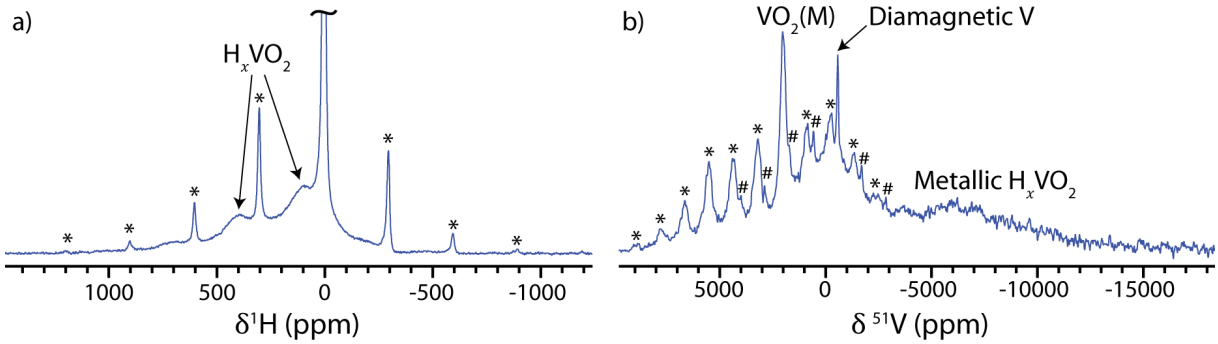

Figure 5.11: a) ^{1}H and b) ^{51}V NMR spectra of electrochemically hydrogenated VO_2 nanoparticles, recorded at 4.70 T and 60 kHz MAS using a Hahn echo pulse sequence. The ^{51}V spectrum was acquired in steps of 5000 ppm between carrier frequencies of 5000 ppm and −20000 ppm and summed to produce the spectrum shown above. Spinning sidebands are marked with asterisks or hash marks.

5.4.4 Electrochemical Hydrogenation – Elevated Temperature

The electrochemistry was subsequently performed at elevated temperatures in an attempt to achieve a greater extent of electrochemical hydrogenation for bulk VO_2 (Figure 5.12a). For temperatures up to 150 °C, the degree of hydrogenation increased (Figure 5.12b), forming the same orthorhombic phases observed for catalytic hydrogenation, first O1a then O1b, as shown by ^{1}H NMR spectroscopy (Figure 5.12d) and Rietveld refinement of the XRD patterns (Figure 5.12c). The ^{51}V NMR spectra (Figure 5.12e) further show a progressive loss of the insulating VO_2 resonance at 2065 ppm and the appearance of broad features at negative shifts, which correspond to vanadium ions in a metallic environment. $V^{(0)}$ and V^{5+} impurities can also be seen in the ^{51}V NMR spectra for the samples electrochemically hydrogenated at 100 °C and 150 °C, which are negligible by XRD but are much more readily observed via ^{51}V NMR spectroscopy since the signals are noticeably sharper than those of the H_xVO_2 phases.

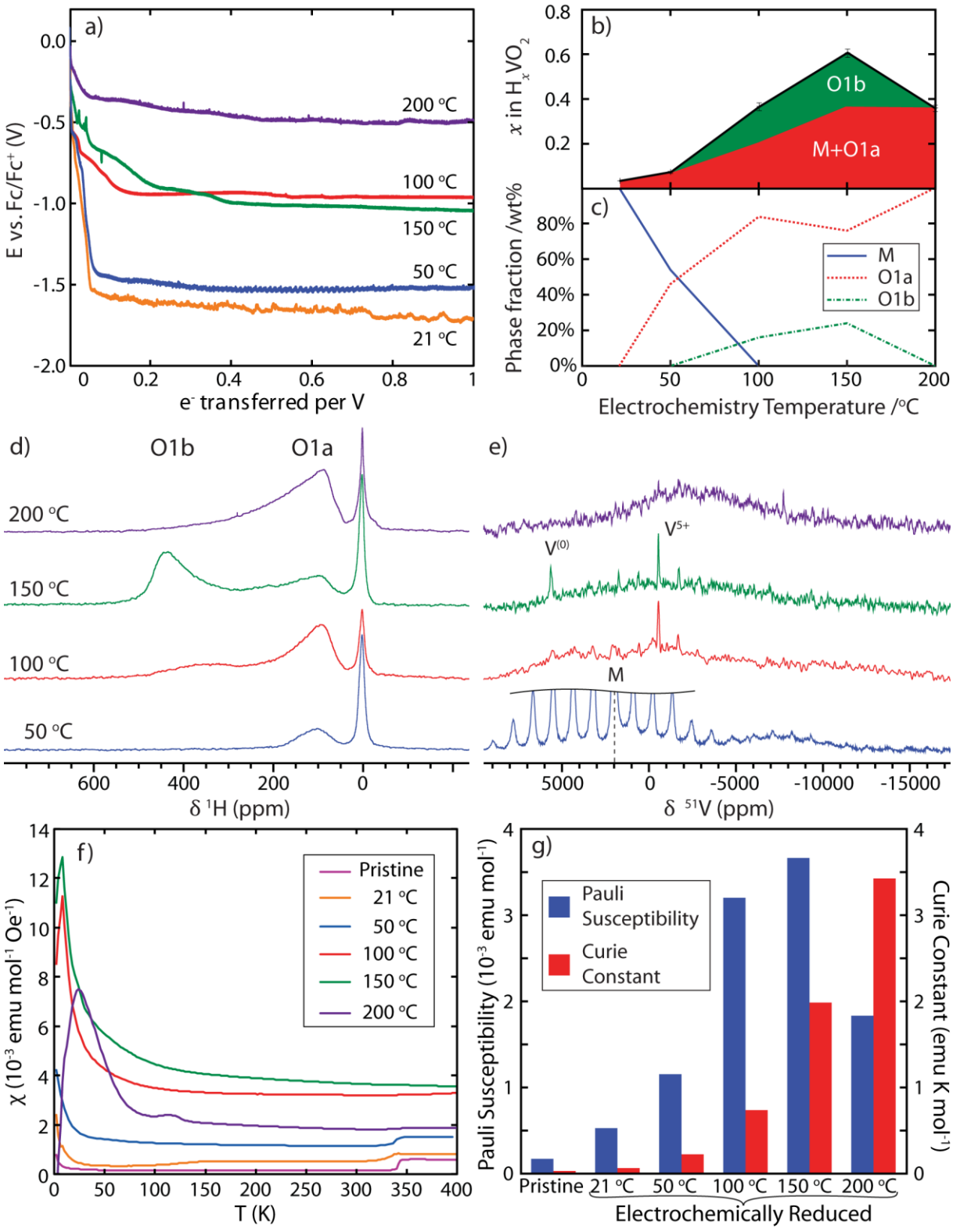

Figure 5.12: Characterization of VO_2 electrochemically hydrogenated as a function of temperature: a) the voltage profiles; b) the hydrogen content determined from quantitative ^{1}H NMR spectroscopy; c) the phase fractions of the monoclinic (M) and two orthorhombic phases (O1a and O1b) determined from Rietveld analysis of the powder XRD; the d) ^{1}H and e) ^{51}V NMR spectra; f) the ZFC magnetic susceptibility data; and g) the fitted Pauli and Curie paramagnetic components of the magnetic susceptibility. The ^{1}H NMR spectra in (d) represent the isotropic slices of the MATPASS spectra which were recorded at 4.70 T, 40 kHz MAS and a sample temperature of ~30 °C; note that these spectra are not quantitative. The ^{51}V NMR spectra in (e) were recorded at 4.70 T and 60 kHz MAS using a Hahn echo pulse sequence and variable offset cumulative spectra (VOCS) acquisition. The Pauli component of

the susceptibility is taken as the susceptibility measured at 300 K, to avoid any contribution from the MIT, and the Curie constant, C, was found by fitting the low temperature tail to the function $\chi = \frac{C}{T-\Theta} + \chi_0$, where Θ is the Weiss constant and χ_0 is the temperature-independent paramagnetism.

The susceptibility data (Figure 5.12f) corroborate these results; Figure 5.12g shows the Curie and Pauli paramagnetic components as fitted from the low temperature tail and the high temperature asymptote respectively of the magnetic susceptibility. As expected, the Pauli paramagnetism increases for samples prepared at up to 150 °C due to the increasing hydrogenation, which is accompanied by the addition of electrons, increasing the density of states at the Fermi level; the Curie paramagnetism also increases for the samples prepared at 100 °C and 150 °C due to the localized paramagnetic O1b phase. Furthermore, the loss of the MIT can be seen for electrochemical hydrogenation above 50 °C. A maximum in the susceptibility, corresponding to antiferromagnetic ordering, is observed for the samples metallised at the highest three temperatures, at Néel temperatures of ∼8 K for the 100 °C and 150 °C samples and ∼25 K for the 200 °C sample; see below for a discussion of the 200 °C sample. The fit of the Curie–Weiss paramagnetic component used only points above the Néel temperature.

The ^{17}O NMR spectra recorded for ^{17}O enriched samples at high and low temperature also reflect the progressive formation of O1a and then O1b with increasing electrochemistry temperature up to 150 °C (Figure 5.13a). The sample which was electrochemically hydrogenated at 50 °C retains the insulating monoclinic VO_2 signals at 753 and 814 ppm in the low temperature spectrum, as was also observed for the room temperature sample (Figure 5.6f). Then in the spectrum recorded above the MIT, the negatively Knight-shifted signal of the metallic phase is again observed at the more negative shift of −550 ppm, compared to −505 ppm for pristine VO_2; in the same way as for the room temperature electrochemical hydrogenation, this is evidence of the electron doping associated with hydrogen intercalation, which increases the density of states at the Fermi level, and hence the Knight shift. Moreover, because this is the same shift as was observed for the room temperature sample, this suggests that the degree of hydrogenation of the monoclinic phase is the same for both samples; the 50 °C sample differs in that it also contains the O1a phase.

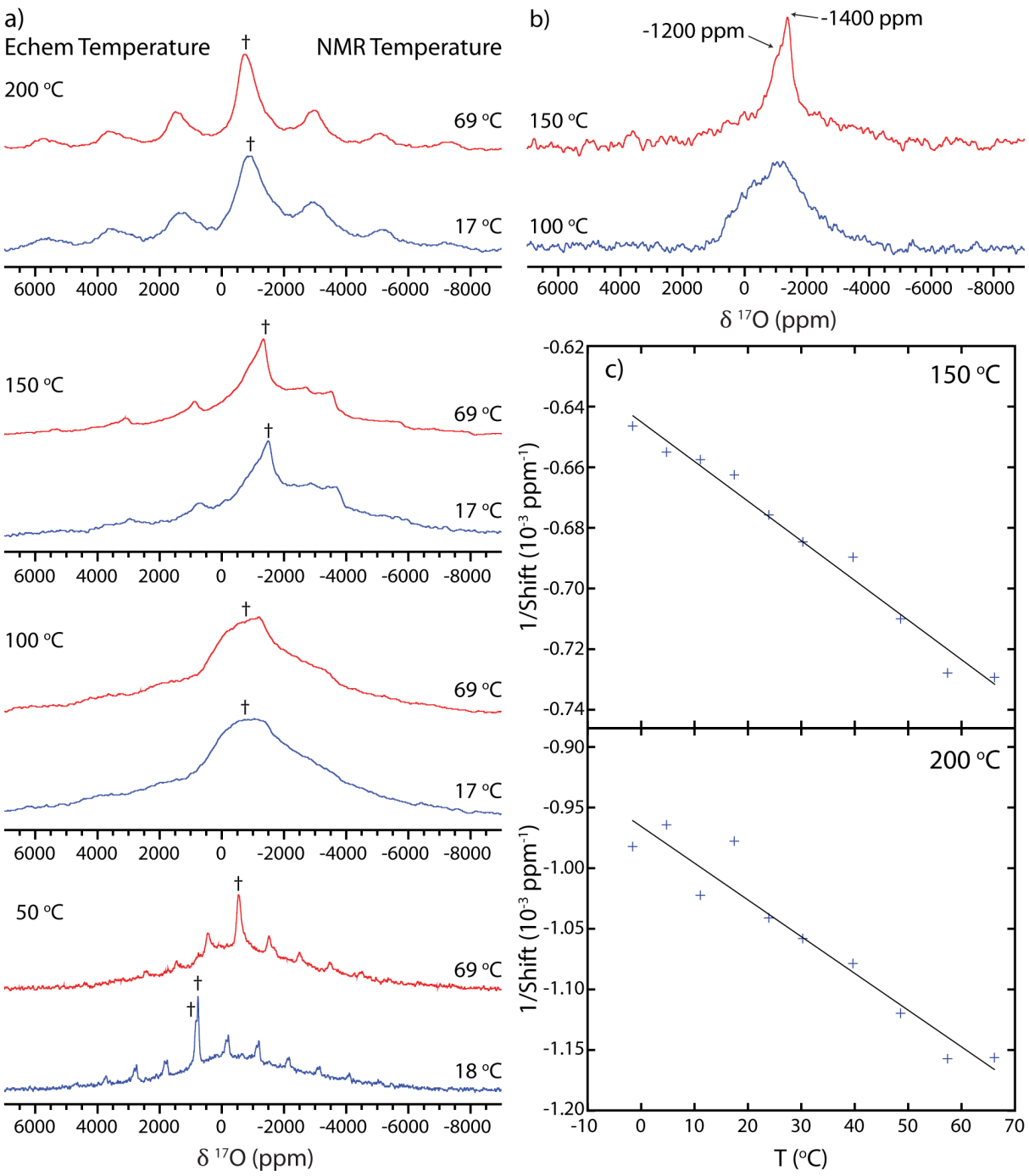

Figure 5.13: a) ^{17}O NMR spectra of ^{17}O-enriched H_xVO_2, electrochemically hydrogenated between 50 °C and 200 °C, recorded above and below the VO_2 MIT temperature, using a Hahn echo pulse sequence. The isotropic resonances are marked with a dagger. b) The isotropic slices of the ^{17}O MATPASS NMR spectra for ^{17}O-enriched H_xVO_2 electrochemically hydrogenated at 100 °C and 150 °C. c) Plots of reciprocal ^{17}O shift against temperature for ^{17}O enriched H_xVO_2 electrochemically gated at 150 °C and 200 °C, recorded with a Hahn echo. The sample electrochemically hydrogenated at 50 °C was recorded at 7.05 T and 40 kHz MAS, all other spectra were recorded at 4.70 T and 60 kHz MAS.

For the sample electrochemically hydrogenated at 100 °C, the insulating monoclinic VO_2 signals are no longer present in the low temperature ^{17}O NMR spectrum, nor is the sharp metallic signal observed in the high temperature spectrum; both spectra instead exhibit a very broad signal with unresolved sidebands, centred at ca. −1100 ppm; this can be more readily

seen in the MATPASS spectrum (Figure 5.13b, bottom). The shift of this signal is independent of temperature, so can be assigned as the metallic O1a phase with a core-polarisation negative Knight shift. Again, the shift is more negative than that for pure VO_2 above the MIT (−505 ppm) due to the greater density of states at the Fermi level, and the width of the signal may indicate a distribution of local environments or doping levels. The signal from the O1b phase cannot be distinguished, possibly because it is too broad; the peaks in the XRD pattern of VO_2 electrochemically metallised at 100 °C are also very broad (see Appendix D), suggesting a distribution of lattice parameters or low crystallinity. Based on the appearance of O1a for this 100 °C sample, it is likely that the O1a phase present in the sample hydrogenated at 50 °C is responsible for the broad background observed in the ^{17}O spectra of that sample, both above and below the MIT.

The sample electrochemically hydrogenated at 150 °C shows a sharper ^{17}O NMR signal at ca. −1500 ppm as well as a shoulder at −1200 ppm; again, this can be more easily seen in the MATPASS spectrum (Figure 5.13b, top). The sharp signal exhibits a Curie–Weiss temperature dependence (Figure 5.13c, top), so is assigned to the localised paramagnetic O1b phase; the paramagnetic shift is negative due to the polarisation mechanism of the orthogonal V 3*d* t_{2g} and O 2*s* orbitals,[51] and becomes less negative with increasing temperature. The shift of the shoulder is independent of temperature and is assigned to the O1a phase, once more with a more negative Knight shift.

The greater electrochemical hydrogenation at higher temperatures could be due to a number of factors. One consideration is that above 67 °C the pristine VO_2 is in the metallic rutile phase, which will afford better electrical transport between particles in the electrode as well as presumably reducing the barrier to formation of the orthorhombic phases which are structurally more similar; indeed, no monoclinic phase remains after performing the electrochemistry at 100 °C and above. However, the amount of hydrogenation appears to increase systematically with temperature, rather than there being a step change between the 50 °C and 100 °C samples.

A second explanation is that the differences in the activation energies of the hydrogenation reaction and the limiting side reaction(s) will result in different temperature dependences of the reaction rates; the potential of the plateau in the electrochemistry becomes less negative with increasing temperature (Figure 5.12a), which indicates that the limiting process becomes more facile. In particular, the rate of hydrogen diffusion will increase at higher temperatures, reducing the overpotential required to drive the hydrogenation reaction.

By 200 °C the degree of hydrogenation is lowered, which is presumably because competing side reactions such as hydrogen evolution or electrolyte decomposition have now become faster again relative to the hydrogenation reaction, and moreover yields pure O1a, as shown by the XRD pattern (Appendix D) and ^{1}H NMR spectrum (Figure 5.12d). However, rather than the bulk susceptibility being dominated by the Pauli paramagnetism of the metallic O1a phase, with little of the Curie paramagnetism associated with the O1b phase, the susceptibility actually shows a decrease in the Pauli paramagnetism and the largest Curie constant of all the samples (Figure 5.12g). This suggests that the O1a phase now contains localised paramagnetic defects.

The ^{17}O NMR spectra recorded after electrochemical metallisation of an isotopically enriched sample at 200 °C support this conclusion (Figure 5.13a). A signal is observed at ca. −800 ppm which exhibits a Curie–Weiss temperature dependence (Figure 5.13c, bottom), further suggesting the presence of paramagnetic defects in the O1a phase; the paramagnetic shift is negative due to the polarisation mechanism and becomes less negative with increasing temperature. For this sample, the paramagnetic defects can only be observed in the ^{17}O NMR spectrum, because paramagnetic vanadium centres relax too quickly to be observed *via* ^{51}V NMR, and the hydrogen must be in a metallic environment, rather than being in the vicinity of a defect, because the ^{1}H NMR spectrum exhibits a Knight shift. Nevertheless, the paramagnetic centres dominate the bulk magnetic susceptibility measurements, rather than the metallic contribution; the greater density of paramagnetic defects in this sample is also consistent with the higher Néel temperature observed in the bulk magnetic susceptibility (Figure 5.12f).

5.4.5 Electrolyte Gating of Thin Films

To compare the electrochemical metallisation experiments on bulk VO_2 with the previous studies on thin films, a 200 nm VO_2 film was grown on a 0.5 mm TiO_2 (001) substrate and electrolyte gated with EMIm TFSI; the film and substrate were then crushed and lightly hand-ground with a mortar and pestle to allow it to be packed into an NMR sample rotor. As the film cannot be separated from the substrate, there is a 2500-fold dilution of the sample which makes recording the ^{1}H NMR spectrum challenging, and the ^{51}V NMR spectrum essentially impossible using the current substrates. The conventional background-subtracted ^{1}H NMR spectrum (Figure 5.14a, top) is dominated by diamagnetic impurities, either from the TiO_2 substrate or the sample surface, obscuring any signal from the gated VO_2. However, by applying a T_1 filter, the diamagnetic resonances can be largely removed as they relax more slowly (Figure 5.14a, bottom); this leaves signals that relax more quickly, such as metallic

H_xVO_2 environments with T_1 ~ 0.03 s. Indeed, in the T_1 filtered ^{1}H NMR spectrum a resonance can be observed at 115 ppm, where metallic H_xVO_2 was observed in the electrochemically metallized bulk samples. The same signal was not observed in the T_1 filtered ^{1}H NMR spectrum of a VO_2 thin film before electrolyte gating (Figure 5.14b). Although these experiments are approaching the sensitivity limits of NMR spectroscopy, they suggest that electrolyte gating experiments of thin films also result in hydrogenation of the VO_2, due to ionic liquid breakdown.

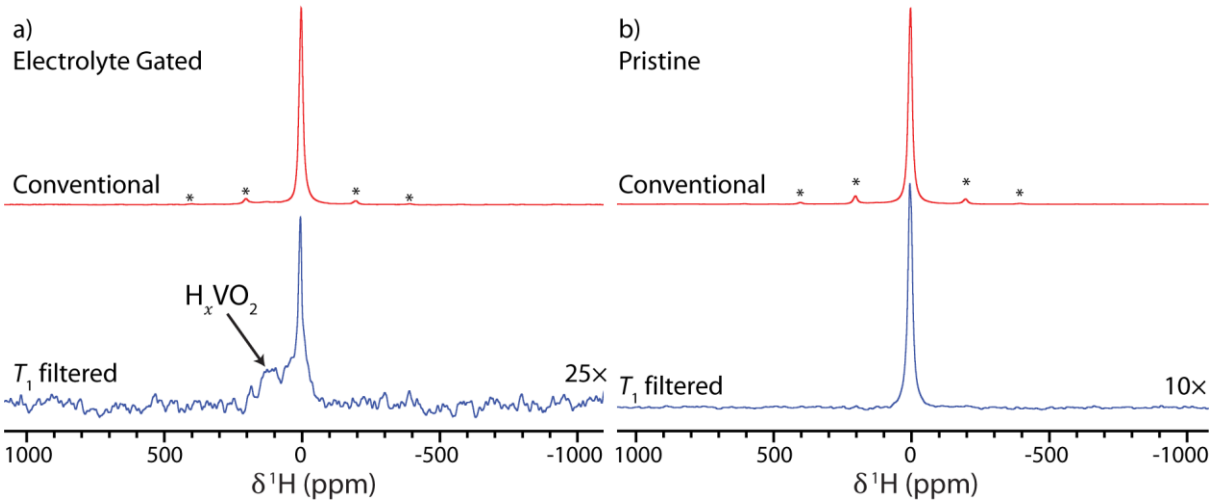

Figure 5.14: ^{1}H NMR spectra of a 200 nm VO_2 thin film on 0.5 mm TiO_2 a) with and b) without electrolyte gating, recorded at 4.70 T, 40 kHz MAS and a sample temperature of ~40 °C, with spinning sidebands marked by asterisks. The conventional spectrum was obtained with a recycle delay of 0.05 s using a DEPTH pulse sequence[179] and subtracting the background. The T_1 filtered spectrum was recorded by taking the difference between background-subtracted spectra with recycle delays of 0.05 s and 0.1 s, scaling the spectra to remove as much as possible of the diamagnetic signals. The spectra with recycle delays of 0.05 s were recorded with 2.72 million scans each for the sample and the background, and the spectra with recycle delays of 0.1 s were recorded with 0.68 million scans.

5.4.6 Electrochemical Hydrogenation – Mechanism

Having established that VO_2 can be hydrogenated electrochemically with an ionic liquid electrolyte, the obvious question is: where does the hydrogen come from? One possibility could be electrolysis of H_2O which is invariably present in ionic liquids due to their hygroscopic nature,[201] given that hydrogenation of VO_2 by water electrolysis has previously been demonstrated.[164,165] However, even after drying the ionic liquid under vacuum for 2 days, electrochemical reduction of VO_2 at 100 °C still gave a similar level of hydrogenation, with a greater hydrogen content than can be explained by the water content (1.9 μmol of water in the ionic liquid as determined by Karl Fischer titration, 27 μmol of hydrogen in the electrochemically hydrogenated VO_2). Another potential source of hydrogen is the ionic liquid itself, and for 1,3-dialkyl-imidazolium ionic liquids, such as EMIm TFSI, the most acidic

proton is the "carbene" proton between the nitrogen atoms of the imidazolium cation, so-called because on deprotonation it forms an N-heterocyclic carbene which is stabilized by the adjacent nitrogen lone pairs;[202] this deprotonation is driven by the low potential at the VO_2 during reduction.[197]

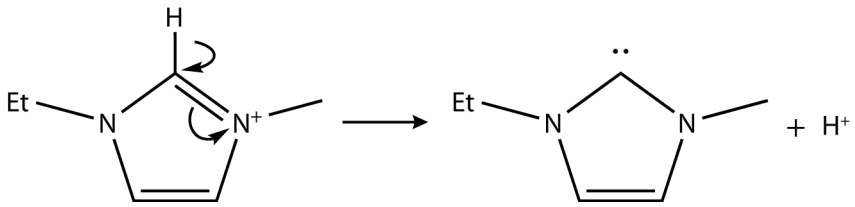

To test this hypothesis, a sample of EMIm TFSI was prepared where the carbene proton had been selectively exchanged for deuterium; this was achieved by stirring EMIm TFSI in excess D_2O at 50 °C for 24 hours before drying off the D_2O *in vacuo.* An ~90 at% isotopic substitution in the ionic liquid was confirmed by ^1H and ^2H NMR spectroscopy (Figure 5.15a). Performing the electrochemical hydrogenation at 100 °C with the selectively deuterated ionic liquid decreased the ^1H content of the H_xVO_2 accordingly, as determined by ^1H NMR spectroscopy. The ^2H NMR spectra (Figure 5.15b) then show deuterium incorporated in both the O1a and O1b environments, as well as a sharp signal at 0 ppm, due again to diamagnetic decomposition products. This provides compelling evidence that it is the carbene hydrogen of the EMIm TFSI ionic liquid that is intercalated into the VO_2 upon electrochemical reduction. The breakdown of the ionic liquid is also evident when removing the ionic liquid after an experiment: for electrochemical reduction at room temperature, the originally clear ionic liquid becomes strongly discoloured, and at higher temperatures it becomes dark brown.

By recording the ^2H NMR spectrum at different fields, the chemical shift anisotropy (CSA) and quadrupolar contributions to the sideband manifold can be deconvoluted. At lower fields the sideband manifold is dominated by the axial quadrupolar tensor, indicative of an axial bonding environment, and at higher fields the sideband manifold is dominated by a shift anisotropy. The spectra were modelled at each field, the parameters for which are shown in Table 5.4. These parameters were found by fitting the quadrupolar tensor at 4.70 T, the CSA tensor at 11.75 T and then the Euler angles (α, β, γ) relating these two tensors at 7.05 T, before iteratively minimising the difference at each field to yield a consistent fit. The solution is not perfect and may not be unique as changing the relative orientations of the tensors can lead to large and non-monotonic changes in the sideband manifold, which are difficult to search using

a local-optimisation routine. Nevertheless, the fit is reasonably consistent between fields and reproduces the major features, so the tensor parameters are likely to be approximately correct.

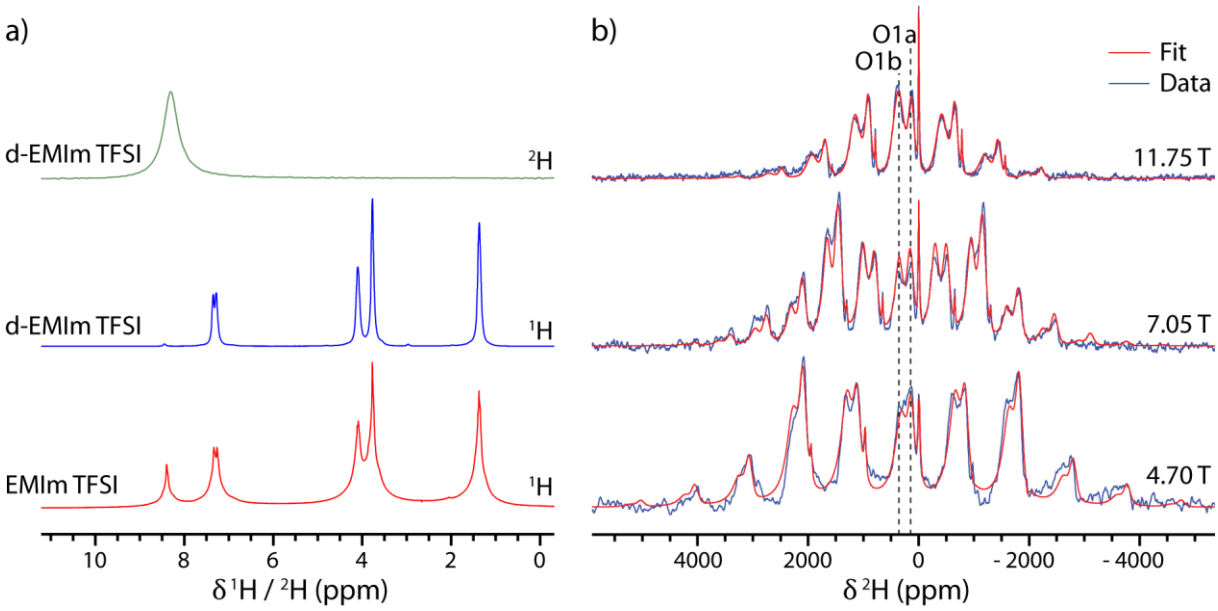

Figure 5.15: a) The ^{1}H NMR spectrum of pristine EMIm TFSI and the ^{1}H and ^{2}H NMR spectra after stirring in D_2O and subsequent drying, showing selective deuteration of the carbene hydrogen at 8.3 ppm. Spectra were recorded static at 7.05 T with a single-pulse experiment. b) ^{2}H NMR spectra of VO_2 after electrochemical metallisation at 100 °C with deuterated EMIm TFSI, recorded at fields of 4.70 T, 7.05 T and 11.75 T using a Hahn echo pulse sequence. The spectra at 4.70 T and 7.05 T were recorded at 30 kHz MAS, the spectrum at 11.75 T was recorded at 60 kHz MAS.

Table 5.4: Fitted chemical shift anisotropy (CSA) and asymmetry (η), quadrupolar frequency (ν_Q) and asymmetry (η_Q), and Euler angles relating the two tensors (α, β, γ), for the deuterium environments in D_xVO_2.

	CSA /ppm	$\boldsymbol{\eta}$	$\boldsymbol{\nu_Q}$ **/kHz**	$\boldsymbol{\eta_Q}$	**α /°**	**β /°**	**γ /°**
O1a	−1750	0.86	270	0.00	0	45	0
O1b	1410	0.99	230	0.00	0	45	0

The quadrupolar frequencies (ν_Q) of O1a and O1b were found to be ~270 kHz and ~230 kHz respectively; this suggests that the hydrogen bonding of the H/D atoms to other oxygen atoms in VO_2 is reasonably weak, as hydrogen bonding reduces the electric field gradient,[203,204] with slightly stronger hydrogen bonding in the O1b phase. Furthermore, as stronger hydrogen bonding would require a greater distortion to bring the oxygen atoms closer together, this means that a large distortion around the intercalated hydrogen atoms would not be expected in H_xVO_2.

Further evidence for this mechanism is seen by using ionic liquids with different imidazolium-based cations: the more protic 1-ethylimidazolium bis(trifluoromethylsulfonyl)imide (EIm

TFSI) and the less protic 1-ethyl-2,3-dimethylimidazolium bis(trifluoromethanesulfonyl)imide (EM_2Im TFSI). Similar degrees of hydrogenation were observed for these three ionic liquids (Table 5.5), with the variation ascribed to small differences between the energy of the hydrogenation reaction and the limiting side reaction(s) and/or sample-to-sample variations; however, there is a difference in the voltage profiles observed during the electrochemical reduction (Figure 5.16b): the acidity of the cations increases in the order EM_2Im < EMIm < EIm, and a less negative potential is observed following the same trend. At first glance the EM_2Im cation does not appear to have available protons, however it is possible to deprotonate the methyl group to form an N-heterocyclic olefin.[205]

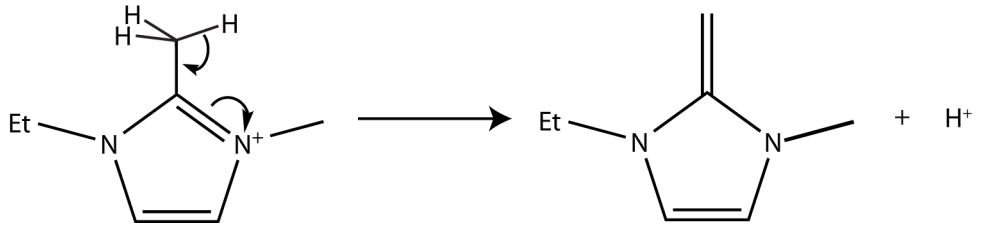

Table 5.5: Degree of hydrogenation (x in H_xVO_2) from quantitative ^1H NMR for VO_2 electrochemically metallised at room temperature with different TFSI ionic liquids.

	EIm	**EMIm**	**EM_2Im**	**DEME**
x	0.049(3)	0.037(2)	0.091(5)	0.028(2)

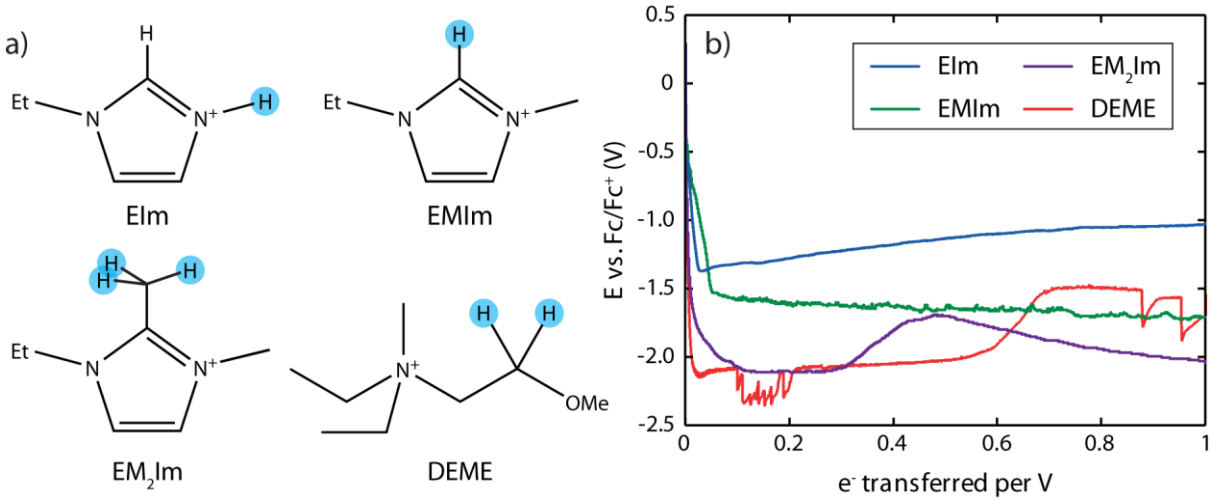

Figure 5.16: a) Different ionic liquid cations, with the most acidic proton highlighted. b) Voltage profiles for VO_2 electrochemically reduced at room temperature with TFSI based ionic liquids with different cations.

For electrolyte gating with non-imidazolium-based ionic liquids, it seems likely that hydrogen intercalation is also involved in the electrochemical metallisation of VO_2; this was tested for diethylmethyl(2-methoxyethyl)ammonium bis(trifluoromethylsulfonyl)imide (DEME TFSI), another commonly used ionic liquid for electrolyte gating experiments,[154,160,163] for which hydrogenation was also observed after electrochemical reduction. The low observed potential (Figure 5.16b) suggests that the cation is not very acidic, but the most likely mechanism of deprotonation is *via* the formation of a stabilized methoxyethyl group and a neutral tertiary amine:

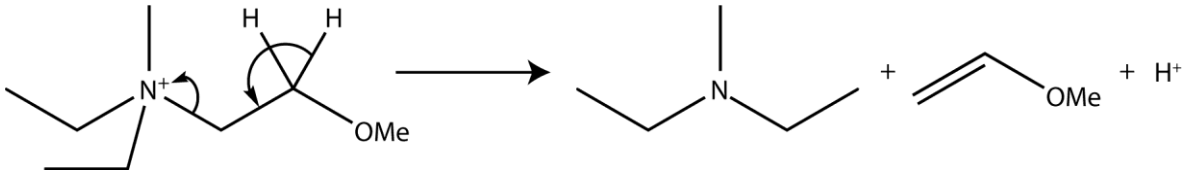

To determine the onset voltage of VO_2 hydrogenation, bulk VO_2 composite films were electrochemically reduced as a function of potential (Figure 5.17). There is not a sharp step in hydrogenation, but rather hydrogenation increases progressively with more negative voltage, which is consistent with a solid-solution rather than a two-phase reaction, before plateauing at ca. −0.75 V when some side-reaction prevents further hydrogenation. This is a less negative potential than in the galvanostatic experiment (ca. −1.6 V, Figure 5.7) because the overpotential is decreased when the potential is fixed and current allowed to respond, compared to when a fixed (higher) current is applied. The maximum amount of hydrogenation observed, $x = 0.021$, is slightly lower than for galvanostatic reduction ($x = 0.037$); this is ascribed to differences between batches of VO_2 composite films, most likely in particle size, or to the lower overpotential.

The onset voltage of VO_2 hydrogenation, ca. −0.5 V vs. Fc/Fc^+, is significantly less negative than the reported cathodic stability of EMIm TFSI on a glassy carbon electrode (−2.5 V vs. Fc/Fc^+);[200] however, this is not surprising since electrolyte stability is highly dependent on the electrode against which it is measured. Although EMIm TFSI is stable to a low voltage against an inert electrode, VO_2 catalyses the breakdown which can therefore happen at a much less negative voltage. This can clearly be seen in Figure 5.8a, when the current is reversed the cathodic limit on the Pt electrode is more than a volt more negative than it was on the VO_2 electrode. Furthermore, because VO_2 partakes in the reaction, the change in free energy is not simply that required to decompose the electrolyte but is lowered by the free energy released by reducing the VO_2, and the voltage is thus correspondingly less negative.

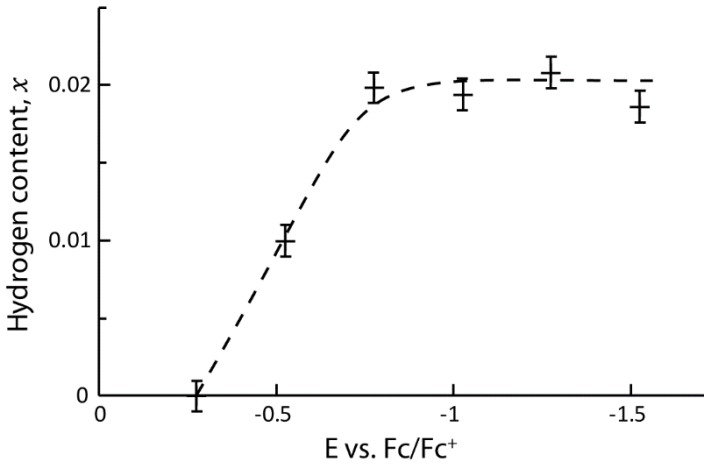

Figure 5.17: Hydrogen content x, from quantitative ^{1}H NMR, as a function of limiting voltage for electrochemical reduction of bulk VO_2 composite films with EMIm TFSI.

This work should be contrasted with that of Lu et al. who performed similar electrochemical hydrogenation experiments using thin films of $SrCoO_{2.5}$ and the ionic liquids EMIm BF_4 and DEME TFSI.[206] They added D_2O to the ionic liquids before heating to 100 ^oC and then performed the electrochemistry; they subsequently observed ^{2}H ions from SIMS in the gated material and therefore concluded that the hydrogen arose from H_2O (D_2O) in the ionic liquid. Although this is a different material, it is possible that the heating caused exchange of the labile proton on the ionic liquid for deuterium, and hence that the hydrogenation is also due to decomposition of the ionic liquid in this case. However, further investigation would be required to unambiguously determine the source of hydrogen in this different system, particularly because the potential at which the oxide is reduced may be important in determining the mechanism of hydrogenation.

The experiments on the electrochemical reduction of VO_2 presented here do not rule out the presence of oxygen vacancies, but they suggest that hydrogenation could be a sufficient explanation for the metallisation, particularly for certain classes of ionic liquids and if large overpotentials (gating voltages) are used. The electrochemical reaction of the VO_2 in this case is

$$VO_2 + xH^+ + xe^- \rightarrow H_xVO_2$$

However, even in systems where oxygen vacancies may dominate, such as WO_3 and $SrCoO_{2.5}$,[161,162,206] hydrogen could still play an important role in the electrochemistry; this hydrogen would most likely come from decomposition of the ionic liquid, although as discussed above, the balance between water and electrolyte decomposition may depend on both

the system and the applied potential. The charge balancing of metal reduction in the metal oxide MO_n by loss of oxygen can be written as

$$MO_n \rightarrow MO_{n-x} + \frac{x}{2} O_2$$

However, this above formulation of the process is too simplistic because it is a purely chemical reaction and O_2 cannot be generated at the anode (where the reduction occurs). Instead the proposed reaction must occur by two electrochemical half-reactions, at the negative (metal oxide) and positive (gate/counter) electrodes respectively:

$$MO_n + 2xe^- \rightarrow MO_{n-x} + xO^{2-} \qquad \text{(Negative electrode)}$$

$$xO^{2-} \rightarrow \frac{x}{2} O_2 + 2xe^- \qquad \text{(Positive electrode)}$$

Transport of O^{2-} between the electrodes is formally required, which could occur as H_2O, formed from the protons liberated *via* electrolyte decomposition, rather than as a free O^{2-} ion. I.e.

$$MO_n + 2xH^+ + 2xe^- \rightarrow MO_{n-x} + xH_2O \qquad \text{(Negative electrode)}$$

$$xH_2O \rightarrow \frac{x}{2} O_2 + 2xH^+ + 2xe^- \qquad \text{(Positive electrode)}$$

This reaction has direct analogies with the onset of so-called conversion reactions in battery electrodes where Li_2O is generated along with the reduction of the metal ions, eventually to the metal (e.g. $CoO + 2Li^+ + 2e^- \rightarrow Co + Li_2O$).[120,207] These conversion reactions can also commence with lithiation (intercalation) before conversion, which is again analogous to the proton intercalation observed here in VO_2.

5.5 Conclusions

Electrochemical metallisation of micron-sized VO_2 particles with imidazolium ionic liquids has been shown to be associated with intercalation of protons and concomitant reduction of the V^{4+} ions, ^1H NMR spectra with a positive Knight shift due to the metallisation providing a clear signature of this event. There is also evidence for the same hydrogenation in thin films of VO_2. In the case of 1,3-dialkyl-imidazolium-based ionic liquids, which are common for previously reported electrolyte gating experiments, the hydrogenation is due to deprotonation of the ionic liquid, specifically the "carbene" hydrogen of the imidazolium cation; this has been shown by selectively substituting this hydrogen for deuterium.

Electrochemical reduction of bulk VO_2 at room temperature does not afford complete metallisation, but rather localized metallisation in the vicinity of the intercalated hydrogen, which is in contrast to thin film electrolyte gating experiments; greater hydrogenation could, however, be achieved for nanoparticulate VO_2. Increasing the temperature of the electrochemistry also yields greater hydrogenation, forming first a metallic orthorhombic phase and then a second localized paramagnetic orthorhombic phase with a greater degree of hydrogenation; a schematic phase diagram for H_xVO_2 is shown in Figure 5.18. A mixture of the same orthorhombic phases was also observed for catalytically hydrogenated VO_2, for which the resistivity was shown to decrease by a factor of 500 compared to that of pristine VO_2. The degree of hydrogenation can be measured by quantitative ^{1}H NMR spectroscopy, and the Pauli and Curie paramagnetic components of the two orthorhombic phases can be tracked *via* ^{1}H, ^{17}O and ^{51}V NMR spectroscopy; in particular, the ^{17}O Knight shift in the metallic phase is a sensitive probe of the density of states at the Fermi level and hence the degree of electron doping, and variable temperature experiments for both ^{1}H and ^{17}O can be used to assign the Curie paramagnetic phases.

These results should be taken into consideration when developing a device based on electrolyte gating of VO_2 thin films: the carbene species formed on deprotonation of the ionic liquid is very reactive and will cause decomposition of the electrolyte; this is not a sustainable long-term reaction. However, as hydrogenation is the cause of the metallisation, an alternative electrochemical system can be formulated to intentionally and reversibly intercalate hydrogen, which could allow the practical realization of electrolyte gating in devices. Finally, these results suggest that the protons produced by electrolyte degradation may be involved in oxygen extraction mechanisms in this and other electrochemically-gated systems.

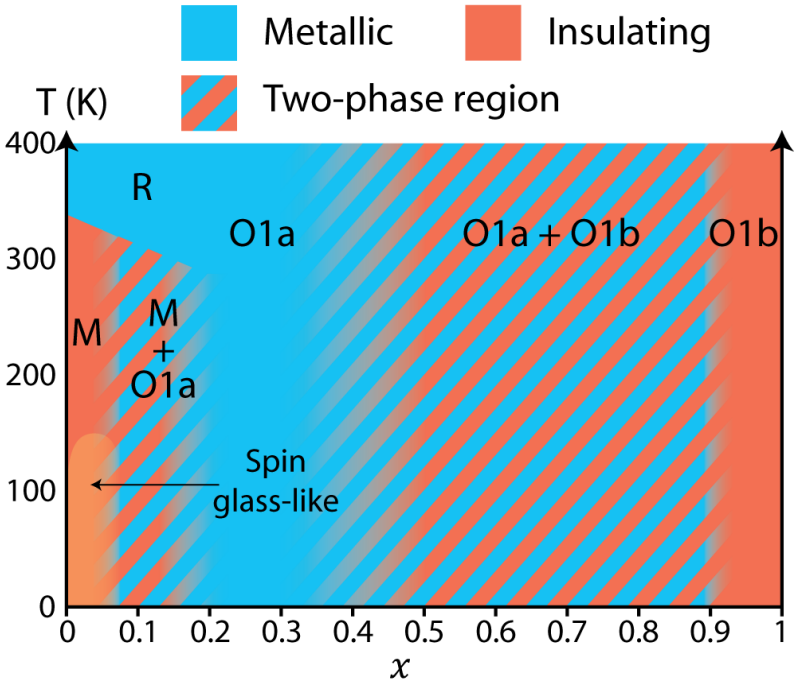

Figure 5.18: Schematic phase diagram of H_xVO_2, showing the monoclinic (M), rutile (R) and two orthorhombic phases (O1a and O1b), with two-phase regions cross hatched. Boundaries were estimated from the compositions of the H_xVO_2 samples studied in this work, rather than being rigorously mapped. The M and O1b phases are insulating while the R and O1a phases are metallic. The single-phase rutile (R) region for $x \approx 0.1$ above the MIT temperature was determined by variable temperature XRD, see Appendix D.

Chapter 6: Conclusions and Outlook

Solid-state NMR spectroscopy has been successfully applied to study different examples of paramagnetic and metallic systems. The additional hyperfine interactions present in these materials, while challenging in some cases, have been exploited to gain further insight into the crystal and electronic structures. Specifically, paramagnetic shifts have been identified by their (generally) strong temperature dependence, and the faster NMR relaxation of both paramagnetic and metallic shifts has been used both to confirm the electronic structure and to allow these phases to be selectively observed, including in a thin film of hydrogenated VO_2, which is very much at the sensitivity limits of conventional NMR.

The spectral broadening induced by the hyperfine interactions has generally been overcome in this work by fast MAS and/or sideband separation (MATPASS) experiments; however, where these techniques are not possible, acquiring sufficient signal-to-noise and resolution remains difficult. For example, in variable temperature experiments the accessible MAS rates are much reduced, and the relaxation during the correspondingly longer rotor synchronised delays in a MATPASS experiment reduces the signal beyond detectable limits, given the fast hyperfine-induced relaxation. This is primarily a hardware issue, requiring faster spinning MAS probes which can operate over a wider temperature range; while not technologically unreasonable, such probes are by no means standard.

The utility of ^{17}O NMR has been demonstrated for all the systems studied. It has been used to: identify the sites in monoclinic Sm_2O_3 and Eu_2O_3 and as a proxy for the thermal dependence of the magnetic properties of Sm^{3+} and Eu^{3+} in the cubic sesquioxides; to probe the local structure and oxide-ion motion in *Ln*-substituted CeO_2 and to reveal the surface oxygen environments in CeO_2 nanoparticles; and to determine the electronic structure of reduced phases of VO_2, while being a sensitive measure of the density of states in metallic phases. To record these spectra, the samples were isotopically enriched with ^{17}O, and different procedures had to be developed for the different materials: the monoclinic lanthanide sesquioxides required high temperature enrichment to yield the correct phase, while the CeO_2 nanoparticles required low temperature enrichment to avoid sintering; VO_2, on the other hand, necessitated a multi-step synthesis to achieve the desired oxidation state of the enriched oxide. Furthermore, the importance of handling enriched samples under an inert atmosphere, for the study of surfaces, was highlighted by the observed exchange of the first layer surface oxygen atoms in CeO_2 with natural isotopic abundance H_2O or O_2 on exposure to air. These procedures add to

the existing enrichment methods in the literature, allowing different types of materials to be studied with ^{17}O NMR. However, improvements could still be made to these procedures, especially for the high temperature enrichments above 1000 °C: at these temperatures, the ^{17}O can also exchange for ^{16}O in the quartz and alumina containers used, which are a large reservoir of natural-abundance oxygen atoms, potentially reducing the enrichment level significantly. An alternative method would be to use a metal container; in this case, the issues would be to ensure complete sealing, as well as to avoid oxidation of the metal, which would also consume the ^{17}O.

The surface-selectivity achievable with DNP for ^{17}O NMR of CeO_2 is striking, however the applicability to other systems may be hindered by the inhomogeneous broadening of spectra at the low temperatures typical for DNP. At room temperature, the electron relaxation is generally too fast to allow significant saturation of the ESR transition and hence nuclear enhancement; however, it may be possible to develop new radicals with longer electron relaxation times for DNP at higher temperatures, although there will undoubtedly be lower enhancements.

Endogenous DNP of ^{17}O is still in its infancy and requires further optimisation of the choice of dopant as well as the optimal concentration. However, moderate enhancements have been achieved and if further improvements can be made, endogenous DNP could make study feasible of samples with very low masses, or for which isotopic enrichment is not possible. One such system is the interfaces in CeO_2 nanocomposite films:[208] these interfaces comprise only a small fraction of the sample, of which, as a thin film, there is already a low mass, so they represent an extreme challenge for study by NMR. DNP could be one means of enhancing the signal, but as the interfaces are not external surfaces, they would not be hyperpolarised by an exogenous radical, hence the need for endogenous DNP.

One fundamental question that remains for both exogenous and endogenous ^{17}O DNP is the role of spin diffusion: spin diffusion is expected to be slow for quadrupolar nuclei and is strongly affected by concentration, however hyperpolarisation of ^{17}O nuclei far from a radical source has still been observed in this work, and the hyperpolarisation must be transferred somehow. Spin diffusion may be more facile in CeO_2, however, due to the cubic symmetry of the oxygen site for which the quadrupolar coupling vanishes. One way to investigate this phenomenon would be to perform systematic experiments as a careful function of enrichment level.

Arguably the biggest area in which further work could be undertaken based on this thesis is the study of other electrolyte gated systems, such as WO_3 and $SrCoO_3$. Although hydrogenation was shown to be the dominant mechanism of metallisation for VO_2, this is likely to be dependent on the system, and oxygen vacancies may dominate for other materials. Oxygen vacancies, however, as the absence of an atom, are harder to unambiguously identify using NMR. One option would be to reduce a sample and then re-oxidise it in the presence of ^{17}O, e.g. by adding $H_2{}^{17}O$ to the electrolyte; a ^{17}O NMR signal in the material would then be evidence of oxygen vacancies. Proving that the electrochemical formation of oxygen vacancies is mediated by protons in the form of water, on the other hand, could be achieved by the reverse procedure: ^{17}O labelling the material and then testing for a $H_2{}^{17}O$ NMR signal in the electrolyte. Another interesting related area would be to attempt similar electrochemical metallisation experiments, but using Li^+ ions rather than hydrogen; some initial results have suggested irreversible metallisation of VO_2 when electrolyte gating experiments were performed with a Li^+ containing electrolyte was used,[159] but a reversible system has not yet been demonstrated.

Solid-state NMR is a powerful probe of local structure, providing mechanistic and structural information which is not available from traditional long-range techniques. Although ssNMR of paramagnetic and metallic systems is undoubtedly more challenging than the equivalent experiments for diamagnetic samples, it is nevertheless feasible for many materials, such as those reported in this work, and hopefully it has been shown that the wealth of information that can be obtained justifies the extra effort required.

References

(1) Levitt, M. H. *Spin Dynamics: Basics of Nuclear Magnetic Resonance*, 2nd ed.; John Wiley & Sons: Chichester, 2008.

(2) Duer, M. J. *Introduction to Solid-State NMR Spectroscopy*; Blackwell Publishing Ltd: Oxford, 2004.

(3) Apperley, D. C.; Harris, R. K.; Hodgkinson, P. *Solid-State NMR: Basic Principles & Practise*; Momentum Press: New York, 2012.

(4) MacKenzie, K. J.; Smith, M. E. *Multinuclear Solid-State Nuclear Magnetic Resonance of Inorganic Materials*; Elsevier Science: Oxford, 2002.

(5) Pell, A. J.; Pintacuda, G.; Grey, C. P. Paramagnetic NMR in Solution and the Solid State. *Prog. Nucl. Magn. Reson. Spectrosc.* **2019**, *111*, 1–271.

(6) Ashbrook, S. E.; Smith, M. E. Solid State ^{17}O NMR—an Introduction to the Background Principles and Applications to Inorganic Materials. *Chem. Soc. Rev.* **2006**, *35* (8), 718–735.

(7) Gerothanassis, I. P. Oxygen-17 NMR Spectroscopy: Basic Principles and Applications (Part I). *Prog. Nucl. Magn. Reson. Spectrosc.* **2010**, *56* (2), 95–197.

(8) Ménétrier, M.; Saadoune, I.; Levasseur, S.; Delmas, C. The Insulator-Metal Transition upon Lithium Deintercalation from $LiCoO_2$: Electronic Properties and ^{7}Li NMR Study. *J. Mater. Chem.* **1999**, *9* (5), 1135–1140.

(9) Grey, C. P.; Dupré, N. NMR Studies of Cathode Materials for Lithium-Ion Rechargeable Batteries. *Chem. Rev.* **2004**, *104* (10), 4493–4512.

(10) Kong, X.; Terskikh, V. V; Khade, R. L.; Yang, L.; Rorick, A.; Zhang, Y.; He, P.; Huang, Y.; Wu, G. Solid-State ^{17}O NMR Spectroscopy of Paramagnetic Coordination Compounds. *Angew. Chemie Int. Ed.* **2015**, *54* (16), 4753–4757.

(11) Seymour, I. D.; Middlemiss, D. S.; Halat, D. M.; Trease, N. M.; Pell, A. J.; Grey, C. P. Characterizing Oxygen Local Environments in Paramagnetic Battery Materials via ^{17}O NMR and DFT Calculations. *J. Am. Chem. Soc.* **2016**, *138* (30), 9405–9408.

(12) Halat, D. M.; Dervişoğlu, R.; Kim, G.; Dunstan, M. T.; Blanc, F.; Middlemiss, D. S.; Grey, C. P. Probing Oxide-Ion Mobility in the Mixed Ionic–Electronic Conductor $La_2NiO_{4+\delta}$ by Solid-State ^{17}O MAS NMR Spectroscopy. *J. Am. Chem. Soc.* **2016**, *138* (36), 11958–11969.

(13) Halat, D. M.; Dunstan, M. T.; Gaultois, M. W.; Britto, S.; Grey, C. P. Study of Defect Chemistry in the System $La_{2-x}Sr_xNiO_{4+\delta}$ by ^{17}O Solid-State NMR Spectroscopy and Ni K-Edge XANES. *Chem. Mater.* **2018**, *30* (14), 4556–4570.

(14) McCarty, R. J.; Stebbins, J. F. Transition Metal Dopant Cation Distributions in MgO and CaO: New Inferences from Paramagnetically Shifted Resonances in ^{17}O, ^{25}Mg, and ^{43}Ca NMR Spectra. *J. Phys. Chem. C* **2016**, *120* (20), 11111–11120.

(15) Martel, L.; Magnani, N.; Vigier, J.-F.; Boshoven, J.; Selfslag, C.; Farnan, I.; Griveau, J.-C.; Somers, J.; Fanghänel, T. High-Resolution Solid-State Oxygen-17 NMR of Actinide-Bearing Compounds: An Insight into the 5f Chemistry. *Inorg. Chem.* **2014**, *53* (13), 6928–6933.

(16) Bastow, T. J.; Stuart, S. N. ^{17}O NMR in Simple Oxides. *Chem. Phys.* **1990**, *143* (3), 459–467.

(17) Overhauser, A. W. Polarization of Nuclei in Metals. *Phys. Rev.* **1953**, *92* (2), 411–415.

(18) Carver, T. R.; Slichter, C. P. Polarization of Nuclear Spins in Metals. *Phys. Rev.* **1953**, *92* (1), 212–213.

(19) Becerra, L. R.; Gerfen, G. J.; Bellew, B. F.; Bryant, J. A.; Hall, D. A.; Inati, S. J.; Weber, R. T.; Un, S.; Prisner, T. F.; McDermott, A. E.; Fishbein, K. W.; Kreischer, K. E.; Temkin, R. J.; Singel, D. J.; Griffin,

R. G. A Spectrometer for Dynamic Nuclear Polarization and Electron Paramagnetic Resonance at High Frequencies. *J. Magn. Reson. Ser. A* **1995**, *117* (1), 28–40.

(20) Lesage, A.; Lelli, M.; Gajan, D.; Caporini, M. A.; Vitzthum, V.; Miéville, P.; Alauzun, J.; Roussey, A.; Thieuleux, C.; Mehdi, A.; Bodenhausen, G.; Copéret, C.; Emsley, L. Surface Enhanced NMR Spectroscopy by Dynamic Nuclear Polarization. *J. Am. Chem. Soc.* **2010**, *132* (44), 15459–15461.

(21) Rossini, A. J.; Zagdoun, A.; Lelli, M.; Lesage, A.; Copéret, C.; Emsley, L. Dynamic Nuclear Polarization Surface Enhanced NMR Spectroscopy. *Acc. Chem. Res.* **2013**, *46* (9), 1942–1951.

(22) Berruyer, P.; Emsley, L.; Lesage, A. DNP in Materials Science : Touching the Surface. *eMagRes* **2018**, *7*, 93–104.

(23) Cheetham, A. K.; Dobson, C. M.; Grey, C. P.; Jakeman, R. J. B. Paramagnetic Shift Probes in High-Resolution Solid-State NMR. *Nature* **1987**, *328* (6132), 706–707.

(24) Grey, C. P.; Smith, M. E.; Cheetham, A. K.; Dobson, C. M.; Dupree, R. Yttrium-89 Magic Angle Spinning NMR Study of Rare-Earth Pyrochlores: Paramagnetic Shifts in the Solid State. *J. Am. Chem. Soc.* **1990**, *112* (12), 4670–4675.

(25) George, N. C.; Brgoch, J.; Pell, A. J.; Cozzan, C.; Jaffe, A.; Dantelle, G.; Llobet, A.; Pintacuda, G.; Seshadri, R.; Chmelka, B. F. Correlating Local Compositions and Structures with the Macroscopic Optical Properties of Ce^{3+}-Doped $CaSc_2O_4$, an Efficient Green-Emitting Phosphor. *Chem. Mater.* **2017**, *29* (8), 3538–3546.

(26) Abragam, A.; Bleaney, B. *Electron Paramagnetic Resonance of Transition Ions*; Clarendon Press: Oxford, 1970.

(27) Morrison, C. A.; Leavitt, R. P. Spectroscopic Properties of Triply Ionized Lanthanides in Transparent Host Crystals. In *Handbook on the Physics and Chemistry of Rare Earths*; Gschneidner, K. A. J., Eyring, L., Eds.; North Holland Publishing Company, 1982; Vol. 5, pp 461–692.

(28) Carrettin, S.; Concepción, P.; Corma, A.; López Nieto, J. M.; Puntes, V. F. Nanocrystalline CeO_2 Increases the Activity of Au for CO Oxidation by Two Orders of Magnitude. *Angew. Chemie Int. Ed.* **2004**, *43* (19), 2538–2540.

(29) Qi, G.; Yang, R. T.; Chang, R. MnO_x-CeO_2 Mixed Oxides Prepared by Co-Precipitation for Selective Catalytic Reduction of NO with NH_3 at Low Temperatures. *Appl. Catal. B Environ.* **2004**, *51* (2), 93–106.

(30) Galvita, V. V.; Poelman, H.; Bliznuk, V.; Detavernier, C.; Marin, G. B. CeO_2-Modified Fe_2O_3 for CO_2 Utilization via Chemical Looping. *Ind. Eng. Chem. Res.* **2013**, *52* (25), 8416–8426.

(31) Trovarelli, A. Catalytic Properties of Ceria and CeO_2-Containing Materials. *Catal. Rev.* **1996**, *38* (4), 439–520.

(32) Kevane, C. J.; Holverson, E. L.; Watson, R. D. Electrolytic Conduction in Calcium-Doped Solid Cerium Oxide. *J. Appl. Phys.* **1963**, *34* (7), 2083–2087.

(33) Inaba, H.; Tagawa, I. Ceria-Based Solid Electrolytes. *Solid State Ionics* **1996**, *83* (1–2), 1–16.

(34) Etsell, T. H.; Flengas, S. N. Electrical Properties of Solid Oxide Electrolytes. *Chem. Rev.* **1970**, *70* (3), 339–376.

(35) Kudo, T. Oxygen Ion Conduction of the Fluorite-Type $Ce_{1-x}Ln_xO_{2-x/2}$ (Ln = Lanthanoid Element). *J. Electrochem. Soc.* **1975**, *122* (1), 142–147.

(36) Tuller, H. L. Doped Ceria as a Solid Oxide Electrolyte. *J. Electrochem. Soc.* **1975**, *122* (2), 255.

(37) Kudo, T. Mixed Electrical Conduction in the Fluorite-Type $Ce_{1-x}Gd_xO_{2-x/2}$. *J. Electrochem. Soc.* **1976**, *123* (3), 415.

(38) Baertsch, C. D.; Jensen, K. F.; Hertz, J. L.; Tuller, H. L.; Vengallatore, S. T.; Spearing, S. M.; Schmidt, M. A. Fabrication and Structural Characterization of Self-Supporting Electrolyte Membranes for a Micro

Solid-Oxide Fuel Cell. *J. Mater. Res.* **2004**, *19* (9), 2604–2615.

(39) Ishihara, T. Nickel–Gd-Doped CeO_2 Cermet Anode for Intermediate Temperature Operating Solid Oxide Fuel Cells Using $LaGaO_3$-Based Perovskite Electrolyte. *Solid State Ionics* **2000**, *132* (3–4), 209–216.

(40) Belsey, N. A.; Shard, A. G.; Minelli, C. Surface Chemistry. In *Nanomaterial Characterization*; Tantra, R., Ed.; John Wiley & Sons, Ltd, 2016; pp 153–178.

(41) Morin, F. J. Oxides Which Show a Metal-to-Insulator Transition at the Neel Temperature. *Phys. Rev. Lett.* **1959**, *3* (1), 34–36.

(42) Gro Nielsen, U.; Skibsted, J.; Jakobsen, H. J. β-VO_2—a V(IV) or a Mixed-Valence V(III)–V(V) Oxide—Studied by ^{51}V MAS NMR Spectroscopy. *Chem. Phys. Lett.* **2002**, *356* (1–2), 73–78.

(43) Chudnovskiy, F.; Luryi, S.; Spivak, B. Switching Device Based on First-Order Metal- Insulator Transition Induced by External Electric Field. *Futur. Trends Microelectron. Nano Millenn.* **2002**, 148–155.

(44) Driscoll, T.; Kim, H. T.; Chae, B. G.; Di Ventra, M.; Basov, D. N. Phase-Transition Driven Memristive System. *Appl. Phys. Lett.* **2009**, *95* (4), 93–96.

(45) Jeong, J.; Aetukuri, N.; Graf, T.; Schladt, T. D.; Samant, M. G.; Parkin, S. S. P. Suppression of Metal-Insulator Transition in VO_2 by Electric Field-Induced Oxygen Vacancy Formation. *Science* **2013**, *339* (6126), 1402–1405.

(46) Leighton, C. Electrolyte-Based Ionic Control of Functional Oxides. *Nat. Mater.* **2019**, *18* (1), 13–18.

(47) Haeberlen, U. *Advances in Magnetic Resonance; Suppl. 1*; Waugh, J. S., Ed.; Academic Press: New York, 1976.

(48) Slichter, C. P. *Principles of Magnetic Resonance*, 3rd ed.; Springer-Verlag: New York, 1989.

(49) Man, P. P. Quadrupolar Interactions. In *NMR of Quadrupolar Nuclei in Solid Materials*; Wasylishen, R. E., Ashbrook, S. E., Wimperis, S., Eds.; Wiley, 2012; pp 3–17.

(50) Vega, A. J. Quadrupolar Nuclei in Solids. In *NMR of Quadrupolar Nuclei in Solid Materials*; Wasylishen, R., Ashbrook, S., Wimperis, S., Eds.; Wiley, 2012; pp 17–44.

(51) Carlier, D.; Ménétrier, M.; Grey, C. P.; Delmas, C.; Ceder, G. Understanding the NMR Shifts in Paramagnetic Transition Metal Oxides Using Density Functional Theory Calculations. *Phys. Rev. B* **2003**, *67* (17), 174103.

(52) Clément, R. J.; Pell, A. J.; Middlemiss, D. S.; Strobridge, F. C.; Miller, J. K.; Whittingham, M. S.; Emsley, L.; Grey, C. P.; Pintacuda, G. Spin-Transfer Pathways in Paramagnetic Lithium Transition-Metal Phosphates from Combined Broadband Isotropic Solid-State MAS NMR Spectroscopy and DFT Calculations. *J. Am. Chem. Soc.* **2012**, *134* (41), 17178–17185.

(53) Pintacuda, G.; John, M.; Su, X.-C.; Otting, G. NMR Structure Determination of Protein−Ligand Complexes by Lanthanide Labeling. *Acc. Chem. Res.* **2007**, *40* (3), 206–212.

(54) Bleaney, B. Nuclear Magnetic Resonance Shifts in Solution Due to Lanthanide Ions. *J. Magn. Reson.* **1972**, *8* (1), 91–100.

(55) Elliott, R. J.; Stevens, K. W. H. The Theory of Magnetic Resonance Experiments on Salts of the Rare Earths. *Proc. R. Soc. London. Ser. A. Math. Phys. Sci.* **1953**, *218* (1135), 553–566.

(56) Bennett, L. H.; Watson, R. E.; Carter, G. C. Relevance of Knight Shift Measurements to the Electronic Density of States. *J. Res. Natl. Bur. Stand. Sect. A Phys. Chem.* **1970**, *74A* (4), 569–610.

(57) Alloy Data Center - The Alloy Physics Section Metallurgy Division Institute For Materials Research - National Bureau Of Standards. The Knight Shift. *Prog. Mater. Sci.* **1976**, *20* (PART 1), 3–21.

(58) Mott, N. F.; Jones, H. *The Theory of the Properties of Metals and Alloys*; Clarendon Press: Oxford, 1936.

(59) Knight, M. J.; Felli, I. C.; Pierattelli, R.; Emsley, L.; Pintacuda, G. Magic Angle Spinning NMR of Paramagnetic Proteins. *Acc. Chem. Res.* **2013**, *46* (9), 2108–2116.

(60) Korringa, J. Nuclear Magnetic Relaxation and Resonnance Line Shift in Metals. *Physica* **1950**, *16* (7–8), 601–610.

(61) Werbelow, L. G. Relaxation Theory for Quadrupolar Nuclei. In *Encyclopedia of Magnetic Resonance*; John Wiley & Sons, Ltd, 2011.

(62) Abragam, A. *The Principles of Nuclear Magnetism*; The international series of monographs on physics; Oxford University Press: Oxford, 1961.

(63) Heitjans, P.; Schirmer, A.; Indris, S. NMR and β-NMR Studies of Diffusion in Interface-Dominated and Disordered Solids. In *Diffusion in Condensed Matter: Methods, Materials, Models*; Heitjans, P., Kärger, J., Eds.; Springer, 2005.

(64) Keeler, J. *Understanding NMR Spectroscopy*, 2nd ed.; Wiley-Blackwell, 2005.

(65) Zhou, L.; Leskes, M.; Liu, T.; Grey, C. P. Probing Dynamic Processes in Lithium-Ion Batteries by in Situ NMR Spectroscopy: Application to $Li_{1.08}Mn_{1.92}O_4$ Electrodes. *Angew. Chemie - Int. Ed.* **2015**, *54* (49), 14782–14786.

(66) Kleinberg, R. .; Horsfield, M. . Transverse Relaxation Processes in Porous Sedimentary Rock. *J. Magn. Reson.* **1990**, *88* (1), 9–19.

(67) Zhang, G. Q.; Hirasaki, G. J. CPMG Relaxation by Diffusion with Constant Magnetic Field Gradient in a Restricted Geometry: Numerical Simulation and Application. *J. Magn. Reson.* **2003**, *163* (1), 81–91.

(68) Leskes, M.; Grey, C. P. Finite Pulse Effects in CPMG Pulse Trains on Paramagnetic Materials. *Phys. Chem. Chem. Phys.* **2015**, *17* (34), 22311–22320.

(69) Siegel, R.; Nakashima, T. T.; Wasylishen, R. E. Signal-to-Noise Enhancement of NMR Spectra of Solids Using Multiple-Pulse Spin-Echo Experiments. *Concepts Magn. Reson. Part A* **2005**, *26A* (2), 62–77.

(70) Thankamony, A. S. L.; Wittmann, J. J.; Kaushik, M.; Corzilius, B. Dynamic Nuclear Polarization for Sensitivity Enhancement in Modern Solid-State NMR. *Prog. Nucl. Magn. Reson. Spectrosc.* **2017**, *102–103*, 120–195.

(71) Can, T. V.; Caporini, M. A.; Mentink-Vigier, F.; Corzilius, B.; Walish, J. J.; Rosay, M.; Maas, W. E.; Baldus, M.; Vega, S.; Swager, T. M.; Griffin, R. G. Overhauser Effects in Insulating Solids. *J. Chem. Phys.* **2014**, *141* (6).

(72) Michaelis, V. K.; Smith, A. A.; Corzilius, B.; Haze, O.; Swager, T. M.; Griffin, R. G. High-Field ^{13}C Dynamic Nuclear Polarization with a Radical Mixture. *J. Am. Chem. Soc.* **2013**, *135* (8), 2935–2938.

(73) Lee, D.; Bouleau, E.; Saint-bonnet, P.; Hediger, S.; Paëpe, G. De. Ultra-Low Temperature MAS-DNP. *J. Magn. Reson.* **2016**, *264*, 116–124.

(74) Chakrabarty, T.; Goldin, N.; Feintuch, A.; Houben, L.; Leskes, M. Paramagnetic Metal-Ion Dopants as Polarization Agents for Dynamic Nuclear Polarization NMR Spectroscopy in Inorganic Solids. *ChemPhysChem* **2018**, 1–5.

(75) Sauvée, C.; Rosay, M.; Casano, G.; Aussenac, F.; Weber, R. T.; Ouari, O.; Tordo, P. Highly Efficient, Water-Soluble Polarizing Agents for Dynamic Nuclear Polarization at High Frequency. *Angew. Chemie Int. Ed.* **2013**, *52* (41), 10858–10861.

(76) Zagdoun, A.; Casano, G.; Ouari, O.; Schwarzwälder, M.; Rossini, A. J.; Aussenac, F.; Yulikov, M.; Jeschke, G.; Coperet, C.; Lesage, A.; Tordo, P.; Emsley, L. Large Molecular Weight Nitroxide Biradicals Providing Efficient Dynamic Nuclear Polarization at Temperatures up to 200 Kelvin. *J. Am. Chem. Soc.* **2013**, *135*, 12790–12797.

(77) Zhao, L.; Pinon, A. C.; Emsley, L.; Rossini, A. J. DNP-Enhanced Solid-State NMR Spectroscopy of Active Pharmaceutical Ingredients. *Magn. Reson. Chem.* **2018**, *56* (7), 583–609.

(78) Mathies, G.; Jain, S.; Reese, M.; Griffin, R. G. Pulsed Dynamic Nuclear Polarization with Trityl Radicals. *J. Phys. Chem. Lett.* **2016**, *7* (1), 111–116.

(79) Adachi, G.; Imanaka, N. The Binary Rare Earth Oxides. *Chem. Rev.* **1998**, *98* (4), 1479–1514.

(80) Yang, S.; Shore, J.; Oldfield, E. Oxygen-17 Nuclear Magnetic Resonance Spectroscopic Study of the Lanthanide Oxides. *J. Magn. Reson.* **1992**, *99* (2), 408–412.

(81) Van Vleck, J. H. *Handbook of Optics: The Theory of Electric and Magnetic Susceptibilities*; Oxford Univ. Press: Oxford, 1965.

(82) Saiki, A.; Ishizawa, N.; Mizutani, N.; Kato, M. Structural Change of C-Rare Earth Sesquioxides Yb_2O_3 and Er_2O_3 as a Function of Temperature. *Yogyo Kyokai-Shi* **1985**, *93* (10), 649–654.

(83) Lewis, W. B.; Jackson, J. A.; Lemons, J. F.; Taube, H. Oxygen-17 NMR Shifts in Aqueous Solutions of Rare-Earth Ions. *J. Chem. Phys.* **1962**, *36* (3), 694–701.

(84) Golding, R.; Halton, M. A Theoretical Study of the ^{14}N and ^{17}O N.M.R. Shifts in Lanthanide Complexes. *Aust. J. Chem.* **1972**, *25* (12), 2577.

(85) Lai, W.; Haile, S. M. Impedance Spectroscopy as a Tool for Chemical and Electrochemical Analysis of Mixed Conductors: A Case Study of Ceria. *J. Am. Ceram. Soc.* **2005**, *88* (11), 2979–2997.

(86) Kharton, V. V.; Kovalevsky, A. V.; Viskup, A. P.; Figueiredo, F. M.; Yaremchenko, A. A.; Naumovich, E. N.; Marques, F. M. B. Oxygen Permeability of $Ce_{0.8}Gd_{0.2}O_{2-\delta}$–$La_{0.7}Sr_{0.3}MnO_{3-\delta}$ Composite Membranes. *J. Electrochem. Soc.* **2000**, *147* (7), 2814–2821.

(87) Fu, Y. P.; Wen, S. B.; Lu, C. H. Preparation and Characterization of Samaria-Doped Ceria Electrolyte Materials for Solid Oxide Fuel Cells. *J. Am. Ceram. Soc.* **2008**, *91* (1), 127–131.

(88) Wattanathana, W.; Veranitisagul, C.; Wannapaiboon, S.; Klysubun, W.; Koonsaeng, N.; Laobuthee, A. Samarium Doped Ceria (SDC) Synthesized by a Metal Triethanolamine Complex Decomposition Method: Characterization and an Ionic Conductivity Study. *Ceram. Int.* **2017**, *43* (13), 9823–9830.

(89) Cioateră, N.; Pârvulescu, V.; Rolle, A.; Vannier, R. N. Effect of Strontium Addition on Europium-Doped Ceria Properties. *Solid State Ionics* **2009**, *180* (9–10), 681–687.

(90) Balazs, G. B.; Glass, R. S. Ac Impedance Studies of Rare Earth Oxide Doped Ceria. *Solid State Ionics* **1995**, *76* (1–2), 155–162.

(91) Adler, S. B.; Smith, J. W.; Reimer, J. A. Dynamic Monte Carlo Simulation of Spin-Lattice Relaxation of Quadrupolar Nuclei in Solids. Oxygen-17 in Yttria-Doped Ceria. *J. Chem. Phys.* **1993**, *98* (9), 7613–7620.

(92) Kim, N.; Stebbins, J. F. Vacancy and Cation Distribution in Yttria-Doped Ceria: An ^{89}Y and ^{17}O MAS NMR Study. *Chem. Mater.* **2007**, *19* (23), 5742–5747.

(93) Kim, N.; Hsieh, C. H.; Stebbins, J. F. Scandium Coordination in Solid Oxides and Stabilized Zirconia: ^{45}Sc NMR. *Chem. Mater.* **2006**, *18* (16), 3855–3859.

(94) Heinzmann, R.; Issac, I.; Eufinger, J.-P.; Ulbrich, G.; Lerch, M.; Janek, J.; Indris, S. Observing Local Oxygen Interstitial Diffusion in Donor-Doped Ceria by ^{17}O NMR Relaxometry. *J. Phys. Chem. C* **2016**, *120* (16), 8568–8577.

(95) Cromer, D. T. The Crystal Structure of Monoclinic Sm_2O_3. *J. Phys. Chem.* **1957**, *61* (6), 753–755.

(96) Momma, K.; Izumi, F. VESTA 3 for Three-Dimensional Visualization of Crystal, Volumetric and Morphology Data. *J. Appl. Crystallogr.* **2011**, *44* (6), 1272–1276.

(97) Meyer, G.; Morss, L. R. Synthesis of Lanthanide and Actinide Compounds. In *Topics in f-Element Chemistry*; Sinha, S. P., Ed.; Springer Science & Business Media: Dordrecht, 2012; Vol. 2.

(98) WoŁcyrz, M.; Kepinski, L. Rietveld Refinement of the Structure of CeOCl Formed in Pd/CeO_2 Catalyst: Notes on the Existence of a Stabilized Tetragonal Phase of La_2O_3 in LaPdO System. *J. Solid State Chem.*

1992, *99* (2), 409–413.

(99) Yakel, H. L. A Refinement of the Crystal Structure of Monoclinic Europium Sesquioxide. *Acta Crystallogr. Sect. B* **1979**, *35* (3), 564–569.

(100) Coelho, A. A. Indexing of Powder Diffraction Patterns by Iterative Use of Singular Value Decomposition. *J. Appl. Crystallogr.* **2003**, *36* (1), 86–95.

(101) Bielecki, A.; Burum, D. P. Temperature Dependence of ^{207}Pb MAS Spectra of Solid Lead Nitrate. An Accurate, Sensitive Thermometer for Variable-Temperature MAS. *J. Magn. Reson. Ser. A* **1995**, *116*, 215–220.

(102) Thurber, K. R.; Tycko, R. Measurement of Sample Temperatures under Magic-Angle Spinning from the Chemical Shift and Spin-Lattice Relaxation Rate of ^{79}Br in KBr Powder. *J. Magn. Reson.* **2009**, *196* (1), 84–87.

(103) Hung, I.; Zhou, L.; Pourpoint, F.; Grey, C. P.; Gan, Z. Isotropic High Field NMR Spectra of Li-Ion Battery Materials with Anisotropy >1 MHz. *J. Am. Chem. Soc.* **2012**, *134* (4), 1898–1901.

(104) Oldfield, E.; Coretsopoulos, C.; Yang, S.; Reven, L.; Lee, H. C.; Shore, J.; Han, O. H.; Ramli, E.; Hinks, D. ^{17}O Nuclear-Magnetic-Resonance Spectroscopic Study of High-Tc Superconductors. *Phys. Rev. B* **1989**, *40* (10), 6832–6849.

(105) Massiot, D.; Fayon, F.; Capron, M.; King, I.; Le Calvé, S.; Alonso, B.; Durand, J.-O.; Bujoli, B.; Gan, Z.; Hoatson, G. Modelling One- and Two-Dimensional Solid-State NMR Spectra. *Magn. Reson. Chem.* **2002**, *40* (1), 70–76.

(106) Kentgens, A. P. M. A Practical Guide to Solid-State NMR of Half-Integer Quadrupolar Nuclei with Some Applications to Disordered Systems. *Geoderma* **1997**, *80* (3–4), 271–306.

(107) Florian, P.; Massiot, D.; Humbert, G.; Coutures, J. P. Etude Par RMN de ^{17}O et ^{89}Y Des Formes C et B de l'oxyde d'Yttrium Y_2O_3. *Comptes Rendus Académie des Sciences - Serie II*. 1995, pp 99–104.

(108) Profeta, M.; Benoit, M.; Mauri, F.; Pickard, C. J. First-Principles Calculation of the ^{17}O NMR Parameters in Ca Oxide and Ca Aluminosilicates: The Partially Covalent Nature of the Ca−O Bond, a Challenge for Density Functional Theory. *J. Am. Chem. Soc.* **2004**, *126* (39), 12628–12635.

(109) White, J. A.; Van Vleck, J. H. Sign of Knight Shift in Samarium Intermetallic Compounds. *Phys. Rev. Lett.* **1961**, *6* (8), 412–413.

(110) Grey, C. P.; Cheetham, A. K.; Dobson, C. M. Temperature-Dependent Solid-State ^{119}Sn MAS NMR of $Nd_2Sn_2O_7$, $Sm_2Sn_2O_7$, and $Y_{1.8}Sm_{0.2}Sn_2O_7$. Three Sensitive Chemical-Shift Thermometers. *J. Magn. Reson. Ser. A* **1993**, *101* (3), 299–306.

(111) Gruber, J. B.; Leavitt, R. P.; Morrison, C. A.; Chang, N. C. Optical Spectra, Energy Levels, and Crystal-field Analysis of Tripositive Rare-earth Ions in Y_2O_3 . IV. C_{3i} Sites. *J. Chem. Phys.* **1985**, *82* (12), 5373–5378.

(112) Chang, N. C.; Gruber, J. B.; Leavitt, R. P.; Morrison, C. A. Optical Spectra, Energy Levels, and Crystal-field Analysis of Tripositive Rare Earth Ions in Y_2O_3. I. Kramers Ions in C_2 Sites. *J. Chem. Phys.* **1982**, *76* (8), 3877–3889.

(113) Shannon, R. D. Revised Effective Ionic Radii and Systematic Studies of Interatomic Distances in Halides and Chalcogenides. *Acta Crystallogr. Sect. A* **1976**, *32* (5), 751–767.

(114) Fuda, K.; Kishio, K.; Yamauchi, S.; Fueki, K. Study on Vacancy Motion in Y_2O_3-Doped CeO_2 by ^{17}O NMR Technique. *J. Phys. Chem. Solids* **1985**, *46* (10), 1141–1146.

(115) Manning, P. S.; Sirman, J. D.; Kilner, J. A. Oxygen Self-Diffusion and Surface Exchange Studies of Oxide Electrolytes Having the Fluorite Structure. *Solid State Ionics* **1996**, *93* (1–2), 125–132.

(116) Kim, N.; Hsieh, C.; Huang, H.; Prinz, F.; Stebbins, J. High Temperature ^{17}O MAS NMR Study of Calcia, Magnesia, Scandia and Yttria Stabilized Zirconia. *Solid State Ionics* **2007**, *178* (27–28), 1499–1506.

(117) Adler, S. B.; Smith, J. W. Effects of Long-Range Forces on Oxygen Transport in Yttria-Doped Ceria: Simulation and Theory. *J. Chem. Soc. Faraday Trans.* **1993**, *89* (16), 3123–3128.

(118) Fernández-García, M.; Rodriguez, J. A. Metal Oxide Nanoparticles. In *Encyclopedia of Inorganic and Bioinorganic Chemistry*; John Wiley & Sons, 2011.

(119) Ren, Y.; Liu, Z.; Pourpoint, F.; Armstrong, A. R.; Grey, C. P.; Bruce, P. G. Nanoparticulate TiO_2(B): An Anode for Lithium-Ion Batteries. *Angew. Chemie Int. Ed.* **2012**, *51* (9), 2164–2167.

(120) Poizot, P.; Laruelle, S.; Grugeon, S.; Dupont, L.; Tarascon, J.-M. Nano-Sized Transition-Metal Oxides as Negative-Electrode Materials for Lithium-Ion Batteries. *Nature* **2000**, *407* (6803), 496–499.

(121) Chen, M. S.; Goodman, D. W. The Structure of Catalytically Active Gold on Titania. *Science* **2004**, *306* (5694), 252–255.

(122) Fu, Q.; Saltsburg, H.; Flytzani-Stephanopoulos, M. Active Nonmetallic Au and Pt Species on Ceria-Based Water-Gas Shift Catalysts. *Science* **2003**, *301* (5635), 935–938.

(123) Peng, L.; Liu, Y.; Kim, N.; Readman, J. E.; Grey, C. P. Detection of Brønsted Acid Sites in Zeolite HY with High-Field ^{17}O-MAS-NMR Techniques. *Nat. Mater.* **2005**, *4* (3), 216–219.

(124) Scolan, E.; Magnenet, C.; Massiot, D.; Sanchez, C. Surface and Bulk Characterisation of Titanium–Oxo Clusters and Nanosized Titania Particles through ^{17}O Solid State NMR. *J. Mater. Chem.* **1999**, *9* (10), 2467–2474.

(125) Wang, M.; Wu, X.-P.; Zheng, S.; Zhao, L.; Li, L.; Shen, L.; Gao, Y.; Xue, N.; Guo, X.; Huang, W.; Gan, Z.; Blanc, F.; Yu, Z.; Ke, X.; Ding, W.; Gong, X.-Q.; Grey, C. P.; Peng, L. Identification of Different Oxygen Species in Oxide Nanostructures with ^{17}O Solid-State NMR Spectroscopy. *Sci. Adv.* **2015**, *1* (1).

(126) Ni, Q. Z.; Daviso, E.; Can, T. V; Markhasin, E.; Jawla, S. K.; Swager, T. M.; Temkin, R. J.; Herzfeld, J.; Griffin, R. G. High Frequency Dynamic Nuclear Polarization. *Acc. Chem. Res.* **2013**, *46* (9), 1933–1941.

(127) Perras, F. A.; Chaudhary, U.; Slowing, I. I.; Pruski, M. Probing Surface Hydrogen Bonding and Dynamics by Natural Abundance, Multidimensional, ^{17}O DNP-NMR Spectroscopy. *J. Phys. Chem. C* **2016**, *120* (21), 11535–11544.

(128) Vitzthum, V.; Miéville, P.; Carnevale, D.; Caporini, M. a.; Gajan, D.; Copéret, C.; Lelli, M.; Zagdoun, A.; Rossini, A. J.; Lesage, A.; Emsley, L.; Bodenhausen, G. Dynamic Nuclear Polarization of Quadrupolar Nuclei Using Cross Polarization from Protons: Surface-Enhanced Aluminium-27 NMR. *Chem. Commun.* **2012**, *48* (14), 1988.

(129) Lund, A.; Hsieh, M.-F.; Siaw, T.-A.; Han, S.-I. Direct Dynamic Nuclear Polarization Targeting Catalytically Active ^{27}Al Sites. *Phys. Chem. Chem. Phys.* **2015**, *17* (38), 25449–25454.

(130) Blanc, F.; Sperrin, L.; Jefferson, D. A.; Pawsey, S.; Rosay, M.; Grey, C. P. Dynamic Nuclear Polarization Enhanced Natural Abundance ^{17}O Spectroscopy. *J. Am. Chem. Soc.* **2013**, *135* (8), 2975–2978.

(131) Li, W.; Wang, Q.; Xu, J.; Aussenac, F.; Qi, G.; Zhao, X.; Gao, P.; Wang, C.; Deng, F. Probing the Surface of γ-Al_2O_3 by Oxygen-17 Dynamic Nuclear Polarization Enhanced Solid-State NMR Spectroscopy. *Phys. Chem. Chem. Phys.* **2018**, *20* (25), 17218–17225.

(132) Perras, F. A.; Boteju, K. C.; Slowing, I. I.; Sadow, A. D.; Pruski, M. Direct ^{17}O Dynamic Nuclear Polarization of Single-Site Heterogeneous Catalysts. *Chem. Commun.* **2018**, *54* (28), 3472–3475.

(133) Champouret, Y.; Coppel, Y.; Kahn, M. L. Evidence for Core Oxygen Dynamics and Exchange in Metal Oxide Nanocrystals from In Situ ^{17}O MAS NMR. *J. Am. Chem. Soc.* **2016**, *138* (50), 16322–16328.

(134) Thakur, R. S.; Kurur, N. D.; Madhu, P. K. Swept-Frequency Two-Pulse Phase Modulation for Heteronuclear Dipolar Decoupling in Solid-State NMR. *Chem. Phys. Lett.* **2006**, *426* (4), 459–463.

(135) Paul, S.; Kurur, N. D.; Madhu, P. K. On the Choice of Heteronuclear Dipolar Decoupling Scheme in Solid-State NMR. *J. Magn. Reson.* **2010**, *207* (1), 140–148.

(136) Thurber, K. R.; Tycko, R. Theory for Cross Effect Dynamic Nuclear Polarization under Magic-Angle Spinning in Solid State Nuclear Magnetic Resonance: The Importance of Level Crossings. *J. Chem. Phys.* **2012**, *137* (8), 084508.

(137) Perras, F. A.; Kobayashi, T.; Pruski, M. Natural Abundance O-17 DNP Two-Dimensional and Surface-Enhanced NMR Spectroscopy. *J. Am. Chem. Soc.* **2015**, *137* (26), 8336–8339.

(138) Holmes, L.; Peng, L.; Heinmaa, I.; O'Dell, L. A.; Smith, M. E.; Vannier, R.-N.; Grey, C. P. Variable-Temperature ^{17}O NMR Study of Oxygen Motion in the Anionic Conductor $Bi_{26}Mo_{10}O_{69}$. *Chem. Mater.* **2008**, *20* (11), 3638–3648.

(139) Dutta, P.; Pal, S.; Seehra, M. S.; Shi, Y.; Eyring, E. M.; Ernst, R. D. Concentration of Ce^{3+} and Oxygen Vacancies in Cerium Oxide Nanoparticles. *Chem. Mater.* **2006**, *18* (21), 5144–5146.

(140) Lee, D.; Hediger, S.; De Paëpe, G. Is Solid-State NMR Enhanced by Dynamic Nuclear Polarization? *Solid State Nucl. Magn. Reson.* **2015**, *66*, 6–20.

(141) Amoureux, J. P.; Pruski, M. Theoretical and Experimental Assessment of Single- and Multiple-Quantum Cross-Polarization in Solid State NMR. *Mol. Phys.* **2002**, *100* (10), 1595–1613.

(142) Laachir, A.; Perrichon, V.; Badri, A.; Lamotte, J.; Catherine, E.; Lavalley, J. C.; El Fallah, J.; Hilaire, L.; Le Normand, F.; Quéméré, E.; Sauvion, G. N.; Touret, O. Reduction of CeO_2 by Hydrogen. Magnetic Susceptibility and Fourier-Transform Infrared, Ultraviolet and X-Ray Photoelectron Spectroscopy Measurements. *J. Chem. Soc., Faraday Trans.* **1991**, *87* (10), 1601–1609.

(143) Bugnet, M.; Overbury, S. H.; Wu, Z. L.; Epicier, T. Direct Visualization and Control of Atomic Mobility at {100} Surfaces of Ceria in the Environmental Transmission Electron Microscope. *Nano Lett.* **2017**, *17* (12), 7652–7658.

(144) Wolf, T.; Kumar, S.; Singh, H.; Chakrabarty, T.; Aussenac, F.; Frenkel, A. I.; Major, D. T.; Leskes, M. Endogenous Dynamic Nuclear Polarization for Natural Abundance ^{17}O and Lithium NMR in the Bulk of Inorganic Solids. *J. Am. Chem. Soc.* **2018**, *141*, 451–462.

(145) de Biasi, R. S.; Grillo, M. L. N. Measurement of Small Concentrations of Gadolinium in Ceria (CeO_2) and Magnesia (MgO) Using Electron Magnetic Resonance. *J. Am. Ceram. Soc.* **2008**, *91* (10), 3469–3471.

(146) Borel, A.; Kang, H.; Gateau, C.; Mazzanti, M.; Clarkson, R. B.; Linn Belford, R. Variable Temperature and EPR Frequency Study of Two Aqueous Gd(III) Complexes with Unprecedented Sharp Lines. *J. Phys. Chem. A* **2006**, *110* (45), 12434–12438.

(147) Grieshammer, S.; Grope, B. O. H.; Koettgen, J.; Martin, M. A Combined DFT + U and Monte Carlo Study on Rare Earth Doped Ceria. *Phys. Chem. Chem. Phys.* **2014**, *16* (21), 9974.

(148) Corzilius, B. Theory of Solid Effect and Cross Effect Dynamic Nuclear Polarization with Half-Integer High-Spin Metal Polarizing Agents in Rotating Solids. *Phys. Chem. Chem. Phys.* **2016**, *18* (39), 27190–27204.

(149) Kaushik, M.; Bahrenberg, T.; Can, T. V.; Caporini, M. A.; Silvers, R.; Heiliger, J.; Smith, A. A.; Schwalbe, H.; Griffin, R. G.; Corzilius, B. Gd(III) and Mn(II) Complexes for Dynamic Nuclear Polarization: Small Molecular Chelate Polarizing Agents and Applications with Site-Directed Spin Labeling of Proteins. *Phys. Chem. Chem. Phys.* **2016**, *18* (39), 27205–27218.

(150) Venkataswamy, P.; Rao, K. N.; Jampaiah, D.; Reddy, B. M. Nanostructured Manganese Doped Ceria Solid Solutions for CO Oxidation at Lower Temperatures. *Appl. Catal. B Environ.* **2015**, *162*, 122–132.

(151) Goodenough, J. B. The Two Components of the Crystallographic Transition in VO_2. *J. Solid State Chem.* **1971**, *3* (4), 490–500.

(152) Rice, T. M.; Launois, H.; Pouget, J. P. Comment on "VO_2: Peierls or Mott-Hubbard? A View from Band Theory." *Phys. Rev. Lett.* **1994**, *73* (22), 3042–3042.

(153) Khomskii, D. I. *Transition Metal Compounds*; Cambridge University Press: Cambridge, 2014.

(154) Nakano, M.; Shibuya, K.; Okuyama, D.; Hatano, T.; Ono, S.; Kawasaki, M.; Iwasa, Y.; Tokura, Y. Collective Bulk Carrier Delocalization Driven by Electrostatic Surface Charge Accumulation. *Nature* **2012**, *487* (7408), 459–462.

(155) Chen, S.; Wang, X. J.; Fan, L.; Liao, G.; Chen, Y.; Chu, W.; Song, L.; Jiang, J.; Zou, C. The Dynamic Phase Transition Modulation of Ion-Liquid Gating VO_2 Thin Film: Formation, Diffusion, and Recovery of Oxygen Vacancies. *Adv. Funct. Mater.* **2016**, *26* (20), 3532–3541.

(156) Gupta, S. N.; Pal, A.; Muthu, D. V. S.; Anil Kumar, P. S.; Sood, A. K. Metallic Monoclinic Phase in VO_2 Induced by Electrochemical Gating: In Situ Raman Study. *EPL* **2016**, *115* (17001).

(157) Jeong, J.; Aetukuri, N. B.; Passarello, D.; Conradson, S. D.; Samant, M. G.; Parkin, S. S. P. Giant Reversible, Facet-Dependent, Structural Changes in a Correlated-Electron Insulator Induced by Ionic Liquid Gating. *Proc. Natl. Acad. Sci.* **2015**, *112* (4), 1013–1018.

(158) Passarello, D.; Altendorf, S. G.; Jeong, J.; Rettner, C.; Arellano, N.; Topuria, T.; Samant, M. G.; Parkin, S. S. P. Evidence for Ionic Liquid Gate-Induced Metallization of Vanadium Dioxide Bars over Micron Length Scales. *Nano Lett.* **2017**, *17* (5), 2796–2801.

(159) Dahlman, C. J.; LeBlanc, G.; Bergerud, A.; Staller, C.; Adair, J.; Milliron, D. J. Electrochemically Induced Transformations of Vanadium Dioxide Nanocrystals. *Nano Lett.* **2016**, *16* (10), 6021–6027.

(160) Singh, S.; Abtew, T. A.; Horrocks, G.; Kilcoyne, C.; Marley, P. M.; Stabile, A. A.; Banerjee, S.; Zhang, P.; Sambandamurthy, G. Selective Electrochemical Reactivity of Rutile VO_2 towards the Suppression of Metal-Insulator Transition. *Phys. Rev. B* **2016**, *93* (12), 1–8.

(161) Altendorf, S. G.; Jeong, J.; Passarello, D.; Aetukuri, N. B.; Samant, M. G.; Parkin, S. S. P. Facet-Independent Electric-Field-Induced Volume Metallization of Tungsten Trioxide Films. *Adv. Mater.* **2016**, *28* (26), 5284–5292.

(162) Cui, B.; Werner, P.; Ma, T.; Zhong, X.; Wang, Z.; Taylor, J. M.; Zhuang, Y.; Parkin, S. S. P. Direct Imaging of Structural Changes Induced by Ionic Liquid Gating Leading to Engineered Three-Dimensional Meso-Structures. *Nat. Commun.* **2018**, *9*, 3055.

(163) Shibuya, K.; Sawa, A. Modulation of Metal-Insulator Transition in VO_2 by Electrolyte Gating-Induced Protonation. *Adv. Electron. Mater.* **2016**, *2*, 1500131.

(164) Katase, T.; Endo, K.; Tohei, T.; Ikuhara, Y.; Ohta, H. Room-Temperature-Protonation-Driven On-Demand Metal-Insulator Conversion of a Transition Metal Oxide. *Adv. Electron. Mater.* **2015**, *1*, 1500063.

(165) Sasaki, T.; Ueda, H.; Kanki, T.; Tanaka, H. Electrochemical Gating-Induced Reversible and Drastic Resistance Switching in VO_2 Nanowires. *Sci. Rep.* **2015**, *5*, 17080.

(166) Chen, Y.; Wang, Z.; Chen, S.; Ren, H.; Wang, L.; Zhang, G.; Lu, Y.; Jiang, J.; Zou, C.; Luo, Y. Non-Catalytic Hydrogenation of VO_2 in Acid Solution. *Nat. Commun.* **2018**, *9* (1), 818.

(167) Yoon, H.; Choi, M.; Lim, T.-W.; Kwon, H.; Ihm, K.; Kim, J. K.; Choi, S.-Y.; Son, J. Reversible Phase Modulation and Hydrogen Storage in Multivalent VO_2 Epitaxial Thin Films. *Nat. Mater.* **2016**, *15* (10), 1113–1119.

(168) Wei, J.; Ji, H.; Guo, W.; Nevidomskyy, A. H.; Natelson, D. Hydrogen Stabilization of Metallic Vanadium Dioxide in Single-Crystal Nanobeams. *Nat. Nanotechnol.* **2012**, *7* (6), 357–362.

(169) Chippindale, A. M.; Dickens, P. G.; Powell, A. V. Synthesis, Characterization, and Inelastic Neutron Scattering Study of Hydrogen Insertion Compounds of VO_2(Rutile). *J. Solid State Chem.* **1991**, *93* (2), 526–533.

(170) Filinchuk, Y.; Tumanov, N. A.; Ban, V.; Ji, H.; Wei, J.; Swift, M. W.; Nevidomskyy, A. H.; Natelson, D. In Situ Diffraction Study of Catalytic Hydrogenation of VO_2 : Stable Phases and Origins of Metallicity. *J. Am. Chem. Soc.* **2014**, *136* (22), 8100–8109.

(171) Lynch, G. .; Segel, S. .; Sayer, M. Nuclear Magnetic Resonance Study of Polycrystalline VO_2. *J. Magn. Reson.* **1974**, *15* (1), 8–18.

(172) *Gmelins Handbuch Der Anorganischen Chemie, Vanadium, Vol: B1*, 8th ed.; Chemie gmbh weinheim/bergstr, 1967.

(173) Rice, C. E.; Robinson, W. R. Structural Changes in the Solid Solution $(Ti_{1-x}V_x)_2O_3$ as x Varies from Zero to One. *J. Solid State Chem.* **1977**, *21* (2), 145–154.

(174) Rogers, K. D. An X-Ray Diffraction Study of Semiconductor and Metallic Vanadium Dioxide. *Powder Diffr.* **1993**, *8* (4), 240–244.

(175) Ghedira, M.; Vincent, H.; Marezio, M.; Launay, J. C. Structural Aspects of the Metal-Insulator Transitions in $V_{0.985}Al_{0.015}O_2$. *J. Solid State Chem.* **1977**, *22* (4), 423–438.

(176) Bachmann, H.G.; Ahmed, F.R.; Barnes, W. H. The Crystal Structure of Vanadium Pentoxide. *Zeitschrift fuer Krist. Krist. Krist. Krist.* **1961**, *115*, 110–131.

(177) Schneider, C. A.; Rasband, W. S.; Eliceiri, K. W. NIH Image to ImageJ: 25 Years of Image Analysis. *Nat. Methods* **2012**, *9* (7), 671.

(178) Pecher, O.; Halat, D. M.; Lee, J.; Liu, Z.; Griffith, K. J.; Braun, M.; Grey, C. P. Enhanced Efficiency of Solid-State NMR Investigations of Energy Materials Using an External Automatic Tuning/Matching (EATM) Robot. *J. Magn. Reson.* **2017**, *275*, 127–136.

(179) Robin Bendall, M.; Gordon, R. E. Depth and Refocusing Pulses Designed for Multipulse NMR with Surface Coils. *J. Magn. Reson.* **1983**, *53* (3), 365–385.

(180) De Souza, A. C.; Pires, A. T. N.; Soldi, V. Thermal Stability of Ferrocene Derivatives and Ferrocene-Containing Polyamides. *J. Therm. Anal. Calorim.* **2002**, *70* (2), 405–414.

(181) Bizzarri, C.; Conte, V.; Floris, B.; Galloni, P. Solvent Effects of Ionic Liquids: Investigation of Ferrocenes as Electrochemical Probes. *J. Phys. Org. Chem.* **2011**, *24* (4), 327–334.

(182) Matsumiya, M.; Terazono, M.; Tokuraku, K. Temperature Dependence of Kinetics and Diffusion Coefficients for Ferrocene/Ferricenium in Ammonium-Imide Ionic Liquids. *Electrochim. Acta* **2006**, *51* (7), 1178–1183.

(183) Liebsch, A.; Ishida, H.; Bihlmayer, G. Coulomb Correlations and Orbital Polarization in the Metal-Insulator Transition of VO_2. *Phys. Rev. B* **2005**, *71* (8), 085109.

(184) Eyert, V. VO_2: A Novel View from Band Theory. *Phys. Rev. Lett.* **2011**, *107* (1), 2–5.

(185) Brito, W. H.; Aguiar, M. C. O.; Haule, K.; Kotliar, G. Metal-Insulator Transition in VO_2: A DFT + DMFT Perspective. *Phys. Rev. Lett.* **2016**, *117* (5), 056402.

(186) Clark, S. J.; Segall, M. D.; Pickard, C. J.; Hasnip, P. J.; Probert, M. J.; Refson, K.; Payne, M. C. First Principles Methods Using {CASTEP}. *Z. Krist.* **2005**, *220*, 567–570.

(187) Pickard, C. J.; Mauri, F. All-Electron Magnetic Response with Pseudopotentials: {NMR} Chemical Shifts. *Phys. Rev. B* **2001**, *63*, 245101.

(188) Yates, J. R.; Pickard, C. J.; Mauri, F. Calculation of NMR Chemical Shifts for Extended Systems Using Ultrasoft Pseudopotentials. *Phys. Rev. B* **2007**, *76*, 24401.

(189) Profeta, M.; Mauri, F.; Pickard, C. J. Accurate First Principles Prediction of ^{17}O NMR Parameters in SiO_2 : Assignment of the Zeolite Ferrierite Spectrum. *J. Am. Chem. Soc.* **2003**, *125* (2), 541–548.

(190) Perdew, J. P.; Burke, K.; Ernzerhof, M. Generalized Gradient Approximation Made Simple. *Phys. Rev. Lett.* **1996**, *77* (18), 3865–3868.

(191) Geller, S.; Romo, P.; Remeika, J. P. Refinement of the Structure of Scandium Sesquioxide. *Zeitschrift für Krist. Mater.* **1967**, *124* (1–6), 136–142.

(192) Restori, R.; Schwarzenbach, D.; Schneider, J. R. Charge Density in Rutile, TiO_2. *Acta Crystallogr. Sect. B Struct. Sci.* **1987**, *43* (3), 251–257.

(193) Longo, J. M.; P, K. A Refinement of the Structure of VO_2. *Acta Chem. Scand.* **1970**, *24* (2), 420.

(194) Bonhomme, C.; Gervais, C.; Babonneau Florenceand Coelho, C.; Pourpoint, F.; Azais, T.; Ashbrook, S. E.; Griffin, J. M.; Yates, J. R.; Mauri, F.; Pickard, C. J. First-Principles Calculation of NMR Parameters Using the Gauge Including Projector Augmented Wave Method: A Chemist's Point of View. *Chem. Rev.* **2012**, *112*, 5733.

(195) Umeda, J. J.; Kusumoto, H.; Narita, K.; Yamada, E. Nuclear Magnetic Resonance in Polycrystalline VO_2. *J. Chem. Phys.* **1965**, *42* (1965), 1458.

(196) Meng, Y.; Aldous, L.; Belding, S. R.; Compton, R. G. The Hydrogen Evolution Reaction in a Room Temperature Ionic Liquid: Mechanism and Electrocatalyst Trends. *Phys. Chem. Chem. Phys.* **2012**, *14* (15), 5222.

(197) DeVos, N.; Maton, C.; Stevens, C. V. Electrochemical Stability of Ionic Liquids: General Influences and Degradation Mechanisms. *ChemElectroChem* **2014**, *1* (8), 1258–1270.

(198) Mydosh, J. A. *Spin Glasses: An Experimental Introduction*; Taylor & Francis: London, 1993.

(199) Qazilbash, M. M.; Brehm, M.; Chae, B.-G.; Ho, P.-C.; Andreev, G. O.; Kim, B.-J.; Yun, S. J.; Balatsky, A. V; Maple, M. B.; Keilmann, F.; Kim, H.-T.; Basov, D. N. Mott Transition in VO_2 Revealed by Infrared Spectroscopy and Nano-Imaging. *Science* **2007**, *318* (5857), 1750–1753.

(200) Mousavi, M. P. S.; Dittmer, A. J.; Wilson, B. E.; Hu, J.; Stein, A.; Bühlmann, P. Unbiased Quantification of the Electrochemical Stability Limits of Electrolytes and Ionic Liquids. *J. Electrochem. Soc.* **2015**, *162* (12), A2250–A2258.

(201) Krannich, M.; Heym, F.; Jess, A. Characterization of Six Hygroscopic Ionic Liquids with Regard to Their Suitability for Gas Dehydration: Density, Viscosity, Thermal and Oxidative Stability, Vapor Pressure, Diffusion Coefficient, and Activity Coefficient of Water. *J. Chem. Eng. Data* **2016**, *61* (3), 1162–1176.

(202) Hollóczki, O.; Gerhard, D.; Massone, K.; Szarvas, L.; Németh, B.; Veszprémi, T.; Nyulászi, L. Carbenes in Ionic Liquids. *New J. Chem.* **2010**, *34* (12), 3004.

(203) Kim, G.; Blanc, F.; Hu, Y. Y.; Grey, C. P. Understanding the Conduction Mechanism of the Protonic Conductor CsH_2PO_4 by Solid-State NMR Spectroscopy. *J. Phys. Chem. C* **2013**, *117* (13), 6504–6515.

(204) Blinc, R.; Hadži, D. Deuteron Quadrupole Coupling and Hydrogen Bonding in Crystals. *Nature* **1966**, *212* (5068), 1307–1309.

(205) Saptal, V. B.; Bhanage, B. M. N-Heterocyclic Olefins as Robust Organocatalyst for the Chemical Conversion of Carbon Dioxide to Value-Added Chemicals. *ChemSusChem* **2016**, *9* (15), 1980–1985.

(206) Lu, N.; Zhang, P.; Zhang, Q.; Qiao, R.; He, Q.; Li, H.-B.; Wang, Y.; Guo, J.; Zhang, D.; Duan, Z.; Li, Z.; Wang, M.; Yang, S.; Yan, M.; Arenholz, E.; Zhou, S.; Yang, W.; Gu, L.; Nan, C.-W.; Wu, J.; Tokura, Y.; Yu, P. Electric-Field Control of Tri-State Phase Transformation with a Selective Dual-Ion Switch. *Nature* **2017**, *546* (7656), 124–128.

(207) Yamakawa, N.; Jiang, M.; Grey, C. P. Investigation of the Conversion Reaction Mechanisms for Binary Copper(II) Compounds by Solid-State NMR Spectroscopy and X-Ray Diffraction. *Chem. Mater.* **2009**, *21* (14), 3162–3176.

(208) Yang, S. M.; Lee, S.; Jian, J.; Zhang, W.; Lu, P.; Jia, Q.; Wang, H.; Won Noh, T.; Kalinin, S. V.; MacManus-Driscoll, J. L. Strongly Enhanced Oxygen Ion Transport through Samarium-Doped CeO_2 Nanopillars in Nanocomposite Films. *Nat. Commun.* **2015**, *6*, 1–8.

(209) Dervişoğlu, R.; Middlemiss, D. S.; Blanc, F.; Lee, Y.-L.; Morgan, D.; Grey, C. P. Joint Experimental and Computational ^{17}O and ^{1}H Solid State NMR Study of $Ba_2In_2O_4(OH)_2$ Structure and Dynamics. *Chem. Mater.* **2015**, *27* (11), 3861–3873.

(210) Dovesi, R.; Erba, A.; Orlando, R.; Zicovich-Wilson, C. M.; Civalleri, B.; Maschio, L.; Rérat, M.; Casassa, S.; Baima, J.; Salustro, S.; Kirtman, B. Quantum-Mechanical Condensed Matter Simulations with CRYSTAL. *Wiley Interdiscip. Rev. Comput. Mol. Sci.* **2018**, *8* (4), e1360.

(211) Desmarais, J. K.; Erba, A.; Dovesi, R. Generalization of the Periodic LCAO Approach in the CRYSTAL Code to G-Type Orbitals. *Theor. Chem. Acc.* **2018**, *137* (2), 28.

(212) El-Kelany, K. E.; Ravoux, C.; Desmarais, J. K.; Cortona, P.; Pan, Y.; Tse, J. S.; Erba, A. Spin Localization, Magnetic Ordering, and Electronic Properties of Strongly Correlated Ln_2O_3 Sesquioxides (Ln=La, Ce, Pr, Nd). *Phys. Rev. B* **2018**, *97* (24), 245118.

(213) Casey, A. T. Theoretical Principles of Paramagnetism. In *Theory and Applications of Molecular Paramagnetism*; Boudreaux, E. A., Mulay, L. N., Eds.; John Wiley & Sons: New York, 1976; pp 27–66.

(214) Condon, E. U.; Shortley, G. H. *The Theory of Atomic Spectra*; Cambridge University Press: Cambridge, 1935.

Appendix A: XRD Data for Sm_2O_3, Eu_2O_3 and Sm/Eu-Substituted CeO_2

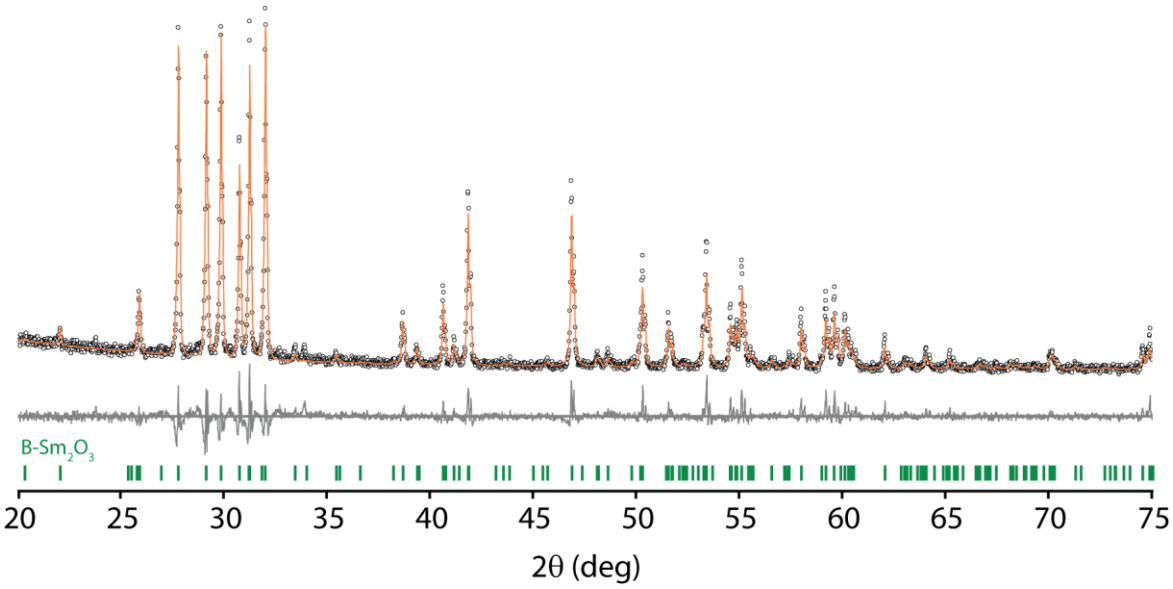

Figure A.1: XRD pattern and Rietveld refinement for monoclinic Sm_2O_3 (*C*2/*m*) after ^{17}O enrichment at 1200 °C.

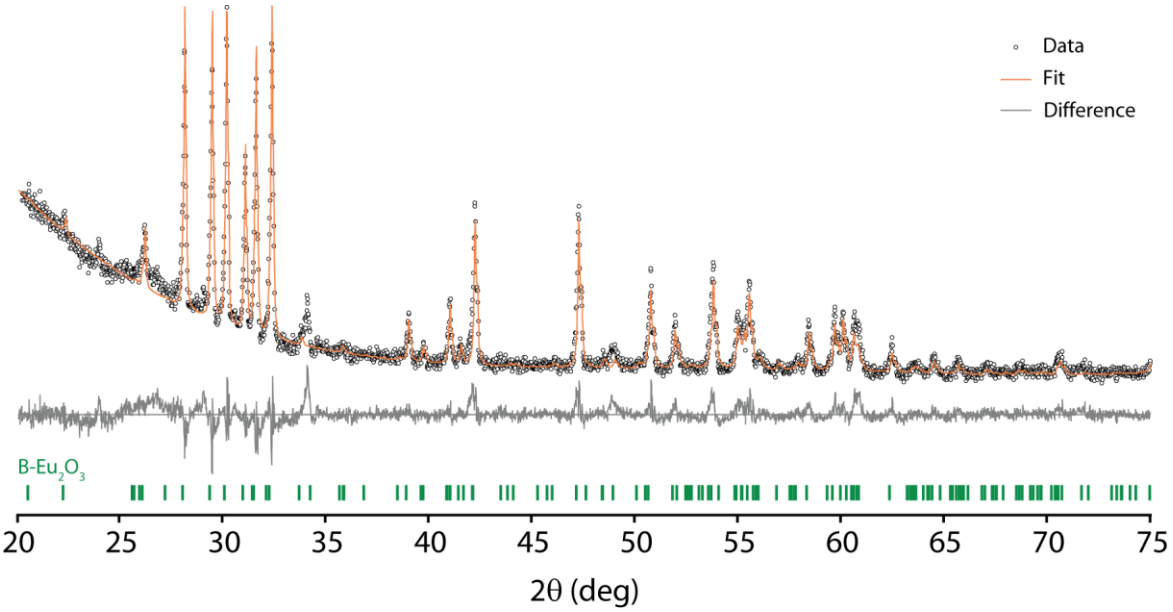

Figure A.2: XRD pattern and Rietveld refinement for monoclinic Eu_2O_3 (*C*2/*m*) after ^{17}O enrichment at 1200 °C.

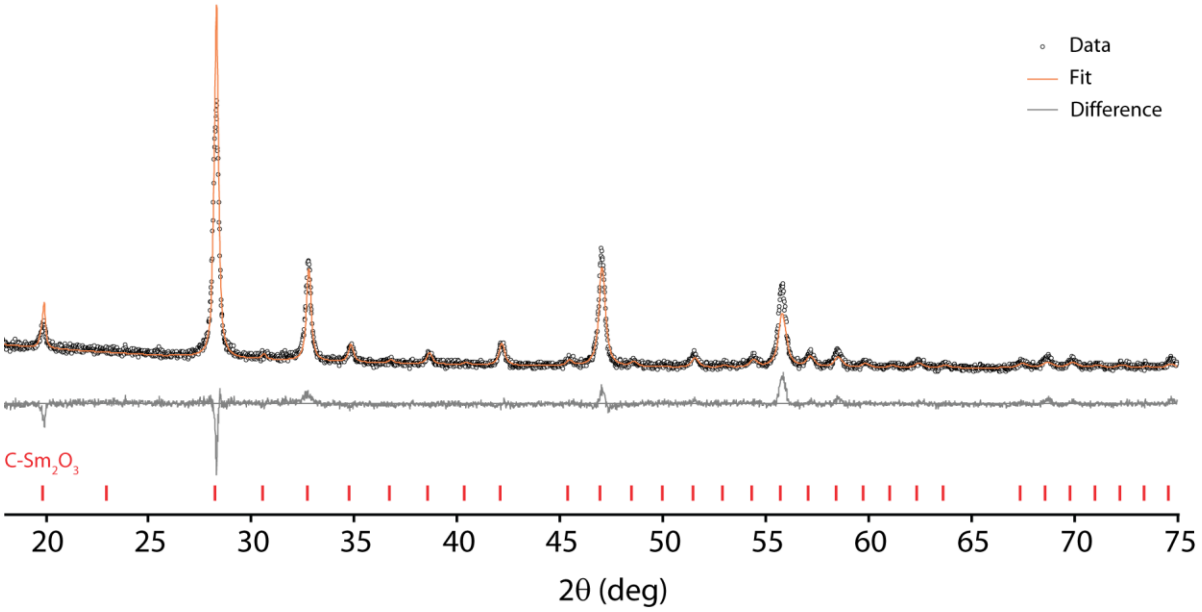

Figure A.3:XRD pattern and Rietveld refinement for cubic Sm_2O_3 ($Ia\bar{3}$) prepared by decomposing $Sm(OH)_3$ at 750 ºC followed by ^{17}O-enrichment at 750 ºC.

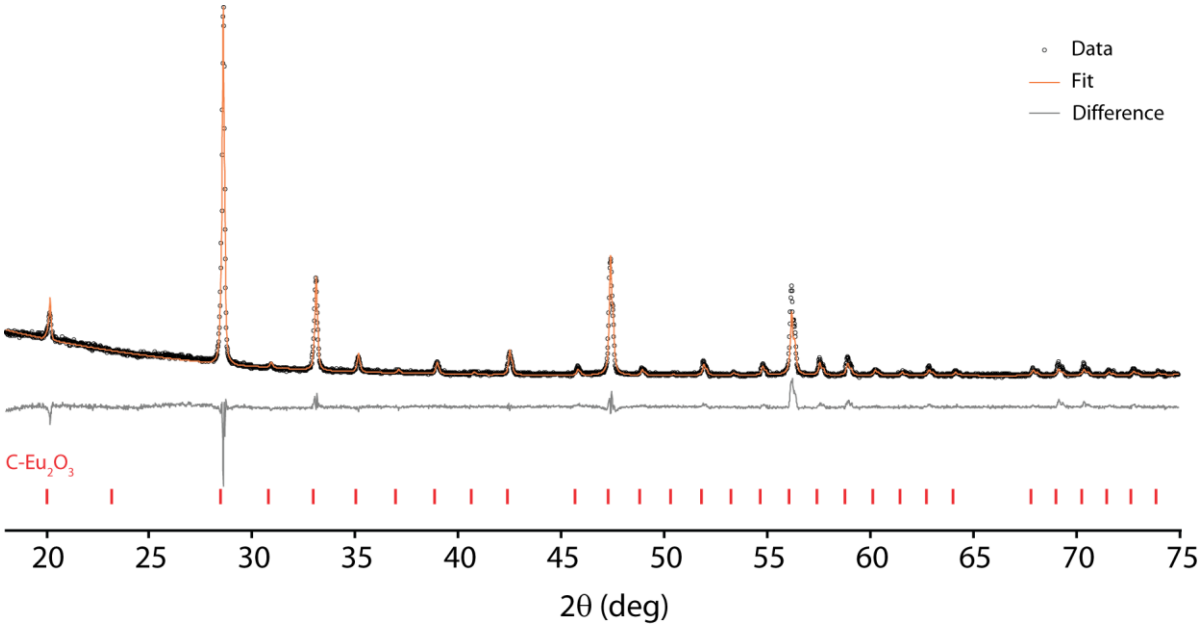

Figure A.4: XRD pattern and Rietveld refinement for cubic Eu_2O_3 ($Ia\bar{3}$) after ^{17}O enrichment at 1000 ºC.

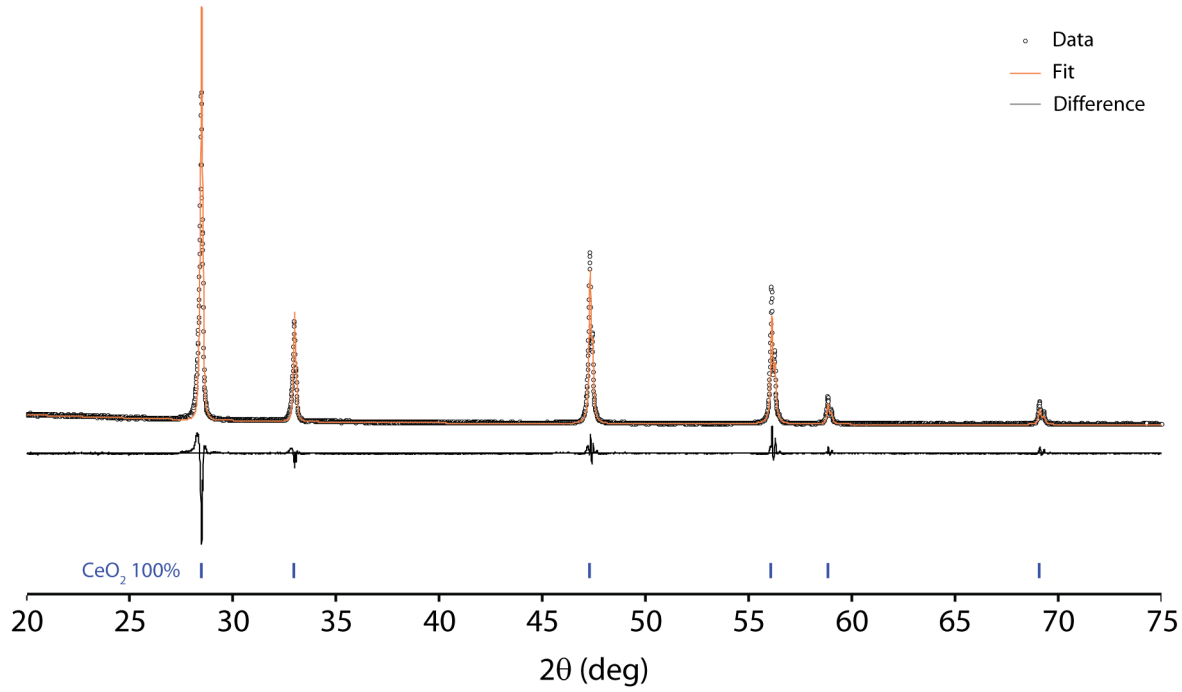

Figure A.5: XRD pattern and Rietveld refinement for 15 at% Sm-substituted CeO_2 ($Fm\bar{3}m$).

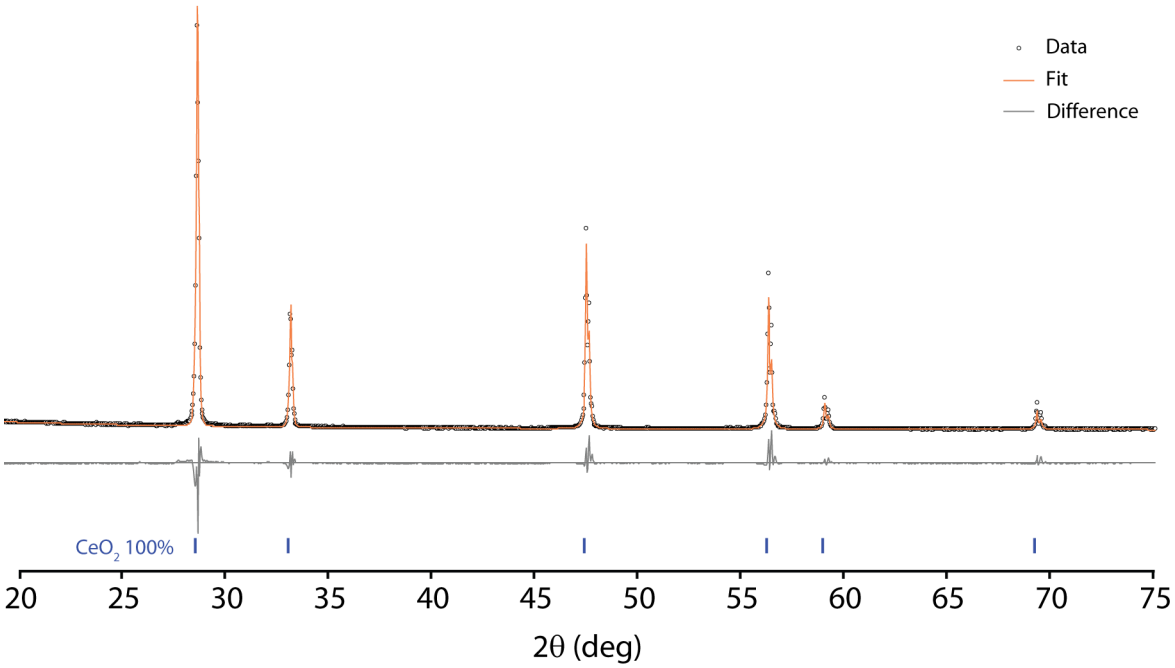

Figure A.6: XRD pattern and Rietveld refinement for 15 at% Eu-substituted CeO_2 ($Fm\bar{3}m$).

Appendix B: DFT Shift Calculations for Y_2O_3, Sm_2O_3 and Eu_2O_3

All the DFT calculations presented in this appendix were performed by Jae Lee, University of Cambridge.

The ^{17}O NMR parameters for the monoclinic Y_2O_3 phase (isostructural to monoclinic Sm_2O_3 and Eu_2O_3)[107] were calculated with the CASTEP code using a 700 eV energy cut-off and a <0.03 $Å^{-1}$ Monkhorst-Pack *k*-mesh sampling.[186–188] On-the-fly pseudopotentials with the PBE functional were used. The structure was fully relaxed using the CASTEP default convergence criteria and a 10^{-5} eV energy convergence limit. The calculated chemical shieldings were converted to chemical shifts using the previously determined relation $\delta_{iso} = 223.7 - 0.888\times\sigma_{iso}$.[209] The calculated chemical shifts and quadrupolar coupling constants (Table B.1) are in good agreement with the experimental values of Florian et al.,[107] with the exception that the experimental assignment of O2 and O4 appears to be incorrect and should be reversed; this assignment by Florian et al. was tentatively based on the trend in average Y–O bond length, as it was not possible to calculate chemical shifts at the time, so this minor error is not unexpected.

Table B.1: DFT-calculated ^{17}O chemical shifts and quadrupolar coupling constants of oxygen sites in monoclinic Y_2O_3. Experimental values are from Florian et al.[107]

Site	δ_{iso} (calc) /ppm	δ_{iso} (exp) /ppm	C_Q (calc) /MHz	C_Q (exp) /MHz	Coordination
O1	323.5	313	2.0	1.8	Square pyramidal (5)
O2	375.3	383	0.7	0.6	~Tetrahedral (4)
O3	356.0	346	1.0	1.2	Trigonal pyramidal (4)
O4	382.2	377	0.5	0.7	~Tetrahedral (4)
O5	255.5	242	0.9	0.8	~Octahedral (6)

Ab initio calculations of the hyperfine coupling constant and electric field gradient parameters for monoclinic Sm_2O_3 and Eu_2O_3 were calculated using the CRYSTAL code.[210] A standard B3LYP functional with 20% or 35% of the Hartree–Fock exchange component (termed 'Hyb20' and 'Hyb35', respectively) was used, as recently demonstrated for ^{17}O shift calculations of paramagnetic systems.[11] Experimental cell structures of Sm_2O_3 and Eu_2O_3 were fully relaxed using the CRYSTAL default criteria with a self-consistent field (SCF) cycle convergence of 10^{-7} Hartree. A Monkhorst-Pack *k*-mesh of 6×6×6 was used in all cases.

For the lanthanides, a combined core pseudopotential and Gaussian basis set developed by Erba *et al*. was used which treats the 4*f* levels as valence states.[211] In accordance with the previous study on Ln_2O_3 systems, the oxygen basis set developed by Towler *et al.* was used, with an integration grid consisting of 99 radial points and 1454 angular points.[212] This oxygen basis set was not specifically developed for hyperfine calculations, which need accurate treatment of the core states; more extended oxygen basis sets such as the IGLO-III set were attempted, but resulted in SCF instabilities, presumably arising from the 'mixing' of two basis sets with different qualities.

The computed values of C_Q for both phases show a reasonable agreement to the size predicted from structural arguments (and also from the nutation behaviour): for Sm_2O_3, O2, O4, and O5 all show small values of C_Q (0.67, 0.26, and 0.15 MHz, respectively) whereas O3 and O1 show larger values of 1.34 and 1.09 MHz, A similar result is observed for Eu_2O_3, although the calculated C_Q for O3 is arguably smaller than expected (as compared to Sm_2O_3). There are some differences in the predicted ordering of the hyperfine coupling constants A_{iso} for each site between Sm_2O_3 and Eu_2O_3, but for both the O2 and O4 sites are predicted to be the most paramagnetically shifted.

Table B.2: Lattice parameters of experimental and DFT-relaxed monoclinic structures of Sm_2O_3 and Eu_2O_3. Experimental structures were obtained from the ICSD with collection codes 34291 (Sm_2O_3)[95] and 8056 (Eu_2O_3)[99].

	Expt	Hyb20	Hyb35
Monoclinic Sm_2O_3			
a / Å	14.177	14.198	14.163
b / Å	3.633	3.659	3.648
c / A	8.847	8.880	8.861
β / deg	99.96	99.36	99.34
Monoclinic Eu_2O_3			
a / Å	14.111	14.173	14.122
b / Å	3.602	3.621	3.615
c / A	8.808	8.864	8.826
β / deg	100.037	99.597	99.532

Table B.3: DFT-calculated isotropic hyperfine coupling constants (A_{iso}), quadrupolar coupling constants (C_Q), and the quadrupolar asymmetry parameter η_Q for the monoclinic phase of Sm_2O_3.

Monoclinic Sm_2O_3						
	Hyb20			Hyb35		
Site	A_{iso} / MHz	C_Q / MHz	η_Q	A_{iso} / MHz	C_Q / MHz	η_Q
O1 (4*i*)	−3.78	1.04	0.14	−3.48	1.34	0.31
O2 (4*i*)	−4.92	0.74	0.28	−4.44	0.67	0.35
O3 (4*i*)	−3.60	1.19	0.74	−3.36	1.09	1.00
O4 (4*i*)	−4.38	0.18	0.08	−4.02	0.26	0.91
O5 (2*e*)	−2.22	0.25	0.89	−2.04	0.15	0.24

Table B.4: DFT-calculated isotropic hyperfine coupling constants (A_{iso}), quadrupolar coupling constants (C_Q), and the quadrupolar asymmetry parameter η_Q for the monoclinic phase of Eu_2O_3.

Monoclinic Eu_2O_3						
	Hyb20			Hyb35		
Site	A_{iso} / MHz	C_Q / MHz	η_Q	A_{iso} / MHz	C_Q / MHz	η_Q
O1 (4*i*)	−2.16	1.38	0.38	−2.04	1.57	0.41
O2 (4*i*)	−4.68	0.12	0.69	−4.02	0.37	0.41
O3 (4*i*)	−3.12	0.45	0.42	−2.64	0.67	0.79
O4 (4*i*)	−3.24	0.48	0.78	−3.18	0.46	0.38
O5 (2*e*)	−2.16	0.42	0.43	−2.04	0.17	0.29

Appendix C: Derivations of the Spin of Lanthanides

"…it can be shown that…"

J. H. Van Vleck, The Theory of Electric and Magnetic Susceptibilities
A. T. Casey, Theory and Applications of Molecular Paramagnetism
A. Abragam and B. Bleaney, Electron Paramagnetic Resonance of Transition Ions

In the presence of low-lying electronic states, which are mixed into the ground-state, the electron spin can be calculated using perturbation theory.[81,213] The wavefunction of a given level with total angular momentum quantum numbers J and M is, to first order,

$$\psi_{JM} = |JM\rangle - \sum_{J'M' \neq JM} \frac{\langle JM|\hat{H}^{(1)}|J'M'\rangle}{E_{J'M'} - E_{JM}} |J'M'\rangle, \tag{C.1}$$

where $|JM\rangle$ are the unperturbed wavefunctions and E_{JM} their energies. The perturbing Hamiltonian due to the applied field, B_0, which is assumed to be aligned along z, is given by

$$\hat{H}^{(1)} = \mu_B(\hat{L}_z + 2\hat{S}_z)B_0 = \mu_B(\hat{J}_z + \hat{S}_z)B_0. \tag{C.2}$$

Because the states are eigenfunctions of $\hat{J}_z$, this term does not contribute to the off-diagonal matrix elements in (C.1) and the perturbed wavefunction can be written

$$\psi_{JM} = |JM\rangle - \mu_B B_0 \left(\sum_{J'M' \neq JM} \frac{\langle JM|\hat{S}_z|J'M'\rangle}{E_{J'M'} - E_{JM}} |J'M'\rangle \right). \tag{C.3}$$

The spin of this level can then be calculated by

$$\langle S_z\rangle_{JM} = \langle JM|\hat{S}_z|JM\rangle - \mu_B B_0 \left(\sum_{J'M' \neq JM} \frac{|\langle JM|\hat{S}_z|J'M'\rangle|^2}{E_{J'M'} - E_{JM}} \right). \tag{C.4}$$

The first term can be derived by projecting the spin onto the total angular momentum. This is performed in §C.1 and yields

$$\langle S_z\rangle_{JM}^{(0)} = \langle JM|\hat{S}_z|JM\rangle = (g_J - 1)M, \tag{C.5}$$

where the Landé g-factor is

$$g_J = \frac{3}{2} + \frac{S(S+1) - L(L+1)}{2J(J+1)}. \tag{C.6}$$

The non-zero off-diagonal matrix elements can be shown to be[213,214]

$$\begin{aligned} \langle JM|\hat{S}_z|J+1\ M\rangle &= f(J+1)\sqrt{(J+1)^2 - M^2} \\ \langle JM|\hat{S}_z|J-1\ M\rangle &= f(J)\sqrt{J^2 - M^2} \\ f(J) &= \sqrt{\frac{[J^2 - (L-S)^2][(L+S+1)^2 - J^2]}{4J^2(4J^2-1)}}. \end{aligned} \tag{C.7}$$

Consequently, only adjacent states can be mixed, and only levels with the same M. (C.4) can therefore be written with two terms for mixing of the higher and lower states respectively, noting that if either state does not exist, the corresponding value of $f(J)$ will be zero:

$$\begin{aligned} \langle S_z\rangle_{JM} &= (g_J - 1)M - \mu_B B_0 \left(\frac{f(J+1)^2[(J+1)^2 - M^2]}{\lambda(J+1)} - \frac{f(J)^2[J^2 - M^2]}{\lambda J} \right) \\ &= \langle S_z\rangle_{JM}^{(0)} + \langle S_z\rangle_{JM}^{(1)}, \end{aligned} \tag{C.8}$$

where λ is the spin–orbit coupling constant. The expectation value of the spin over the state J, is then found by a Boltzmann weighting over the levels, M:

$$\langle S_z\rangle_J = \frac{\sum_{-J}^{+J} \langle S_z\rangle_{JM} \exp\left(\frac{-M g_J \mu_B B_0}{kT}\right)}{\sum_{-J}^{+J} \exp\left(\frac{-M g_J \mu_B B_0}{kT}\right)}. \tag{C.9}$$

In the paramagnetic regime, $kT \gg g_J \mu_B B_0$, so that the denominator is approximately $2J + 1$, and the exponential term in the numerator can be expanded to first order:

$$\begin{aligned} \langle S_z\rangle_J &= \frac{1}{2J+1} \sum_{M=-J}^{+J} \left(\langle S_z\rangle_{JM}^{(0)} + \langle S_z\rangle_{JM}^{(1)} \right) \left(1 - \frac{M g_J \mu_B B_0}{kT} \right) \\ &= \frac{1}{2J+1} \sum_{M=-J}^{+J} \left(\langle S_z\rangle_{JM}^{(0)} - \frac{M g_J \mu_B B_0 \langle S_z\rangle_{JM}^{(0)}}{kT} + \langle S_z\rangle_{JM}^{(1)} + \frac{M g_J \mu_B B_0 \langle S_z\rangle_{JM}^{(1)}}{kT} \right). \end{aligned} \tag{C.10}$$

The first and last terms sum to zero because they contain only odd powers of M. The second term is

$$\frac{1}{2J+1}\sum_{M=-J}^{+J} -\frac{\mu_B B_0 g_J\left(g_J-1\right)M^2}{kT} = -\frac{\mu_B B_0 g_J\left(g_J+1\right)}{3kT}J(J+1), \qquad \text{(C.11)}$$

using the fact that $\sum_{-J}^{+J} M^2 = \frac{1}{3}J(J+1)(2J+1)$. This is the Curie contribution to the spin.

Performing the same summations on the third term in (C.10),

$$\frac{1}{2J+1}\sum_{M=-J}^{+J}\langle S_z\rangle_{JM}^{(1)} = -\mu_B B_0\left[\frac{f(J+1)^2\left[(J+1)^2-\frac{1}{3}J(J+1)\right]}{\lambda(J+1)} - \frac{f(J)^2\left[J^2-\frac{1}{3}J(J+1)\right]}{\lambda J}\right]$$

$$= -\frac{\mu_B B_0}{3\lambda}[f(J+1)^2(2J+3) - f(J)^2(2J-1)]$$

$$= -\frac{\mu_B B_0}{3\lambda}\left\{\frac{[(J+1)^2-(L-S)^2][(L+S+1)^2-(J+1)^2](2J+3)}{4(J+1)^2(2J+1)(2J+3)}\right.$$

$$\left. -\frac{[J^2-(L-S)^2][(L+S+1)^2-J^2](2J-1)}{4J^2(2J+1)(2J-1)}\right\}$$

$$= -\frac{\mu_B B_0}{3\lambda}\frac{1}{4J^2(J+1)^2(2J+1)}\{[(J+1)^2-(L-S)^2][(L+S+1)^2-(J+1)^2]J^2$$

$$-[J^2-(L-S)^2][(L+S+1)^2-J^2](J+1)^2\}$$

$$= -\frac{\mu_B B_0}{3\lambda}\frac{1}{4J^2(J+1)^2(2J+1)}[(L-S)^2(L+S+1)^2-J^2(J+1)^2][J^2-(J+1)^2]$$

$$= -\frac{\mu_B B_0}{3\lambda}\frac{1}{4J^2(J+1)^2}[(L-S)^2(L+S+1)^2-J^2(J+1)^2]$$

$$= -\frac{\mu_B B_0}{3\lambda}\frac{[(S-L)(L+S+1)]^2-[J(J+1)]^2}{4J^2(J+1)^2}$$

$$= -\frac{\mu_B B_0}{3\lambda}\frac{[S(S+1)-L(L+1)]^2-[J(J+1)]^2}{4J^2(J+1)^2}$$

$$= -\frac{\mu_B B_0}{3\lambda}\frac{[S(S+1)-L(L+1)+J(J+1)][S(S+1)-L(L+1)-(J+1)]}{[2J(J+1)]^2}$$

$$= -\frac{\mu_B B_0\left(g_J-1\right)\left(g_J-2\right)}{3\lambda} \qquad \text{(C.12)}$$

where, in the penultimate step, the numerator is a difference of two squares. This is the Van Vleck, temperature independent contribution to the spin. Once again, the expression in terms

of g_J is essentially fortuitous, rather than reflecting the fundamental importance of the Landé g-factor.

C.1 Calculating $\langle S_z \rangle_{JM}$

The Fermi contact shift is dependent on the z component of the spin, $\langle S_z \rangle_J$. When both spin, $\boldsymbol{S}$, and orbital, $\boldsymbol{L}$, angular momenta are present, in the Russell–Saunders coupling limit, they couple to give a total angular momentum, $\boldsymbol{J}$. The $\boldsymbol{S}$ and $\boldsymbol{L}$ can then be considered to be processing rapidly about $\boldsymbol{J}$, so that only their projection along $\boldsymbol{J}$ remains. To calculate $\langle S_z \rangle_J$, first the projection of $\boldsymbol{S}$ along $\boldsymbol{J}$ must be calculated:

$$\begin{aligned} \hat{\boldsymbol{S}}_J &= \left(\frac{\hat{\boldsymbol{S}}.\hat{\boldsymbol{J}}}{|\hat{\boldsymbol{J}}|}\right)\left(\frac{\hat{\boldsymbol{J}}}{|\hat{\boldsymbol{J}}|}\right) \\ &= \left(\frac{\hat{\boldsymbol{S}}.\hat{\boldsymbol{J}}}{|\hat{\boldsymbol{J}}|^2}\right)\hat{\boldsymbol{J}}. \end{aligned} \tag{C.13}$$

Then to find $\hat{\boldsymbol{S}}.\hat{\boldsymbol{J}}$, consider $\left(\hat{\boldsymbol{S}}+\hat{\boldsymbol{J}}\right)^2$,

$$\begin{aligned} \left(\hat{\boldsymbol{S}}+\hat{\boldsymbol{J}}\right)^2 &= \hat{\boldsymbol{S}}^2+\hat{\boldsymbol{J}}^2+2\hat{\boldsymbol{S}}.\hat{\boldsymbol{J}} \\ \hat{\boldsymbol{S}}.\hat{\boldsymbol{J}} &= \frac{1}{2}\left[\left(\hat{\boldsymbol{S}}+\hat{\boldsymbol{J}}\right)^2-\hat{\boldsymbol{S}}^2+\hat{\boldsymbol{J}}^2\right]. \end{aligned} \tag{C.14}$$

Using $\hat{\boldsymbol{J}} = \hat{\boldsymbol{L}} + \hat{\boldsymbol{S}}$,

$$\left(\hat{\boldsymbol{S}}+\hat{\boldsymbol{J}}\right)^2 = \left(\hat{\boldsymbol{L}}+2\hat{\boldsymbol{S}}\right)^2 = \hat{\boldsymbol{L}}^2+4\hat{\boldsymbol{S}}^2+4\hat{\boldsymbol{L}}.\hat{\boldsymbol{S}}, \tag{C.15}$$

and, finding $\hat{\boldsymbol{L}}.\hat{\boldsymbol{S}}$ from

$$\begin{aligned} \hat{\boldsymbol{J}}^2 &= \left(\hat{\boldsymbol{L}}+\hat{\boldsymbol{S}}\right)^2 = \hat{\boldsymbol{L}}^2+\hat{\boldsymbol{S}}^2+2\hat{\boldsymbol{L}}.\hat{\boldsymbol{S}} \\ \hat{\boldsymbol{L}}.\hat{\boldsymbol{S}} &= \frac{1}{2}\left[\hat{\boldsymbol{J}}^2-\hat{\boldsymbol{L}}^2-\hat{\boldsymbol{S}}^2\right], \end{aligned} \tag{C.16}$$

then, substituting (C.16) into (C.15) and then into (C.14),

$$\hat{\boldsymbol{S}}.\hat{\boldsymbol{J}} = \frac{1}{2}\left[\hat{\boldsymbol{J}}^2+\hat{\boldsymbol{S}}^2-\hat{\boldsymbol{L}}^2\right]. \tag{C.17}$$

Substituting (C.17) into (C.13) and replacing the squared operators by their eigenvalues,

$$\widehat{\boldsymbol{S}}_J = \frac{J(J+1) + S(S+1) - L(L+1)}{2J(J+1)}\hat{\boldsymbol{J}} = \big(g_J - 1\big)\hat{\boldsymbol{J}}. \tag{C.18}$$

As shown, this is typically written in terms of the Landé g-factor, equation (C.6), although it should be stressed that this is simply for convenience, and does not imply that the spin arises from the magnetic moment given by g_J.

The z component of the spin is then found by projecting along z:

$$\begin{aligned} \hat{S}_z &= \widehat{\boldsymbol{S}}_{\boldsymbol{J}}.\boldsymbol{z} = \big(g_J - 1\big)\hat{\boldsymbol{J}}.\boldsymbol{z} = \big(g_J - 1\big)\hat{J}_z \\ \langle S_z\rangle_{JM} &= \big(g_J - 1\big)\langle J_z\rangle_{JM} = \big(g_J - 1\big)M \end{aligned} \tag{C.19}$$

C.2 The Landé *g*-factor when $J = 0$

When $J = 0$, for instance in the ground state of Eu^{3+}, the Landé g-factor has an undefined value using the usual formula:

$$g_J = \frac{3}{2} + \frac{S(S+1) - L(L+1)}{2J(J+1)}. \tag{C.20}$$

However, by exploiting the fact that it is only possible to have $J = 0$ if $J = S - L$, the formula can be rewritten,[12] and by refactorising the numerator, this allows cancellation of the division by zero:

$$\begin{aligned} g_J &= \frac{3}{2} + \frac{S(S+1) - L(L+1)}{2(S-L)(S-L+1)} \\ g_J &= \frac{3}{2} + \frac{(S-L)(S+L+1)}{2(S-L)(S-L+1)} \\ g_J &= \frac{3}{2} + \frac{(S+L+1)}{2(S-L+1)} \\ g_J &= 2 + L, \end{aligned} \tag{C.21}$$

where in the last step $L = S$ is used, which must also be the case if $J = 0$.

Appendix D: XRD data for H_xVO_2

Figures D.1 to D.7 show the powder XRD patterns of selected H_xVO_2 samples, the identified phases and the Rietveld refinements. The purpose of the analysis is to identify the phases present and quantify the phase fractions, but the data is of insufficient quality for a full refinement of the atomic positions and displacement parameters and this was not attempted; these are the most likely causes of the discrepancies between the Rietveld refinements and the data. The atomic positions were fixed as shown in Table D.1.

Table D.1: Atomic positions in VO_2 and H_xVO_2.

Phase	**Atom**	**x**	**y**	**z**
VO_2 M	V	0.240	0.982	0.032
	O	0.106	0.21	0.203
	O	0.416	0.735	0.316
H_xVO_2 O1a & O1b	V	0	0	0
	O	0.279	0.311	0

The zero error was determined for the films from the PTFE reflection at $2\theta = 18.21^o$. A preferred orientation along the [110] direction was observed for the orthorhombic phases and corrected for; although the preferred orientation effect could be removed for the Pd/H_xVO_2 sample by sprinkling the powder on vacuum grease, the signal intensity was then much lower, and this was also not possible for the PTFE films. The lattice parameters and phase fractions were then refined (Table D.2).

To determine the hydrogen content of the orthorhombic phases from the cell parameters, the relationship between the orthorhombic distortion and the hydrogen content was determined from the data of Chippindale et al.[169] (Figure D.8). The total hydrogen content of the sample could then be predicted by multiplying the hydrogen content of each phase by the phase fraction; the contribution from the monoclinic phase, if present, cannot be reliably determined from the cell parameters, so is not included in this approach.

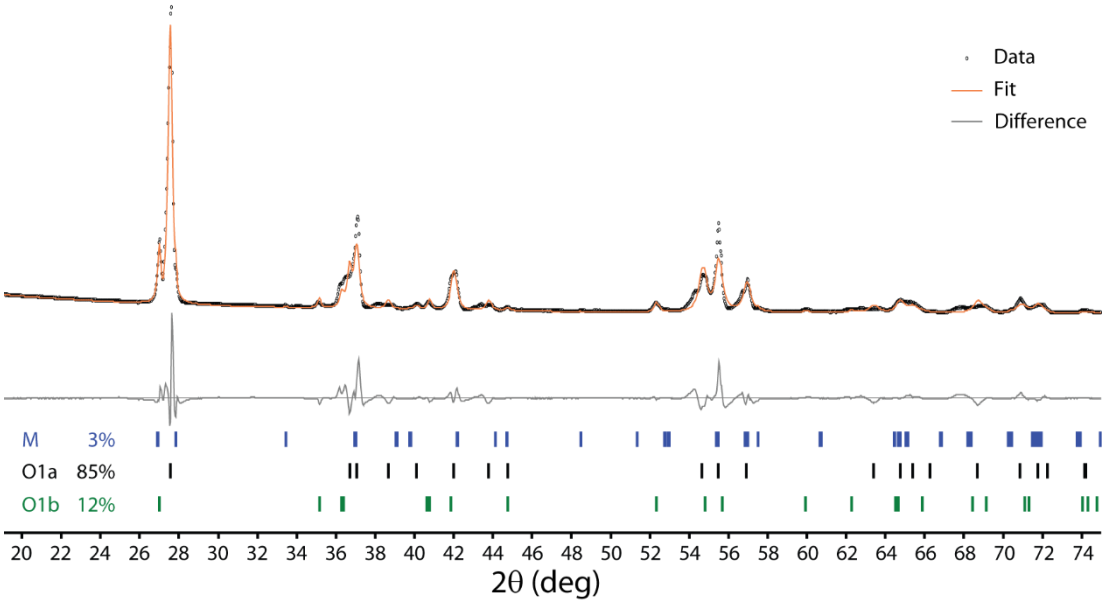

Figure D.1: XRD pattern and Rietveld refinement of VO_2 catalytically hydrogenated at 180 ºC with 25% H_2/N_2.

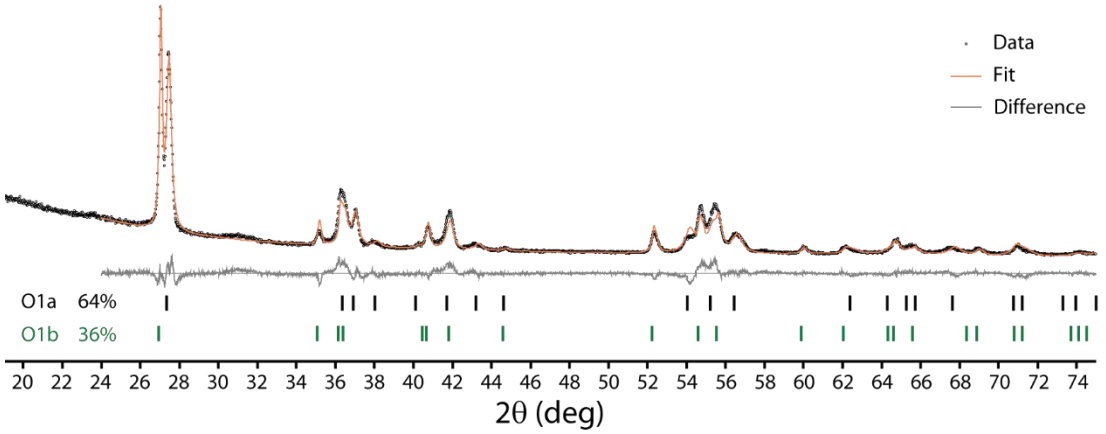

Figure D.2: XRD pattern and Rietveld refinement of VO_2 catalytically hydrogenated at 220 ºC with 5% H_2/Ar.

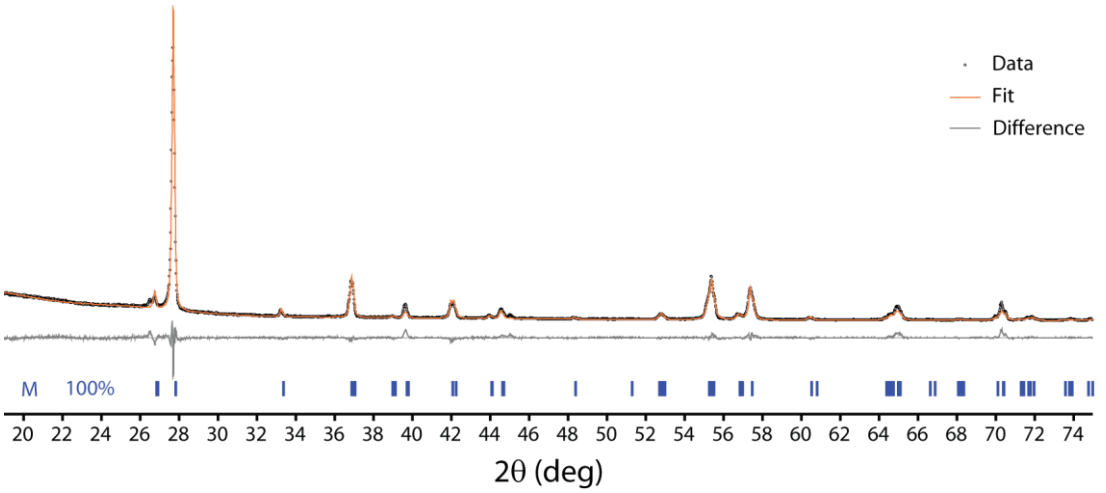

Figure D.3: XRD pattern and Rietveld refinement of VO_2 electrochemically hydrogenated at 21 ºC.

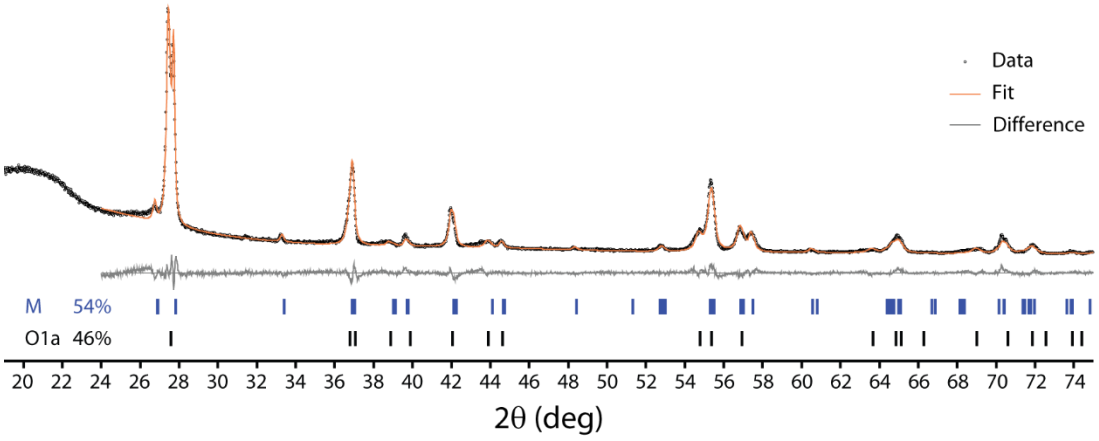

Figure D.4: XRD pattern and Rietveld refinement of VO_2 electrochemically hydrogenated at 50 ºCc.

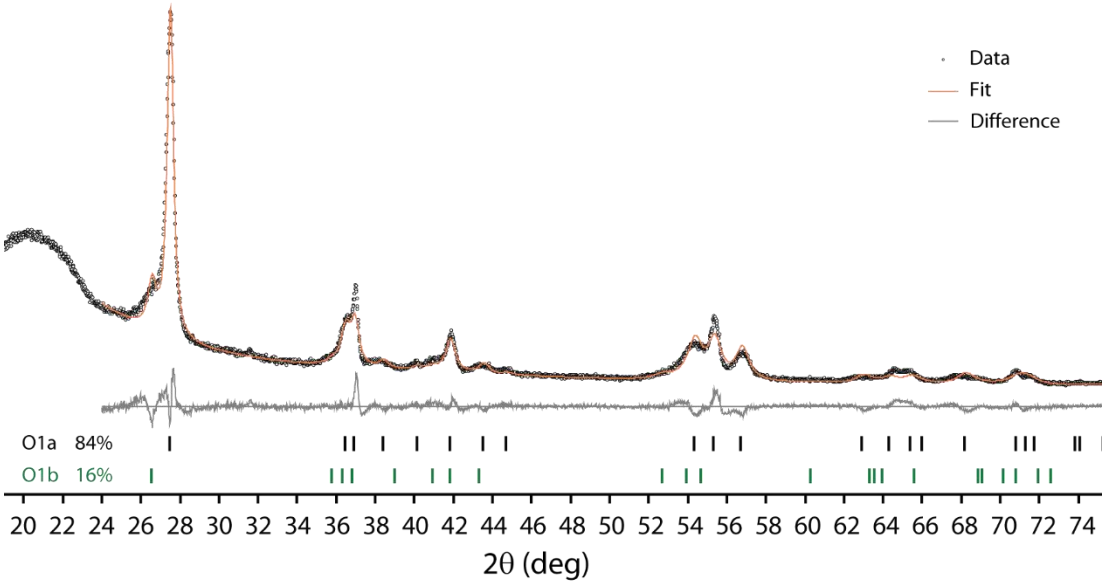

Figure D.5: XRD pattern and Rietveld refinement of VO_2 electrochemically hydrogenated at 100 ºC

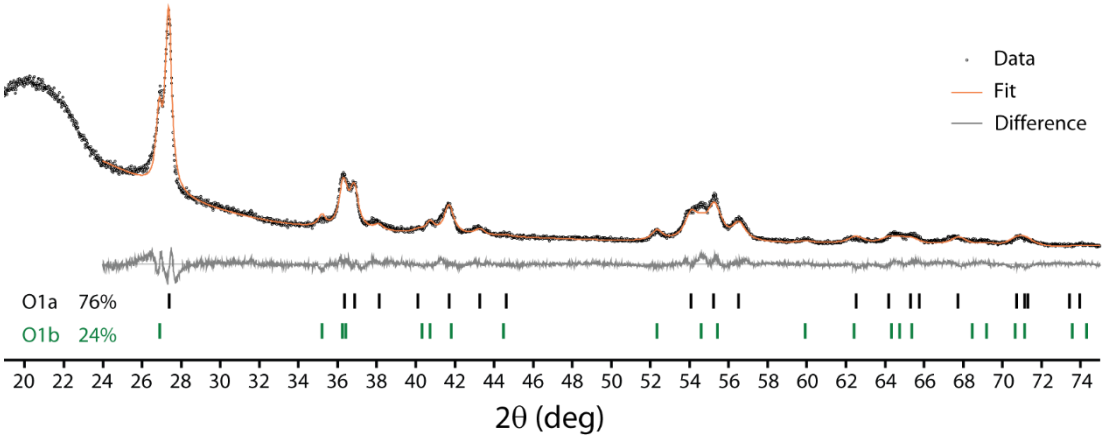

Figure D.6: XRD pattern and Rietveld refinement of VO_2 electrochemically hydrogenated at 150 ºC.

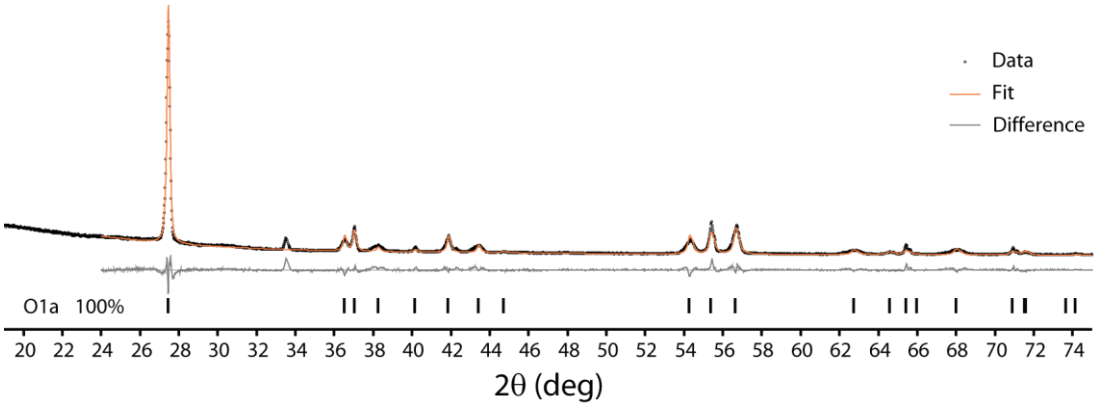

Figure D.7: XRD pattern and Rietveld refinement of VO_2 electrochemically hydrogenated at 200 ºC. The peak at $2\theta = 33.5^{o}$ is ascribed to an unknown impurity or minor product.

Table D.2: Phase fractions and lattice parameters of the monoclinic and two orthorhombic phases in different H_xVO_2 samples, as well as the hydrogen content, x, of the phase as determined from the orthorhombic distortion. The contribution of the phase to the total hydrogen content of the sample, x_{eff}, is found by multiplying the hydrogen content of the phase by its phase fraction, and the total hydrogen content of the sample, x_{tot}, is then predicted by summing the contributions from each phase.

		Pristine VO_2	**Catalytic Hydrogenation**		**Electrochemical Hydrogenation**				
			180 ºC 25% H_2	220 ºC 5% H_2	21 ºC	50 ºC	100 ºC	150 ºC	200 ºC
M	wt%	100%	2.6%		100%	54.1%			
	a	5.753	5.753		5.756	5.755			
	b	4.526	4.526		4.527	4.526			
	c	5.383	5.383		5.384	5.380			
	β	122.6	122.6		122.6	122.6			
O1a	wt%		85.5%	64.2%		45.9%	83.5%	75.6%	100.0%
	a		4.494	4.494		4.515	4.491	4.494	4.489
	b		4.654	4.729		4.631	4.688	4.718	4.704
	c		2.877	2.895		2.874	2.895	2.899	2.885
	x		0.329	0.508		0.224	0.417	0.484	0.462
	x_{eff}		0.280	0.326		0.103	0.348	0.366	0.462
O1b	wt%		11.9%	35.8%			16.5%	24.4%	
	a		4.444	4.455			4.545	4.470	
	b		4.941	4.935			4.944	4.930	
	c		2.981	2.990			2.895	2.974	
	x		1.144	1.103			0.889	1.051	
	x_{eff}		0.153	0.395			0.147	0.256	
Total	x_{tot}		0.433	0.721		0.103	0.495	0.622	0.462

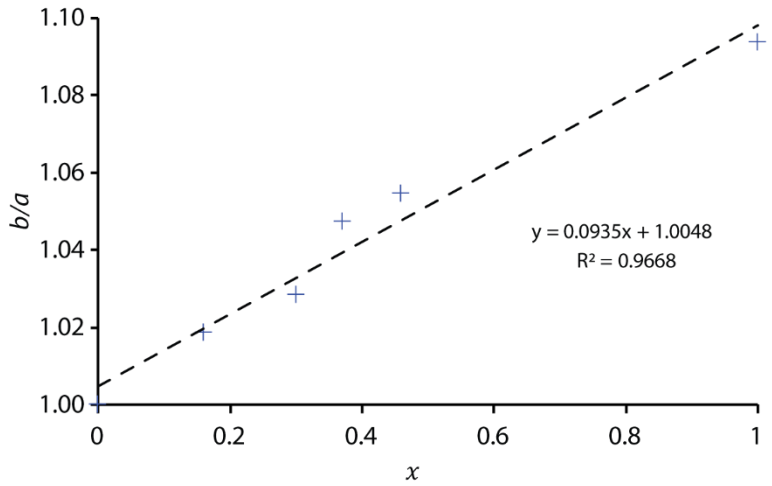

Figure D.8: The orthorhombic distortion, b/a, plotted against the hydrogen content, x in H_xVO_2, for the data of Chippindale et al.[169]

Figure D.9 shows a comparison of the hydrogen contents determined by quantitative ^{1}H NMR and Rietveld analysis of the powder XRD patterns. The positive correlation supports the assignment of the lower and higher shift regions of the ^{1}H NMR spectrum to the O1a and O1b phases respectively, and the use of the orthorhombic distortion to predict the hydrogen content from the unit cell parameters. However, there is also both scatter in the values greater than the predicted uncertainty as well as systematic deviation. The scatter is most likely due the difficulty in accurately determining the phase fractions from Rietveld analysis with broad peaks, as small changes in amplitude correspond to large changes in mass fraction. The quantitative ^{1}H NMR also generally predicts a lower hydrogen content than the XRD analysis; this is most likely due to NMR skin depth effects: the metallic nature of the samples reduces radiofrequency penetration so that the sample is not fully excited and the ^{1}H NMR signal is reduced. This was be circumvented for the catalytically hydrogenated Pd/H_xVO_2 samples by grinding with KBr, and for these samples, the NMR and XRD determined hydrogen contents are in better agreement. However, for the electrochemically hydrogenated VO_2, the PTFE films could not be ground with KBr, and although the presence of PTFE reduces the skin depth effect, there is still a notable contribution. It can also be seen that the skin depth effect contributes mostly to the metallic O1a phase, rather than to the paramagnetic O1b phase.

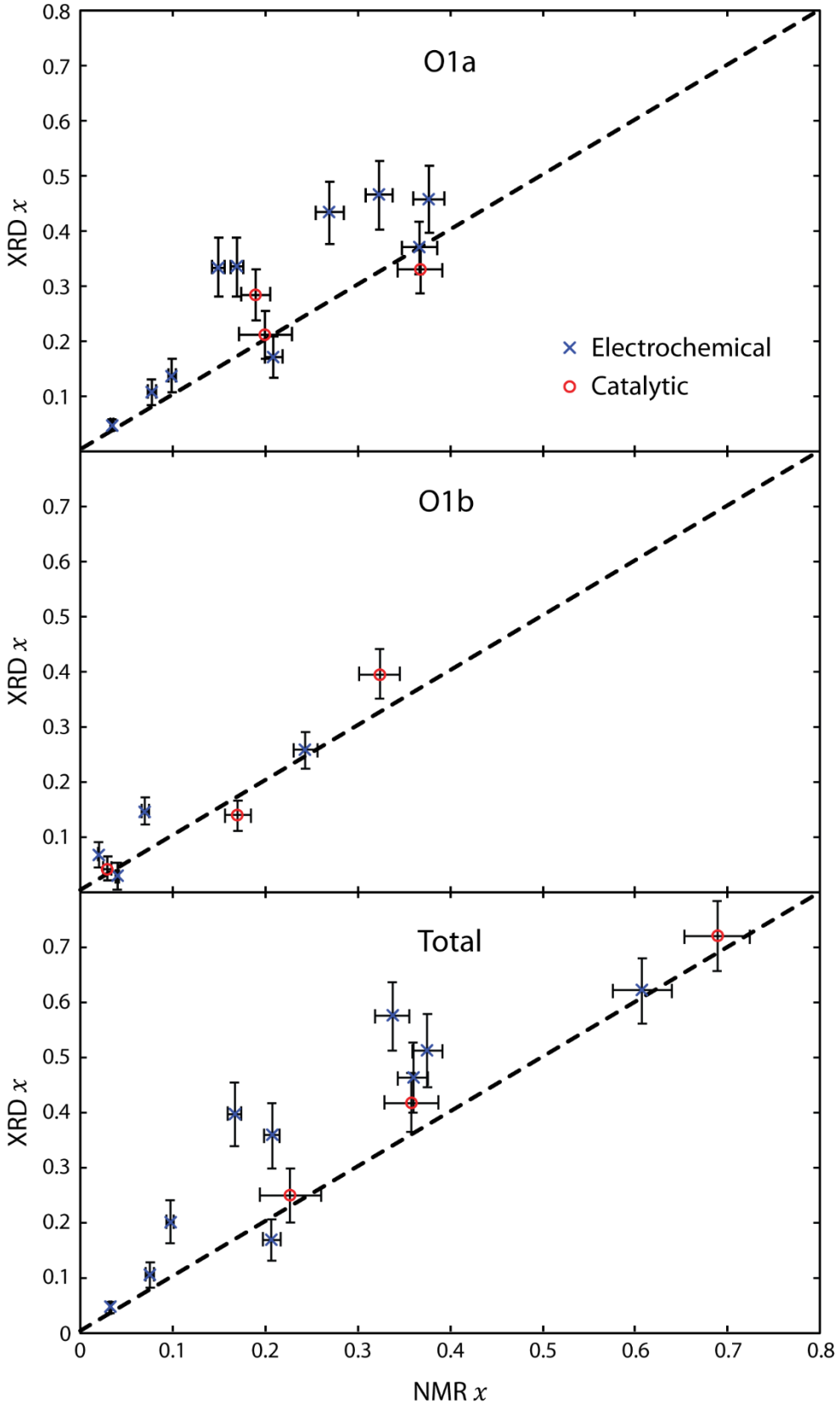

Figure D.9: Comparison of the hydrogen content of each orthorhombic phase and the total hydrogen content for various H_xVO_2 samples as determined by quantitative ^1H NMR and by the unit cells and phase fractions from Rietveld refinement of the powder XRD patterns. The dashed line indicates 1:1 agreement between the methods.

Variable Temperature XRD

To determine the effect of heating to above the MIT temperature on the two-phase M + O1a region of the phase diagram, variable temperature XRD patterns were recorded for VO_2 electrochemically metallised at 50 °C, $x \approx 0.1$. XRD patterns were recorded at room temperature, 100 °C, and then room temperature again, using a heated sample holder built in-house, in reflection mode, with a beryllium window. Figure D.10 shows two expanded sections of the XRD patterns: in both room temperature patterns, there are two reflections around 2θ = 28° corresponding to the M and O1a phases, which coalesce into the single rutile reflection at 100 °C. The same effect is observed in the 2θ = 54° – 58° region, and in particular the orthorhombic peak at 2θ = 54.7° is not present in the 100 °C pattern. This shows that the two-phase M + O1a region of the phase diagram at room temperature becomes a single rutile (R) phase above the MIT, due to a greater solubility of hydrogen in the rutile phase compared to the monoclinic phase. The M and O1a phases are again observed after cooling down to room temperature, indicating that this phase transition is reversible.

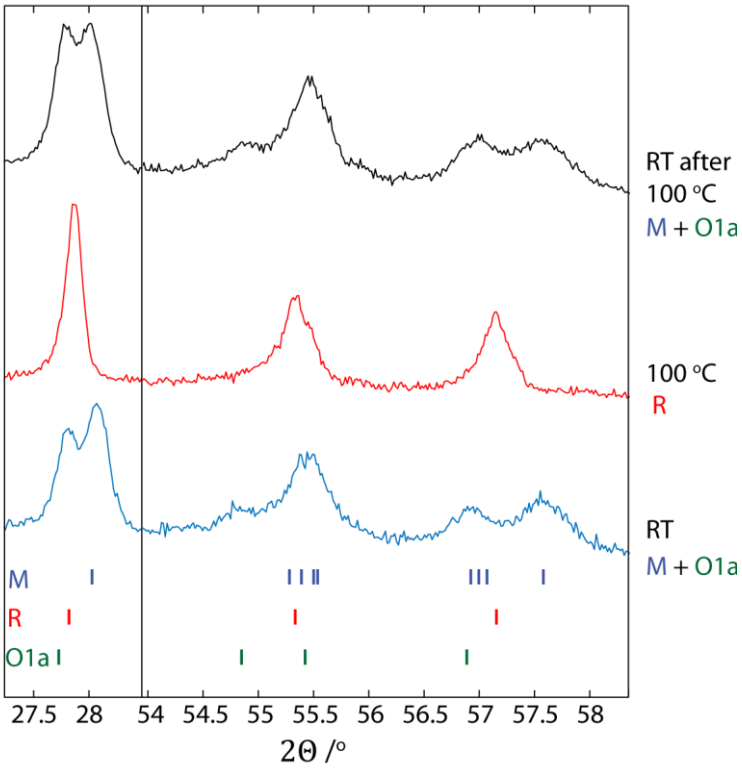

Figure D.10: Selected regions of the XRD patterns of VO_2 electrochemically metallised at 50 °C, recorded at room temperature, 100 °C, and then room temperature again.